

Corrosion of Aluminum Alloys in Wastewater Treatment Aeration Tanks

by

John Scott Pavelich

A thesis submitted in partial fulfillment of the requirements for the degree of

Master of Science

in

Materials Engineering

Department of Chemical and Materials Engineering  
University of Alberta

© John Scott Pavelich, 2017

# Abstract

Severe localized corrosion was found throughout an aeration tank of a modular wastewater treatment plant. Specifically, pitting, crevice corrosion, galvanic corrosion, and intergranular corrosion (IGC) were observed on the 5000 and 6000 series aluminum alloys used in the tank's construction. One of the suspected environmental causes of corrosion was an aeration tank process additive, namely a coagulant – either aluminum sulphate (Alum) or polyaluminum chloride (PACl; Isopac). Laboratory scale corrosion cells were designed to isolate, simulate, and evaluate the corrosivity of the coagulants (in relevant quantities) on the metallic alloys of construction. Additionally, due to presence of deposit found throughout the tank (resulting in under-deposit corrosion), fabricated crevices were installed on the tested alloys to help simulate crevice corrosion environments. The solution conditions in the cells were monitored throughout the duration of the immersion testing in order to assess whether the cells were within normal operating conditions of the corroded aeration tank. A series of material characterizations and mass change measurements were performed on the corrosion coupons post-testing to evaluate and rank the corrosivity of the coagulants.

Results from the laboratory scale testing revealed that both coagulants led to localized corrosion of the 5000 and 6000 series aluminum alloys – in the form of pitting, crevice corrosion, and IGC. Therefore, it can be concluded that neither Isopac nor Alum should be used in aeration tanks constructed of the aluminum alloys tested in this study. Whilst the immersion testing did not simulate all

conditions observed and measured in the corroded tank, the testing did allow for the study of the isolated, corrosive effects of either Isopac or Alum on the tested alloys. It can be reasoned that even though the coagulants led to similar corrosion observed in the tank, the coagulants themselves are not the sole cause of the aforementioned corrosion; ultimately, additional factors and conditions in the aeration tank could be deemed more corrosive than merely the coagulants.

# Dedication

This work is dedicated to my family.

Thank you for your unwavering support and allowing me to forge my own future.

# Acknowledgements

I would first like to thank my mentor, Dr. John Nychka, whom I have been fortunate to have worked with during my undergraduate and graduate education. It has truly been an honour and privilege to have been trained and provided guidance from such an innovative researcher and teacher. I will always be grateful for his kindness, patience, and utmost understanding.

Next, this project would not have been possible without the excellent assistance of Terry Runyon. Her efforts and support have helped me greatly through both the celebrated and challenging aspects of this project.

I am also grateful to the staff at EPCOR, particularly David Rector who brought this project to the university and financed the research performed within this thesis. I would also like to thank Marco Braat, and the rest of the wastewater treatment operations and maintenance staff, who facilitated and worked with myself and John to conduct the necessary site inspections and failure analyses; ultimately providing the foundation to this research. Next, I would like to thank the various project managers – David Lesanko, Saifuddin Molla, and Kelvin Guobadia – who I got to interface with during the course of my degree. Finally, a special thanks to Dr. Rasha Maal-Bared for providing insight into wastewater microbiology, and a much needed “biological perspective” to this project.

I am also thankful for the discussions and support of the former and current group members of the Materials at the Interface lab. Their feedback and outside perspectives were an invaluable asset. Additional thanks to both Dr. James Sawada and Dr. Stojan Djokic for their valuable discussions on chemistry/electrochemistry and insights into conducting research.

Next, I would like to thank the various technical staff I had the privilege of collaborating with during graduate school. First, thanks to Gayle Hatchard, Dr.

Nathan Gerein, and Dr. Mengshan Yu for both performing and teaching me how to collect beautiful SEM images and EDX data. Thanks to both Shiraz Merali and Diane Caird for conducting XRD. An additional, special thanks to Diane for aiding in both the interpretation of the collected XRD patterns, and the development of the sample preparation procedure presented herein. Next, thanks to Wayne Moffat and his laboratory staff for performing the necessary FTIR work, and recommending the particular techniques selected, and subsequent sample preparation methods utilized, in this work. Thanks to Guangcheng Chen for performing ICP-MS, and Rod Arychuk and the staff at Sherritt Technologies for performing ICP-MS and ICP-OES on the metal alloys used herein. Thanks to the staff in the CME machine shop for providing valuable consultations in the fabrication of the corrosion coupons used in the immersion testing. Finally, thanks to Walter Boddez for lending me the power supply, which allowed for the surprisingly challenging, electrolytic etching of the 5000 series aluminum alloys.

I would also like to thank my family for their love and support. In particular, I am especially appreciative of my mother, Audrey, and father, Brad – both of whom have Master’s degrees. It feels fitting to recite the old – and in this case, slightly adjusted – adage: like father, like mother, like son.

Last, but not least, a special thanks to my friends who have been supportive of my continuous pursuit of further education. I truly appreciate the time I got to spend with them, which, in turn, provided much needed respite during this degree.

# Table of Contents

List of Figures.....	xii
List of Tables .....	xxxvi
List of Abbreviations .....	xl
List of Symbols .....	xlii
<b>Chapter 1 – Introduction</b> .....	<b>1</b>
<b>1.1 – Project Background</b> .....	<b>1</b>
<b>1.2 – Thesis Structures and Objectives</b> .....	<b>8</b>
<b>1.3 – References</b> .....	<b>10</b>
<b>Chapter 2 – Background</b> .....	<b>11</b>
<b>2.1 – Wastewater Treatment Process and Aeration Tanks</b> .....	<b>11</b>
<b>2.2 – Relevant Material Applications and Failures in WWTPs</b> .....	<b>22</b>
<b>2.3 – Basics of Electrochemical and Corrosion Reactions</b> .....	<b>25</b>
<b>2.4 – Corrosion Thermodynamics</b> .....	<b>29</b>
<b>2.5 – Corrosion Kinetics</b> .....	<b>33</b>
<b>2.6 – Modes of Corrosion</b> .....	<b>36</b>
2.6.1 – Pitting Corrosion .....	38
2.6.2 – Crevice Corrosion.....	43
2.6.3 – Galvanic Corrosion.....	48
2.6.4 – Intergranular Corrosion .....	52
<b>2.7 – Passivity and Depassivation of Aluminum</b> .....	<b>54</b>
2.7.1 – Environmental Factors.....	57
2.7.2 – Metallurgical and Stress Factors .....	60
<b>2.8 – Summary</b> .....	<b>61</b>

<b>2.9 – References</b> .....	62
<b>Chapter 3 – Design of Experiments</b> .....	72
<b>3.1 – Design of Lab Scale Immersion Corrosion Cell Study</b> .....	73
3.1.1 – Coupon Design and Fabrication .....	75
3.1.2 – Electrolyte and Apparatus Design and Fabrication .....	84
3.1.3 – In Situ Monitoring of Key Process Indicators .....	86
<b>3.2 – Coupon Characterization</b> .....	89
3.2.1 – Macro Photography .....	90
3.2.2 – Stereo Microscopy.....	93
3.2.3 – Deposit Characterization .....	93
3.2.3.1 – <i>Energy Dispersive X-ray (EDX) Spectroscopy</i> .....	93
3.2.3.2 – <i>X-ray Diffraction (XRD)</i> .....	94
3.2.3.3 – <i>Fourier Transform Infrared (FTIR) Spectroscopy</i> .....	95
3.2.4 – Mass Change Measurements .....	96
<b>3.3 – References</b> .....	97
<b>Chapter 4 – Results and Discussion</b> .....	100
<b>4.1 – Coupon Characterization</b> .....	100
4.1.1 – Macro Photography .....	101
4.1.2 – Stereo Microscopy.....	105
4.1.3 – Deposit Characterization .....	125
4.1.3.1 – <i>Energy Dispersive X-ray (EDX) Spectroscopy</i> .....	125
4.1.3.2 – <i>X-ray Diffraction (XRD)</i> .....	130
4.1.3.3 – <i>Fourier Transform Infrared (FTIR) Spectroscopy</i> .....	131
4.1.4 – Mass Change Measurements .....	137
<b>4.2 – In Situ Monitoring Results</b> .....	140

<b>4.3 – Summary</b> .....	148
<b>4.4 – References</b> .....	150
<b>Chapter 5 – Conclusions and Future Work</b> .....	152
<b>5.1 – Conclusions</b> .....	152
<b>5.2 – Future Work</b> .....	155
<b>Bibliography</b> .....	157
<b>Appendix A – Examination of Aeration Tank Components</b> .....	173
<b>A-1.0 – Introduction</b> .....	173
A-1.1 – Background .....	173
A-1.2 – Summary of Inspection Findings .....	174
A-1.3 – Scope .....	182
A-1.4 – Summary of Failure Investigation.....	184
<b>A-2.0 – Investigation</b> .....	187
A-2.1 – Visual and Non-destructive Examination .....	187
A-2.1.1 – Wall .....	187
A-2.1.2 – Floor .....	189
A-2.1.3 – Tubular Tie .....	195
A-2.1.4 – Aeration Line Bracket .....	204
A-2.2 – Chemical Analysis .....	212
A-2.2.1 – Inductively Coupled Plasma Mass Spectroscopy (ICP-MS) and ICP Optical Emission Spectroscopy (ICP-OES) .....	214
A-2.2.2 – X-Ray Diffraction (XRD) .....	217
A-2.2.3 – Fourier Transform Infrared Spectroscopy (FTIR) .....	219
A-2.3 – Scanning Electron Microscopy (SEM) .....	220
A-2.3.1 – Floor .....	220

<i>A-2.3.1.1 – Pit Cross-section</i> .....	220
<i>A-2.3.1.2 – Pit Deposit</i> .....	222
A-2.3.2 – Tubular Tie.....	223
<i>A-2.3.2.1 – Unmounted Cross-section</i> .....	223
<i>A-2.3.2.2 – Mounted Cross-section</i> .....	227
<i>A-2.3.2.3 – Pit Deposit</i> .....	230
<i>A-2.3.2.4 – Grain Line Scans</i> .....	232
A-2.3.3 – Aeration Line Bracket.....	235
<i>A-2.3.3.1 – Mounted Cross-section and Pit Deposit</i> .....	235
A-2.3.4 – Deposit Compositions .....	242
A-2.4 – Metallographic Examination and Hardness Testing .....	245
A-2.4.1 – Optical Microscopy (OM).....	246
<i>A-2.4.1.1 – Wall Cross-section</i> .....	246
<i>A-2.4.1.2 – Floor Pit Cross-section</i> .....	247
<i>A-2.4.1.3 – Tubular Tie – Hole Circumference Cross-section</i> .....	252
<i>A-2.4.1.4 – Tubular Tie – Hole Axial Cross-section</i> .....	258
<i>A-2.4.1.5 – Tubular Tie – End Circumference Cross-section</i> .....	264
<i>A-2.4.1.6 – Aeration Line Bracket Cross-section</i> .....	266
A-2.4.2 – Hardness Testing (HT).....	274
<b>A-3.0 – Discussion</b> .....	275
A-3.1 – Corrosion Modes and Environmental Causes .....	275
A-3.2 – Component Fabrication.....	280
<b>A-4.0 – Conclusions and Path Forward</b> .....	283
A-4.1 – Conclusions .....	283
A-4.2 – Path Forward .....	285

<b>A-5.0 – Sample Calculations</b> .....	286
<b>A-6.0 – References</b> .....	287
<b>Appendix B – Volume to Surface Area Ratio of Aeration Tank</b> .....	290
<b>B-1.0 – Calculations</b> .....	290
<b>B-2.0 – References</b> .....	293
<b>Appendix C – Raw Process Data from Aeration Tank</b> .....	294
<b>Appendix D – Corrosion Coupon Photographs</b> .....	299
<b>Appendix E – Fourier Transform Infrared (FTIR) Peak Data</b> .....	306
<b>E-1.0 – Peak Data</b> .....	306
<b>E-2.0 – References</b> .....	308
<b>Appendix F – Corrosion Cell Monitoring Data</b> .....	309

# List of Figures

Figure 1-1: Through wall corrosion (indicated by the dotted oval) of a tubular tie immediately adjacent to aeration piping [1]. .....3

Figure 1-2: “Pit measurements taken from the deepest identified pit on the floor of the aeration tank. After brushing deposits clear.” [1] The gauge indicates that the pit is ~4 mm deep (~42% of the thickness assuming 9.53 mm / 0.375 inch thickness) [1]......3

Figure 1-3: Partial schematic of the aeration tank, along with images (including macrophotographs, cross-sections, and micrographs) acquired from key locations/aluminum alloy components, namely: collected wall cross-section (a), pitting on wall tooling marks (b), tubular tie in contact with aeration piping (c), tank floor (d), and an aeration piping bracket (e). Four modes of corrosion (pitting, crevice, galvanic, and IGC) were identified. Deposit(s) were removed to aid in the macrophotography. Scale on ruler is in mm. ....4

Figure 1-4: Complex systems map of some of the factors, and their relationships, which affect the corrosion of aluminum. The solid arrows indicate *there is* a relationship while the dashed arrows indicate *there may be* relationship. The factors in the light blue boxes were controlled in the immersion testing. Conversely, the factors in the purple boxes were established at the start, and monitored over the duration, of testing. Note that only dissolved oxygen concentration and chloride concentration were monitored in the oxidizing agents and process fluid composition, respectively. ....7

Figure 2-1: Basic overall process flow diagram of the WWTP in this study. For simplicity, all three trains are combined into one in the figure and are contained within the pink-dashed box. The aeration tank and identified corrosion is contained within the “Activated Sludge Bioreactor”, which is emphasized by the red asterisk.

.....16

Figure 2-2: Representative image of a functioning aeration tank in the WWTP examined in this study. The camera is located at the upstream end of the tank (opposite end from the anoxic zone). The arrow points in the direction of the flow of process fluid.....19

Figure 2-3: The Pourbaix diagram for the aluminum-water system at 25 °C [36,39]. Generally, the concentration of aluminum ions in solution is assumed to be equal to  $10^{-6}$ ; therefore, the lines with -6 should be used as the boundaries. (Reproduced with permission from NACE International, Houston, TX. All rights reserved. [39]. © NACE International 1974.).....32

Figure 2-4: The eight forms of corrosion as per Fontana and Dillon [46].....37

Figure 2-5: Variations in the cross-sectional shape of pits as a means for visual identification [49,55]. (Reproduced with permission from NACE International, Houston, TX. All rights reserved. [55]. © NACE International 2002.) .....39

Figure 2-6: Mechanism of pitting corrosion in a typical grade of aluminum alloy exposed to an aqueous chloride solution [47,58]. The  $Al(OH)_3$  in this cross-section is forming a tubercle. (Reproduced with permission from Elsevier Ltd, Kidlington, UK. All rights reserved. [47]. © Elsevier Ltd 2004.) .....41

Figure 2-7: Galvanic series of various metals in seawater [33,94]. These are open-circuit potentials and they were measured with a saturated calomel reference electrode (SCE; 0.241 V vs SHE at 25 °C) [33]. The aluminum alloys and grade 304 stainless steel potentials are each highlighted with a pink-dashed box. The dark boxes indicate active behavior of select active-passive alloys [33]. (Reproduced with permission from ASM International, Materials Park, OH. All rights reserved.

[33]. © ASM International 2000.) .....49

Figure 2-8: Passive layers formed on aluminum and aluminum alloys [47]. Also included in this schematic are adsorption phenomena caused by external environmental factors such as processing (i.e., rolling or extrusion) [47]. (Reproduced with permission from Elsevier Ltd, Kidlington, UK. All rights reserved. [47]. © Elsevier Ltd 2004.) .....55

Figure 2-9: Schematics of the (a) penetration, (b) adsorption, and (c) film rupture mechanisms which lead to passivity breakdown [36,105]. (Reproduced with permission from Springer, Berlin, Germany. All rights reserved. [105]. © Springer 1990.) .....56

Figure 3-1: Schematic of a lab scale immersion corrosion cell indicating the coupon and fixturing.....73

Figure 3-2: Representative images of corrosion coupons with dimension and crevice former labels. The crevice former(s) on the tube and sheet coupons were hose clamps and washers, respectively.....79

Figure 3-3: Overall image of corrosion coupons in beakers or containers during the 28 day experiment.....85

Figure 3-4: Macro photography set-up (nylon hook suspended from light table adjustable metal hook; camera lens focuses on coupon; LED lights are fully adjustable, and their orientation relative to the coupon are changed in order to allow for proper oblique lighting.....91

Figure 4-1: Representative images of corrosion coupons, before and after the 28-day immersion testing, from the twelve electrolyte-alloy combinations. Both scale

bars are 1 cm. ....102

Figure 4-2: Representative image of tarnish build-up on the aluminum alloy coupons throughout the 28-day immersion testing. Electrolyte-alloy combination presented is Isopac-5086. The coupon was still wet and the scale bar is 1 cm. ..103

Figure 4-3: Representative image of the lack of tarnish build-up on the stainless steel coupons throughout the 28-day immersion testing. The coupon was still wet (and in this image, exposed to Isopac) and the scale bar is 1 cm. ....103

Figure 4-4: 5086/5083 coupons which exhibited deposit on and adjacent to the crevice surface. The coupon on the left was in Isopac solution, while the coupon on the right was in DIUF. Scale bar is 1 cm. ....104

Figure 4-5: Representative image of a tubercle on a 5086/5083 coupon in DIUF, before (left photo) and after (right photo) removal. A small, round-shaped pit can be observed beneath the removed tubercle. ....106

Figure 4-6: IGC (white arrows) identified on the surface of a 6061 coupon that was exposed to Isopac. ....107

Figure 4-7: Composite images of four alloys before and after being immersed in Isopac solution, as well as after cleaning. Metal loss can be identified in the “After Testing, After Cleaning” images, and it appears as pits. Scale bar is 5 mm.....109

Figure 4-8: Corrosion (black arrows) on the crevice surface of 5086 alloy in Isopac solution. This metal loss signifies that crevice corrosion has occurred. Arrows are also oriented parallel to the grinding marks. Scale bar is 0.25 mm. ....110

Figure 4-9: Additional image of corrosion (black arrows) on the crevice surface of 5086 alloy in Isopac solution. Again, crevice corrosion has occurred. Arrows are

also oriented parallel to the grinding marks. Scale bar is 0.25 mm. ....111

Figure 4-10: Corrosion (black arrows) on the crevice surface of 6061 alloy in Isopac solution. Deposit is also observed on the surface (white arrows). Arrows are also oriented parallel to the grinding marks. Scale bar is 0.25 mm. ....112

Figure 4-11: 5086/5083 alloy in Isopac solution; both of the exposed and crevice surfaces (top and bottom of picture, respectively). Deposit (white arrows) and corrosion damage (black arrows) is also observed. ....112

Figure 4-12: 304 alloy in Isopac solution; both of the exposed (top of picture) and crevice (bottom of picture) surfaces. Deposit is also observed on the surfaces (white arrows). ....113

Figure 4-13: Representative image of gouging (white arrows) on the 5086 and 6061 alloy coupons, in all electrolytes, due to surface preparation using a lathe. Scale bar is 0.25 mm. ....114

Figure 4-14: Composite images of alloys before and after being immersed in Alum solution, as well as after cleaning. Metal loss can be identified in the “After Testing, After Cleaning” images, and it appears as pits. Scale bar is 5 mm. ....115

Figure 4-15: Corrosion damage (black arrows) and deposit (white arrows) on the 5086 alloy crevice surface in Alum solution. Arrows are also oriented parallel to the grinding marks. Scale bar is 0.25 mm. ....116

Figure 4-16: Corrosion damage (black arrows) and deposit (white arrows) on the 6061 alloy crevice surface in Alum solution. Arrows are also oriented parallel to the grinding marks. Scale bar is 0.5 mm. ....117

Figure 4-17: Corrosion damage (black arrows) and deposit (white arrows) on the 5086/5083 alloy crevice surface (bottom of picture) in Alum solution. Deposit (top white arrows) can also be observed on the exposed surface (top of picture). ....117

Figure 4-18: 304 alloy in Alum solution; both of the exposed (top of picture) and crevice (bottom of picture) surfaces. Deposit is also observed on both surfaces (white arrows). .....118

Figure 4-19: Composite images of alloys before and after being immersed in DIUF, as well as after cleaning. Metal loss can be identified in the “After Testing, After Cleaning” images, and it appears as pits. Scale bar is 5 mm. ....119

Figure 4-20: Corrosion damage (black arrows) and deposit (white arrows) on the 5086 alloy crevice surface in DIUF. ....120

Figure 4-21: Corrosion damage (black arrows) and deposit (white arrows) on the 6061 alloy crevice surface in DIUF. ....121

Figure 4-22: Corrosion damage (black arrows) and deposit (white arrows) on the 5086/5083 alloy crevice surface in DIUF. Above the deposit (top of image) is the exposed surface, while below the deposit (bottom of image) is the crevice surface. ....121

Figure 4-23: 304 alloy in Alum solution; both of the exposed (top of picture) and crevice (bottom of picture) surfaces. Deposit is also observed on the surface (white arrows). Scale bar is 0.25 mm. ....122

Figure 4-24: Composite images of all twelve electrolyte-alloy combinations after immersion and cleaning. Scale bar is 5 mm. ....124

Figure 4-25: Representative BSE image of deposit collected from tube coupons. The three green numbers cover the locations where EDX data was acquired. Image taken at a 20 kV accelerating voltage and a 7 mm working distance. ....126

Figure 4-26: Representative BSE image of deposit collected from sheet coupons. The three green numbers cover the locations where EDX data was acquired. IGC (white arrows) can be identified on the crevice surface (right side of image; exposed surface is on the left side of the image, beyond the deposit). Image taken at a 20 kV accelerating voltage and a 11 mm working distance. ....126

Figure 4-27: Representative XRD patterns of deposit collected from eight of the twelve electrolyte-alloy combinations. ....131

Figure 4-28: Representative FTIR spectra of 5086, 6061, and 5086/5083 alloys in Isopac solution. ....133

Figure 4-29: Representative FTIR spectra of 5086, 6061, and 5086/5083 alloys in Alum solution.....134

Figure 4-30: Representative FTIR spectra of 5086 and 6061 alloys in DIUF.....135

Figure 4-31: Representative FTIR spectra of nylon present in the deposits of the 304 alloy in all three electrolytes, and on the 5086/5083 alloy in both Isopac solution and DIUF.....136

Figure 4-32: Average mass loss measurements for the twelve electrolyte-alloy combinations used in immersion testing.....138

Figure 4-33: Average T, DO, and pH measurements for the four alloys in Isopac solution compared to the Isopac solution control. The shaded region in each graph

is the operating range of the aeration tank. ....	146
Figure 4-34: Average T, DO, and pH measurements for the four alloys in Alum solution compared to the Alum solution control. The shaded region in each graph is the operating range of the aeration tank. ....	146
Figure 4-35: Average T, DO, and pH measurements for the four alloys in DIUF compared to the DIUF control. The shaded region in each graph is the operating range of the aeration tank. ....	147
Figure 4-36: Average Cl <sup>-</sup> measurements for select immersion cells compared to relevant control solution. The shaded region in each graph is the operating range of the aeration tank, while the green dashed line is the detectability limit of the Cl <sup>-</sup> probe (at 0.1 mg/L). ....	147
Figure A-1: Through wall corrosion (indicated by the dotted oval) of a tubular tie immediately adjacent to aeration piping [1]. ....	177
Figure A-2: “Pit measurements taken from the deepest identified pit on the floor of the aeration tank. After brushing deposits clear.” [1] The gauge indicates that the pit is ~4 mm deep (~42% of the thickness assuming 9.53 mm / 0.375 inch thickness) [1]. ....	177
Figure A-3: Localized corrosion on brackets, shown with direct (left) and oblique (right) lighting [1]. ....	178
Figure A-4: Pipe support under brackets of an aeration line [1]. Pipe support exposed to both direct (left) and oblique (right) lighting conditions [1]. ....	178

Figure A-5: “Crusty top hat” deposits (white arrows) on the tank wall in close proximity to the end of an aeration line and diffusers [1].....178

Figure A-6: Before (left) and after (right) removal of “sludge” deposits (dashed rectangle) from the aeration tank floor [1].....179

Figure A-7: First type of under-deposit corrosion identified on the floor and welds of the aeration tank (after brushing off the deposits) [1]. .....179

Figure A-8: Second type of under-deposit corrosion identified on tooling marks along a wall of the aeration tank (after brushing off the deposits) [1]. “Regions directly below “X” are pitting damage, showing multiple pits within pits. Vertical striations are the tooling damage discussed throughout.” [1].....180

Figure A-9: “Crusty top hat” deposit on tooling marks located on vertical wall of gusset plates [1]. Images taken before (left) and after (right) removal of the deposit [1]. 1 mm divisions on the ruler in the right image [1].....180

Figure A-10: Before (left) and after (right) removal of “crusty top hat” deposits from horizontal wall welds [1].....181

Figure A-11: Circular floor section removed from TK-3100-1 (arrow in the photo points north) [2]. .....181

Figure A-12: “Section of webbing cut from northwest corner, bottom horizontal bend of TK-3100-1; section tip (white arrow) was notched to prevent crack formation/propagation.” [2] .....182

Figure A-13: Partial schematic of the aeration tank, along with images (including macrophotographs, cross-sections, and micrographs) acquired from key locations/aluminum alloy components, namely: collected wall cross-section (a),

pitting on wall tooling marks (b), tubular tie in contact with aeration piping (c), tank floor (d), and an aeration piping bracket (e). Four modes of corrosion (pitting, crevice, galvanic, and IGC) were identified. Deposit(s) were removed to aid in the macrophotography. Scale on ruler is in mm. ....186

Figure A-14: Wall section collected from aeration tank. Scale is in mm. ....188

Figure A-15: As collected cut-out of floor section. Note the pits still contain metal shavings/other debris produced during removal the section from the aeration tank. (Blue arrow points north). Hole in the center is due to the hole saw used to extract the disc. Scale is in mm.....191

Figure A-16: Close-up of large pit. Round pits within pits and undercutting (white arrows) can be observed. Scale is in mm.....192

Figure A-17: Close-up of small pits. Scale is in mm.....192

Figure A-18: Stereomicroscope images of small floor pit, with varying amounts of indirect lighting. Alignment of the rolling direction with some features in the pits (white arrows; parallel to rolling direction) can also be observed.....193

Figure A-19: Location of pit depth measurements. Scale is in mm.....193

Figure A-20: Bottom surface of collected cut-out of floor section. Scale is in mm. ....194

Figure A-21: Corrosion (as small, irregular shaped pits) on the bottom of the aeration tank floor. Images collected with varying amounts of indirect lighting. Scale is in mm.....195

Figure A-22: Corrosion (as small, irregular shaped pits) on the bottom of the aeration tank floor. Images collected with varying amounts of indirect lighting. Scale is in mm. ....195

Figure A-23: As collected north section of removed tubular tie. Arrow points north and scale is 300 mm. ....198

Figure A-24: As collected south section of removed tubular tie. Arrow points north and scale is 300 mm. ....198

Figure A-25: Hole in north section of tubular tie. Composite image with focus on the outside (top image) and inside (bottom image) of the tie. Arrow points north. Scale is in mm. ....199

Figure A-26: Pits on opposite side of through-wall hole. Images collected with varying amounts of indirect lighting. Scale is in mm. ....200

Figure A-27: North end of north section of the tubular tie. Arrow points north. Scale is in mm. ....200

Figure A-28: Original outer diameter material near the hole in the north section of the tubular tie. ....201

Figure A-29: South end of south portion of the tubular tie. Arrows written on the tie point north. Scale is in mm. ....201

Figure A-30: Pits in south section of tubular tie. Images collected with varying amounts of indirect lighting. ....202

Figure A-31: South-most section of south portion of the tubular tie. Arrow points north. Scale is in mm. ....202

Figure A-32: Close-up of small pits (from above composite images).....203

Figure A-33: As collected photo of bracket, with nuts, washers, and bolts (hardware). Arrow on the bracket points towards the north wall of the aeration tank. Scale is in mm. ....207

Figure A-34: As collected photo of bracket side, with hardware. Scale is in mm. ....207

Figure A-35: Bottom of bracket with hardware removed. Scale is in mm. ....208

Figure A-36: As collected photo of the top of the bracket, with hardware removed. Arrow on the bracket points towards the north wall of the aeration tank. Scale is in mm. ....208

Figure A-37: Close-up on bracket pits and surface fabrication markings (white arrows). Scale is in mm.....209

Figure A-38: Deep pits found immediately adjacent to where washers were installed. Images collected with varying amounts of indirect lighting. Scale is in mm. ....209

Figure A-39: Pitting identified on the side of the bracket. Images collected with varying amounts of indirect lighting. Scale is in mm. ....209

Figure A-40: Pit depths on the top of the bracket. Arrow on the bracket points towards the north wall of the aeration tank. Scale is in mm. ....210

Figure A-41: Pit depths on the bottom of the bracket. Scale is in mm. ....	211
Figure A-42: Pit depths on the side of the bracket. Scale is in mm. ....	211
Figure A-43: Representative indexed XRD pattern for the “North Section Hole – Inside” deposit. ....	219
Figure A-44: Composite BSE image of the large 5.1 cm diameter pit. Able to discern pits within pits. ....	221
Figure A-45: Close-up of pits within pits (BSE image). ....	221
Figure A-46: Deposit within pits; image of the deepest pit (BSE image). Abrasion marks from handling can be seen in the foreground (bottom half of the image within the pit) as curved scatches. ....	222
Figure A-47: Top overview image of large pit. Dots indicate where EDX data was collected (BSE image). ....	223
Figure A-48: BSE image of large pit on the outer circumference of the cross-section. Deposit (white arrows) and IGC (black arrows) are also present. Note the dot on the sectioned surface was made with a Sharpie® marker in order to identify location of interest (black dashed oval). ....	224
Figure A-49: Close-up on IGC (black arrows) and deposit (white arrows) at the large pit opening (BSE image). ....	225
Figure A-50: Close-up BSE image of IGC (black arrows) and deposit (white arrows) at the bottom of the large pit opening. ....	225

Figure A-51: Additional close-up BSE image of deposit (white arrows) on the pit surface, as well as IGC (black arrows). .....226

Figure A-52: Close-up BSE image of deposit (white arrows) on the pit surface, as well as IGC (black arrows) around an entire grain. There also appears to be deposit build-up between the grains (white arrows).....226

Figure A-53: Close-up on IGC (black arrows) in Figure A-52 (BSE image). Note the cracking within the corrosion product formed at metal grain boundaries. ....227

Figure A-54: BSE image of the mounted cross-section. Pitting (white arrows) and IGC (black arrows) observed on the outer circumference of the cross-section. ...228

Figure A-55: Close-up on IGC (black arrows) at the tie surface (from Figure A-54; BSE image). Precipitates (white arrows) can also be observed.....228

Figure A-56: BSE image of another location on the tubular tie exhibiting signs of pitting (white arrows) and IGC (black arrows). Some staining (black dashed oval) was found below the IGC. The staining is an artifact from the etching process. 229

Figure A-57: Close-up BSE image of IGC (from Figure A-56).....229

Figure A-58: Close-up BSE image of IGC and corroded grains (from Figure A-56). Figure demonstrates the progression of corrosion of the tie from initial IGC to entirely corroded grains which naturally drop out due to gravity or fluid motion. ....230

Figure A-59: BSE image of pit in mounted tie cross-section. Numbers indicate where EDX data was collected. ....231

Figure A-60: BSE image of pit in mounted tie cross-section. Numbers indicate where EDX data was collected. ....232

Figure A-61: BSE image of mounted tie cross-section. Boxes show locations where line scans were performed on grains.....233

Figure A-62: BSE image of tie, near the outer circumference (Top left). Locations of line scans performed on a grain are shown. Graphs show EDX results for: Line 1 (Top Right), Line 2 (Bottom Left), and Line 3 (Bottom Right). ....234

Figure A-63: BSE image of tie, near the center (mid thickness) (Top left). Locations of line scans performed on a grain are shown. Graphs show EDX results for: Line 1 (Top Right), Line 2 (Bottom Left), and Line 3 (Bottom Right). ....234

Figure A-64: BSE image of tie, near the inner circumference (Top left). Locations of line scans performed on a grain are shown. Graphs show EDX results for: Line 1 (Top Right), Line 2 (Bottom Left), and Line 3 (Bottom Right). ....235

Figure A-65: BSE image of large pit on the top of the bracket. Numbers indicate where EDX data was collected. Tunnelling (white arrows) can also be observed. Green box is the location of Figure A-66. ....237

Figure A-66: Close-up on tunneling (from Figure A-65; BSE image). Numbers indicate where EDX data was collected. A local galvanic cell can be observed between the intermetallic inclusions (white arrows) and the surrounding matrix. ....238

Figure A-67: Close-up on tunneling (from Figure A-65; BSE image). Numbers indicate where EDX data was collected.....239

Figure A-68: BSE image of pitting and tunneling on the side of the bracket. The large green box is the location of Figure A-69, while the small green box is the location of Figure A-70.....	240
Figure A-69: Close-up on tunneling (from Figure A-68; BSE image). Numbers indicate where EDX data was collected.....	240
Figure A-70: Close-up on tunneling (from Figure A-68; BSE image). Green box is the location of Figure A-71.....	241
Figure A-71: Close-up of crystallographic pitting on the tunnel surfaces (from Figure A-70; BSE image). .....	241
Figure A-72: Overall image of etched wall cross-section. The mark near the top right corner (white arrow) is an artifact from the etching process. Scale is in mm. ....	246
Figure A-73: Microstructure of the wall cross-section (center of specimen; from Figure A-72).....	247
Figure A-74: Overall image of the etched floor cross-section. The mark near the bottom right corner (white arrow) is an artifact from the etching process. Scale is in mm. ....	248
Figure A-75: Composite image of the deepest portion of the 5.1 cm pit. Undercutting (white arrow) can also be observed. ....	248
Figure A-76: Tunneling (white arrows) near the bottom of the deepest part of the pit (left of the deepest pit; from Figure A-75). ....	249

Figure A-77a: Close-up on tunneling (white arrows) and crystallographic pitting (black arrows). Figure A-77a is un-etched; from Figure A-76. ....249

Figure A-77b: Close-up on tunneling (white arrows) and crystallographic pitting (black arrows) – after etching same region from Figure A-77a. Figure A-77b is etched; from Figure A-76.....250

Figure A-78: Image of smaller pit (from Figure A-74). Tunnelling (white arrows) can also be observed. Black, white, and green boxes contain Figures A-79, A-80, and A-81, respectively. Tunneling is also observed in the black box.....250

Figure A-79: Tunneling at the bottom of the deepest part of the smaller pit (from Figure A-78).....251

Figure A-80: Close-up on tunneling (white arrows) and crystallographic pitting (black arrows) (from Figure A-78). The left image is un-etched while the right image is etched.....251

Figure A-81: Close-up on tunneling and crystallographic pitting (from Figure A-78). The left image is un-etched while the right image is etched. ....252

Figure A-82: Very small pit at the surface of the floor cross-section exhibiting tunneling (white arrow).....252

Figure A-83: Close-up on tunneling and crystallographic pitting (from Figure A-82). The left image is un-etched while the right image is etched. ....252

Figure A-84: Overall image of etched tubular tie cross-section (in the radial direction; labelled “Hole Circumference”). Scale is in mm. ....253

Figure A-85: Severe corrosion damage on portion of the tie immediately adjacent to the through-wall hole (from Figure A-84).....	254
Figure A-86: IGC and pitting on portion of the tie immediately adjacent to the through-wall hole (from Figure A-85).....	254
Figure A-87: Close-up on IGC and pitting (from Figure A-86). ....	255
Figure A-88: IGC and pitting on the outer diameter of the tie cross-section (from Figure A-84).....	255
Figure A-89: Close-up on IGC and pitting (from Figure A-88). ....	256
Figure A-90: Large pit on the outer diameter of the tie cross-section (from Figure A-84). The black and white boxes contain Figures A-91 and A-92, respectively. ....	256
Figure A-91: IGC and pitting near the bottom of the large pit (from Figure A-90). ....	257
Figure A-92: IGC and pitting near the bottom of the large pit (from Figure A-90). ....	257
Figure A-93: IGC and pitting on the inner diameter of the tie cross-section (from Figure A-84).....	258
Figure A-94: Overall image of etched tubular tie cross-section (in the axial direction; labelled “Hole Axial”). Scale is in mm. ....	259
Figure A-95: Corrosion damage on the inner diameter of the tie cross-section (from Figure A-94). White arrows are perpendicular to the above-mentioned	

directionality of the microstructure.....	260
Figure A-96: Close-up on IGC and pitting (from Figure A-95). .....	260
Figure A-97: Severe corrosion damage on portion of the tie immediately adjacent to the through-wall hole (from Figure A-94).....	261
Figure A-98: Close-up on IGC, pitting, and preferential corrosion in the extrusion or drawing direction (from Figure A-97).....	261
Figure A-99: Large pit on the outer diameter of the tie cross-section (from Figure A-94). The white dashed box contains Figure A-102.....	262
Figure A-100: IGC, pitting, and preferential corrosion in the extrusion or drawing direction at the bottom of the large pit (from Figure A-99).....	262
Figure A-101: Close-up on IGC, pitting, and preferential corrosion in the extrusion or drawing direction at the bottom of the large pit (from Figure A-100). .....	263
Figure A-102: IGC, pitting, and preferential corrosion in the extrusion or drawing direction on the outer diameter of the tie cross-section (from Figure A-99). .....	263
Figure A-103: Overall image of etched tubular tie cross-section (in the radial direction; labelled “End Circumference”). Scale is in mm.....	264
Figure A-104: Large pit on the outer diameter of the tie cross-section (from Figure A-103).....	265
Figure A-105: IGC and pitting at the bottom of the large pit (from Figure A-104). .....	265

Figure A-106: Close-up on IGC and pitting (from Figure A-105). .....	266
Figure A-107: Overall image of etched aeration line bracket cross-section. The mark on the bottom left corner (white arrow) is an artifact from the etching process. Scale is in mm. ....	267
Figure A-108: Large pit on the top of the cross-section (from Figure A-107). The white box contains Figure A-109 while the black box contains Figure A-110. ..	268
Figure A-109: Tunneling near the bottom right of the large pit (from Figure A-108). The left image is un-etched while the right image is etched.....	268
Figure A-110: Close-up on tunneling and crystallographic pitting (from Figure A-108 – near the top right corner). The left image is un-etched while the right image is etched. ....	269
Figure A-111: Tunneling and preferential corrosion in the rolling direction on the left side of the large pit (from Figure A-108). ....	269
Figure A-112: Close-up on tunneling (from Figure A-111). ....	270
Figure A-113: Pits on the bottom right of the cross-section (from Figure A-107). White box contains Figure A-114.....	270
Figure A-114: Close-up on tunneling (from Figure A-113). ....	271
Figure A-115: Pitting, tunneling, and preferential corrosion in the rolling direction on the right side of the cross-section (from Figure A-107). The white and green boxes contain Figures A-116 and A-118, respectively. ....	271

Figure A-116: Tunneling in the cross-section (from Figure A-115). The left image is un-etched while the right image is etched. The green box in the left image is Figure A-117.....	272
Figure A-117: Close-up on tunneling and crystallographic pitting (un-etched; from left image in Figure A-116). .....	272
Figure A-118: Pitting, tunneling, and preferential corrosion in the rolling direction (from Figure A-115). The green box contains Figure A-119. ....	273
Figure A-119: Close-up on tunneling and crystallographic pitting (from Figure A-118). .....	273
Figure C-1: Aeration tank influent flow rate. ....	296
Figure C-2: Aeration tank temperature measurements. ....	296
Figure C-3: Aeration tank dissolved oxygen measurements. ....	297
Figure C-4: Aeration tank pH measurements. ....	297
Figure C-5: Aeration tank Alum and Isopac drip rate. ....	298
Figure D-1: Composite image of corrosion coupons of different alloys in various test solutions.....	300
Figure D-2: Composite image of corrosion coupons of different alloys in various test solutions.....	301

Figure D-3: Composite image of corrosion coupons of different alloys in various test solutions.....302

Figure D-4: Composite image of corrosion coupons of different alloys in various test solutions.....303

Figure D-5: Composite image of corrosion coupons of different alloys in various test solutions.....304

Figure D-6: Composite image of corrosion coupons of different alloys in various test solutions.....305

Figure F-1: Average T, DO, and pH measurements for coupons 1 through 3 compared to the Isopac solution. The shaded region in each graph is the operating range of the aeration tank.....311

Figure F-2: Average T, DO, and pH measurements for coupons 4 through 6 compared to the Alum solution. The shaded region in each graph is the operating range of the aeration tank.....311

Figure F-3: Average T, DO, and pH measurements for coupons 7 through 9 compared to the DIUF solution. The shaded region in each graph is the operating range of the aeration tank.....312

Figure F-4: Average T, DO, and pH measurements for coupons 10 through 12 compared to the Isopac solution. The shaded region in each graph is the operating range of the aeration tank.....312

Figure F-5: Average T, DO, and pH measurements for coupons 13 through 15 compared to the Alum solution. The shaded region in each graph is the operating

range of the aeration tank.....313

Figure F-6: Average T, DO, and pH measurements for coupons 16 through 18 compared to the DIUF solution. The shaded region in each graph is the operating range of the aeration tank.....313

Figure F-7: Average T, DO, and pH measurements for coupons 19 through 21 compared to the Isopac solution. The shaded region in each graph is the operating range of the aeration tank.....314

Figure F-8: Average T, DO, and pH measurements for coupons 22 through 24 compared to the Alum solution. The shaded region in each graph is the operating range of the aeration tank.....314

Figure F-9: Average T, DO, and pH measurements for coupons 25 through 27 compared to the DIUF solution. The shaded region in each graph is the operating range of the aeration tank.....315

Figure F-10: Average T, DO, and pH measurements for coupons 28 through 30 compared to the Isopac solution. The shaded region in each graph is the operating range of the aeration tank.....315

Figure F-11: Average T, DO, and pH measurements for coupons 31 through 33 compared to the Alum solution. The shaded region in each graph is the operating range of the aeration tank.....316

Figure F-12: Average T, DO, and pH measurements for coupons 34 through 36 compared to the DIUF solution. The shaded region in each graph is the operating range of the aeration tank.....316

Figure F-13: Average T, DO, and pH measurements for the control solutions. The shaded region in each graph is the operating range of the aeration tank. ....317

Figure F-14: Average [Cl<sup>-</sup>] measurements for selected immersion cells compared to relevant control solution. The green dashed lines in the graphs containing the Alum (center) and DIUF (right) measurements is the detectability limit of the Cl<sup>-</sup> probe (at 0.1 mg/L). ....317

# List of Tables

Table 2-1: Key process data collected from the aeration tank examined in Appendix A. Information on data collection and analysis provided in Appendix C.....	20
Table 2-2: Typical composition of untreated domestic wastewater [1].....	21
Table 2-3: Standard equilibrium half-cell <sup>†</sup> potentials for select reactions. Standard potential values at 25 °C and unit activity ( $a_{\text{species}} = 1$ or $P_{\text{species}} = 1$ atm) [32,35]. .....	27
Table 2-4: Microorganisms known to cause MIC in aluminum alloys. ....	46
Table 2-5: Open-circuit potentials for relevant aluminum alloys (and temper, if available) and secondary phases based on ASTM G69 (sodium chloride-hydrogen peroxide solution at 25 °C) [47,97]. ....	52
Table 3-1: Summary of testing and characterization methods used in the lab scale immersion corrosion cell experiments. ....	72
Table 3-2: Product standards and alloy details used in this study. ....	75
Table 3-3: Aluminum alloy coupons and respective material standard compositions. .....	77
Table 3-4: Stainless steel alloy coupon and material standard compositions. ....	77
Table 3-5: Average dimensions of corrosion coupons. ....	82
Table 3-6: Average volume of corrosion cell solutions.....	84

Table 3-7: Volume of control solutions. ....	89
Table 4-1: Modes of corrosion identified on the corrosion coupons immersed in the three electrolytes tested in this study. ....	100
Table 4-2: Representative elemental data collected from deposit removed or found on each of the four alloys tested in Isopac solution. ....	127
Table 4-3: Representative elemental data collected from deposit removed or found on each of the four alloys tested in Alum solution. ....	128
Table 4-4: Representative elemental data collected from deposit removed or found on each of the four alloys tested in DIUF. ....	128
Table A-1: Inspection methods performed on aeration tank TK-3100-1 [1,2]. ....	173
Table A-2: Laboratory tests and analysis work performed on samples. ....	183
Table A-3: Wall thickness measurements. ....	188
Table A-4: Floor pit depth measurements. ....	194
Table A-5: Floor thickness measurements. ....	195
Table A-6: Tie thickness measurements. ....	203
Table A-7: Tie diameter measurements. ....	204
Table A-8: Top of bracket pit depth measurements. ....	210

Table A-9: Bottom of bracket pit depth measurements .....	211
Table A-10: Bracket side pit depth measurements .....	212
Table A-11: Bracket width measurements.....	212
Table A-12: Bracket thickness measurements.....	212
Table A-13: Deposit labels and locations of collection .....	213
Table A-14: Composition of components collected from aeration tank TK-3100-1. .....	215
Table A-15: Composition of deposits collected from aeration tank TK-3100-1.	215
Table A-16: XRD results on tested deposits.....	218
Table A-17: EDX data from points in Figure A-47 .....	223
Table A-18: EDX data from numbers in Figure A-59 .....	231
Table A-19: EDX data from numbers in Figure A-60.....	232
Table A-20: EDX data from numbers in Figure A-65.....	237
Table A-21: EDX data from numbers in Figure A-66.....	238
Table A-22: EDX data from numbers in Figure A-67.....	239
Table A-23: EDX data from numbers in Figure A-69.....	241

Table A-24: EDX data from collected deposit specimens.....	243
Table A-25: Hardness values of each component cross-section .....	274
Table A-26: Locations of crevices found on each of the aeration tank components .....	276
Table A-27: Select percentage points of the t-distribution [28]. .....	287
Table C-1: Aeration tank process data.....	295
Table D-1: Coupon numbers for the combination of materials and respective solutions used in this study. ....	299
Table E-1: FTIR peak data of aluminum oxides and hydroxides [1]. .....	306
Table E-2: FTIR peak data of aluminum oxides and hydroxides [2]. .....	307
Table E-3: FTIR peak data of aluminum hydroxide bonds [3].....	307
Table E-4: Characteristic OH wavenumbers in stretching and bending regions [3]. .....	307
Table F-1: Coupon numbers for the combination of materials and respective solutions used in this study. ....	310

# List of Abbreviations

ABS:	Acrylonitrile Butadiene Styrene
ALCOA:	Aluminum Company of America
APB:	Acid-Producing Bacteria
ASTM:	American Society for Testing and Materials
BSE:	Backscattered Electron
CI:	Confidence Interval
DIUF:	De-Ionized Ultra-Filtered Water
DO:	Dissolved Oxygen or Dissolved Oxygen Concentration
EDX:	Energy Dispersive X-Ray Spectroscopy
FTIR:	Fourier Transform Infrared Spectroscopy
HT:	Hardness Testing
ICP-MS:	Inductively Coupled Plasma Mass Spectroscopy
ICP-OES:	Inductively Coupled Plasma Optical Emission Spectroscopy
IGC:	Intergranular Corrosion
ISA:	Ionic Strength Adjuster
ISO:	International Organization for Standardization
MIC:	Microbiologically Influenced Corrosion
MSDS:	Material Safety Data Sheet
NACE:	National Association of Corrosion Engineers
OM:	Optical Microscopy
PACl:	Polyaluminum Chloride
PP:	Polypropylene
RAS:	Return Activated Sludge

SA:	Surface Area
SE:	Secondary Electron
SEM:	Scanning Electron Microscope or Scanning Electron Microscopy
SOB:	Sulphur-Oxidizing Bacteria
SRB:	Sulphate-Reducing Bacteria
T:	Temperature
V/SA:	Volume to surface area ratio
WAS:	Waste Activated Sludge
WEF:	Water Environment Federation
WWTP:	Wastewater Treatment Plant
XRD:	X-Ray Diffraction

# List of Symbols

Symbol	Description	Unit
$a_{\text{species}}$	Activity	–
$c$	Concentration	[mg/L] or [vol %]
[Cl <sup>-</sup> ]	Chloride concentration	[mg/L]
$CI$	Confidence interval	–
$d$	Pit depth or dimension	[mm]
$E^{\circ}$	Standard equilibrium half-cell potential	[V]
$E^{\circ}_{\text{anode}}$	Anode standard equilibrium potential	[V]
$E^{\circ}_{\text{cathode}}$	Cathode standard equilibrium potential	[V]
$E^{\circ}_{\text{cell}}$	Standard equilibrium cell potential	[V]
$E_{\text{cell}}$	Equilibrium cell potential	[V]
$E_{\text{corr}}$	Corrosion or open-circuit potential	[V]
$F$	Faraday's constant, approximately 96485	[J/(V•mol e <sup>-</sup> )]
$\Delta G$	Gibbs free energy change	[J]
$k$	Constant for pitting rate expression	–
$n$	Number or number of moles of electrons	– or [mol e <sup>-</sup> ]
$P_{\text{species}}$	Partial pressure	[atm] or [Pa]
$R$	Gas constant, approximately 8.314	[J/(mol•K)]
$s$	Sample standard deviation	–
$SA$	Surface area	[mm <sup>2</sup> ]
$SA_{\text{E}}$	Edge surface area	[mm <sup>2</sup> ]
$SA_{\text{T}}$	Total surface area	[mm <sup>2</sup> ]
$SA_{\text{E}}/SA_{\text{T}}$	Edge SA to Total SA ratio	[%]

$T$	Temperature	[K] or [°C]
$t$	Time	[min] or [year]
$t_{\alpha/2, n-1}$	t-distribution value	–
$V$	Volume	[mL] or [mm <sup>3</sup> ]
$V/SA$	Volume to surface area ratio	[mL/mm <sup>2</sup> ]
$\bar{x}$	Sample mean (average)	–

## Greek Symbols

Symbol	Description	Unit
$\alpha$	Level of significance	–
$\gamma$	Activity coefficient	[L/mg]
$\phi_{\text{Alum}}$	Alum drip rate	[mL/min]
$\phi_{\text{Influent}}$	Influent flow rate	[m <sup>3</sup> /day]
$\phi_{\text{Isopac}}$	Isopac drip rate	[mL/min]
$\sigma$	Conductivity	[μS/cm]
$\theta$	Degree	[°]

# Chapter 1 – Introduction

## 1.1 Project Background

A major utilities provider owned and operated a modular wastewater treatment plant (WWTP), which was designed to provide wastewater treatment to various oil sands extraction and processing work camps. This WWTP utilized three bioreactors – known as aeration tanks – in three individual trains, to treat the influent wastewater. These aeration tanks used microorganisms and injected air to consume organic constituents in the process fluid. One of three aeration tanks was placed in service for approximately 20 months before being shut down and drained due to scheduled maintenance and suspected leaking.

Multiple inspections [1,2] and failure investigations (Appendix A) performed by the author revealed severe corrosion damage throughout the aeration tank and on collected specimens. The collected specimens examined include: (1) a large portion of tubular tie, (2) one aeration piping bracket, portions of both the tank (3) floor and (4) wall, and varying amounts of (5) deposits removed throughout the tank. The following list summarizes the findings from both the inspections and failure investigations. Moreover, some of the results of both activities are illustrated in Figures 1-1 through 1-3.

- Localized corrosion was observed within the aeration tank, including the tank walls, floor, tubular ties, and aeration piping brackets [1]. The most severe corrosion was identified on the tank floor and tubular ties [1].
- Overall, all corrosion was found to be *underneath* either artificial and/or naturally occurring crevice formers (also known as under-deposit corrosion).

- The tank floor, walls, and aeration piping brackets were found to exhibit three modes of corrosion, namely: pitting, crevice corrosion, and galvanic corrosion. These three modes were also identified on the tubular ties; however, after metallographic examination, intergranular corrosion (IGC) was also found (bringing the total number of corrosion modes observed on the ties to four).
- Alloys used in construction of the wall, floor, and bracket specimens were determined to be both aluminum alloy grades 5086 and 5083. The tubular tie specimen was found to be manufactured from aluminum alloy grade 6061. Finally, visual inspection revealed the aeration piping to be made from grade 304/304L stainless steel [1].
- The corrosion damage appeared to be exacerbated by dissimilar metal interactions, through direct electrical connections between the stainless steel aeration piping and the various aluminum alloy, aeration tank components (ultimately resulting in galvanic corrosion).
- Due to the lack of gasket or dielectric material between the aeration tank and the rest of the WWTP equipment and buildings [1,2], as well as the lack of grounding on the WWTP buildings [2], it appeared as if the aeration tank, remaining WWTP equipment, and the WWTP buildings were all electrically connected. This lack of electrical isolation may have led to stray current corrosion.
- Elements such as chlorine and sulphur were found in the collected specimens. These elements either as ions (such as chloride) or as polyatomic anions (such as sulphate), were from the wastewater process fluid, and are known to cause corrosion in aluminum and aluminum alloys [3,4].

- The presence of elemental aluminum and oxygen, and known crystalline aluminum hydroxides – in addition to the general appearance and morphology of the collected deposits (throughout the aeration tank) – suggest that the deposits contained aluminum corrosion products.



Figure 1-1: Through wall corrosion (indicated by the dotted oval) of a tubular tie immediately adjacent to aeration piping [1].



Figure 1-2: “Pit measurements taken from the deepest identified pit on the floor of the aeration tank. After brushing deposits clear.” [1] The gauge indicates that the pit is ~4 mm deep (~42% of the thickness assuming 9.53 mm / 0.375 inch thickness) [1].

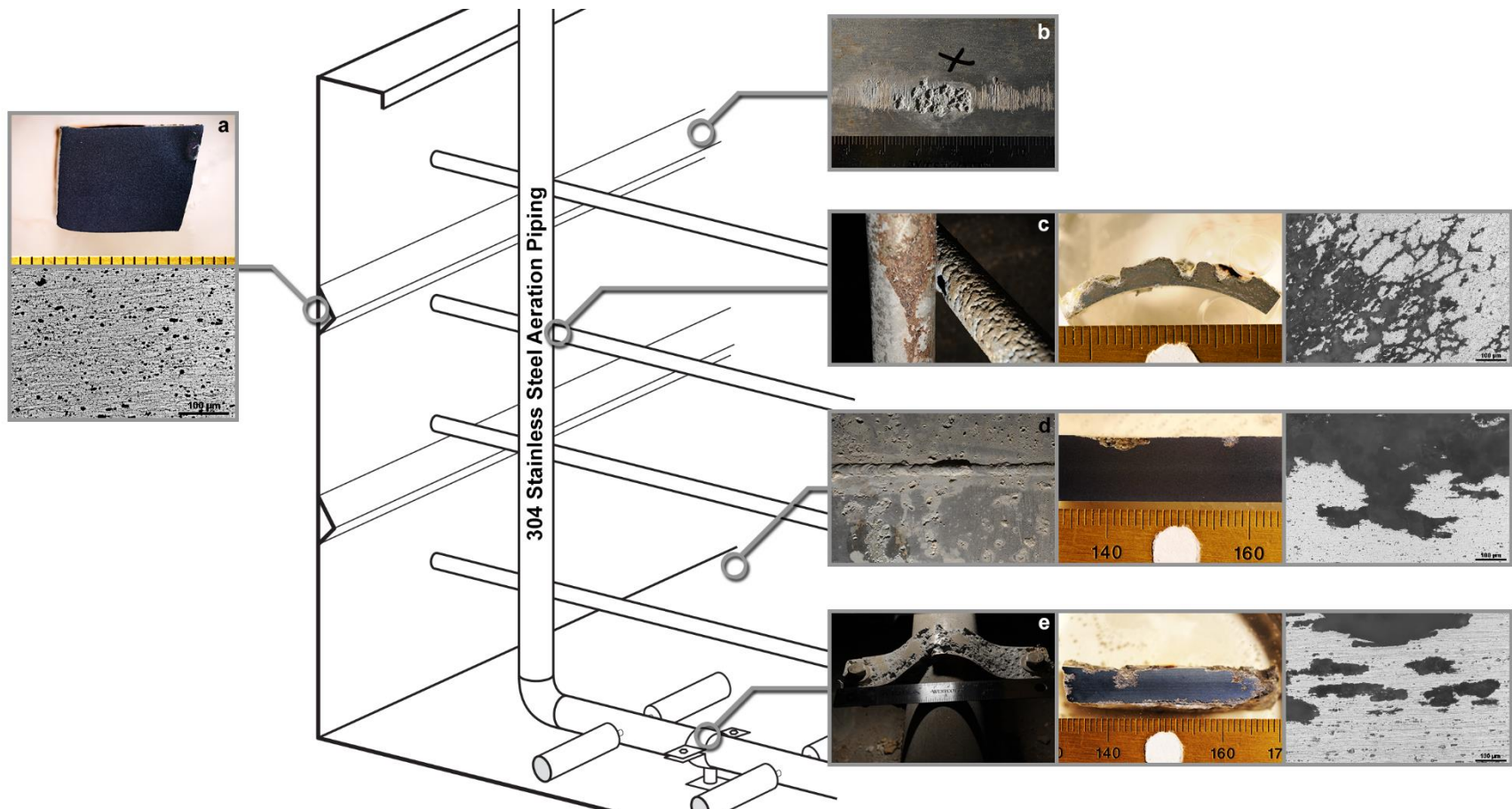


Figure 1-3: Partial schematic of the aeration tank, along with images (including macrophotographs, cross-sections, and micrographs) acquired from key locations/aluminum alloy components, namely: collected wall cross-section (a), pitting on wall tooling marks (b), tubular tie in contact with aeration piping (c), tank floor (d), and an aeration piping bracket (e). Four modes of corrosion (pitting, crevice, galvanic, and IGC) were identified. Deposit(s) were removed to aid in the macrophotography. Scale on ruler is in mm.

From the inspections and failure analyses, there appeared to be three environmental causes of the observed corrosion. These causes were: stray current (1), chemical constituents in the process fluid (including process additives) (2), and biological constituents in the process fluid (resulting in microbiologically influenced corrosion; MIC) (3).

Regarding the stray current, there was not enough evidence to state to what extent or even how stray current may be involved in the aeration tank corrosion. However, there was sufficient evidence to show that the aforementioned four modes of corrosion were *predominant* in the aeration tank, as well as the presence of elements which are corrosive to aluminum.

In terms of the biological constituents in the process fluid, there was ample evidence available to support the involvement of microorganisms in the observed corrosion. This evidence includes: the aeration tank utilizing microorganisms to treat wastewater (1); the presence of naturally occurring crevice formers (as a biofilm) on all of the aeration tank components that were exposed to the process fluid (2); and the morphology of pitting observed on the tank walls, floor, and aeration piping brackets, which is indicative of MIC (3) [5]. Nevertheless, even though there is probable cause to suspect involvement from microorganisms, in order to confirm whether microorganisms are indeed an environmental cause of the observed corrosion, further biological assessments and testing would be required.

Finally, the process fluid itself contained chemical constituents, including (and not limited to) sulphur and chlorine, which can cause corrosion of the aluminum components. There were several potential sources of these elements, which include: chemical constituents which may be naturally present in the wastewater (such as urine, table salt, or dissolved inorganic compounds [6]) (1), compounds which may be produced via metabolic processes of the microorganisms that are treating the wastewater (2), or chemical additives (specifically coagulants) which aid in the treatment of wastewater (such as aluminum sulphate (Alum) or

polyaluminum chloride (PACl; Isopac) (3). Both the naturally present and biologically produced sources of either element may not be easily controlled; due to either source entering or being utilized by the aeration tank. Additionally, evaluating either sources *individual* effects on the corrosion resistance of the aluminum alloys identified in the tank would be exceedingly challenging. There were several, additional, confirmed factors present in the aeration tank, which could have had an effect on the observed corrosion. These factors include: forced aeration and fluid motion, transient process fluid composition, dissimilar metal contact, and the formation of deposit (which can create a crevice) on any surfaces exposed to the process fluid. The relationship between these and other relevant factors – which affect the corrosion of aluminum – are presented below in Figure 1-4. It is, however, possible to *isolate* and evaluate the corrosivity of the individual coagulants to the aluminum alloys used in the construction of the aeration tank. Hence, for the purposes of this thesis – and per request of the WWTPs owner/operator – the corrosivity of either Isopac or Alum on the metal alloys used in the corroded aeration tank were studied.

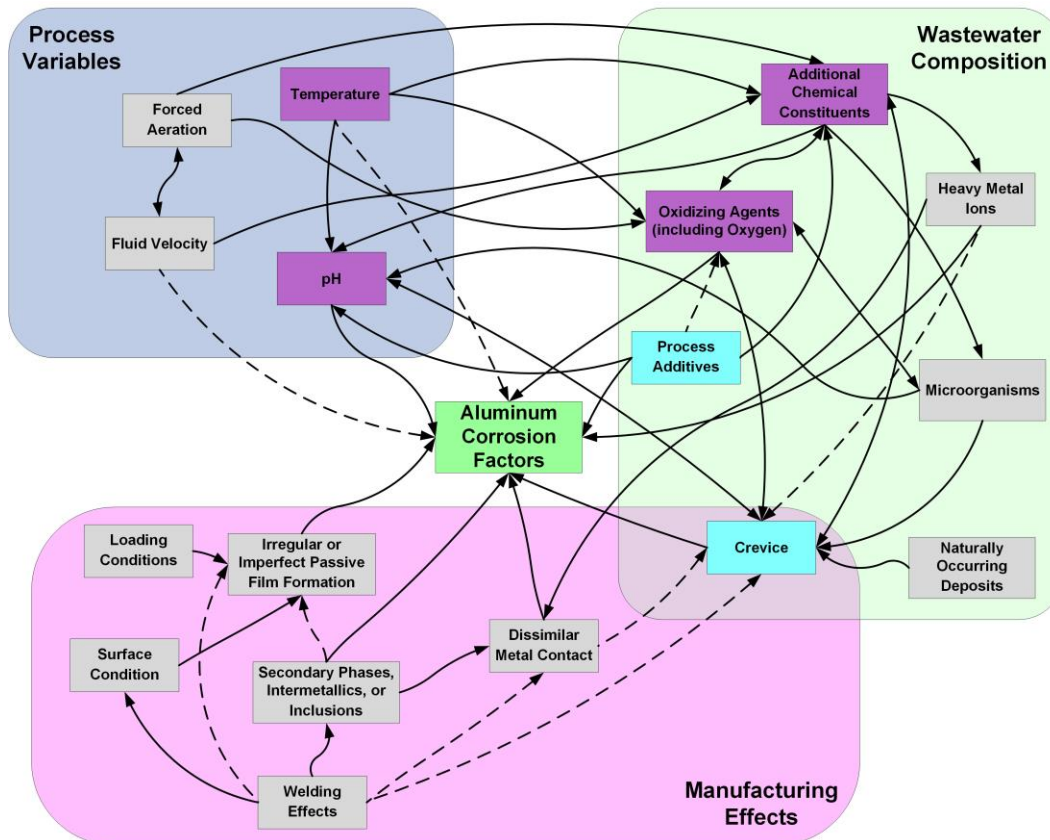


Figure 1-4: Complex systems map of some of the factors, and their relationships, which affect the corrosion of aluminum. The solid arrows indicate *there is* a relationship while the dashed arrows indicate *there may be* relationship<sup>1</sup>. The factors in the light blue boxes were controlled in the immersion testing. Conversely, the factors in the purple boxes were established at the start, and monitored over the duration, of testing. Note that only dissolved oxygen concentration and chloride concentration were monitored in the oxidizing agents and process fluid composition, respectively.

To assess the individual effects of the coagulants, laboratory scale immersion corrosion cells were designed to test fabricated corrosion coupons, which were made from the identified alloys. Additionally, due to the presence of deposit (resulting in under-deposit corrosion) throughout the aeration tank, fabricated crevices (i.e., artificial crevice formers) were installed on all of the coupons. The goal of the crevice former addition was to simulate an environment

<sup>1</sup> It is clear from this figure that the relationships between the presented factors are not very clear at all. The inter-relationships between the factors, and the corrosion of aluminum, are both complex and complicated. It is emphasized that this figure is simplified, and it contains only relevant factors and subsequent relationships.

which could induce crevice corrosion, should such a mode of corrosion occur. Due to the complexity of the aeration tank environment, many of the factors presented in Figure 1-4 were eliminated from the design of the corrosion cells; ultimately permitting the study of only the coagulants. Next, the corrosion cells were monitored (via temperature, pH, dissolved oxygen concentration, and chloride concentration; noted in Figure 1-4) throughout the immersion testing in order to evaluate the parameters relative to the operating conditions of the tank. Finally, to examine, evaluate, and quantify any corrosion damage incurred from the immersion testing, a series of material characterizations and mass change measurements were carried out on the tested corrosion coupons.

## **1.2 Thesis Structure and Objectives**

This thesis is comprised of five chapters and six appendices. Besides the introduction to this work (Chapter 1), the second chapter provides the necessary background required to understand: the wastewater treatment process (in addition to the use of coagulants), corrosion (including electrochemistry, thermodynamics, kinetics, modes of corrosion, and important factors in corrosion), and relevant materials applications and failures in wastewater treatment. Next, the third chapter provides essential information on the design of the laboratory scale immersion corrosion cells. Moreover, this chapter also contains the procedures and material characterization techniques used to monitor the corrosion cells and examine the corrosion coupons, respectively. The fourth chapter contains the results and discussion of the corrosion testing, material characterizations, and applicability of the study to the corroded aeration tank. Finally, the conclusions of the aforementioned testing, monitoring, and characterization of the corrosion coupons, as well as how they relate to the corroded aeration tank is presented in Chapter 5. Items for future work are also provided in Chapter 5.

Appendix A of this thesis is comprised of the relevant site inspection and failure analysis information, which was performed during the course of this thesis.

Moreover, the findings in Appendix A helped initiate and define the scope of the corrosion study conducted in the body of this thesis. Next, Appendices B and C contain the significant aeration tank dimensions and raw process data, respectively, used to design the laboratory scale corrosion experiments. Finally Appendices D, E, and F contain additional corrosion coupon macrophotographs collected during coupon characterization (Appendix D), referenced aluminum oxide and hydroxide Fourier Transform Infrared (FTIR) spectroscopy data (Appendix E), and additional immersion cell monitoring data (Appendix F).

In summary, the objectives of the corrosion experiments conducted in this study are as follows:

1. Design laboratory scale immersion corrosion cells which assess the corrosivity of the coagulants under artificial crevice former conditions. Additionally, monitor the temperature, pH, dissolved oxygen concentration, and chloride concentration of the corrosion cells – throughout the duration of the immersion testing – and evaluate the cells' parameters relative to the operating ranges of the aeration tank.
2. Determine the corrosivity of the isolated WWTP coagulants (Isopac and Alum), as well as de-ionized ultra-filtered (DIUF) water (the control solution), on the metal alloys identified in the corroded aeration tank. Assess whether, if any, corrosion could be identified or quantified on the tested corrosion coupons.
3. Determine if the conditions in the aeration tank would be more or less corrosive than those of the laboratory scale corrosion cells.

### 1.3 References

- [1] J.S. Pavelich, J.A. Nychka, Preliminary Findings Report: Visual Inspection and Corrosion Assessment of the EPCOR Borealis Waste Water Treatment Plant, Edmonton, AB, 2013.
- [2] J.S. Pavelich, J.A. Nychka, Additional Inspection Report: Additional Visual Inspection and Corrosion Assessment of the EPCOR Borealis Wastewater Treatment Plant, Edmonton, AB, 2014.
- [3] C. Vargel, Corrosion of Aluminium, Elsevier Ltd, Kidlington, UK, 2004.
- [4] J.R. Davis, ed., Corrosion of Aluminum and Aluminum Alloys, ASM International, Materials Park, OH, 1999. doi:10.1361/caaa1999.
- [5] B.J. Little, J.S. Lee, Microbiologically Influenced Corrosion, John Wiley & Sons, Inc., Hoboken, NJ, 2007.
- [6] L. Metcalf, H.P. Eddy, eds., Wastwater Engineering Treatment and Resource Recovery, 5th ed., McGraw-Hill Education, New York, NY, 2014.

# Chapter 2 – Background

## 2.1 Wastewater Treatment Process and Aeration Tanks

Wastewater is described by Metcalf and Eddy as “essentially the water supply of the community after it has been used in a variety of applications and which now contains constituents that render it unsuitable for most uses without treatment” [1]. Major contaminants of concern within wastewater include: suspended solids (such as feces and toilet paper); biodegradable organics (such as proteins, carbohydrates, fats, and urine); disease causing organisms (also known as pathogens – such as *E. Coli* bacteria and Norwalk virus) and parasites; nutrients (carbon, hydrogen, oxygen, sulphur, nitrogen and phosphorus), pollutants (such as pesticides); refractory (poorly biodegradable) organics (such as surfactants); heavy metals (such as arsenic, chromium, copper, iron, lead, and nickel); and dissolved inorganics (such as sulphate and chloride containing compounds) [1–4]. The wastewater treatment process is designed to use purification processes observed in nature (such as streams and rivers which self-purify) to the maximum level and rate possible, and in a controlled environment [1–3]. Treatment capabilities are further enhanced to remove other contaminants “that are not normally subjected to natural processes”, as well as to treat solids that are generated throughout the process [2]. Overall, wastewater treatment is performed by a series of steps that can be broadly categorized into the following treatments as listed by Spellman [2]:

1. Preliminary Treatment: Removes materials that could damage process equipment or would inhibit treatment capacity without being treated.
2. Primary Treatment: Removes floatable and settleable solids (may not be present in all treatment plants).
3. Secondary Treatment: Removes organic matter by reactions with microorganisms. Microorganisms convert organics and other nutrients to stable solids, carbon dioxide, and more microorganisms.

4. Advanced Waste Treatment (also known as Tertiary Treatment): Uses physical, chemical, and biological processes to remove additional organic matter and pollutants (not present in all treatment plants).
5. Disinfection: Removes microorganisms to eliminate or reduce the possibility of disease or contamination when the process fluid is discharged.
6. Sludge Treatment: Stabilizes the solids removed from wastewater during treatment, removes water from the sludge (therefore decreasing the total sludge volume), and inactivates pathogenic organisms. (Sludge is the mixture of settleable solids and water removed from various tanks in the wastewater treatment process [2].)

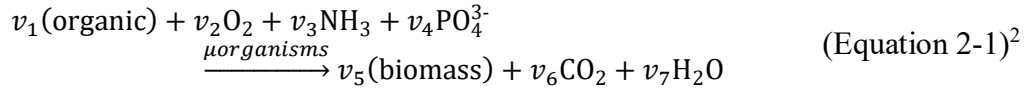
The wastewater treatment process can be accomplished using multiple treatment sub-processes (henceforth known as unit processes) and types of equipment [2]. The various unit processes – and their respective equipment – are described in greater detail by Metcalf and Eddy [1], Spellman [2], Davis [3], Bitton [4], and the Water Environment Federation (WEF) [5]<sup>1</sup>. Moreover, the configurations of equipment used to treat wastewater are numerous; given that wastewater can be from domestic, commercial, industrial, and naturally occurring environmental sources [1–5]. Finally, different equipment and treatment processes are performed in order to meet the required level of purification for the final effluent [1–5]. Information related to the wastewater treatment process shall only pertain to the municipal wastewater treatment plant (WWTP) in this study.

Critical to all WWTPs is the use of microorganisms to perform metabolic processes to convert dissolved and particulate biodegradable constituents into

---

<sup>1</sup> Each of these books provides extensive information on the various aspects of wastewater treatment. To aid the reader in selecting which book to read for a particular purpose, the author proposes the following approach. To learn the basics of the wastewater treatment process – in a simple manner, especially for the activated sludge process – as well as process troubleshooting, refer to Spellman [2]. To acquire detailed wastewater treatment process design, unit selection, and configuration information, refer to either Metcalf and Eddy [1], Davis [3], or the WEF [5]. For information on wastewater microbiology refer to Metcalf and Eddy [1] and Bitton [4]. Finally, for detailed information on material selection for WWTPs, refer to WEF [5].

stable end products [1]. This process can be simply represented in the following generalized equation (Equation 2-1) for aerobic (conditions in which free or dissolved oxygen is present [2]) biological oxidation of organic material (as stated by Metcalf and Eddy [1]):



Where  $v_x$  are stoichiometric coefficients, organic is used as a short form for organic material,  $\mu_{\text{organisms}}$  is used as a short form for microorganisms, and biomass is either new or growing microorganisms along with new organic materials as the result of the conversion of organic matter and nutrients [1]. The removal of carbonaceous material is the biological conversion of carbon-based, organic matter in wastewater to biomass (also called carbon oxidation) [1,2,5]. Microorganisms are also used to remove nitrogen and phosphorus present in wastewater process fluid [1–5]. Specific bacteria are capable of oxidizing ammonia to nitrite and nitrate (known as nitrification), while other bacteria reduce the oxidized nitrogen to gaseous nitrogen (known as denitrification) [1–4]. Meanwhile, the incorporation of inorganic phosphorus into the microorganism biomass leads to phosphorus removal [1,3,4]. There are other reactions of organic matter and nutrients such as sulphur with microorganisms, leading to either oxidized or reduced ions such as sulfate or sulfide under appropriate aerobic or anaerobic conditions (conditions in which no oxygen – free or combined – is present) [1,2,4]. No further discussion will be given to the various conversions between microorganisms and wastewater constituents, as well as produced reaction products and metabolites. For more information on wastewater microbiology, descriptions on the aforementioned nutrient reactions (including carbon oxidation, nitrification, denitrification, and phosphorus removal),

---

<sup>2</sup> Equation 2-1 provides a descriptive – rather than predictive – model for aerobic oxidization of organic matter. There are many preceding and proceeding reactions (which also involve microorganisms) that are related to this reaction, which are more accurate and would be better suited for any predictive modelling purposes.

and the various other reactions between present nutrients and organic matter, refer to books [1–5].

The wastewater treatment process examined here is a “turn-key” activated sludge WWTP, and is illustrated in Figure 2-1. This plant is also of modular construction, meaning that each of the unit processes were preassembled mechanically and electrically off-site and skid mounted. Upon receiving the plant, the steel skids were positioned into necessary order for the wastewater treatment process to occur. The unit processes that comprise this plant were described by the facilities’ owner/operators as follows. Influent wastewater is pumped to the pre-screening unit, where debris and solids are removed. This removal process is used to help protect downstream equipment from clogging or damage, in addition to save space for subsequent treatment [1–3]. Next the pre-screened wastewater flows into the equalization tank. The purpose of the equalization tank is two-fold: first to diminish any and all influent flow surges and upsets [1–3], and second to create homogeneous, non-septic (wastewater that has no dissolved oxygen present [2]) process fluid, for the downstream equipment, through mixing by aeration [1–3]. The wastewater is then pumped to three *Activated Sludge Bioreactors*, whose individual capacity is 33% of the incoming process fluid. Note that the remaining treatment of wastewater in this process is comprised of three identical trains, each of which contains an activated sludge bioreactor and downstream equipment. Hence, for the purposes of this explanation, only a single train is explained.

The bioreactors can be separated into two compartments: the anoxic zone (conditions in which no free elemental oxygen is present, but only oxygen bonded in oxidized compounds such as nitrate are present [1,2]) and the aerobic zone (the aerobic zone will henceforth be known as the aeration tank). From the equalization tank, the wastewater first enters the anoxic zone. In this compartment, denitrification occurs via conversion by microorganisms and slow mixing [1,2]. The process fluid then flows over the weir into the aeration tank where further biological treatment of the wastewater is carried out through the use of aerobic bacteria to

remove organic contaminants by metabolic processes [1–3]; leading to nitrification and decomposition of carbonaceous organic matter [1]. Air is injected into the tank in order to meet the oxygen requirements of the system and to provide adequate mixing [1–3]. Further description of the aeration tanks is provided in subsequent paragraphs in this section. After biological treatment, the wastewater flows to a clarifier where separation and sedimentation can occur. Depending on the mass of the solids relative to water, solids heavier than water will settle (biological solids known as sludge are removed from the tank bottom) or float (residual oil and grease known as scum are removed from the top of the tank) [1–3]. The clarifier effluent then flows to a micro-drum rotary drum strainer for final screening of solids. Here the strainer uses a 15 to 20  $\mu\text{m}$  sized mesh screen to remove residual suspended solids and microorganisms [1,2]. The strained process fluid then flows into a three-part micro-drum dosing, scum, and backwash tank. This tank serves three purposes: the first is to provide backwashing for other plant units (backwash portion of tank), the second is to store scum (scum portion of tank), and the third is to store the treated effluent (dosing portion of tank). From the dosing tanks of the three trains, the treated effluent is then distributed; ending treatment of process fluid in this plant.

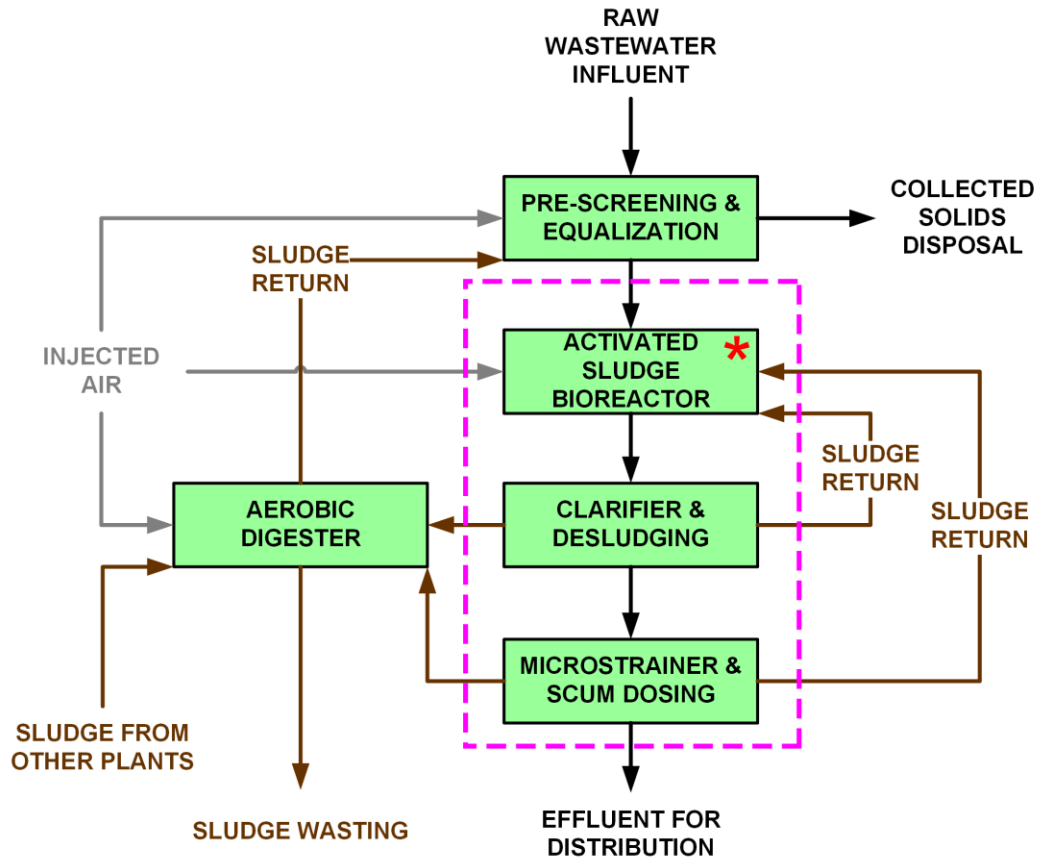


Figure 2-1: Basic overall process flow diagram of the WWTP in this study. For simplicity, all three trains are combined into one in the figure and are contained within the pink-dashed box. The aeration tank and identified corrosion is contained within the “Activated Sludge Bioreactor”, which is emphasized by the red asterisk.

The collected sludge from the clarifier and backwash tank is either pumped directly back to the anoxic zone or to the aerobic digester. This recycled sludge is known as return activated sludge (RAS) and it is used to maintain the biological treatment occurring in the bioreactor [1–3]. The aerobic digester is designed to treat – through aeration and mixing – the incoming sludge so it can either be used again in the wastewater treatment process, or be disposed. Any sludge that is discarded is known as waste activated sludge (WAS). In either case, the digestion (also known as stabilization) treatment of the sludge is accomplished by reducing the sludge volume (in part by the decomposition of carbonaceous organic matter), stabilizing the organic matter, and inactivating any pathogenic organisms [1,2,4]. Further information on the aerobic digester and processes such as stabilization can be found in references [1], [2], [4], and [5]. After digestion, the treated sludge is fed to the

solids handling centrifuge. The centrifuge provides dewatering of the solids [1–3]. From the centrifuge, the treated solids will be discharged while the separated liquid will be pumped back to the equalization tank.

Coagulants can be added to wastewater to aid in sedimentation of both colloidal and suspended solids, and the removal of phosphorus [1–6]. Coagulation is the destabilization of colloidal particles, leading to particle growth due to subsequent particle collisions [1,2]. These particles can lump together into flocs which can then settle [1,2]. Common coagulants used in wastewater treatment are metal salts such as aluminum sulphate (Alum;  $\text{Al}_2(\text{SO}_4)_3 \cdot 14\text{H}_2\text{O}$ ) and prehydrolyzed metal salts such as polyaluminum chloride (Isopac; PACl;  $\text{Al}_2(\text{OH})_x\text{Cl}_{6-x}$   $0 < x < 6$ ) [1–5]. Details on chemical coagulation reactions and related theory are beyond the scope of this work. Further information on coagulation pertaining to Alum and PACl can be found in books by Metcalf and Eddy [1], Spellman [2], Davis [3], and the WEF [5] as well as papers by Jiang [7] and Tang et al. [8]. Both coagulants have been used, at separate times and in liquid solution, in the WWTP in this study. Furthermore, both of these chemicals dissociate in water [9,10] and were dripped in the upstream end of the aeration tank before being added to the downstream clarifier.

Described by Spellman [2], “the activated sludge process<sup>3</sup> is a treatment technique in which wastewater and reused biological sludge full of living microorganisms are mixed and aerated”; leading to conversion and treatment of wastewater constituents. The active sludge is comprised of organic solids plus bacteria, fungi, protozoa, rotifers, and nematodes [1–3]; yet, Davis [3] suggests that bacteria are the greatest population of microorganisms present in wastewater treatment. As the microorganisms interact with the process fluid and air in the aeration tank, they consume the organic material and oxygen; consequently leading

---

<sup>3</sup> The activated sludge process is a type of suspended growth process [1]. Metcalf and Eddy [1] define the suspended growth process as a “biological treatment process in which the microorganisms responsible for the conversion of the organic matter or other constituents in the wastewater to gases and cell tissues are maintained in suspension within the liquid”.

to growth and reproduction (as previously shown in Equation 2-1) [1–6]. Flocculation (the gathering of fine particles into larger particles) occurs as the growing organisms and organic matter are mixed and group together, followed by settling of the formed flocs in the downstream clarifier [1–4,6]. Regarding the removal of heavy metals, microorganisms will adsorb or complex the metals which may lead to subsequent metal transformation and precipitation [1]. The use of RAS in the bioreactor allows for continuous metabolism and flocculation of organic materials; however, due to the constant growth and aging of the activated sludge, some of the sludge has to be treated and disposed of as WAS [2]. The aeration tank and anoxic zone (as the activated sludge bioreactor) are critical components to the secondary treatment of organic matter and nutrients in the WWTP of this study. Without functioning aeration tanks, biological treatment of wastewater could not be performed; therefore leading to an inoperable WWTP.

A representative image of the examined aeration tank in this wastewater treatment process is shown below in Figure 2-2. Additional aeration tank images, and the layout of internal components, can be found in Appendix A or in previous reports [11,12] written by the author. All three aeration tanks are rectangular prisms, with the same dimensions (approximately 17.1 m length x 3 m width x 3 m height). As reported in Appendix A, the aeration tank examined was constructed of three materials. The walls and floor were made of dual certified 5086/5083 grade aluminum. Meanwhile, the tubular ties were fabricated from 6061 grade aluminum and the aeration piping was 304/304L grade stainless steel. As previously mentioned about the modular construction, the aeration tanks were mounted on steel skids. Moreover, the aeration tanks were not electrically isolated from the steel floor [12].



Figure 2-2: Representative image of a functioning aeration tank in the WWTP examined in this study. The camera is located at the upstream end of the tank (opposite end from the anoxic zone). The arrow points in the direction of the flow of process fluid.

Key process data of the aeration tank examined in this study is presented in Table 2-1. Also included in this table is the influent flow rate, as well as the drip rate of Isopac and Alum when each was individually being added to the tank. The occurrence of a neutral pH<sup>4</sup>, ambient temperature, and dissolved oxygen are consistent with a functioning aeration tank [1,2]. Moreover, the presence of chloride can be attributed to urine, in addition to other contaminants that could be present in wastewater [1]. As mentioned at the start of this section, there are potentially many constituents of concern – from a corrosion perspective – in wastewater [1–5]. These constituents are numerous in number and may be present in many forms. Moreover, with seasonal variations and possible additions of waste from other sources (such as other municipal or industrial wastewater), the constituents present and their concentration in wastewater can vary. Therefore, no

---

<sup>4</sup> pH is a measure of the activity – or typically the concentration – of hydrogen ions in solution. It can be calculated by taking the negative logarithm of the hydrogen ion activity (or hydrogen ion concentration multiplied by its respective activity coefficient).

attempt was made to determine the detailed composition of matter present in the aeration tank wastewater. For some insight into the composition of wastewater, Table 2-2 contains the typical composition of untreated domestic wastewater as reported by Metcalf and Eddy [1]. It is emphasised that only relevant constituents related to corrosion and this study are presented in Table 2-2.

Table 2-1: Key process data collected from the aeration tank examined in Appendix A. Information on data collection and analysis provided in Appendix C.

<b>Metric</b>	<b>Mean</b>	<b>Minimum</b>	<b>Maximum</b>	<b>CI</b>
Influent Flow Rate [m <sup>3</sup> /day]	185	22	292	3
pH	7.1	5.8	7.8	0.0
DO Concentration [mg/L]	2.07	0.10	6.10	0.06
Temperature [°C]	22.9	17.8	27.4	0.2
Isopac Flow Rate [mL/min]	13.0	8.8	22.0	0.9
Alum Flow Rate [mL/min]	22.4	1.4	32.0	0.8
Chloride Concentration* [mg/L]	190	173	207	NR
Conductivity* [μS/cm]	NR	1269	1294	NR

CI: 95% Confidence Interval<sup>5</sup>; DO: Dissolved Oxygen; NR: Not Reported

\* Both the conductivity and chloride concentration were measured from one of the other two, active aeration tanks. Neither parameter could be measured in the corroded aeration tank, since the tank was removed from service and drained.

---

<sup>5</sup> Refer to Chapter 3 for the equations used to calculate the confidence intervals.

Table 2-2: Typical composition of untreated domestic wastewater<sup>6</sup> [1].

Constituent	Concentration [mg/L] <sup>†</sup>		
	Low Strength	Medium Strength	High Strength
Total Solids	537	806	1612
Total Dissolved Solids	374	560	1121
Total Suspended Solids	130	195	389
Total Nitrogen	23	35	69
Organic Nitrogen	10	14	29
Free Ammonia	14	20	41
Nitrites	0	0	0
Nitrates	0	0	0
Total Phosphorus	3.7	5.6	11.0
Organic Phosphorus	2.1	3.2	6.3
Inorganic Phosphorus	1.6	2.4	4.7
Chlorides	39	59	118
Sulphate	24	36	72
Oil and Grease	51	76	153

<sup>†</sup>: Low strength, medium strength, and high strength concentrations are based on an approximate wastewater flowrate of 570 L/capita•d (150 gal/capita•d), 380 L/capita•d (100 gal/capita•d), and 190 L/capita•d (50 gal/capita•d), respectively [1].

It is again emphasized that there is little information present in Table 2-2 on how the various constituents listed are interacting in wastewater. Additionally, it should be noted that the concentration of chlorides in the aeration tank wastewater examined in this study is nearly twice as high as the “high strength” concentration of untreated domestic wastewater. No attempt was made to collect the sulphate concentration in the wastewater of the aeration tank examined in this study.

From the variety of potential constituents within wastewater, along with the addition of chemical coagulants and the presence of microorganisms in the treatment of said wastewater, there appear to be *many* possible factors which could cause corrosion. Further discussion of corrosion and relevant corrosion case studies in wastewater treatment is presented in the subsequent sections of this chapter.

---

<sup>6</sup> Not included in Table 2-2 are concentrations of any heavy metals or mineral cations and anions that may be present in domestic wastewater. For some insight into what elements are present in an aeration tank – specifically in dried sludge and deposit found at the bottom of the tank – refer to Appendix A Section 2.2.1.

## 2.2 Relevant Material Applications and Failures in WWTPs

Directly from WEF's book [5] "the environment in which most wastewater treatment systems operate is not defined specifically in the design process. As such, materials engineers are not called on to select adequate materials for the design service intended." Moreover, there are instances where a bill of materials is not available, or any additional considerations were made for process equipment to withstand any particular, unspecified operating condition [5]. These circumstances can lead to some uncertainty in the materials used – or more importantly, materials which *should* be used in a WWTP.

The typical material of construction for most process vessels in municipal WWTPs is reinforced concrete [1,3,5,13]. This material choice is especially true for aeration tanks that are left open to the atmosphere [1]. Meanwhile, process piping used to transport wastewater between equipment and unit processes include: reinforced concrete, carbon steel (which **requires** appropriate coating for corrosion protection [5]), cast iron, ductile iron, stainless steel (such as grades 304 and 316), and polymers (such as polyethylene, polypropylene, and polyvinyl chloride – which is the most common plastic piping material [2,5]) [1–3,5,13]. The exact material selected for transport of said wastewater depends heavily on the wastewater composition, as well as physical and chemical properties.

Aluminum alloys are used in WWTPs primarily for auxiliary equipment or in architectural applications [5,13–15]. Auxiliary equipment, where aluminum alloys are used, include: bar screens/grating, hatch and chamber covers, slide gates, stop logs/gates, weir plates, troughs, and appurtenances [5,13–15]. Meanwhile, examples of where aluminum alloys have been used for architectural applications include: hand railings, stairs, ladders, platforms, floor grating, tread plate, doors, windows, conduit, lighting fixtures, and ventilation ducts [5,14,15]. Both the Aluminum Company of America (ALCOA) [14] and the Aluminum Association [15] suggest that aluminum alloys could be used for tanks/vessels and piping;

however, neither entity provides any data on process conditions, or in what unit processes and related equipment the aluminum alloys could be applied. Contrary to both ALCOA and the Aluminum Association, the WEF [5] explicitly states that caution and discretion should be applied when selecting aluminum alloys for immersion applications in wastewater treatment. The WEF goes on to say that aluminum alloys “typically are not used in wastewater treatment systems because of the difficulty of corrosion control” [5].

There is little literature available for corrosion testing and failures of aluminum alloys in WWTPs. Stowell [16] mentioned that corrosion damage had been observed on aluminum pump frames; yet he does not provide any details on the application of the pumps, or if the pumps were immersed in the wastewater process fluid. Ailor [17] had performed immersion testing with several aluminum alloy coupons – including grades 5086 and 6061 – in two locations within a wastewater treatment plant: the raw sewage influent grit tanks and the final-treated effluent river discharge. After one year of immersion, no appreciable corrosion damage was noted on the aluminum alloys in the grit tank; however, localized corrosion was observed on nearly all aluminum alloys, including grades 5086 and 6061, in the effluent discharge [17]. Severe corrosion was reported by Kumar and Stephenson [18] of an aluminum ladder that had been installed in a primary treatment clarifier. The relatively new aluminum ladder – immersed in the process fluid of the concrete clarifier – had corroded badly below the clarifier water line [18]. No compositional information was supplied of the process fluid, or how long the ladder had been installed in the clarifier.

Stainless steel alloys such as grade 304 are used in a number of applications including some process equipment and piping, auxiliary equipment or in architectural applications [1–3,5,13,19]. Process equipment, where stainless steel alloys are used, include: smaller aeration tanks, activated sludge digestion tanks, disinfection chambers, and centrifuges [13]. Alternatively, auxiliary equipment or architectural applications where stainless steel is used include: pump shafts and

impellers, bearings, screens, screen and sediment rakes, air-diffuser piping (also called aeration piping), process fluid piping, fasteners, anchor bolts, handrails, stairs, platforms, and chemical containment [1–3,5,13]. Both the WEF [5] and Bennett and Nixon [13] discuss the use of stainless steel alloys in wastewater treatment – in immersed service, rather than just auxiliary or support systems – in greater detail. Furthermore, Tuthill [19] has written a brief set of guidelines for the use of stainless steel alloys in WWTP piping.

As opposed to aluminum alloys, there is more literature available for corrosion testing and failures of stainless steel alloys in WWTPs; particularly austenitic and duplex stainless steels. For the purposes of this thesis, only testing of grades 304 and 316 (both austenitic grades) will be discussed. Ailor [17] also immersed 304 stainless steel coupons, in the same conditions and timeframe, as mentioned previously. No noticeable corrosion was detected on the 304 alloy in either the grit tank or effluent discharge [17]. Englert and Müller [20] performed thirty day immersion tests with grade 304 coupons in process fluid collected from an anaerobic digester. Localized corrosion was found on the coupons and was believed to have been induced by microorganisms [20]. Several immersion studies performed by Iversen [21–23] determined that welded 304 and 316 alloy coupons may or may not corrode – either in aerobic or anaerobic digesters or final settling tanks (vessel before effluent is discharged). Localized corrosion was observed in the alloys under specific environmental conditions: namely a sufficient chloride concentration and presence of microorganisms [21,22]. Kovach et al. [24] mentioned two cases in which grade 316 had corroded in WWTPs: the first in an anaerobic digester and the second in a pipe downstream of a final settling tank. In both cases it was suggested that microorganisms contributed to the localized corrosion [24]. Collected WWTP operator inspections and field tests collected and performed by Mathiesen *et al.* [25] describe localized corrosion of both 304 and 316 grades near the final stage of the wastewater treatment process. Again, the involvement of microorganisms was believed to be the cause of corrosion [25]. Finally, a modular WWTP with 304 grade stainless steel process vessels – including

an anoxic zone, aeration tank, and downstream (secondary) clarifier – was inspected by the author [26]. No observable corrosion damage was identified on any of the inspected equipment, including the aeration tank and clarifier [26]. There was, however, severe corrosion on what was believed to be aluminum scaffolding, which was immersed and had been left in the aeration tank [26].

From the aforementioned literature, both aluminum and stainless steel alloys have been utilized in WWTPs, with stainless steel being more widely used and studied than aluminum. Moreover, corrosion damage has been observed in both types of materials, under certain circumstances – as previously mentioned, when exposed to wastewater. There was, conversely, little mention of aluminum alloys being used in the construction of activated sludge aeration tanks or any modular WWTPs. Companies such as ADI Water Solutions Ltd. [27], NatureClean [28], and CORIX® [29] construct modular WWTPs with aluminum alloys; however, any related material performance data, failures, or case studies of aluminum alloys as wastewater treatment process vessels are not available. Since corrosion was the identified failure mode throughout the presented case studies (as well as in Appendix A), a discussion of the phenomena that is corrosion, as well as how corrosion manifests itself, will be presented in the following section.

### **2.3 Basics of Electrochemical and Corrosion Reactions**

Corrosion can be defined as the unwanted deterioration of a material which results from either a chemical or electrochemical reaction with its environment [30–38]. This unwanted deterioration can manifest visually as loss of material, formation of corrosion products (examples occurring on metals being tarnish, deposits, or tubercles [30,31]), or both. Moreover, the occurrence of corrosion can lead to undesirable changes in materials' physical – mechanical being especially of concern – and chemical properties. Due to the various degradation phenomena which are encapsulated in the definition of corrosion (such as high temperature oxidation of metals and chemical degradation of polymers [32,34,36]), discussion

in this work shall only pertain to electrochemical corrosion of metals in aqueous (containing water) environments. Moreover, only aluminum alloys – more specifically, 5086 and 6061 grades – will be used in discussion of the various topics in the following paragraphs (since these alloys were found to be corroded in Appendix A and reports by the author [11,12]).

Four components of an electrochemical cell are required in order to facilitate aqueous, electrochemical corrosion (henceforth known as corrosion) [32–35,37,38]. These components are known as the anode, cathode, electrolyte, and electron bridge [32–35,37,38]. The anode is the location on the metal surface where metal atoms oxidize (i.e., give up electrons) and then enter, as ions, into the electrolyte – a chemical substance which contains the ions (along with potentially many other chemical and biological species) and allows for migration of ions to the their respective anode and cathode sites [30]. This redox reaction, also known as anodic dissolution, is presented in Equation 2-2 for the generic metal atom, M [32–38].



Where  $e$  is the electrons produced, while  $m$  corresponds to the oxidation state of the metal ion and – in the case of this simple expression – the number valence electrons. For corrosion, the anode site is normally where metal atoms dissociate and metal loss occurs – or, in the context of this thesis, corrosion occurs. Moreover, regarding aluminum alloys, the metal atom (also called the reducing agent in the electrochemical reaction) typically represented by M is aluminum (Al). Aluminum’s typical oxidation state is  $Al^{3+}$ , as shown in Table 2-3.

The cathode is the location where chemical species in the electrolyte are reduced (i.e., gain electrons). Cathodes, generally, are also found on the metal surface; however, they can also be on other locations including previously formed corrosion products, artificial crevices, or anything connected to the anode with

sufficient electrical conductivity. The path which allows electrons to travel from the anode to cathode sites is known as the electron bridge. In most corrosion reactions, this electron bridge is the metal itself. A general expression for the reduction reaction (which is concomitant to the oxidation reaction in Equation 2-2) occurring at the cathode is describe in Equation 2-3 for the generic oxidizing agent (cathodic reactant), X [32–38].



In Equation 2-3, e is the electrons consumed, while x is the oxidation state of the oxidizing agent species and the number of valence electrons. It should be noted that the state of either X or its respective ion are not listed in Equation 2-3. This is because the oxidizing agent(s) may be in several states including as a gas or dissolved (labelled as aqueous). Moreover, the addition of electrons to the ions will lead to a change in oxidation number that may result in the formation of another ion with a different oxidation state, or a complete atom/compound.

Table 2-3: Standard equilibrium half-cell<sup>†</sup> potentials for select reactions. Standard potential values at 25 °C and unit activity ( $a_{\text{species}} = 1$  or  $P_{\text{species}} = 1 \text{ atm}$ ) [32,35].

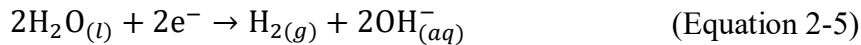
Electrode Reaction	$E^{\circ}$ , [V vs. SHE <sup>‡</sup> ]	
$\text{Au}^{3+} + 3e^{-} \rightarrow \text{Au}$	1.498	Noble or Cathodic  ↑
$\text{O}_2 + 4\text{H}^{+} + 4e^{-} \rightarrow 2\text{H}_2\text{O}$	1.229	
$\text{Pt}^{2+} + 2e^{-} \rightarrow \text{Pt}$	1.18	
$\text{Hg}^{2+} + 2e^{-} \rightarrow \text{Hg}$	0.797	
$\text{O}_2 + 2\text{H}_2\text{O} + 4e^{-} \rightarrow 4\text{OH}^{-}$	0.401	
$\text{Cu}^{2+} + 2e^{-} \rightarrow \text{Cu}$	0.342	
$2\text{H}^{+} + 2e^{-} \rightarrow \text{H}_2$ (SHE)	0.000	
$\text{Pb}^{2+} + 2e^{-} \rightarrow \text{Pb}$	-0.126	
$\text{Ni}^{2+} + 2e^{-} \rightarrow \text{Ni}$	-0.257	
$\text{Fe}^{2+} + 2e^{-} \rightarrow \text{Fe}$	-0.440	
$\text{Cr}^{3+} + 3e^{-} \rightarrow \text{Cr}$	-0.744	↓ Active or Anodic
$2\text{H}_2\text{O} + 2e^{-} \rightarrow \text{H}_2 + 2\text{OH}^{-}$	-0.820	
$\text{Al}^{3+} + 3e^{-} \rightarrow \text{Al}$	-1.662	
$\text{Mg}^{2+} + 2e^{-} \rightarrow \text{Mg}$	-2.356	

<sup>†</sup>: The term “half-cell” can also be called: electrode, redox, reduction, oxidation (if the reactions are written in the opposite direction as listed in the table), and as the emf series [32]. The word standard indicates specific environmental conditions at which the potential measurements were collected. <sup>‡</sup>: Standard Hydrogen Electrode

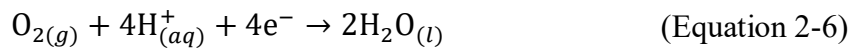
Depending on the conditions of the electrolyte (such as the temperature, pH, conductivity, and constituent concentrations), in addition to what chemical or biological species are present, a number of different oxidizing agents may lead to subsequently several different reactions at the cathode sites [32–35,37,38]. Due to the potentially numerous number of oxidizing agents, further discussion shall only pertain to reduction reactions involving hydrogen, oxygen, and water. Additional oxidizing agents, and their half-cell reactions are listed in Table 2-3<sup>7</sup>. For aqueous solutions absent of oxygen (deaerated), and with a pH < 7, the hydrogen ions act as the oxidizing agent in the cathode reaction which produces hydrogen gas (Equation 2-4) [32].



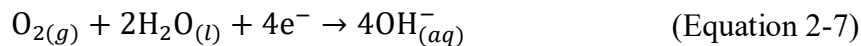
Next, for deaerated, aqueous solution with a pH ≥ 7, water itself consumes electrons to form hydrogen gas and hydroxide ions (Equation 2-5) [32].



When oxygen is present in the solution, the solution is said to be aerated. Hence, for aerated solution with a pH < 7, the oxygen molecule and hydrogen ions participate in the cathode reaction to produce water (Equation 2-6) [32].



Finally, for aerated solutions with a pH ≥ 7, both the oxygen and water molecules participate in the reaction to form hydroxide ions (Equation 2-7) [32].




---

<sup>7</sup> By no means is this list of redox reactions complete. Given the right environmental conditions, there could potentially be dozens of other oxidizing agents. One of the challenges in identifying and mitigating corrosion is determining the oxidizing agents present – and related cathodic reactions – as well as any additional chemical reactions which either precede or follow the corrosion reaction.

The respective standard equilibrium potentials for Equation 2-4 through 2-7 are provided in Table 2-3. Moreover, it can be observed in Table 2-3 that the half-cell reactions which contain oxygen (Equations 2-6 and 2-7) have higher potentials than the reactions that are deaerated (Equations 2-4 and 2-5). Therefore, in aqueous solutions with oxygen present, reactions containing oxygen will likely be the preferential cathodic reactions. Depending on the pH – as well as if there are additional constituents in the electrolyte or stronger oxidizing agents present – either reactions in Equations 2-6 or 2-7 will occur. Both anode and cathode half-cell reactions are required in order to complete the overall cell reaction; leading to the formation of a corrosion cell.

## 2.4 Corrosion Thermodynamics

In order to better understand corrosion – or rather: could corrosion occur? – an understanding of the relevant thermodynamics must be discussed. (Again, discussion shall only pertain to aluminum.) In order for corrosion to occur, there must be a sufficient negative change in Gibbs free energy to enable the corrosion cell reaction [32–38]. An expression which relates the Gibbs free energy change to an accompanying electrochemical reaction is shown in Equation 2-8.

$$\Delta G = -nFE_{\text{cell}} \quad (\text{Equation 2-8})$$

Where:  $\Delta G$  is the change in Gibbs free energy (units of joules; J),  $n$  is the number of moles of electrons (unit charges) transferred per unit of reaction (units of mol  $e^-$ ),  $F$  is Faraday's constant (approximately 96485) coulombs (joule/volt) per mole of electrons (units of C/mol  $e^-$ ), and  $E_{\text{cell}}$  is the equilibrium potential of the cell reaction – in this case the corrosion cell (units of V) [32–38]. It can be observed that if the cell potential is positive, the Gibbs free energy change will be negative; indicating that the reaction will be spontaneous and can occur as described by the combined half-cell reactions. Meanwhile, if the cell potential is negative, the change in free energy will be positive which indicates that the reaction is non-spontaneous and

will not occur. The equilibrium cell potential can be calculated for the cell reaction using Equation 2-9, which is known as the Nernst Equation [32–38].

$$E_{\text{cell}} = E_{\text{cell}}^{\circ} - \frac{RT}{nF} \ln \frac{\prod a_{\text{products}}}{\prod a_{\text{reactants}}} \quad (\text{Equation 2-9})^8$$

Where:  $E_{\text{cell}}^{\circ}$  is standard equilibrium cell potential (units of V),  $R$  is the universal gas constant (approximately 8.314) joules per mole Kelvin (units of J/(mol•K)),  $T$  is temperature (units of K), and the  $a$ 's are the activities of the product and reactant species in the cell reaction (activities are unitless) [32–38]. Four points need to be emphasized from Equation 2-9. First, the second term in the Equation allows for the calculation of the cell potential when the corrosion reaction is not at standard conditions (i.e. when the temperature is not at 25 °C and when the activities of the produced or reacted species are not equal to 1). Second,  $E_{\text{cell}}^{\circ}$  can be calculated by subtracting the standard anodic reaction half-cell potential from the standard cathodic reaction half-cell potential, as shown in Equation 2-10.

$$E_{\text{cell}}^{\circ} = E_{\text{cathode}}^{\circ} - E_{\text{anode}}^{\circ} \quad (\text{Equation 2-10})$$

Third, the activities of each species can be calculated by multiplying the concentration ( $c$ ) of the element or compound by its respective activity coefficient ( $\gamma$ ). In many cases, the concentration of the species is used in calculation of the cell potential instead of activity<sup>9</sup>. For gaseous species, the partial pressure ( $P_{\text{species}}$ ) is used instead of concentration. The fourth, and final point, is that the activities of pure substances such as solids and liquids – including water – are equal to 1.

From the position of the aluminum half-cell reaction in Table 2-3, it is easy to see that, from theory, aluminum is very anodic to most other half-cell reactions.

---

<sup>8</sup> The Nernst equation presented in Equation 2-9 represents the combined Nernst half-cell equations for the two individual electrode reactions.

<sup>9</sup> This would imply that the activity coefficient is equal to 1. Usually, the activity coefficient of each species is unknown. Moreover, in ambient conditions, it is very possible that the activity coefficient may have negligible effects on the concentration, and successively calculated activity.

When coupled to metals such as copper, lead, nickel, iron, and chromium, aluminum is implicated in the anode reaction (while any of the listed metals will be the cathode reaction, or site at which the cathode reaction occurs). Under standard, equilibrium conditions the corrosion cell potentials can easily be calculated using Equation 2-10. The  $E_{\text{cell}}$  values (which under standard conditions is equal to  $E^{\circ}_{\text{cell}}$ ) for the aforementioned metals connected aluminum are: 2.004 V, 1.536 V, 1.405 V, 1.222 V, and 0.918 V, respectively. The potentials for the reactions with aluminum are all positive, signifying that there is a sufficient driving force for aluminum to oxidize; consequently leading to aluminum corrosion. If aluminum is not connected to a more noble metal, and is present in either aerated or deaerated water, aluminum will still act as the anode half-cell reaction to the applicable oxidizing agents and reactions listed in Equations 2-4 through 2-7 (their respective standard equilibrium half-cell potentials are also listed in Table 2-3). In all four possible electrochemical cells, the cell potentials (if calculated) would be found to be positive, further indicting that there is a driving force for aluminum to oxidize. It is possible, however, for other reactions – that may be chemical or electrochemical – to occur instead (due to having a greater driving force), which could prevent aluminum from completely reacting and producing ions in the electrolyte. Further knowledge of the possible reactions and thermodynamic data is required in order to determine if corrosion can occur in a given system (metal or alloy in an aqueous solution).

Pourbaix diagrams (also known as E-pH diagrams) can be used to quickly identify which species is stable at a given potential and pH [32–38]. These diagrams use known information of the various electrode and chemical reactions which could occur in a system. The Pourbaix diagram for aluminum in water is plotted in Figure 2-3. Further information on the reactions and how to construct Pourbaix diagrams can be found in books [32,33,35–37], or in Pourbaix’s famous book: *Atlas of Electrochemical Equilibria in Aqueous Solutions* [39].

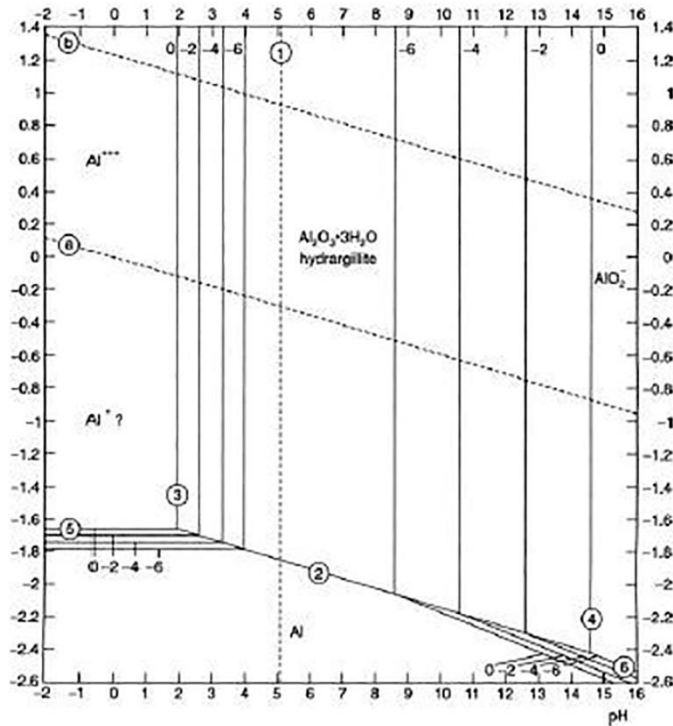


Figure 2-3: The Pourbaix diagram for the aluminum-water system at 25 °C [36,39]. Generally, the concentration of aluminum ions in solution is assumed to be equal to  $10^{-6}$ ; therefore, the lines with  $-6$  should be used as the boundaries. (Reproduced with permission from NACE International, Houston, TX. All rights reserved. [39]. © NACE International 1974.)

It can be observed in Figure 2-3 that aluminum is stable in water between the pH range of approximately 4 and 9 [39], due to the formation of a passivating film ( $\text{Al}_2\text{O}_3$ ). Passivation will be discussed near the end of this chapter. Moreover, aluminum is found to corrode at pH values less than 4 and greater than 9 (aluminum is amphoteric [38]). At this time, it should be noted that Pourbaix diagrams are very limited. The limitations of these diagrams are described by McCafferty [35], Revie and Uhlig [38], and Pourbaix [39] as follows:

1. Pourbaix diagrams are for equilibrium conditions. (In reality, the actual conditions may be far from equilibrium.)
2. These diagrams are constructed for pure metals in water (and at 25 °C). These diagrams do not consider metal alloys with one primary element and small amounts of alloying elements (such as aluminum alloy grades 5086

and 6061), or alloys comprised of two or more primary alloying elements (such as grade 304 stainless steel). With an increase in amount of alloying elements there requires an increased number of chemical reactions and subsequent thermodynamic calculations to generate the diagrams.

3. Diagrams do not consider if the metal or alloy is passive; or rather, the degree of passive film perfection (there could be defects or pores which decrease the protectiveness of the film). Additionally, the diagrams do not consider localized corrosion. (Further discussion on passivation is provided in later sections in this chapter.)
4. The accuracy of the diagrams depends on the accuracy of the thermodynamic data available. Moreover, data for complex electrolytes and constituents may be unavailable.
5. The pH value in the diagrams is for the local pH value – in direct contact with the metal surface – rather than the pH of the entire electrolyte. Therefore, even though the bulk pH may be easily measured, it may not represent the actual pH in the localized environment.

With these limitations, great discretion must be applied when trying to predict the performance of a metal or alloy in an electrolyte that is not pure water. Ultimately, Pourbaix diagrams express what is energetically possible; or, in simple terms, if a given reaction can occur. Even if a stated reaction is said to occur, it does not necessarily indicate what actually occurs, or how fast the reaction(s) proceed. Therefore, experimental kinetic studies are required in order to provide further information on the occurrence and progression of corrosion.

## **2.5 Corrosion Kinetics**

If there is a sufficient thermodynamic driving force for corrosion to occur, the two questions to ask next are: (1) will corrosion occur and (2) at what rate? Even if a given corrosion reaction is spontaneous, it doesn't necessarily mean it will occur and proceed quickly – aluminum is an excellent example in this context.

To answer the first question, a little knowledge of electrochemical kinetics is required. It is emphasised here that not much of an understanding of the mechanism(s) of kinetics as applied to electrochemistry is necessary to comprehend the work performed in this study. Furthermore, there are entire chapters and sections of books dedicated to this topic. Hence, the author recommends the following books by: Stansbury and Buchanan [32], Davis [33], Fontana [34], McCafferty [35], Roberge [37], and Revie and Uhlig [38] for more information.

As described by Fontana [34], electrochemical reaction rates can be limited by numerous physical and chemical factors. Hence, these reactions are said to be either polarized or diminished by these environmental factors [34]. Polarization can be divided into three types: activation polarization, concentration polarization, and resistance polarization (also called Ohmic drop) [37]. Activation polarization is a complex function which describes the charge transfer kinetics of a given electrochemical reaction, at the metal-electrolyte interface [34,37]. A simplified example by Fontana [34] describes how in the reduction of hydrogen ions, activation polarization is governed by the adsorption, electron transfer, combination of hydrogen atoms, and the formation and release of hydrogen gas bubbles ( $H_2$ ). Concentration polarization describes the kinetics of mass transport (diffusion, migration, and convection) of species in the electrolyte [34,37]. In the same example by Fontana [34], concentration polarization is governed by the movement of hydrogen ions and hydrogen gas bubbles to and from the metal surface. It can be recognized that activation polarization describes phenomena at the metal-electrolyte interface, while concentration polarization describes species movement in the bulk solution. Activation polarization is usually the controlling factor during corrosion in electrolytes containing high concentrations of active species (such as in strongly acidic and basic solutions) [34,37]. Meanwhile, concentration polarization usually predominates when the concentration of the active species is low (such as in dilute or aerated solutions) [34,37]. Finally,

resistance polarization accounts for the electrolytic resistance of the electrolyte<sup>10</sup> [37]. This form of polarization becomes important when the anode and cathode sites of the corrosion cell are separated by larger distances, while still being electrically coupled via electron bridge [37].

Regarding the second question about rates of corrosion, there are two general ways to determine corrosion rates: electrochemical and non-electrochemical methods. There are further ways to segregate types of corrosion tests based on the type (or mode; discussed later in this chapter) of corrosion expected, as well as where the test is performed (such as in the laboratory, pilot-plant studies, or in the field – in actual service conditions or *in situ* [34]). Nevertheless, for the purposes of this thesis, the two categories will be sufficient. The electrochemical methods rely heavily on the understanding of the polarization behaviour as described in the previous paragraph. Moreover, no electrochemical techniques were used in this study. Common electrochemical methods used to measure corrosion rates include potentiodynamic polarization, linear polarization resistance, and electrochemical impedance spectroscopy [33,38,40].

Non-electrochemical methods usually involve setting up a laboratory or *in situ* corrosion experiment with coupons made from the alloys which corrosion rates are desired. Common standards which can be followed for performing laboratory, immersion corrosion tests include ASTM G31 [41] and ISO 11845 [42]. Conversely, standards which can be followed for conducting in-service, immersion corrosion tests include ASTM G4 [43] and NACE RP0497 [44]. After immersing the coupons in the electrolyte – or more appropriately, service conditions of interest – for a set duration, the corrosion rate is ascertained by measuring some change to either the coupon or the electrolyte. Physical and chemical change measurements include: coupon mass loss, thickness or depth, chemical analysis of the electrolyte,

---

<sup>10</sup> Technically the ohmic drop also accounts for the resistance of electron movement in the electron bridge. However, due to metals having high electrical conductivity [33], the resulting ohmic drop is orders of magnitude smaller than the ohmic drop observed in the electrolyte.

and gasometric techniques (when one of the reaction products produced from the corrosion is a gas) [33,35]. If either mass loss or thickness measurements are collected, the corrosion rate can be successfully determined by taking either measurement and dividing it over the period of time the corrosion test was performed. Depending on the required units of the corrosion rate – such as mass loss over time (units of grams/year) or wall/thickness loss over time (units of either millimeters/year or mils penetration/year) – an appropriate expression for the corrosion rate can be generated. In creating this kind of expression, it is assumed that the metal loss occurs uniformly across the exposed surface of the tested metal (known as uniform corrosion [33–35]). Unfortunately, corrosion may manifest itself in a localized manner, such as in pitting or crevice corrosion [33–35], as is often the case for passivating metals such as aluminum alloys. The rates of corrosion for these localized corrosion modes cannot be determined by the procedure previously listed. A more appropriate way to quantify the rate of localized corrosion would be by measuring the deepest part of the localized metal loss (relative to the initial thickness of the metal) and dividing it over the time of exposure during testing. Hence, discretion is required in accurately quantifying the corrosion rate. Further discussion on how corrosion forms, and associated ways to evaluate said forms of corrosion are provided in the following section.

## **2.6 Modes of Corrosion**

It is convenient to classify corrosion based on the visual appearance of a corroded metal [34]. From Fontana's [34] schema, there are eight forms (also known as types or modes) of corrosion, and they are identified based on how the corrosion damage manifests itself and the resulting morphology. The eight forms of corrosion are listed as follows [33–35]:

1. Uniform (also known as general [33,34]) corrosion
2. Galvanic (also known as dissimilar metal or two metal [34,35]) corrosion
3. Crevice corrosion (includes under-deposit corrosion [33])

4. Pitting
5. Intergranular corrosion (also includes exfoliation [33])
6. Dealloying (also known as selective leaching or parting [34])
7. Erosion corrosion (includes cavitation erosion and fretting corrosion [33])
8. Environmentally assisted cracking (includes stress-corrosion cracking and corrosion fatigue [33])

These modes of corrosion are presented as schematics below in Figure 2-4. Moreover, these schematics are further divided into three groups, as per criteria by Dillon [45] which classifies the modes based on their ease of identification. Group one modes are easily identifiable by ordinary (low magnification; naked eye) visual examination [46]. Identification of group two modes may require additional examination tools (such as a stereomicroscope) [46]. Finally, group three modes require higher magnification examination tools (such as optical microscopy or scanning electron microscopy of metallographic specimens) in order to identify them [46].

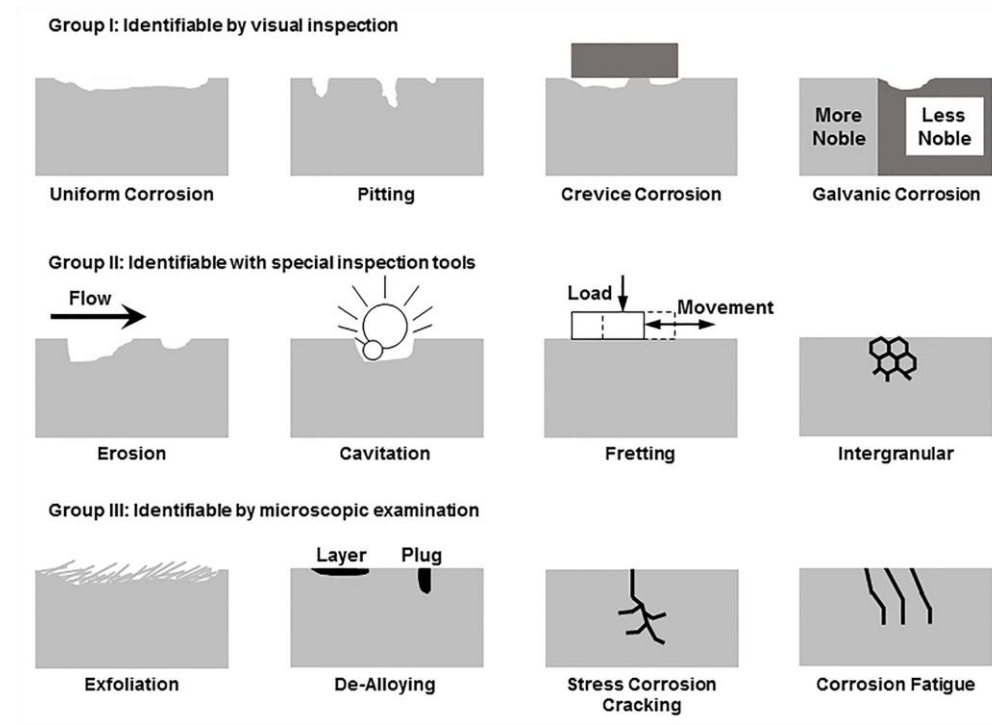


Figure 2-4: The eight forms of corrosion as per Fontana and Dillon [46].

Since only pitting, crevice, galvanic, and intergranular corrosion were identified in Appendix A, only these modes will be discussed in the subsequent subsections. Additionally, as previously stated, only aluminum alloy grades 5086 and 6061 will be used in discussion – as examples when necessary – of the various topics in the following sections. Furthermore, even though stray current was suggested as a *possible* cause of the corrosion observed in Appendix A and reports by the author [11,12], stray current will not be discussed due to its lower *probability* of occurrence. At present, it is unknown whether stray current corrosion is occurring; however, there is sufficient evidence to show that the aforementioned four modes of corrosion are present and *predominant* in the aeration tank.

### 2.6.1 Pitting Corrosion

Pitting is a type of highly localized corrosion that produces defined cavities (pits) which extend from the surface into the metal [30,31,33,34,46]. As described by Davis [33], this mode “occurs when one area of a metal becomes anodic with respect to the rest of the surface or when highly localized changes in the corrodent (electrolyte) in contact with the metal, as in crevices, cause accelerated localized attack.” Pitting corrosion leads to localized metal loss (via anodic dissolution); whereas in uniform corrosion, the anode and cathode reaction sites are continuously moving on the metal surface – leading to fairly uniform metal loss [33]. Aluminum alloys – which are passivating metals – are known to suffer from pitting corrosion (or other modes) and usually do not succumb to uniform corrosion in neutral (pH ~ 7), aqueous electrolytes [36,47,48].

Pitting corrosion may propagate into different shapes (illustrated in Figure 2-5), which can be classified and described using the standards ASTM G46 [49] or ISO 11463 [50]. It should be noted that visual examination of a pitted surface may only reveal the pit opening to be round, elongated, or irregular in shape [49,50]. To acquire more information on whether corrosion had occurred beneath the surface, or how the pit may have propagated, examination of the cross-section is required

[49,50]. Shapes of pit cross-sections can be hemispherical, cup-like, or completely irregular, and in some instances, they may appear to tunnel into or undercut the metal [46]. Moreover, under high magnification examination of aluminum alloys, the pit walls may appear as simple, geometric shapes which are conducive to attack of select crystallographic planes of the alloy [51–54]. Finally, pits can appear uncovered or covered with corrosion products [46]. Regarding aluminum alloys, pits are usually found to be covered with, as described by Vargel [47], “white, voluminous and gelatinous pustules of alumina gel  $\text{Al}(\text{OH})_3$ ”, also known as tubercles [30].

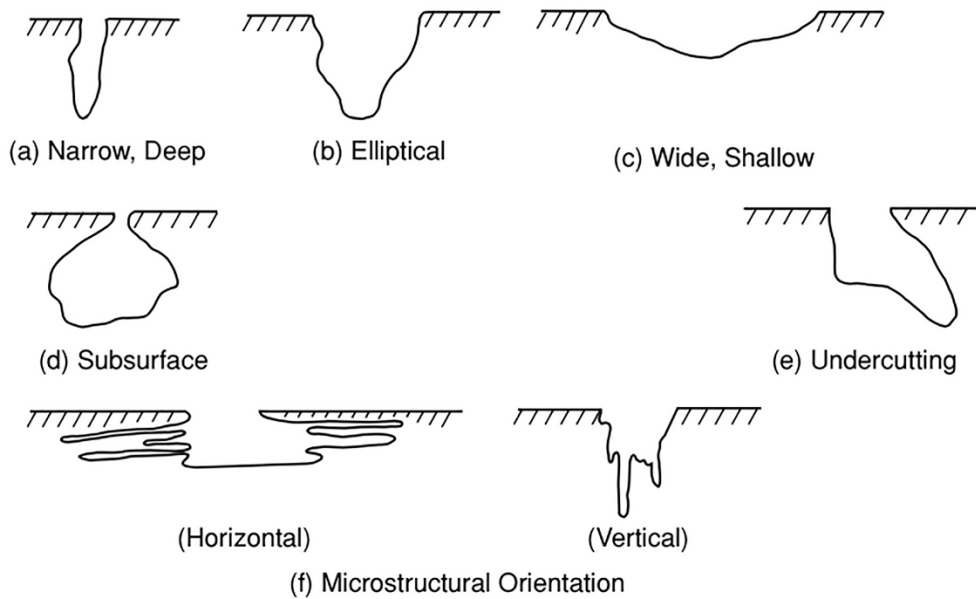
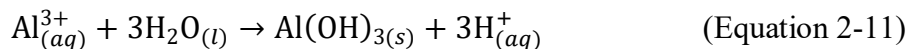


Figure 2-5: Variations in the cross-sectional shape of pits as a means for visual identification [49,55]. (Reproduced with permission from NACE International, Houston, TX. All rights reserved. [55]. © NACE International 2002.)

Pitting corrosion involves both an initiation (where some amount of time passes while pits are induced; also known as nucleation) and propagation stage (also known as growth) [33–35]. There is still some debate on how pit initiation occurs (the three proposed mechanisms and contributing factors will be discussed in a later section in this chapter); however, pit propagation is more widely

understood [33–35,47,48,56,57]. Vargel [47] describes<sup>11</sup> the pit propagation mechanism for aluminum alloys in aqueous chloride solutions as follows (depicted in Figure 2-6).

After pitting has initiated, oxidation occurs at the bottom of the formed cavity, with anodic dissolution of aluminum (as per Equation 2-2 for Al to Al<sup>3+</sup>) [47]. Meanwhile, the concurrent reduction reaction at the cathode site(s) is one of the reactions listed in Equations 2-4 through 2-7 [47]. The cathodic half-cell reactions can occur on regions of the metal surface outside or on the edge of the formed cavity, or on more noble inclusions or precipitates (such as copper and Al<sub>3</sub>Fe shown in Figure 2-6) near the surface of the alloy [47]. If the anode remains stationary and stable, the dissolution of Al will lead to the formation of a pit [47]. An excess of hydroxide ions (OH<sup>-</sup>) – either through consumption of hydrogen ions (H<sup>+</sup>) in Equations 2-4 or 2-6, or formation of OH<sup>-</sup> in Equations 2-5 or 2-7 – will create an alkaline pH outside of the pit [47]. The presence of Al<sup>3+</sup> – through diffusion from inside the pit – and OH<sup>-</sup> leads to the formation of Al(OH)<sub>3</sub> at the mouth of the pit [47]. As Al<sup>3+</sup> is produced at the bottom of the pit (causing pit growth), an electrical field is created which causes the chlorine ions (chlorides; Cl<sup>-</sup>) to migrate towards the pit bottom in order to neutralize the build-up of charge; leading to the formation of AlCl<sub>3</sub> (or the complex AlCl<sub>4</sub><sup>-</sup> as shown in Figure 2-6) [47]. Hydrolysis of the AlCl<sub>3</sub> leads to the formation of Al(OH)<sub>3</sub> according to the reaction in Equation 2-11 [47].



The production of hydrogen ions (H<sup>+</sup>) leads to acidification in the bottom of the pit to a pH < 3<sup>12</sup> [47]. With the low pH and increasing concentration of Cl<sup>-</sup>, the electrolyte within the pit becomes very aggressive; subsequently leading to

---

<sup>11</sup> Note that Vargel's [47] description of pit propagation is similar to – and believed to be based on – the description by Reboul et al. [58]. Vargel's description, however, is more simplistic and provides the relevant chemical and electrochemical reactions.

<sup>12</sup> If you go back to the Pourbaix diagram (Figure 2-3) you'll see that the aluminum is no longer passive.

continuous (autopropagation) of the pit [47]. The low pH leads to the reduction of  $H^+$  (via further oxidation of Al) to hydrogen gas ( $H_2$ ), which forms bubbles and pushes any suspended  $Al(OH)_3$  inside the pit to the pit opening [47]. Accumulation of the  $Al(OH)_3$  corrosion products leads to the formation of either a dome or volcano shaped deposit; which in turn covers the pit opening [47]. This mound of corrosion product – which closes a region of localized metal loss – is known as a tubercle [30]. Depending on how well the deposit covers the mouth of the pit – as well as prevents the movement of ions into and out of the pit – the growth of the pit may decrease or stop entirely [47].

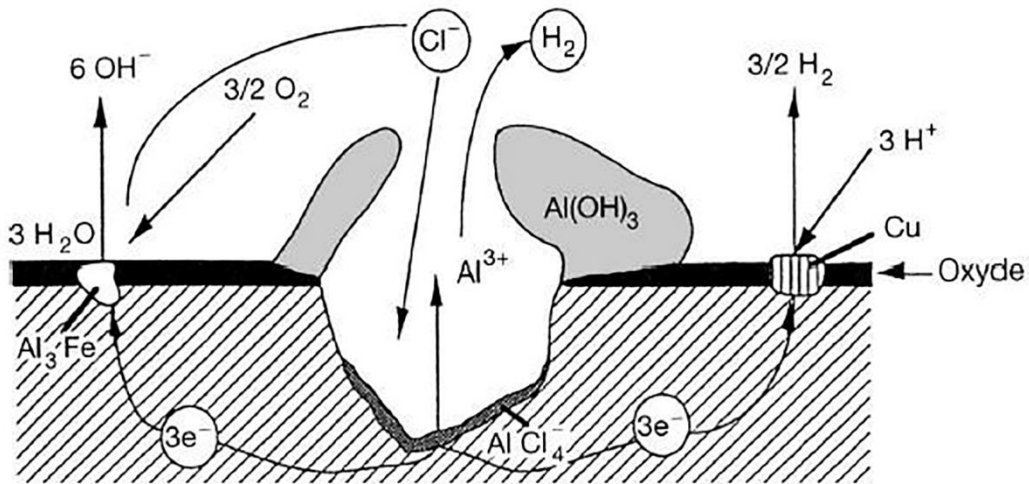
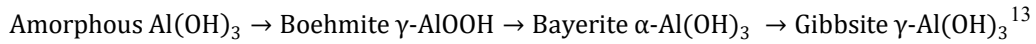


Figure 2-6: Mechanism of pitting corrosion in a typical grade of aluminum alloy exposed to an aqueous chloride solution [47,58]. The  $Al(OH)_3$  in this cross-section is forming a tubercle. (Reproduced with permission from Elsevier Ltd, Kidlington, UK. All rights reserved. [47]. © Elsevier Ltd 2004.)

Further information on pitting corrosion and mechanisms can be found in books by: Davis [33], Fontana [34], McCafferty [35], and Uhlig [36]; as well as papers by: Kaesche [53], Wood *et al.* [54], Soltis [56], Reboul and Baroux [57], Reboul *et al.* [58], McCafferty [59], Foley [60], Kolotyarkin [61], Frankel [62,63], Galvele [64], Szklarska-Smialowska [65–67], and Böhni [68].

As  $Al(OH)_3$  is produced at room temperature (approximately 25 °C for our purposes) it precipitates as white, gelatinous pustules [47]. There are some

discrepancies about the aging process of the precipitated, amorphous alumina  $\text{Al}(\text{OH})_3$  to crystalline aluminum hydroxide [36,47,48,69–71]. For the purposes of this work, the aging process – as presented by Uhlig [36] and Vargel [47] – for the subsequent crystalline structures formed is as follows (with crystallographic designations by Wefers and Misra [69]):



As previously mentioned, to determine the rate of corrosion for pitting, depth measurements can be collected from the deepest part of the pit (relative to the undisturbed metal surface). The measurements can then be divided by the exposure time in order to obtain a value of the corrosion rate. Aziz and Godard [72–74] had shown that the rate of pitting of aluminum alloys immersed in fresh waters follows a cubic rate expression with respect to time (Equation 2-12).

$$d = kt^{1/3} \quad (\text{Equation 2-12})^{14}$$

Where  $d$  is the pit depth,  $t$  is time, and  $k$  is a constant which is a function of the aluminum alloy and the environmental conditions (including temperature, pH, electrolyte composition, fluid velocity, etc.) [47,72]. Two considerations must be taken into account for use of Equation 2-12 in predicting pit depths: first, the time scale to which this equation was developed for is over months [72]. Hence, this equation may not be useful for predicting the behavior of pitting during a short interval of time (such as four weeks). Second,  $k$  is heavily influenced by the aluminum alloy tested (including chemistry, processing, and surface condition) as well as the environmental conditions to which the alloy was exposed. Therefore, values for  $k$  may not be readily available for a specific electrolyte-alloy

---

<sup>13</sup> Gibbsite ( $\text{Al}(\text{OH})_3$ ) is also known as Hydrargillite ( $\text{Al}_2\text{O}_3 \cdot 3\text{H}_2\text{O}$ ) [48,69]. Both names and chemical formulas can be used, but Gibbsite is preferred in the USA and UK [69,70].

<sup>14</sup> This kinetic expression supports the notion that the pit growth rate will decrease or stop entirely once the pit opening is covered in deposit [47].

combination, or the values would first have to be obtained through immersion testing of said electrolyte-alloy combination.

Finally, different aluminum alloy grades have varying resistances to pitting – due to their purity, and the presence and distribution of phases [33,48]. A list compiled by Davis [33,48] shows, in decreasing order, the relative resistance to pitting for the various series of aluminum alloys as: 1XXX (nearly pure aluminum grades), 5XXX (e.g. 5086 and 5083), 3XXX, 6XXX (e.g. 6061), 7XXX, and 2XXX [33,48].

## 2.6.2 Crevice Corrosion

Crevice corrosion is a form of localized attack that occurs in, or immediately adjacent to, an area on a metal surface that is shielded from exposure to the contents of a bulk environment (electrolyte) [30,31,33,34]. This shielded area – which has its own local environment – appears as a narrow opening or space (known as a crevice or an occlusion), which is formed between the metal surface and an additional surface (either metallic or non-metallic) [30,31,33,34]. This additional surface (known as a crevice former) can be from a number of sources that can be broadly classified either as naturally occurring or artificial [75]. Naturally occurring crevices are created by the contents of the electrolyte, such as: sediment, debris, deposits (such as corrosion products and tubercles; known as under-deposit or deposit corrosion [30,31]), or biofouling (i.e., accumulation of microorganisms on the surface of a material; known as microbiologically influenced corrosion (MIC) [30,31]) [33,34,75]. Meanwhile, artificial crevices are created during the design and subsequent manufacturing, fabrication, and assembly of a component or equipment [33,34,75]. Examples of artificial crevices – as provided by Davis [33] – include: beneath gaskets, washers, coatings, or insulation; between flanges, threaded joints, riveted seams, or lap joints; and anywhere two or more surfaces are in close contact (such as in Appendix A between the aeration piping and tubular ties). Additional locations of artificial crevices are identified in Appendix A and reports by the

author [11,12], which include: gaps in welds or in the profile of the weld (e.g., at the weld toe or the bead start-stop locations); and surfaces with deep scratches/gouges formed from machining, grinding, tooling, or handling of the alloys.

Crevice corrosion occurs when either an occlusion or crevice limits access of the bulk electrolyte to a localized area on the metal surface [33–35]. The composition of the local electrolyte changes due to reactions between the metal surface and local electrolyte – including anodic dissolution of metal and reduction of oxygen or  $H^+$  – as well as stagnation from a lack of replenishment from the bulk electrolyte (i.e., the transport of constituents to the local electrolyte is very limited due to the small gap between the metal surface and crevice former) [33–35]. This separation and change in local electrolyte composition leads to the metal surface, in the crevice, becoming anodic (active) relative to the metal surface outside of the crevice – which itself becomes cathodic (noble) [33,35]. Hence, anodic dissolution (Equation 2-2) of the metal within the crevice occurs [33–35]. Concurrently, the reduction reaction (Equation 2-3) occurs with oxidizing agents – such as oxygen or  $H^+$  – outside of the crevice, in the bulk electrolyte [33–35]. The cathode site is typically the metal surface outside of the crevice [33–35]. This difference in concentration between the bulk and local electrolyte constituents – which leads to localized corrosion in the crevice – has also been called a concentration cell [34,35,48]. Moreover, the term *differential aeration cell* (or oxygen concentration cell) is used to describe a concentration cell in which oxygen is depleted within the local electrolyte and is subsequently reduced outside of the crevice [34,35,48]. Over time, the continued separation and change in local electrolyte leads to the formation of an acidic environment that – depending on the contents of the electrolyte – may contain higher concentrations of aggressive constituents such as  $Cl^-$  [33–35].

As with pitting, crevice corrosion can be divided into two stages: initiation and growth [35]. However, unlike pitting corrosion, more is understood regarding how crevice corrosion initiates [33–35]. The application of a crevice former – as

described previously as subsequently isolating the local electrolyte and forming a corrosion cell between the metal in the crevice and the bulk electrolyte – is the initiation stage of crevice corrosion [33–35]. Meanwhile, the propagation stage for crevice corrosion follows the same mechanism as described previously for pitting [32–35].

An additional type of crevice corrosion that is likely to have occurred in the aeration tank (as discussed in Appendix A) is MIC. This form of under-deposit corrosion occurs when microorganisms, which in a sessile state (attached to something immobile and solid [76]), form a biofilm on a metal surface [46,76,77]. This biofilm (which can be aerobic, anaerobic, or both<sup>15</sup> [76,77]) can lead to corrosion in several ways, which can be broadly divided into two categories as per Little and Lee [77]. The first category is the formation of concentration cells, typically with oxygen or other ions – including metals – in the electrolyte [77]. Bacteria which form biofilms that produce copious amounts of extracellular polymer substances – subsequently creating concentration cells – are known as “slime-forming” bacteria [46,76,77]. The second category is comprised of reactions occurring within and caused by the presence of biofilms [77]. Some of these reactions include: sulphur oxidation, sulphate reduction, acid and hydrogen production, metal oxidation, and metal reduction [46,76,77]. Moreover, some of the bacteria that cause the aforementioned reactions are: sulphur-oxidizing bacteria (SOB), sulphate-reducing bacteria (SRB), and acid-producing bacteria (APB) [46,76,77]. A list of microorganisms – specifically bacteria or fungi – known to cause corrosion of aluminum are presented below in Table 2-4

---

<sup>15</sup> In many instances the biofilm can start with aerobic conditions and subsequently change to anaerobic conditions [76,77,108]. This change can lead to a composite biofilm with the bottom layer (in contact with the metal surface) being anaerobic and the top layer (in contact with the electrolyte) being aerobic [76,77,108].

Table 2-4: Microorganisms known to cause MIC in aluminum alloys.

Genus or Species	Bacteria or Fungi	Reference
<i>Desulfovibrio desulfuricans</i> <sup>†</sup>	Bacteria	[77–79]
<i>Desulfovibrio vulgaris</i> <sup>†</sup>	Bacteria	[77–79]
<i>Desulfovibrio salexigens</i> <sup>†</sup>	Bacteria	[77–79]
<i>Desulfotomaculum orientis</i> <sup>‡</sup>	Bacteria	[79]
<i>Sphaerotilus natans</i>	Bacteria	[77,78]
<i>Pseudomonas aeruginosa</i>	Bacteria	[77,78]
<i>Bacillus cereus</i>	Bacteria	[80]
<i>Serratia marcescens</i>	Bacteria	[80]
<i>Hormoconis resiniae</i>	Fungi	[77]
<i>Cladosporium resiniae</i>	Fungi	[78]

<sup>†</sup>: The species of *Desulfovibrio* found to cause corrosion are provided by Tiller and Booth [79]. The other citations only list the genus *Desulfovibrio*. <sup>‡</sup>: Tiller and Booth [79] suggest that the corrosion of aluminum in the presence of *Desulfotomaculum orientis* is due to the accumulation of precipitated substances during growth of the organism.

As corrosion commences from microorganisms, the damage frequently leads to the formation of tubercles which covers the localized metal loss [36]. A schematic of a tubercle can be observed in the previous section, in Figure 2-6. Due to the various forms of MIC – including the numerous microorganisms involved and ensuing chemical reactions and metabolic processes – as well as the lack of microbial examination and testing in this study, no further discussion shall be given to MIC. Further information on MIC can be found in books by Roberge [46], Borenstein [76], and Little and Lee [77]; as well as papers by: Lane [78], Walsh *et al.* [81], Mansfeld [82], Little and Lee [83], Little *et al.* [84–86], Salvarezza [87], and Videla [88].

It should be noted that localized metal loss underneath the crevice can appear similar to that of a pit [32,33,40,48]. The formation of a tubercle from pitting may lead to the creation of an oxygen concentration cell; causing crevice corrosion. Conversely, as mentioned by Davis [33], pitting corrosion may be induced by crevice corrosion. Furthermore, Kelly *et al.* [40] state – as an example – that “pitting can be viewed as crevice corrosion on a smaller scale, with either micropores or surface heterogeneities acting to form the crevice.” Hence, if unaware of the circumstances or conditions of the metal surface and electrolyte prior to observing

this localized metal loss, it can be difficult to determine whether pitting or crevice corrosion had occurred. Two differences exist between these two modes of corrosion (besides the case(s) in which an artificial crevice former is present): one is electrochemical in nature [35] and the other relates to the induction time of initiation [32]. Regarding the electrochemical differences, McCafferty [35] states that the measured electrode potentials and current densities for pitting and crevice corrosion are different from one-another. Specifically, the pitting potential is more positive than the electrode potential for crevice corrosion, and the current density measured in a pit is higher than what is measured within a crevice [35]. (Pitting and crevice corrosion potentials and current densities are beyond the scope of this work – refer to McCafferty [35] for further details.) Concerning differences in nucleation time, Stansbury and Buchanan [32] suggest that the initiation time for crevice corrosion is very short or nonexistent as compared to pitting.

The rate of crevice corrosion can be determined using the same procedure as listed for pitting corrosion. Moreover, crevice corrosion testing can be performed on specific metal alloys in controlled electrolytes following the procedures listed in ASTM G48 [89] or the guides provided in ASTM G78 [75]. It should be noted that neither of the aforementioned standards, or any committee-approved standards<sup>16</sup> examined by the author, were designed specifically for crevice corrosion testing of aluminum alloys. Finally, further information on crevice corrosion and mechanisms can be found in the aforementioned books by: Davis [33,48], Fontana [34], McCafferty [35], Uhlig [36], and Vargel [47]; as well as papers by: Soltis [56], Reboul and Baroux [57], Foley [60], Frankel [62,63], Böhni [68], De Force and Pickering [90], Rosenfeld [91], Shaw *et al.* [92], and Pourbaix [93].

---

<sup>16</sup> Technical, this does not include the crevice corrosion testing performed by Zeuthen and Kain [109] since their work was only published as a peer-reviewed paper by the American Society for Testing and Materials (ASTM). Furthermore, Zeuthen and Kain [109] do not test any aluminum alloys in their study.

### 2.6.3 Galvanic Corrosion

Galvanic corrosion occurs when the anode and cathode sites of a corrosion cell are formed by dissimilar metals (or one metal and a conducting non-metal) that are electrically and ionically<sup>17</sup> connected [30,31,33–35]. During galvanic coupling<sup>18</sup>, anodic dissolution (Equation 2-2) of the less noble (active) metal increases due to the metal's surface becoming anodic [33,34]. This change in behavior can be represented as an increase (known as anodic polarization [33]) in the active metal's initial potential [32]. This initial potential – known as an open-circuit potential, corrosion potential ( $E_{\text{corr}}$ ), or dissolution potential – is the potential of a material (typically a metal alloy) exposed to a known electrolyte, which is measured relative to a reference electrode [30]. A list containing a range of open-circuit potentials (known as a galvanic series [30]) for a number of different alloys is provided below in Figure 2-7.

---

<sup>17</sup> Ionically connected meaning exposed to the same electrolyte or connected via some path which allows the flow of ions, such as a salt bridge.

<sup>18</sup> A galvanic couple is defined in ASTM G193 [30] as “a pair of dissimilar conductors, commonly metals, in electrical contact in an electrolyte.”

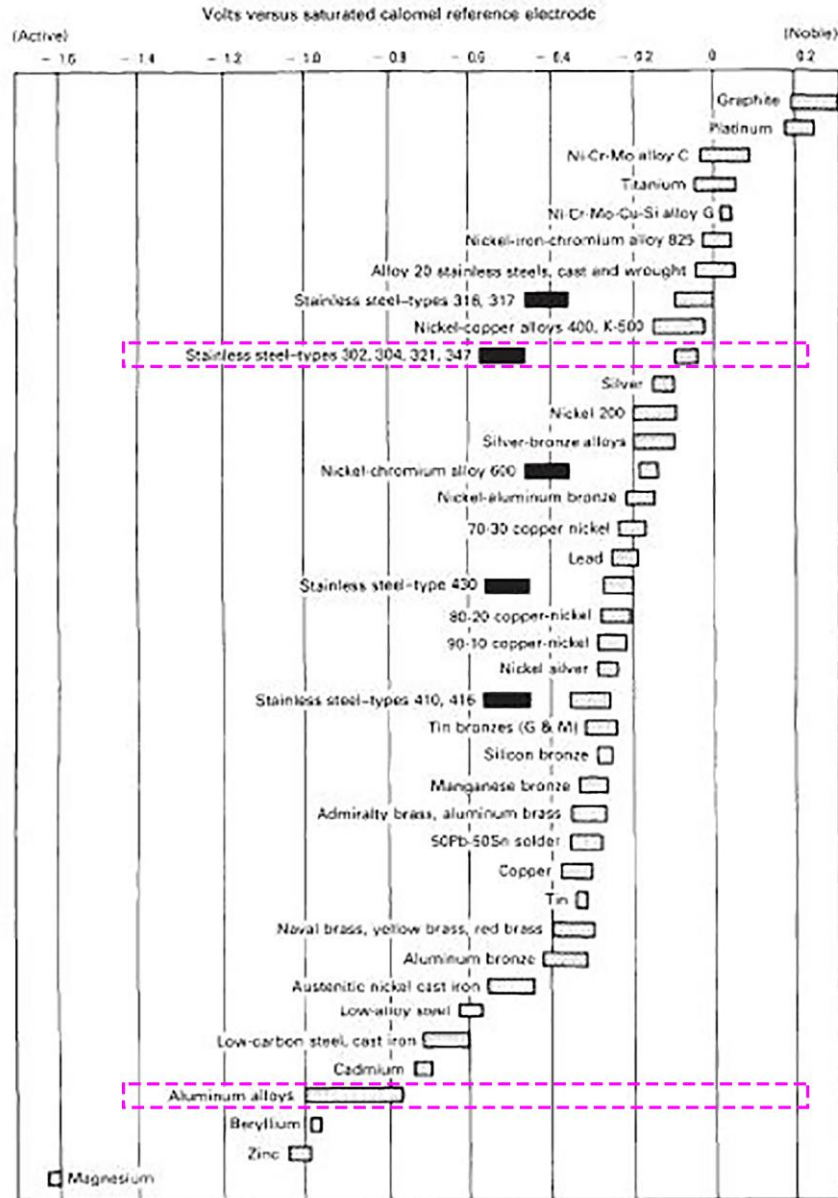


Figure 2-7: Galvanic series of various metals in seawater [33,94]. These are open-circuit potentials and they were measured with a saturated calomel reference electrode (SCE; 0.241 V vs SHE at 25 °C) [33]. The aluminum alloys and grade 304 stainless steel potentials are each highlighted with a pink-dashed box. The dark boxes indicate active behavior of select active-passive alloys [33]. (Reproduced with permission from ASM International, Materials Park, OH. All rights reserved. [33]. © ASM International 2000.)

It should be noted that corrosion potentials can only be determined experimentally through electrochemical measurements [32,33,40]. Moreover, these corrosion potentials are affected by a number of factors, including: conditions of the

electrolyte (such as the temperature, fluid velocity, pH, ion concentration, and presence or lack of oxygen or other strong oxidizers); the tested alloy's chemistry, processing, and surface condition; and the procedure followed to collect the measurements [32,33,40].

Meanwhile, the more noble metal's surface becomes cathodic [33,34] – resulting in a decrease (known as cathodic polarization [33]) in the noble metals corrosion potential [32]. As the noble metal's surface becomes cathodic, there is a decrease in anodic dissolution on the noble metal [32]. This decrease subsequently facilitates an increase in the reduction reactions (Equation 2-3) of oxidizing agents on the metal's surface [32]. Ultimately, this increase in anodic dissolution of the active metal and increase in reduction reactions on the noble metal leads to accelerated corrosion of the active metal and decelerated corrosion of the noble metal [30,32].

There are two key factors – besides the magnitude of difference in open-circuit potentials between the materials in the galvanic couple; providing the driving force – which influence galvanic corrosion: the areas of the anode and cathode, and the distance between the anode and cathode in the galvanic couple [33,34,47]. With a large cathode area and small anode area, the corrosion rate of the anode can be extremely high due to the small area over which anodic dissolution occurs [33,34,47] and hence the high corrosion current density. Conversely, a small cathode area and large anode area leads to a lower corrosion rate of the anode due to the large area that facilitates anodic dissolution [33,34,47]. Regarding the effect of distance between the anode and cathode, if the galvanic couple is in close physical proximity or in direct contact, it will suffer greater galvanic effects (i.e., corrosion of the anode) than if the galvanic couple was farther apart [33,34,47].

Examples of galvanic corrosion can be observed throughout the aeration tank, specifically between the aluminum alloy grades 5086, 5083, or 6061 and the 304/304L grade stainless steel. In this corrosion cell, the aluminum alloys are the

anode sites while the stainless steel provides the cathode sites (which is supported by the relative positions of aluminum alloys and 304 stainless steel in Figure 2-7). In order to minimize galvanic effects between dissimilar metals, alloys with similar open-circuit potentials should be selected [32–34]. Additionally, galvanic effects between dissimilar metals can both exacerbate and accelerate existing corrosion damage (via mixed modes, which will be discussed at the end of this chapter) or mitigate any corrosion damage which would normally occur (via cathodic protection<sup>19</sup> with sacrificial anodes).

Testing for galvanic corrosion can be performed by following the guidelines as per ASTM G71 [95]. Galvanic series can be developed by following the guidelines as per ASTM G82 [94]. Moreover, for aluminum alloys, the measurement of corrosion potentials can be performed as per ASTM G69 [96]. Finally, further information on galvanic corrosion can be found in the aforementioned books by: Davis [33,48], Fontana [34], Uhlig [36], and Vargel [47]; as well as the paper by Reboul and Baroux [57].

Galvanic corrosion is generally observed on a large scale (as shown in Appendix A or reports by the author [11,12]); however, even at the microscopic level, galvanic effects can be experienced between different phases in a metal alloy, as well as between inclusions or precipitates and the surrounding metal matrix. This behaviour can also be observed in grain boundaries, which will be discussed in the next and final mode of corrosion presented in this study.

---

<sup>19</sup> Cathodic protection (CP) minimizes corrosion of a chosen metal structure by forcing a current – either through impressed current or sacrificial anodes – to prevent the corrosion cell reactions that normally would have otherwise occurred [33]. The effects of cathodic protection can be visualized using the aluminum Pourbaix diagram (Figure 2-3). Depending on the pH of the system, CP would drop the potential (E) from an active region (e.g., Al<sup>3+</sup>) to an immune region (e.g., Al).

## 2.6.4 Intergranular Corrosion

Intergranular corrosion (IGC) is the preferential, localized dissolution of material in or adjacent to the grain boundaries of a metal alloy [30,31,33,34]. This selective dissolution is induced by potential differences between any precipitates, intermetallic phases, or impurities that form at the grain boundaries and regions in the grains that are immediately adjacent to the boundaries [33,34,47]. These differences in potential lead to the formation of a galvanic couple, and successive dissolution of the more anodic material [33], in this case the metal at or near the grain boundary. The open-circuit potentials, based on ASTM G69, for relevant aluminum alloys and secondary phases are presented below in Table 2-5. Additionally, the occurrence and mechanism of intergranular corrosion varies for each alloy system [33,34,47].

Table 2-5: Open-circuit potentials for relevant aluminum alloys (and temper, if available) and secondary phases based on ASTM G69 (sodium chloride-hydrogen peroxide solution at 25 °C) [47,97].

Aluminum Alloy or Phase	$E_{\text{corr}}$ , [V vs. SCE <sup>†</sup> ]	
Si	- 0.17	Cathodic ↑  ↓ Anodic
Al <sub>3</sub> Ni	- 0.43	
Al <sub>2</sub> Cu	- 0.44 or - 0.64	
Al <sub>3</sub> Fe	- 0.47	
6061-T6	- 0.74	
5086	- 0.76	
Al <sub>6</sub> Mn	- 0.76	
5083	- 0.78	
Al <sub>2</sub> CuMg	- 0.91	
Al <sub>3</sub> Mg <sub>2</sub>	- 1.15	
Mg <sub>2</sub> Si	- 1.19	

<sup>†</sup>: Saturated calomel electrode (0.241 V vs SHE at 25 °C [33])

In aluminum alloys, IGC is induced by the potential differences between the grains and the adjacent grain-boundaries or grain-boundary regions [32–34,47,48]. Whether selective dissolution occurs on the grain boundaries or material adjacent to the boundaries depends on the class of aluminum alloy [32,33,47,48]. For 5XXX series aluminum alloys, IGC occurs when the anodic constituent Al<sub>3</sub>Mg<sub>2</sub>

( $\beta$  phase; also written as  $\text{Al}_5\text{Mg}_8$  [47,57]) forms a continuous path along the grain boundaries [32,33,47,98–100] through improper materials processing. This continuous path of precipitates preferentially corrodes due to the formation of a galvanic cell between the cathodic grains and anodic precipitates [32,33,47,98–100]. Meanwhile, for 6XXX series alloys, whilst some have mentioned that IGC is typically less observed [33,48], Davis [33] reports that IGC has been detected in very aggressive electrolytes. IGC of 6XXX series in chloride-containing, aqueous electrolytes has been identified by both Shaw *et al.* [92] and Minoda and Yoshida [101]<sup>20</sup>. Uhlig [36], Vargel [47], and Davis [48] also state 6XXX series alloys are prone to IGC; however, Vargel [47] suggests the penetration of IGC is only over a small number of grain layers. Regarding the cause of IGC in 6XXX series, Stansbury and Buchanan [32], Uhlig [36], and Davis [48] state that when there is an excess amount of silicon – more than enough to meet the stoichiometric requirements to form  $\text{Mg}_2\text{Si}$  (also called  $\beta$  phase) – insoluble silicon will precipitate at the grain boundaries. This precipitated silicon is cathodic relative to the anodic, adjacent grain-boundary material; hence, the adjacent grain-boundary material corrodes [32,36,48]. Minoda and Yoshida [101] also state that corrosion of material adjacent to the grain boundaries occurs. However, these authors [101] suggest that IGC in 6XXX series alloys – particularly grade 6061 – is due to the presence of precipitate free zones (anodic) adjacent to the grain boundaries (cathodic), which selectively corrode. Nevertheless, whatever the exact cause, IGC has been observed in 6XXX series alloys.

As stated with galvanic corrosion, IGC can also exacerbate existing corrosion damage via mixed modes. Moreover, the occurrence of IGC around entire grains can cause the grains to “drop out”, leading to accelerated corrosion rates [34,48]. This form of corrosion, as well as the loss of entire grains, can be observed in Appendix A for the extruded grade 6061 tubular ties operating in a high chloride electrolyte.

---

<sup>20</sup> Minoda and Yoshida [101] observed IGC in extruded grade 6061 exposed to a chloride-containing, aqueous environment.

Testing for IGC in aluminum alloys can be performed by following the guidelines as per ASTM G67 [102], ASTM G110 [103], and ISO 11846 [104]. Finally, further information on IGC can be found in the aforementioned books by: Stansbury and Buchanan [32], Davis [33,48], Fontana [34], Uhlig [36], and Vargel [47]; as well as papers by: Kaesche [53], Reboul and Baroux [57], and Frankel [63].

## 2.7 Passivity and Depassivation of Aluminum

Aluminum and aluminum alloys owe their corrosion resistance to the natural formation of a passive aluminum oxide ( $\text{Al}_2\text{O}_3$ ) [35,36,47,48]<sup>21</sup>, which is an adherent, inert, and continuous film. This film formation phenomena is known as passivation, and it results in significantly reduced rates of corrosion [30,31,35]. Regarding the aluminum passive film, this 4 to 10 nm, colourless oxide forms spontaneously when aluminum is exposed to air – such as during processing of aluminum alloys – and it can repair itself instantaneously in the presence of an oxidizing media (including both air and water) [35,47,48]. The oxide is comprised of two layers, which are depicted below in Figure 2-8. The first layer, which is immediately adjacent to the aluminum, is compact and comprised of amorphous  $\text{Al}_2\text{O}_3$  [36,47,48,57]. The second layer, between the amorphous  $\text{Al}_2\text{O}_3$  and environment, is an aluminum hydroxide (or hydrated aluminum oxide) [36,47,48,57]. At room temperature (again, approximately 25 °C for our purposes) the aluminum hydroxide is bayerite [36,47,48,69]. This bayerite layer is porous and can continue to grow in thickness when exposed to water or in the presence of a humid atmosphere [47,48]. Finally, the presence of this passive layer can be observed for aluminum alloys in water between the pH values of approximately 4 and 9, as shown in the previously provided Pourbaix diagram (Figure 2-3<sup>22</sup>) [39].

---

<sup>21</sup> Stainless steels are also passivating alloys; however, unlike aluminum alloys which derive their passivating film from their primary alloying element (aluminum), chromium additions (greater than 10.5 to 12 weight percent) lead to the formation of a passive chromium oxide ( $\text{Cr}_2\text{O}_3$ ) [35,36,110], [111]. For the purposes of this thesis, and since aluminum alloys were found to have corroded in Appendix A and reports by the author [11,12], only passivation and passivation breakdown of aluminum alloys shall be discussed.

<sup>22</sup> At room temperature, Pourbaix [39] lists the aluminum hydroxide in the passive region as gibbsite. Meanwhile, Uhlig [36], Vargel [47], and Davis [48] state that bayerite is formed at room

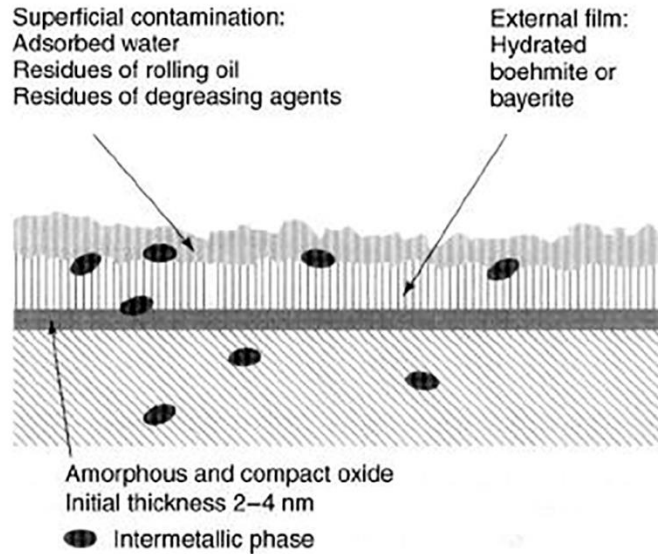


Figure 2-8: Passive layers formed on aluminum and aluminum alloys [47]. Also included in this schematic are adsorption phenomena caused by external environmental factors such as processing (i.e., rolling or extrusion) [47]. (Reproduced with permission from Elsevier Ltd, Kidlington, UK. All rights reserved. [47]. © Elsevier Ltd 2004.)

In environments which are believed to be indicative of passivation (such as water at a pH of approximately 7), aluminum alloys can still succumb to localized modes of corrosion, such as pitting and crevice corrosion [36,47,48]. This occurrence is due to a breakdown in the passive film (known as depassivation [31]), which results in corrosion of the underlying alloy material. Moreover, this breakdown in passive film (which is the initiation stage for pitting and aids in initiation of crevice corrosion [33–35]), and the associated physics and chemistry which describes it, are still not fully understood [35,36,56,68]. Three main mechanisms have been discussed by most authors, which describe passivity breakdown [35,36,56,68]. These mechanisms are: (1) the penetration mechanism, (2) the adsorption mechanism (also referred to as the film thinning mechanism), and (3) the film rupture mechanism [35,36,56,68]. Schematics of these three mechanisms are presented below in Figure 2-9.

---

temperature; however, all three authors say gibbsite can form during aging of the aluminum hydroxide. Therefore, both aluminum hydroxides will be considered possible for the hydrated passive film.

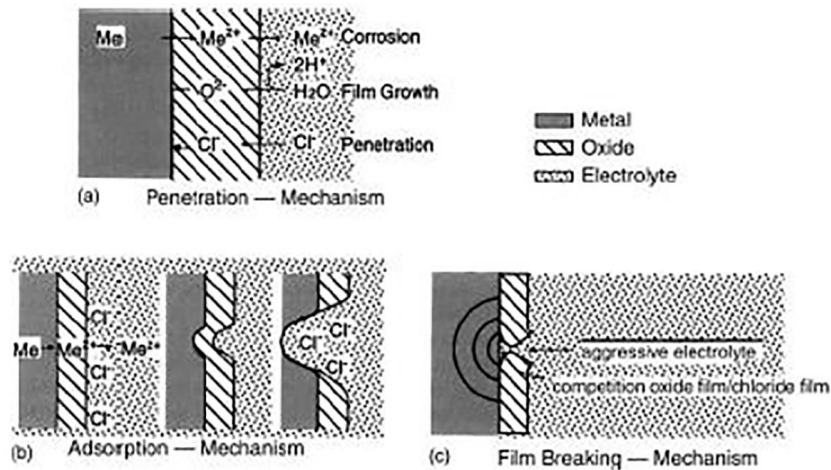


Figure 2-9: Schematics of the (a) penetration, (b) adsorption, and (c) film rupture mechanisms which lead to passivity breakdown [36,105]. (Reproduced with permission from Springer, Berlin, Germany. All rights reserved. [105]. © Springer 1990.)

Further discussion on each of these mechanisms is beyond the scope of this work. For more information, refer to books by McCafferty [35] and Uhlig [36] as well as papers by Soltis [56] and Böhni [68]. A common factor in all three mechanisms is the presence of aggressive ions, such as those listed below, which interact with the pre-existing passive film [35,36,56,68].

Aggressive anions known to cause depassivation and subsequent localized corrosion in aluminum have been compiled by Galvele [106] and are listed as: chloride ( $\text{Cl}^-$ )<sup>23</sup>, bromide ( $\text{Br}^-$ ), iodide ( $\text{I}^-$ ), perchlorate ( $\text{ClO}_4^-$ ), nitrate ( $\text{NO}_3^-$ ), and thiocyanate ( $\text{SCN}^-$ ). Not included in this list is sulphate ( $\text{SO}_4^{2-}$ ); however, Vargel [47], Davis [48], and Godard and Torrible [107] suggest that  $\text{SO}_4^{2-}$  can cause localized corrosion in aluminum.

Besides the aforementioned anions, there are other factors which can cause or exacerbate localized corrosion in aluminum. These factors – grouped as either environmental or metallurgical and stress – are presented in the following

<sup>23</sup> Chlorides are also listed by Galvele [106] to cause depassivation and localized corrosion in stainless steels.

subsections for aluminum in freshwater<sup>24</sup>. At this time, the author emphasises that the following factors are generalized, and some of them (specifically fluid velocity, temperature, and presence of oxygen) have what appear to be conflicting effects on corrosion. Ultimately, great discretion is required when predicting the corrosion resistance (or more challenging: the corrosion rate) of a given metal in an aqueous environment. Understanding of the many metallurgical and environmental variables – in addition to the design, processing, assembly, application, and operation of said metal in the environment – are critical in eliminating, or at least mitigating, corrosion.

### 2.7.1 Environmental Factors

The following headings and bullet points contain the environmental factors, and their effects, which influence localized corrosion in aluminum.

#### *Naturally occurring deposits:*

- Sediment, debris, biofouling, and other deposits formed from the electrolyte can lead to crevice corrosion [32,33,36,47,48].

#### *Heavy metal ions:*

- Ions from metals such as copper, lead, mercury, and nickel – which are more noble than aluminum – can reduce to a solid on the aluminum alloy surface [13,32,33,36,47,48]. This reduction may lead to localized corrosion of aluminum due to aluminum oxidizing, followed by the creation of a galvanic cell [33,36,47,48].

---

<sup>24</sup> Freshwater is defined by Vargel [47] as water with a total salinity generally less than 1000 mg/L. Spring waters, river waters, and rainwater are all classified as freshwater [47].

*pH:*

- As shown in the aluminum-water Pourbaix diagram (Figure 2-3), the passive film is stable between the pH range of approximately 4 and 9 [13,33,36,39,47,48].

*Presence of oxygen:*

- Oxidizing agents – including oxygen – participate in the corrosion cell, specifically in the reduction reaction (Equation 2-3 for general oxidizing agents; Equation 2-6 or 2-7 for oxygen) [32–38].
- Increasing the oxygen partial pressure leads to an increase in  $E_{\text{cell}}$  (as per Equation 2-9) for the corrosion reaction. Moreover, increasing the presence of dissolved oxygen can lead to an increase in localized corrosion of aluminum [36,47].
- Besides water, oxygen also contributes to the repair of the passive oxide film on aluminum [35,47,48].
- In the absence of halide-salts (e.g., sodium chloride; NaCl), aluminum generally does not succumb to pitting in aerated solutions [48]. Moreover, in high purity water (such as deionized water) at room temperature (approximately 25 °C for our purposes), the corrosion resistance of aluminum is not significantly decreased by the presence of dissolved oxygen [48].
- In the presence of a deaerated solution, the corrosion of aluminum is very slow [36,48]. The removal of oxygen (as well as other strong oxidizing agents) may lead to the prevention of pitting due to the removal of species necessary to support the reduction reaction (Equation 2-3) [36].
- From the above-listed points, it appears that oxygen's relationship with aluminum in water is rather complex. It can be summarized that oxygen can induce localized corrosion in aluminum when there is the presence of anions that lead to passive film breakdown (such as  $\text{Cl}^-$ ).

*Temperature:*

- Increasing temperature decreases the solubility, and hence, the concentration of dissolved oxygen [33,35,47]. Conversely, increasing temperature increases  $E_{\text{cell}}$  for the corrosion reaction and, generally, the rate of associated reaction and mass transport kinetics [33,34,36].<sup>25</sup>
- Both Uhlig [36] and Vargel [47] state that as the temperature increases (from approximately 30 to 60 °C) the density and depth of pitting increases and decreases, respectively.

*Conductivity:*

- Conductivity is a measure of the ability of a material – in this case, the electrolyte – to transport current [30,33]. Electrolytes that have a high conductivity easily transport current, and vice-versa [33].
- Generally, increasing the concentration of dissolved species in the electrolyte leads to an increase in conductivity [33]. Furthermore – and again, generally speaking – increasing the electrolyte conductivity leads to an increase in corrosion of the exposed alloy [33,48].

*Fluid velocity:*

- Can aid the kinetics (particularly concentration polarization) of corrosion [32–34,48]. Up to a point, increasing fluid velocity can both increase the presence of oxidizing agents to support the reduction reaction, and remove oxidized species ( $\text{Al}^{3+}$ ) and corrosion products [32–34,48].
- Vargel [47] and Davis [48] state that the pitting resistance of aluminum in slow flowing (above 0.04 m/s [48]), natural waters (also called freshwaters) is better than in stagnant freshwater (with all other factors being constant). Bennett and Nixon [13] also support this assertion.

---

<sup>25</sup> This increase only occurs up to approximately 70 °C; around this temperature, the passive film can react with water to form a protective, boehmite coating [47]. Davis [48] and Uhlig [36] also supports this statement regarding the formation of a protective boehmite layer.

- Non-uniform fluid velocity can create local anode and cathode regions on the alloys' surface by inducing variations in concentration of oxidizing agents and removing corrosion products [32].

## 2.7.2 Metallurgical and Stress Factors

The following headings and bullet points contain the metallurgical and stress factors, and their effects, which influence localized corrosion in aluminum.

### *Surface condition:*

- Dislocations, grain boundaries, and localized deformation (such as scratches and gouges) are preferred anodic dissolution sites [32–34,36,47,48].
- Some material processing (such as cold working) and component fabrication (such as bending and shearing) lead to plastic deformation, which results in an increase in dislocation density and preferred anodic dissolution sites.

### *Secondary phases, intermetallics, or inclusions:*

- Depending on the aluminum alloy (or specifically, the aluminum alloy matrix), these phases or inclusions can act as either anode or cathode sites [32,33,36,47,48]. The size, shape, distribution, and dispersion of these phases or inclusions impact the extent of localized corrosion [32,33,36,47,48].
- If secondary phases precipitate at or immediately adjacent to grain boundaries, IGC can occur [32,33,36,47,48].

### *Irregular or imperfect passive film formation:*

- Discontinuities or pores in the passive film can create small, localized anode sites [32,36].

- Deposits formed on the alloy surface during processing, fabrication, and assembly can also act as anode sites or induce crevice corrosion [32].

*Dissimilar metal contact:*

- If the aluminum alloy is in contact with a more noble material, galvanic effects can occur (potentially leading to galvanic corrosion) [13,32,34,36,47,48].

*Welding effects:*

- The process of welding leads to local heating; subsequently causing phase transformations that form secondary precipitates, variations in grain size and distribution, and the creation of residual stresses [33,36,48]. These changes in the microstructure can induced local differences in potential, which may result in the formation of either local anode or cathode sites [33,36,48].

*Loading conditions:*

- Applied loads or residual stresses can lead to passive film rupture [32]. Note that this factor is only a concern if there are environmental conditions which inhibit immediate repair of the passive film [32].

## **2.8 Summary**

From the information presented in the previous sections, it appears that both wastewater and corrosion of aluminum are quite complicated. Wastewater treatment is an aggressive process and it can create conditions which are highly conducive to corrosion of aluminum and aluminum alloys (further evidence is provided in Appendix A or in reports [11,12] written by the author). The presence of naturally occurring crevice formers (including microorganisms), heavy metals, and other constituents in the wastewater – which are known to cause depassivation and corrosion in aluminum – make the use of aluminum alloys in this environment

a poor choice, especially in the presence of high chloride ion concentrations with ample dissolved oxygen. Furthermore, the application of dissimilar metals and the deformation produced from fabrication of the aeration tank can either induce or further intensify corrosion which may have normally occurred due to the constituents in the wastewater. Ultimately, these many factors can lead to mixed modes and accelerated rates of corrosion. An excellent example of these mixed modes and accelerated corrosion is the contact between the 304 stainless steel aeration piping and the 6061 grade tubular ties (as presented in Appendix A or reports [11,12] written by the author). Pitting, crevice corrosion, galvanic corrosion, and IGC were all observed on the ties. Moreover, through-wall corrosion was identified on the ties which were in direct contact with the aeration piping. With the presence of mixed modes of corrosion, it becomes exceedingly difficult to both predict and minimize the rate of corrosion of the susceptible alloys.

Besides what would be called the “natural occurring” constituents present in the wastewater process fluid, the addition of either Alum or Isopac may also lead to corrosion of aluminum alloys. Both coagulants contain ions ( $\text{SO}_4^{2-}$  for Alum and  $\text{Cl}^-$  for Isopac) which are known to cause localized corrosion in aluminum alloys. Moreover, the material safety data sheet (MSDS) for both coagulants state either compound is corrosive to aluminum [9,10]. Hence, the presence of either chemical addition – in conjunction with naturally occurring crevice formers or other environmental and metallurgical factors – could lead to mixed modes and accelerated corrosion of the aluminum alloys used to construct the aeration tanks.

## **2.9 References**

- [1] L. Metcalf, H.P. Eddy, eds., *Wastewater Engineering Treatment and Resource Recovery*, 5th ed., McGraw-Hill Education, New York, NY, 2014.
- [2] F.R. Spellman, *Handbook of Water and Wastewater Treatment Plant Operations*, Lewis Publishers, New York, NY, 2003.

- [3] M.L. Davis, *Water and Wastewater Engineering Design Principles and Practice*, McGraw Hill, New York, NY, 2010.
- [4] G. Bitton, *Wastewater Microbiology*, 3rd ed., John Wiley & Sons, Inc., Hoboken, NJ, 2005.
- [5] *Design of Municipal Wastewater Treatment Plants: WEF Manual of Practice No. 8 ASCE Manuals and Reports on Engineering Practice No. 76*, 5th ed., McGraw-Hill Professional, 2010.
- [6] R.Y. Surampalli, S.K. Brar, M. Verma, R.D. Tyagi, *Wasterwater Treatment*, in: *Encycl. Chem. Process.*, Taylor and Francis, New York, NY, 2007: pp. 1–14. doi:10.1081/E-ECHP-120008009.
- [7] J.-Q. Jiang, *Development of Coagulation Theory and Pre-Polymerized Coagulants for Water Treatment*, *Sep. Purif. Methods*. 30 (2001) 127–141. doi:10.1081/SPM-100102986.
- [8] H. Tang, F. Xiao, D. Wang, *Speciation, stability, and coagulation mechanisms of hydroxyl aluminum clusters formed by PACl and alum: A critical review*, *Adv. Colloid Interface Sci.* 226 (2015) 78–85. doi:10.1016/j.cis.2015.09.002.
- [9] ClearTech Industries Inc., *Aluminum Sulphate Solution MSDS*, (2015). <http://www.cleartech.ca/msds/alumsulphateliq.pdf>.
- [10] Klearwater Equipment & Technologies Corp., *Isopac Solution MSDS*, (2012). <http://www.klearwater.ca/page3.html>.
- [11] J.S. Pavelich, J.A. Nychka, *Preliminary Findings Report: Visual Inspection and Corrosion Assessment of the EPCOR Borealis Waste Water Treatment Plant*, Edmonton, AB, 2013.
- [12] J.S. Pavelich, J.A. Nychka, *Additional Inspection Report: Additional Visual Inspection and Corrosion Assessment of the EPCOR Borealis Wastewater Treatment Plant*, Edmonton, AB, 2014.
- [13] D.C. Bennett, R.A. Nixon, *Corrosion and Materials Fundamentals for Engineers in Wastewater Treatment Plants & Collection Systems*, 3rd ed., NACE International, Houston, TX, 2016.
- [14] Aluminum Company of America, *Sewage Works Equipment and Supplies*, *Sewage Work. J.* 16 (1944) 1040–1042.
- [15] The Aluminum Association, *Aluminum the modern metal for sewage treatment equipment and plants*, 1970.

- [16] E.R. Stowell, Corrosion in Sewage Works, *Sewage Ind. Waste.* 28 (1956) 328–330. <http://www.jstor.org/stable/25033027>.
- [17] W.H. Ailor, Metals in Wastewater Treatment, *J. Environ. Eng. Div.* 4 (1974) 295–309.
- [18] A. Kumar, L.D. Stephenson, Emerging Corrosion Prevention and Control Technologies for Wastewater Treatment Plants, in: *Corrosion, NACE*, 2005: p. 13.
- [19] A.H. Tuthill, Stainless Steel in Wastewater Treatment Plants, *Water Eng. Manag.* 137 (1990) 31–34.
- [20] G.E. Englert, I.L. Muller, The Corrosion Behaviour of Mild Steel and Type 304 Stainless Steel in Media from an Anaerobic Biodigester, *Int. Biodeterior. Biodegradation.* 37 (1996) 173–180. doi:10.1016/S0964-8305(96)00019-4.
- [21] A. Iversen, MIC on Stainless Steels in Wastewater Treatment Plants, in: *Corrosion, NACE*, 1999: p. 12. <http://www.onepetro.org/mslib/servlet/onepetropreview?id=NACE-99171>.
- [22] A. Iversen, MIC on Stainless Steels in Wastewater Treatment Plants Field Tests and a Risk Assessment, in: *Corrosion, NACE*, 2002: p. 14.
- [23] A. Iversen, MIC on Stainless Steels in Wastewater Treatment - Anaerobic and Aerobic Treatments Influence on Ennoblement and the Passive Surface, in: *Corrosion, NACE*, 2003: p. 17.
- [24] C.W. Kovach, N. Kinsman, A. Iversen, Service Experience with High Performance Stainless Steels in Aggressive Fresh Waters, in: *Corrosion, NACE*, 2002: p. 14.
- [25] T. Mathiesen, E. Rislund, T.S. Nielsen, J.E. Frantsen, U. Tornaes, H.G. Pedersen, P. Nielsen, M.B. Petersen, MIC of Stainless Steel Pipes in Sewage Treatment Plants, in: *Corrosion, NACE*, 2003: p. 21.
- [26] J.S. Pavelich, J.A. Nychka, Preliminary Findings Report: Visual Inspection and Corrosion Assessment of the EPCOR Steepbank Waste Water Treatment Plant, Edmonton, AB, 2014.
- [27] ADI Water Solutions Ltd., (n.d.). <http://www.adiwater.com/index.php/2015-10-16-16-28-28/membrane-bioreactor> (accessed October 31, 2016).

- [28] NatureClean, (n.d.). <http://www.natureclean.com/alibmod.html> (accessed October 31, 2016).
- [29] CORIX, (n.d.). [http://ywaterworks.com/documents/CWS\\_BRO'11\\_MBR.pdf](http://ywaterworks.com/documents/CWS_BRO'11_MBR.pdf) (accessed October 31, 2016).
- [30] NACE/ASTM G193, Standard Terminology and Acronyms Relating to Corrosion, West Conshohocken, PA, 2013. doi:10.1520/G0193-12D.
- [31] ISO 8044, Corrosion of metals and alloys - Basic terms and definitions, Geneva, Switzerland, 2015. [www.iso.org](http://www.iso.org).
- [32] E.E. Stansbury, R.A. Buchanan, Fundamentals of Electrochemical Corrosion, ASM International, Materials Park, OH, 2000.
- [33] J.R. Davis, ed., Corrosion: Understanding the Basics, ASM International, Materials Park, OH, 2000.
- [34] M.G. Fontana, Corrosion Engineering, 3rd ed., McGraw Hill Book Company, New York, NY, 1987.
- [35] E. McCafferty, Introduction to Corrosion Science, Springer, New York, NY, 2010. doi:10.1007/978-1-4419-0455-3.
- [36] R.W. Revie, ed., Uhlig's Corrosion Handbook, 3rd ed., John Wiley & Sons, Inc., Hoboken, NJ, 2011.
- [37] P.R. Roberge, Corrosion Engineering Principles and Practice, McGraw Hill Book Company, New York, NY, 2008. doi:10.1036/0071482431.
- [38] R.W. Revie, H.H. Uhlig, Corrosion and Corrosion Control: An Introduction to Corrosion Science and Engineering, 4th ed., John Wiley & Sons, Inc., Hoboken, NJ, 2008.
- [39] M. Pourbaix, Atlas of Electrochemical Equilibria in Aqueous Solutions, 2nd ed., NACE International, Houston, TX, 1974.
- [40] R.G. Kelly, J.R. Scully, D.W. Shoesmith, R.G. Buchheit, Electrochemical Techniques in Corrosion Science and Engineering, Marcel Dekker, Inc., New York, NY, 2002.
- [41] NACE/ASTM G31, Standard Guide for Laboratory Immersion Corrosion Testing of Metals, West Conshohocken, PA, 2013. doi:10.1520/G0031-12A.

- [42] ISO 11845, Corrosion of metals and alloys - General principles for corrosion testing, Geneva, Switzerland, 1995. [www.iso.org](http://www.iso.org).
- [43] ASTM G4, Standard Guide for Conducting Corrosion Tests in Field Applications, West Conshohocken, PA, 2008. doi:10.1520/G0004-01R08.
- [44] NACE Standard RP0497, Field Corrosion Evaluation Using Metallic Test Specimens, Houston, TX, 2004. [www.nace.org](http://www.nace.org).
- [45] C.P. Dillon, Forms of Corrosion: Recognition and Prevention, NACE International, Houston, TX, 1982.
- [46] P.R. Roberge, Handbook of Corrosion Engineering, McGraw Hill, New York, NY, 2000.
- [47] C. Vargel, Corrosion of Aluminium, Elsevier Ltd, Kidlington, UK, 2004.
- [48] J.R. Davis, ed., Corrosion of Aluminum and Aluminum Alloys, ASM International, Materials Park, OH, 1999. doi:10.1361/caaa1999.
- [49] ASTM G46, Standard Guide for Examination and Evaluation of Pitting Corrosion, West Conshohocken, PA, 2013. doi:10.1520/G0046-94R13.
- [50] ISO 11463, Corrosion of metals and alloys - Evaluation of pitting corrosion, Geneva, Switzerland, 1995. [www.iso.org](http://www.iso.org).
- [51] T.H. Orem, Influence of Crystallographic Orientation on the Corrosion Rate of Aluminum in Acids and Alkalies, J. Res. Natl. Bur. Stand. (1934). 58 (1957) 157–167.  
[http://nvlpubs.nist.gov/nistpubs/jres/58/jresv58n3p157\\_A1b.pdf](http://nvlpubs.nist.gov/nistpubs/jres/58/jresv58n3p157_A1b.pdf).
- [52] M. Baumgärtner, H. Kaesche, Aluminum pitting in chloride solutions: morphology and pit growth kinetics, Corros. Sci. 31 (1990) 231–236.
- [53] H. Kaesche, Pitting Corrosion of Aluminum, and Intergranular Corrosion of Aluminum Alloys, in: R.W. Staehle, B.F. Brown, J. Kruger, A. Agrawal (Eds.), NACE-3, NACE, 1974: pp. 516–525.
- [54] G.C. Wood, W.H. Sutton, J.A. Richardson, T.N.K. Riley, A.G. Malherbe, The Mechanism of Pitting of Aluminum and its Alloys, in: R.W. Staehle, B.F. Brown, J. Kruger, A. Agrawal (Eds.), NACE-3, NACE, 1974: pp. 526–539.
- [55] R. Baboian, ed., NACE Corrosion Engineer's Reference Book, 3rd ed., NACE International, Houston, TX, 2002.

- [56] J. Soltis, Passivity breakdown, pit initiation and propagation of pits in metallic materials - Review, *Corros. Sci.* 90 (2015) 5–22. doi:10.1016/j.corsci.2014.10.006.
- [57] M.C. Reboul, B. Baroux, Metallurgical aspects of corrosion resistance of aluminium alloys, *Mater. Corros.* 62 (2011) 215–233. doi:10.1002/maco.201005650.
- [58] M.C. Reboul, T.J. Warner, H. Mayet, B. Baroux, A ten-step mechanism for the pitting corrosion of aluminium, *Mater. Sci. Forum.* 217–222 (1996) 1553–1558. doi:10.1515/CORRREV.1997.15.3-4.471.
- [59] E. McCafferty, Sequence of steps in the pitting of aluminum by chloride ions, *Corros. Sci.* 45 (2003) 1421–1438. doi:10.1016/S0010-938X(02)00231-7.
- [60] R.T. Foley, Localized Corrosion of Aluminum Alloys—A Review, *Corrosion.* 42 (1986) 277–288. doi:10.5006/1.3584905.
- [61] J.M. Kolotyrkin, Pitting Corrosion of Metals, *Corrosion.* 19 (1963) 261t–268t. <http://www.corrosionjournal.org/doi/pdf/10.5006/0010-9312-19.8.261>.
- [62] G.S. Frankel, Pitting Corrosion of Metals A Review of the Critical Factors, *J. Electrochem. Soc.* 145 (1998) 2186–2198.
- [63] G.S. Frankel, The Effects of Microstructure and Composition on Al Alloy Corrosion, *Corrosion.* 71 (2015) 1308–1320.
- [64] J.R. Galvele, Transport Processes and the Mechanism of Pitting of Metals, *J. Electrochem. Soc.* 123 (1976) 464–474. doi:10.1149/1.2132857.
- [65] Z. Szklarska-Smialowska, Insight into the Pitting Corrosion Behavior of Aluminum Alloys, *Corros. Sci.* 33 (1992) 1193–1202.
- [66] Z. Szklarska-Smialowska, Pitting corrosion of aluminum, *Corros. Sci.* 41 (1999) 1743–1767. doi:10.1016/S0010-938X(99)00012-8.
- [67] Z. Szklarska-Smialowska, Review of Literature on Pitting Corrosion Published Since 1960, *Corrosion.* 27 (1971) 223–233. doi:10.5006/0010-9312-27.6.223.
- [68] H. Bohni, Breakdown of Passivity and Localized Corrosion Processes, *Langmuir.* 3 (1987) 924–930. doi:10.1021/la00078a010.
- [69] K. Wefers, C. Misra, *Oxides and Hydroxides of Aluminum*, 1987.

- [70] R.S. Alwitt, The Aluminum-Water System, in: J.W. Diggle, A.K. Vijn (Eds.), *Oxides Oxide Film.*, Volume 4, Marcel Dekker, Inc., New York, NY, 1976: pp. 169–254.
- [71] G.T. Chandler, R.L. Sindelar, P.S. Lam, Evaluation of Water Chemistry on the Pitting Susceptibility of Aluminum, in: *Corrosion*, 1997: p. 14.
- [72] H.P. Godard, The Corrosion Behavior of Aluminum in Natural Waters, *Can. J. Chem. Eng.* 38 (1960) 167–173. doi:10.1002/cjce.5450380507.
- [73] H.P. Godard, An Insight Into the Corrosion Behavior of Aluminum, *Mater. Perform.* (1981) 9–15.
- [74] P.M. Aziz, H.P. Godard, Pitting Corrosion Characteristics of Aluminum Influence of Magnesium and Manganese, *Ind. Eng. Chem. Res.* 44 (1952) 1791–1795. doi:10.1021/ie50512a028.
- [75] ASTM G78, Standard Guide for Crevice Corrosion Testing of Iron-Base and Nickel-Base Stainless Alloys in Seawater and Other Chloride-Containing Aqueous Environments, West Conshohocken, PA, 2012. doi:10.1520/G0078-01R12.
- [76] S.W. Borenstein, *Microbiologically influenced corrosion handbook*, Woodhead Publishing Ltd, Cambridge, England, 1994.
- [77] B.J. Little, J.S. Lee, *Microbiologically Influenced Corrosion*, John Wiley & Sons, Inc., Hoboken, NJ, 2007.
- [78] R.A. Lane, Under the Microscope: Understanding, Detecting, and Preventing Microbiologically Influenced Corrosion, *J. Fail. Anal. Prev.* 5 (2005) 10–38. doi:10.1361/154770205X65891.
- [79] A.K. Tiller, G.H. Booth, Anaerobic Corrosion of Aluminium by Sulphate-Reducing Bacteria, *Corros. Sci.* 8 (1968) 549–555.
- [80] A. Rajasekar, Y.-P. Ting, Microbial Corrosion of Aluminum 2024 Aeronautical Alloy by Hydrocarbon Degrading Bacteria *Bacillus cereus* ACE4 and *Serratia marcescens* ACE2, *Ind. Eng. Chem. Res.* 49 (2010) 6054–6061. doi:10.1021/ie100078u.
- [81] D. Walsh, D. Pope, M. Danford, T. Huff, The Effect of Microstructure on Microbiologically Influenced Corrosion, *J. Miner. Met. Mater. Soc.* 45 (1993) 22–30. doi:10.1007/BF03222429.
- [82] F. Mansfeld, The interaction of bacteria and metal surfaces, *Electrochim. Acta.* 52 (2007) 7670–7680. doi:10.1016/j.electacta.2007.05.006.

- [83] B.J. Little, J.S. Lee, Microbiologically influenced corrosion: an update, *Int. Mater. Rev.* 59 (2014) 384–393. doi:10.1179/1743280414Y.0000000035.
- [84] B.J. Little, P. Wagner, F. Mansfeld, An Overview of Microbiologically Influenced Corrosion, *Electrochim. Acta.* 37 (1992) 2185–2194.
- [85] B.J. Little, J.S. Lee, R.I. Ray, Diagnosing Microbiologically Influenced Corrosion: A State-of-the-Art Review, *Corrosion.* 62 (2006) 1006–1017. doi:10.5006/1.3278228.
- [86] B. Little, P. Wagner, F. Mansfeld, Microbiologically influenced corrosion of metals and alloys, *Int. Mater. Rev.* 36 (1991) 253–272. doi:10.1179/imr.1991.36.1.253.
- [87] R.C. Salvarezza, M.F.L. de Mele, H.A. Videla, Mechanisms of the Microbial Corrosion of Aluminum Alloys, *Corrosion.* 39 (1983) 26–32. doi:10.5006/1.3580810.
- [88] H.A. Videla, Microbially Induced Corrosion: an Updated Overview, *Int. Biodeterior. Biodegrad.* 48 (2001) 176–201. doi:10.1016/S0964-8305(01)00081-6.
- [89] ASTM G48, Standard Test Methods for Pitting and Crevice Corrosion Resistance of Stainless Steels and Related Alloys by Use of Ferric Chloride Solution, West Conshohocken, PA, 2011. doi:10.1520/G0048-11.
- [90] B. De Force, H. Pickering, A Clearer View of How Crevice Corrosion Occurs, *J. Miner. Met. Mater. Soc.* 47 (1995) 22–27. doi:10.1007/BF03221250.
- [91] I.L. Rosenfeld, Crevice Corrosion of Metals and Alloys, in: R.W. Staehle, B.F. Brown, J. Kruger, A. Agrawal (Eds.), *NACE-3, NACE*, 1974: pp. 373–398.
- [92] B.A. Shaw, M.M. McCosby, A.M. Abdullah, H.W. Pickering, The Localized Corrosion of Al 6XXX Alloys, *J. Miner. Met. Mater. Soc.* 53 (2001) 42–46. doi:10.1007/s11837-001-0087-7.
- [93] M. Pourbaix, Applications of electrochemistry in corrosion science and in practice, *Corros. Sci.* 14 (1974) 25–82.
- [94] ASTM G82, Standard Guide for Development and Use of a Galvanic Series for Predicting Galvanic Corrosion Performance, West Conshohocken, PA, 2014. doi:10.1520/G0082-98R14.

- [95] ASTM G71, Standard Guide for Conducting and Evaluating Galvanic Corrosion Tests in Electrolytes, West Conshohocken, PA, 2014. doi:10.1520/G0071-81R14.
- [96] ASTM G69, Standard Test Method for Measurement of Corrosion Potentials of Aluminum Alloys, West Conshohocken, PA, 2012. doi:10.1520/G0069-12.
- [97] T.D. Burleigh, R.C. Rennick, F.S. Bovard, Corrosion Potential for Aluminum Alloys Measured by ASTM G 69, *Corrosion*. 49 (1993) 683–685. doi:10.5006/1.3316100.
- [98] M.L.C. Lim, R.G. Kelly, J.R. Scully, Overview of Intergranular Corrosion Mechanisms, Phenomenological Observations, and Modeling of AA5083, *Corrosion*. 72 (2016) 198–220. doi:10.5006/1818.
- [99] R. Zhang, R.K. Gupta, C.H.J. Davies, A.M. Hodge, M. Tort, K. Xia, N. Birbilis, The Influence of Grain Size and Grain Orientation on Sensitization in AA5083, *Corrosion*. 72 (2016) 160–168. doi:10.5006/1703.
- [100] R. Zhang, S.P. Knight, R.L. Holtz, R. Goswami, C.H.J. Davies, N. Birbilis, A Survey of Sensitization in 5xxx Series Aluminum Alloys, *Corrosion*. 72 (2016) 144–159. doi:10.5006/1787.
- [101] T. Minoda, H. Yoshida, Effect of Grain Boundary Characteristics on Intergranular Corrosion Resistance of 6061 Aluminum Alloy Extrusion, *Metall. Mater. Trans. A*. 33 (2002) 2891–2898. doi:10.1007/s11661-002-0274-3.
- [102] ASTM G67, Standard Test Method for Determining the Susceptibility to Intergranular Corrosion of 5XXX Series Aluminum Alloys by Mass Loss After Exposure to Nitric Acid (NAMLT Test), West Conshohocken, PA, 2013. doi:10.1520/G0067-13.
- [103] ASTM G110, Standard Practice for Evaluating Intergranular Corrosion Resistance of Heat Treatable Aluminum Alloys by Immersion in Sodium Chloride + Hydrogen Peroxide Solution, West Conshohocken, PA, 2009. doi:10.1520/G0110-92R09.
- [104] ISO 11846, Corrosion of metals and alloys - Determination of resistance to intergranular corrosion of solution heat-treatable aluminium alloys, Geneva, Switzerland, 1995.
- [105] H. Kaesche, *Die Korrosion der Metalle*, 3rd ed., Springer, Berlin, Germany, 1990.

- [106] J.R. Galvele, Present State of Understanding of the Breakdown of Passivity and Repassivation, in: R.P. Frankenthal, J. Kruger (Eds.), *Passiv. Met.*, The Electrochemical Society, Princeton, NJ, 1978: pp. 285–327.
- [107] H.P. Godard, E.G. Torrible, The Effect of Chloride and Sulphate Ions on Oxide Film Growth on Al Immersed in Aqueous Solutions at 25°C, *Corros. Sci.* 10 (1970) 135–142.
- [108] A. Groysman, *Corrosion for Everybody*, Springer, New York, NY, 2010. doi:10.1007/978-90-481-3477-9.
- [109] A.W. Zeuthen, R.M. Kain, Crevice Corrosion Testing of Austenitic, Superaustenitic, Superferritic, and Superduplex Stainless Type Alloys in Seawater, in: R.M. Kain, W.T. Young (Eds.), *ASTM STP 1300 Corros. Test. Nat. Waters Second Vol.*, ASTM International, West Conshohocken, PA, 1997: pp. 91–108.
- [110] S.D. Cramer, B.S. Covino, eds., *ASM Handbook Volume 13B Corrosion: Materials*, ASM International, Materials Park, OH, 2005.
- [111] A. Iversen, B. Leffler, 3.04 – Aqueous Corrosion of Stainless Steels, in: B. Cottis, M. Graham, R. Lindsay, S. Lyon, T. Richardson, D. Scantlebury, H. Stott (Eds.), *Shreir's Corros.*, Elsevier, Oxford, UK, 2010: pp. 1802–1878. doi:10.1016/B978-044452787-5.00091-3.

# Chapter 3 – Design of Experiments

The major experimental goal of this study was to determine the corrosivity of Isopac, Alum, and de-ionized ultra-filtered (DIUF) water (the control solution) on aluminum alloys 5086, dual certified 5086/5083, 6061 and stainless steel 304. The designed corrosion cell experiment, and subsequent characterization techniques employed, are presented below in Table 3-1, along with the anticipated experimental outcomes. To assess the corrosivity of the aforementioned solutions (also referred to as electrolytes) in this study, laboratory scale, immersion corrosion testing was performed.

Table 3-1: Summary of testing and characterization methods used in the lab scale immersion corrosion cell experiments.

Objective	Experimental Technique	Anticipated Outcomes
<p>Determine Solution Corrosivity on Aluminum Alloys 5086, dual certified 5086/5083, 6061 and Stainless Steel 304</p>	<p>ASTM G31 ISO 11845</p> <p>Macro Photography</p> <p>Stereo Microscopy</p> <p>EDX</p> <p>XRD</p> <p>FTIR</p> <p>Mass Change Measurement</p>	<ul style="list-style-type: none"> <li>• Primary guidelines consulted for testing corrosion resistance of alloys in electrolytes</li> <li>• Coupon surface characterization; detect metal loss</li> <li>• Coupon surface characterization</li> <li>• Semi-quantitatively determine elemental composition of corrosion products</li> <li>• Identify crystalline corrosion products</li> <li>• Identify amorphous corrosion products (through identification of chemical bonds)</li> <li>• Quantify coupon metal loss</li> </ul>

### 3.1 Design of Lab Scale Immersion Corrosion Cell Study

The designs of the coupons and apparatus used for the lab scale immersion corrosion cells in this study were based off of the guides listed in both ASTM G31 [1] and ISO 11845 [2]. The parameters utilized for the design of these corrosion cells were: (1) a constant solution volume to coupon surface area ratio, (2) a minimum coupon surface area, and (3) a maximum coupon edge surface area to total coupon surface area ratio. A representative image of a typical immersion corrosion cell designed and used in this study is presented in Figure 3-1.

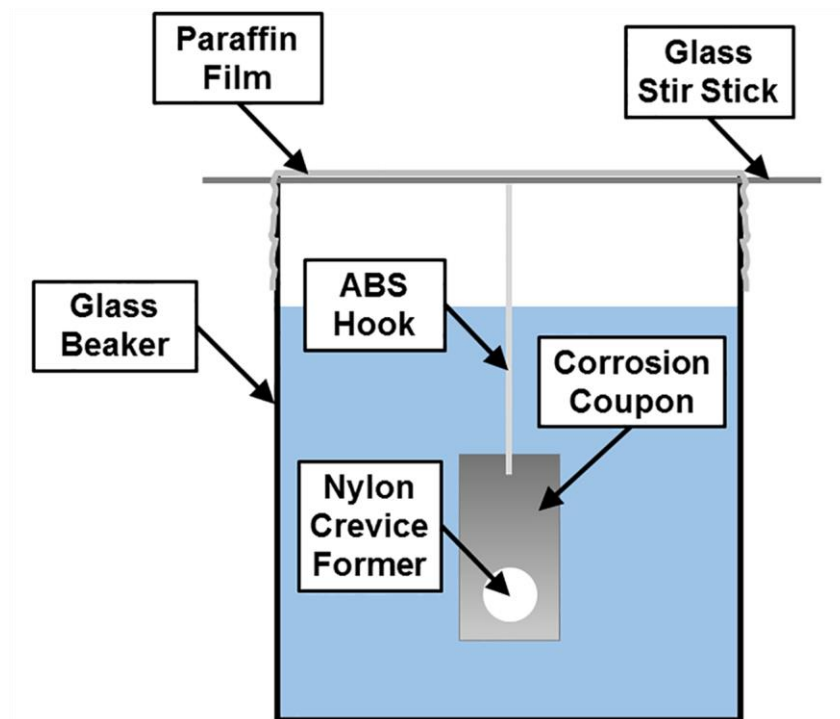


Figure 3-1: Schematic of a lab scale immersion corrosion cell indicating the coupon and fixturing.

The primary and key design parameter for this study was the constant volume to surface area (V/SA) ratio, for which minimum values were recommended in both ASTM G31 [1] and ISO 11845 [2] as 0.2 mL/mm<sup>2</sup> and 0.1 mL/mm<sup>2</sup>, respectively. For the purposes of this study, a V/SA of **0.24 mL/mm<sup>2</sup>** was selected. This ratio is one third of the actual aeration tank V/SA, which was calculated in Appendix B to be approximately 0.72 mL/mm<sup>2</sup>. Moreover, in some

conditions (certain environments and alloy compositions), the rate of corrosion can vary due to changes in the V/SA ratio [3]. Therefore, a sufficient volume of electrolyte should be used in order to prevent depletion of the chemical species which may participate in any corrosion or other relevant chemical reactions. From this ratio the coupon dimensions, total solution volume of the corrosion cell, volume of Alum and Isopac added to solution, and apparatuses selected to contain the corrosion cells were determined from, and subsequently presented in Sections 3.1.1 and 3.1.2.

Next, because of the under-deposit corrosion present throughout the aeration tank (as per Appendix A and reports [4,5] written by the author), fabricated crevices were installed on all of the coupons. The goal of the crevice former addition was to simulate an environment which could induce crevice corrosion, should such a mode of corrosion occur. Further details on the crevice formers and their installation on the coupons are listed in Section 3.1.1.

The duration of the immersion testing was chosen to be 28 days. This amount of time is greater than the common test periods listed in ASTM G31 (between 1 to 10 days [1]), and it should provide enough time for the initiation of corrosion to occur (through first overcoming any initiation period) [3,6,7].

Finally, the corrosion cell solutions' pH, dissolved oxygen (DO) concentration, temperature, and chloride (Cl<sup>-</sup>) concentration were collected in order to monitor the corrosion cell electrolyte, and identify if any drastic changes were to occur throughout the 28 day corrosion experiment. To measure each of these parameters, the coupons were removed from solution. Further details on how these four parameters were measured, as well as the length of time the coupons were out of solution are presented in Section 3.1.3.

### 3.1.1 Coupon Design and Fabrication

Table 3-2 lists the materials (as well as the product type, the material vendors, and their respective locations), which were acquired for fabrication into corrosion coupons. As mentioned in Chapter 1, the 304 stainless steel, dual certified 5086/5083 grade aluminum alloy sheet, and 6061 grade aluminum alloy tube were materials used in construction of the corroding aeration tank. Meanwhile, the 5086 grade aluminum alloy tube was selected as an additional material for corrosion testing because it is, generally speaking, more resistant to localized corrosion (particularly pitting) than 6061 [3,6,8].

Table 3-2: Product standards and alloy details used in this study.

Material Standard	Grade and Temper	Key Dimensions	Shape	Vendors	Location
ASTM B210	5086 H32	NPS <sup>1</sup> 1.5 SCH <sup>2</sup> 80	Tube	McMaster Carr	Elmhurst, IL, USA
ASTM B429	6061 T6	NPS <sup>1</sup> 1.5 SCH <sup>2</sup> 40	Tube	Metals Supermarket	Edmonton, AB, Canada
ASTM B928	5086/5083 <sup>3</sup> H116	4.06 mm Thickness	Sheet	ADI Metals	Ft. Lauderdale, FL, USA
ASTM A240	304 <sup>4</sup>	3.18 mm Thickness	Sheet	Metals Supermarket	Edmonton, AB, Canada

1: NPS stands for Nominal Pipe Size. A nominal pipe size of 1.5 is roughly an average outer diameter of 1.900 inches (48.26 mm). 2: SCH stands for ANSI Schedule number. With a NPS of 1.5, a SCH 40 thickness equals 0.145 inch (3.68 mm), while a SCH 80 thickness equals 0.200 inch (5.08 mm). 3: Dual certified alloy. 4: No temper was specified for the 304 stainless steel designation in ASTM A240.

Prior to coupon preparation, the elemental composition of the four alloy products were measured by a combination of inductively coupled plasma mass spectroscopy (ICP-MS), inductively coupled plasma optical emission spectroscopy (ICP-OES), and a Leco Carbon, Sulphur, and Nitrogen analyzer. This chemical analysis was done in order to confirm that each of the alloy chemistries were within the prescribed elemental ranges as listed in each alloys' respective standard. The elements (more specifically, alloying elements) chosen for quantification were as follows: aluminum (Al), carbon (C), chromium (Cr), copper (Cu), iron (Fe), magnesium (Mg), manganese (Mn), nickel (Ni), nitrogen (N), phosphorus (P),

silicon (Si), sulphur (S), titanium (Ti), and zinc (Zn). Regarding which elements were quantified with a specific technique, the ICP-OES was used for elements of interest at concentrations greater than 0.2 weight percent, as well as Si and P. The other elements, with the exception of C, S, and N were analyzed using the ICP-MS.

Approximately 2.5 g samples were removed from each of the four material products and sent for analysis. Subsequent sample preparation, execution of the aforementioned characterization techniques, and reporting of the elemental data were all completed by Sherritt Technologies' Analytical Laboratory Services Division (Sherritt Technologies Division, Fort Saskatchewan, AB, Canada). The results of the chemical analysis are compared to the chemical composition limits of the standard alloys in Tables 3-3 and 3-4. From the collected data, all sample chemistries were within the specified ranges of the elemental compositions for each material standard alloy. Finally, the alloy tempers were not verified in this study.

Table 3-3: Aluminum alloy coupons and respective material standard compositions.

Coupon / Standard	Element [Weight %]								
	Al	Cr	Fe	Cu	Mg	Mn	Ti	Zn	Si
<b>5086 Tube</b>	Bal.	0.16	0.16	0.02	4.48	0.59	0.02	0.03	0.06
<b>ASTM B210 Gr. 5086 H32</b>	Bal.	0.05 – 0.25	Max 0.5	Max 0.1	3.5 – 4.5	0.2 – 0.7	Max 0.15	0.25	0.4
<b>6061 Tube</b>	Bal.	0.06	0.33	0.19	0.79	0.05	0.02	0.06	0.43
<b>ASTM B429 Gr. 6061 T6</b>	Bal.	0.04 – 0.35	Max 0.7	0.15 – 0.4	0.8 – 1.2	Max 0.15	Max 0.15	Max 0.25	0.4 – 0.8
<b>5086/5083 Sheet</b>	Bal.	0.07	0.31	0.05	4.26	0.46	0.01	0.1	0.07
<b>ASTM B928 Gr. 5083 H116</b>	Bal.	0.05 – 0.25	Max 0.4	Max 0.1	4.0 – 4.9	0.4 – 1.0	Max 0.15	Max 0.25	Max 0.4
<b>ASTM B928 Gr. 5086 H116</b>	Bal.	0.05 – 0.25	Max 0.5	Max 0.1	3.5 – 4.5	0.2 – 0.7	Max 0.15	Max 0.25	Max 0.4

Table 3-4: Stainless steel alloy coupon and material standard compositions.

Coupon / Standard	Element [Weight %]								
	Fe	Cr	Mn	Ni	P	Si	C	S	N
<b>304 Sheet</b>	Bal.	18.6	1.07	8.21	0.02	0.44	0.043	0.001	0.062
<b>ASTM A240 Gr. 304</b>	Bal.	17.5 – 19.5	Max 2.0	8.0 – 10.5	Max 0.045	Max 0.75	Max 0.07	Max 0.03	Max 0.1

Besides the volume to surface area ratio, two additional parameters were used in the design of the coupon, namely: a minimum coupon surface area of 2500 mm<sup>2</sup> (as per ISO 11845 [2]) and a maximum coupon edge surface area to total coupon surface area ratio of 20% (as per ASTM G31 [1]). The minimum surface area – which the total coupon surface area should be greater than – is stated in order to minimize the effects of any surface or metallurgical irregularities in the coupon materials [2]. Meanwhile, the maximum edge to total surface area ratio is provided – and should not be exceeded – in order to minimize any preferential corrosion which may occur on end grains or in locations where the microstructure (including grain orientation, dislocation build-up, or precipitate and inclusion distribution and orientation) may be noticeably different than the bulk material microstructure. Both of these values are desirable in corrosion testing, but are not required. The ISO and ASTM standards only provide guideline values for performing corrosion experiments, and failing to meet some suggested specifications in the standards does not invalidate the corrosion experiment [1,2].

Below are representative images of the corrosion coupons fabricated for this study (Figure 3-2), as well as their orientation when placed in their respective corrosion cells. Three coupons were fabricated per alloy and electrolyte combination; for a total of thirty six coupons (and subsequently thirty six lab scale immersion cells).

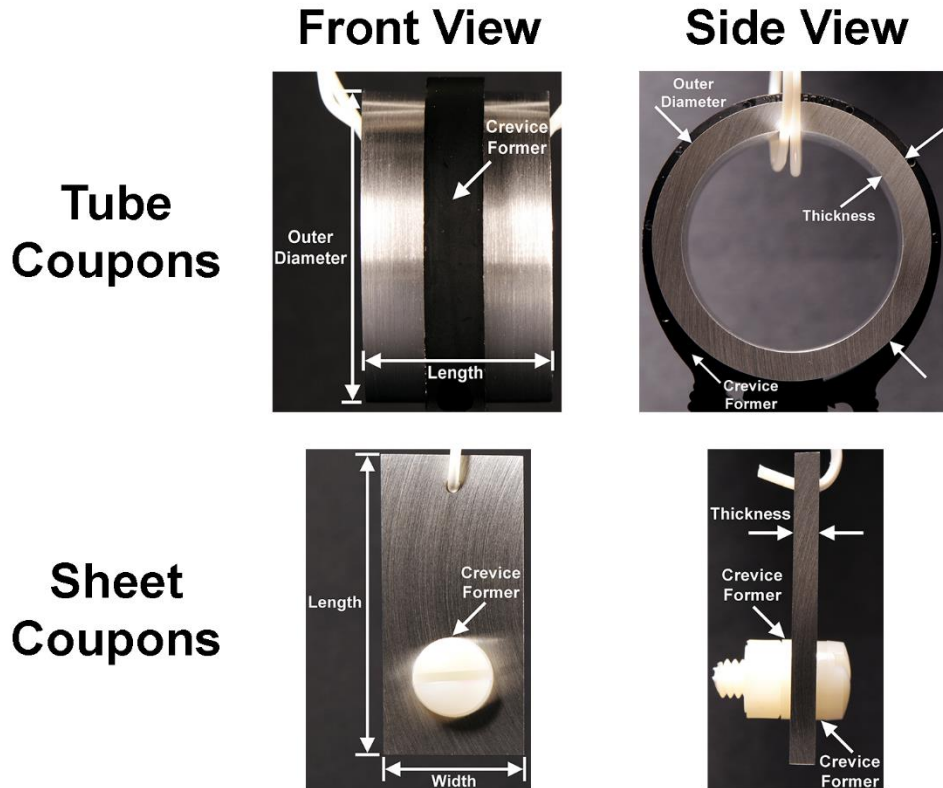


Figure 3-2: Representative images of corrosion coupons with dimension and crevice former labels. The crevice former(s) on the tube and sheet coupons were hose clamps and washers, respectively.

For the 5086 and 6061 tubes, the coupons were cut using a table-top band saw (BS-127P, Baileigh Industrial, Manitowoc, WI, USA) with a steel blade (Steel Blade 10-14 teeth per inch, Baileigh Industrial, Manitowoc, WI, USA) and a non-chlorine, non-sulphur, non-phenol, and non-nitrate bio-degradable lubricant (Baileigh Saw Coolant, Baileigh Industrial, Manitowoc, WI, USA). Cutting was performed at approximately 65 mpm.

For the 304 and 5086/5083 sheets, large sections were sheared from the overall sheet products received from the vendors. These sections were subsequently cut into coupons using a slow speed saw (TechCut4, Allied High Tech Products, Inc., Rancho Dominguez, CA, USA) operating within a range between 150 and 300 rpm with a metal-bonded diamond wafering blade (Allied High Tech Products, Inc., Rancho Dominguez, CA, USA) cooled with a propylene glycol-based lubricant (Low Speed Cutting Fluid, Allied High Tech Products, Inc., Rancho Dominguez,

CA, USA). Next, 6.35 mm and 2.38 mm holes were drilled into the sheet coupons for both installing crevice formers and allowing the coupons to be suspended in solution. TiN coated drill bits with non-corrosive, biodegradable lubricant (Tap Magic Formula 1 Aqueous, Tap Magic®, Steco Corporation, Little Rock, AR, USA) were used to drill the holes. A steel tipped deburring tool (Deburring Tool with Replacement Blade, Power Fist, Princess Auto, Edmonton, AB, Canada) was then used to remove any burrs on the circumference of the 6.35 mm hole.

Ideally, the surface finish of the coupons should be identical with the surface finish of the alloys found in the corroded aeration tank (as per NACE Standard RP0497 [9]). However, matching surface finishes is difficult because the surface finish on alloys varies among mills and individual product heats [9]. Moreover, the mill scale composition, presence of contaminants, and the amount of oxides can also vary, which may lead to varying corrosion initiation times [9]. Therefore, testing coupons with a uniform surface preparation minimizes both the heterogeneous surface finish produced from processing of the material, and as noted in ASTM G78 [10], “the variability of crevice geometry in contact areas”. Hence, the surfaces of the sheet corrosion coupons were wet ground (TwinPrep 3, Allied High Tech Products Inc., Rancho Dominguez, CA, USA) to a 240 grit finish with silicon carbide grit paper (SiC Grit Paper, Allied High Tech Products Inc., Rancho Dominguez, CA, USA). The 240 grit surface finish was also achieved for the tube coupons using a micro-lathe (Unimat 3, EMCO Group, Hallein, Salzburg, Austria) with silicon carbide grit paper. For the edge surfaces of the tube coupons, the same wet grinding equipment used to prepare the sheet coupons was also used. The sequence of grit sizes used to achieve the final surface finish for both coupons was 60 followed by 240.

Due to the variability in grinding, the final dimensions of each coupon were measured. The average dimensions of the coupons are provided in Table 3-5. The outer diameter (tube coupons) or width (sheet coupons), and length were measured using a caliper (Absolute Digimatic Digital Caliper, Mitutoyo, Mississauga, ON,

Canada), and the thickness was measured using a point micrometer (342-351 Digimatic, Mitutoyo, Mississauga, ON, Canada). Three measurements were taken for each dimension of each of the thirty six coupons, except for the length of the tubular coupons which was measured four times. The dimensions were used to calculate the total and edge surface area of the coupons. Also included in Table 3-5 were the calculated two-tailed 95% confidence intervals for each dimension and surface area. In order to use a 95% confidence interval [11], it is assumed that the thickness measurement distribution is normal, the significance level ( $\alpha$ ) is 5%, and a 2-tailed interval is chosen. The following equations were used to determine the confidence intervals.

Sample mean (average) is calculated using Equation 3-1 [11]:

$$\bar{x} = \frac{\sum_{i=1}^n x_i}{n} \quad (\text{Equation 3-1})$$

The sample standard deviation is calculated using Equation 3-2 [11]:

$$s = \sqrt{\frac{\sum_{i=1}^n (x_i - \bar{x})^2}{n-1}} \quad (\text{Equation 3-2})$$

Finally, the confidence interval is calculated using Equation 3-3, which subsequently can be simplified as Equation 3-4 [11]:

$$\bar{x} \pm t_{\alpha/2, n-1} \times \frac{s}{\sqrt{n}} \quad (\text{Equation 3-3})$$

$$\bar{x} \pm CI \quad (\text{Equation 3-4})$$

Table 3-5: Average dimensions of corrosion coupons.

		Average $\pm$ 95% Confidence Interval ( $n = 9$ )					
Alloy	Shape	OD <sup>1</sup> or Width [mm]	Thk <sup>2</sup> [mm]	Length [mm]	Total Surface Area (SA <sub>T</sub> ) [mm <sup>2</sup> ]	Edge Surface Area (SA <sub>E</sub> ) [mm <sup>2</sup> ]	SA <sub>E</sub> /SA <sub>T</sub> [%]
5086	Tube	48.13 $\pm$ 0.04	5.09 $\pm$ 0.02	28.10 $\pm$ 0.52	7618.74 $\pm$ 135.74	1375.39 $\pm$ 4.62	18.1 $\pm$ 0.4
6061	Tube	48.04 $\pm$ 0.03	3.65 $\pm$ 0.02	28.24 $\pm$ 0.38	7541.75 $\pm$ 106.75	1018.05 $\pm$ 4.60	13.5 $\pm$ 0.2
5086 / 5083	Sheet	23.50 $\pm$ 0.26	3.96 $\pm$ 0.06	48.39 $\pm$ 1.21	2578.94 $\pm$ 82.42	569.96 $\pm$ 15.49	22.1 $\pm$ 0.3
304	Sheet	24.61 $\pm$ 0.33	2.95 $\pm$ 0.01	50.47 $\pm$ 0.12	2661.23 $\pm$ 34.96	442.27 $\pm$ 2.60	16.6 $\pm$ 0.1

1: Outer Diameter 2: Thickness

Note that the total surface area calculated excludes the coupon surface area covered by the crevice former(s) and which is in contact with the hook(s) used to suspend the coupons in the corrosion cell. Next, two 5086/5083 coupons in the Isopac electrolyte were slightly below the minimum 2500 mm<sup>2</sup> surface area recommendation (their values were 2397.80 mm<sup>2</sup> and 2430.29 mm<sup>2</sup>, respectively). However, all coupon surface areas met the recommended minimum surface area of 1900 mm<sup>2</sup> as stated in NACE Standard RP0497 [9]. All other coupons exceeded said ISO 11845 [2] recommendation. Finally, the 5086/5083 coupons (all nine coupons) exceeded the maximum edge surface area to total surface area ratio (SA<sub>E</sub>/SA<sub>T</sub>) of 20% as listed in ASTM G31 [1]. The remaining coupons were below said recommended, maximum ratio value (as shown in Table 3-5).

After fabrication, the coupons were cleaned as per ASTM G1 [12] and ASTM G31 [1]. The following cleaning procedure was performed on individual coupons; one coupon at a time. First, the coupons were submerged in a room temperature solution of 5 g corrosion inhibited cleaning powder (Alconox® – Powdered Precision Cleaner, Alconox, Inc., White Plains, NY, USA) dissolved in 200 mL DIUF (Lot # 153940, Fisher Scientific, Ottawa, ON, Canada). Next, the coupons were scrubbed with a sponge in running tap water, followed by rinsing with DIUF. The coupons were then rinsed with acetone (HPLC,  $\geq$  99.9%, SIGMA-

ALDRICH, Oakville, ON, Canada), followed by methanol (HPLC,  $\geq 99.9\%$ , SIGMA-ALDRICH, Oakville, ON, Canada). After rinsing, the coupons were dried with a hot air gun (LCD Heat Gun, DEWALT, Mississauga, ON, Canada) for approximately 5 to 10 seconds to remove any residual methanol. Then, the coupons were stored in a desiccator (Mount Storage Cabinet, Allied High Tech Products, Inc., Rancho Dominguez, CA, USA) for a minimum of 24 hours before the crevice formers were installed. Throughout the cleaning process, the corrosion coupons were handled with nitrile gloves. Stainless steel tweezers were also used to handle the coupons when DIUF, acetone, and methanol rinsing was performed.

The artificial crevice formers selected were 8.89 mm wide polyamide (nylon) hose clamps (Easy-Install Double Snap-Grip Clamps, 46 to 50.5 mm, McMaster Carr, Elmhurst, IL, USA) for the tube coupons, and two 12.8 mm diameter nylon 6,6 washers (Nylon Fasteners, H. Paulin & Co., Toronto, ON, Canada) and nylon 6,6 nuts and screws (12.8 mm diameter Nylon Fasteners, H. Paulin & Co., Toronto, ON, Canada) for the sheet coupons. Nylon is a thermoplastic polymer that has been used in previous immersion experiments as both hose clamps [10,13] and continuous washers [10]. Prior to installation, the crevice formers were cleaned following the same procedure as the corrosion coupons, and subsequently stored in a desiccator for a minimum of 24 hours before installation. The crevice formers were installed on the coupons in the following manner. The hose clamps were tightened to the third last notch; away from being completely closed. Meanwhile, the sheet coupon nuts were torqued to 1.0 N•m with a torque wrench (6.35 mm Drive, 0-1.7 N•m, Dial Torque Wrench, CDI Torque Products, Kenosha, WI, USA). After fitting the crevice formers, the coupons were gently swabbed with methanol soaked cotton balls, and stored in a desiccator for a minimum of 24 hours as per ASTM G1 [12] and ASTM G31 [1]. Nitrile gloves were used to hold the installed crevice former while this additional swabbing step was completed.

### 3.1.2 Electrolyte and Apparatus Design and Fabrication

The concentrations of both coagulants used in the lab scale immersion tests were determined from the collected aeration tank process data provided in Appendix C. The average concentrations of Isopac and Alum used in the aeration tank were calculated to be 0.010 and 0.017 volume %, respectively. With these concentrations, the 0.24 mL/mm<sup>2</sup> V/SA and the exposed surface area of each coupon, the total required solution volume and subsequent amount of coagulant required were calculated for each of the thirty six corrosion cells. The average DIUF, coagulant addition (where applicable), and total solution volume for each alloy and electrolyte combination are presented in Table 3-6. Also included in this table are the two-tailed 95% confidence intervals for each volume.

Table 3-6: Average volume of corrosion cell solutions.

Alloy & Solution Combination		Average $\pm$ 95% Confidence Interval ( $n = 3$ )		
		DIUF Volume [mL]	Coagulant Addition [ $\mu$ L]	Total Volume [mL]
5086	Isopac	1839.7 $\pm$ 35.7	184.0 $\pm$ 3.6	1839.9 $\pm$ 35.7
5086	Alum	1802.0 $\pm$ 173.9	306.3 $\pm$ 29.6	1082.3 $\pm$ 173.9
5086	DIUF	1820.5 $\pm$ 76.8	N/A	1820.5 $\pm$ 76.8
6061	Isopac	1797.4 $\pm$ 50.0	179.7 $\pm$ 5.0	1797.6 $\pm$ 50.0
6061	Alum	1786.0 $\pm$ 118.2	303.6 $\pm$ 20.1	1786.3 $\pm$ 118.2
6061	DIUF	1823.6 $\pm$ 62.9	N/A	1823.6 $\pm$ 62.9
5086 / 5083	Isopac	599.9 $\pm$ 99.4	60.0 $\pm$ 9.9	600.0 $\pm$ 99.4
5086 / 5083	Alum	625.5 $\pm$ 34.6	106.3 $\pm$ 5.9	625.6 $\pm$ 34.6
5086 / 5083	DIUF	623.5 $\pm$ 37.0	N/A	623.5 $\pm$ 37.0
304	Isopac	633.0 $\pm$ 20.4	63.3 $\pm$ 2.0	633.1 $\pm$ 20.4
304	Alum	637.0 $\pm$ 34.5	108.3 $\pm$ 5.9	637.1 $\pm$ 34.5
304	DIUF	637.9 $\pm$ 34.4	N/A	637.9 $\pm$ 34.4

N/A: Not Applicable

The vessels selected for the tube coupons were 2500 mL polypropylene (PP) containers (SP® Multipurpose Containers, Cardinal Health, Dublin, OH, USA). Meanwhile, 1000 mL beakers (Pyrex® heavy duty graduated beaker, SIGMA-ALDRICH, Oakville, ON, Canada) were selected for the sheet coupons. Figure 3-3 is a representative image of both the beakers and containers used to hold all thirty six corrosion cells. Both the beakers and PP containers were cleaned using a

procedure comprised of: scrubbing with a sponge using a solution of corrosion inhibited cleaning powder and tap water, rinsing with tap water, and rinsing with ethanol (100%, Biological Sciences Storeroom, University of Alberta, Edmonton, AB, Canada). The beakers and containers were allowed to air dry after cleaning.

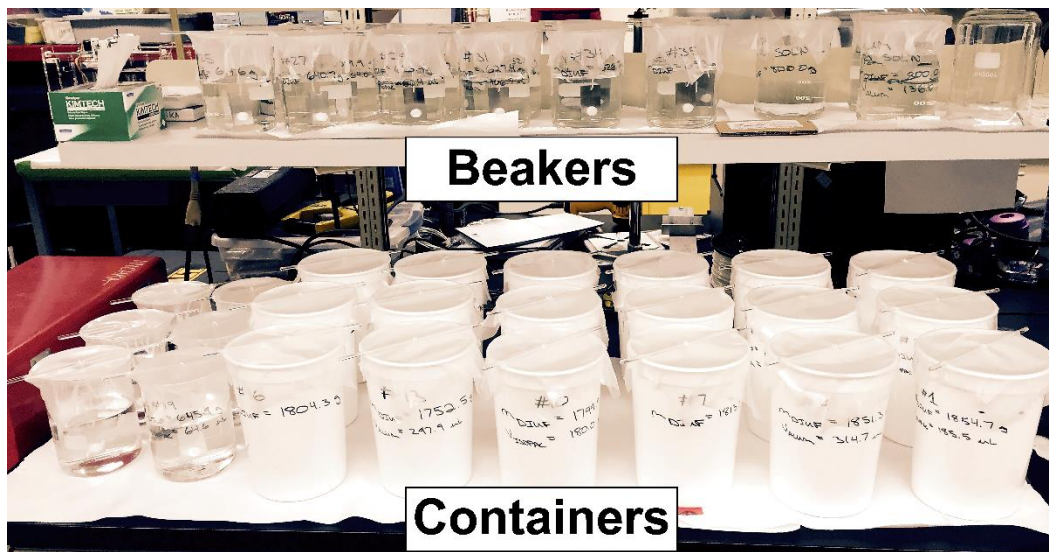


Figure 3-3: Overall image of corrosion coupons in beakers or containers during the 28 day experiment.

Since the concentrations of Alum (CSA 16828-12-9; ClearTech Industries Inc., Saskatoon, SK, Canada) and Isopac (CSA 1347-41-9; Klearwater Equipment & Technologies Co., Calgary, AB, Canada) used in this study were trace in volume, it was assumed that their density equaled the density of the DIUF (Lot #: 154488, Fisher Scientific, Ottawa, ON, Canada) also used in this study. Furthermore, it was assumed that the density of DIUF at standard ambient temperature and pressure was equal to 1.0 g/mL. Therefore, the DIUF volume and total solution volume were measured by weight on a top loading balance (Practum® 5101-1S, Sartorius, Bohemia, NY, USA). The required coagulant was added to each solution using a variable volume pipette (20-200  $\mu$ L and 100-1000  $\mu$ L Eppendorf® Variable Volume Pipettors, SIGMA-ALDRICH, Oakville, ON, Canada). After the coagulant was added, the solution was stirred for approximately one minute using a cleaned glass stir stick (4 mm x 200 mm Stirring Rods, SIGMA-ALDRICH, Oakville, ON, Canada).

For suspending the coupons in the corrosion cells, a combination of a hook and rod were used. 1.75 mm diameter acrylonitrile butadiene styrene (ABS) (ABS Filament, MakerBot, Brooklyn, NY, USA) was chosen to be fabricated into plastic hooks. Meanwhile, glass stir sticks (4 mm x 200 mm Stirring Rods, SIGMA-ALDRICH, Oakville, ON, Canada) were used to support the hook and coupon. The ABS hooks were cleaned using the following procedure: scrubbing with a sponge using a solution of corrosion inhibited cleaning powder and tap water, rinsing with tap water, and rinsing with DIUF. The hooks were allowed to air dry and then were stored in a desiccator for a minimum of 24 hours. The glass stir sticks were cleaned following the same procedure as both the corrosion coupons and crevice formers, except a low-foaming neutral cleaner (Luminox®, Alconox, Inc., White Plains, NY, USA) was used instead of Alconox®. After cleaning, the glass stir sticks were dried with a hot air gun and also stored in a desiccator. For the beakers, the distance between the bottom of the beaker and the bottom of the sheet coupon (short edge) was approximately 1.5 cm. Regarding the containers, the distance between the bottom of the container and the bottom of hose clamp was approximately 3.0 cm.

Finally, when the corrosion experiments were started, paraffin film (Parafilm® M Laboratory Sealing Film, Bemis Company, Inc., Oshkosh, WI, USA) was placed over-top of the beaker and container openings in order to minimize any evaporation effects or contamination from the surrounding atmosphere. The paraffin film, on all of the corrosion cells, was periodically replaced during the 28 day experiment due to wear and damage from repeated opening and closing while collecting measurements.

### 3.1.3 In Situ Monitoring of Key Process Indicators

As previously mentioned, DO concentration,  $\text{Cl}^-$  concentration, temperature, and pH measurements were collected in order to monitor each corrosion cell solution, and identify if any drastic changes were to occur throughout the 28 day corrosion experiment. A portable meter (HQd Portable Meter, HACH,

London, ON, Canada) with a luminescent dissolved oxygen probe (LDO10101, HACH, London, ON, Canada), chloride ion selective electrode probe (ISECl18101, HACH, London, ON, Canada), and a pH probe (PHC30101, HACH, London, ON, Canada) were used to collect data for the four metrics. Note that the temperature measurements were collected using the DO probe, and were collected at the same time as the DO concentration was measured.

The DO and pH probes were prepared, calibrated, and successively conditioned in the corrosion cell solutions as per the procedures listed in their respective user manuals [14,15]. The  $\text{Cl}^-$  probe was prepared, calibrated, and conditioned following the procedures in its user manual [16], but with two modifications. First, no chloride ionic strength adjuster (ISA) buffer was added to either the calibration solutions or the corrosion cell solution when either calibration or conditioning was performed. Second, all corrosion cell solutions, even with chloride ion concentrations less than 10 mg/L, were tested using the same procedure listed in the user manual [16]. The pH probe was calibrated with pH 7.00 (Buffer Solution, pH 7.00, color-coded yellow, Product #: 2283549, HACH, London, ON, Canada) and pH 4.01 (Buffer Solution, pH 4.01, color-coded red, Product #: 2283449, HACH, London, ON, Canada) buffer solutions. Meanwhile, the  $\text{Cl}^-$  probe was calibrated with chloride standard solutions of 100 mg/L (Chloride Standard Solution (0.00282 N), Product #: 2370853, HACH, London, ON, Canada) and 1000 mg/L (Chloride Standard Solution (1648 mg/L NaCl), Product #: 18349, HACH, London, ON, Canada) concentrations. The DO probe did not require any calibration solutions, but instead used a procedure listed in its user manual [14]. Additionally, the DO and pH probes were recalibrated after measuring six cells in a row and three cells in a row, respectively. Moreover, a check standard was run before every use of the pH probe (as per the pH probe manual [15]). If the check standard failed, the pH probe was recalibrated. Conversely, the  $\text{Cl}^-$  probe was recalibrated and conditioned before every cell tested.

The measurement intervals for all four parameters were as follows: before placing the coupon in solution (known henceforth as day 0), day 7, day 14, day 21, and day 28. DO, pH, and temperature were measured for all thirty six corrosion cells throughout the duration of the corrosion experiment. Due to calibration issues as well as long measurement stabilization times,  $\text{Cl}^-$  was measured for only one of three of the corrosion cells (per alloy and electrolyte combination). Therefore, a total of twelve corrosion cells had their  $\text{Cl}^-$  concentration monitored through-out the 28 days.

Measurements were taken from each corrosion cell, after the corrosion coupon was removed from solution. Three measurements were collected for each data point. The measurements were collected from the center of both vessel types, at a height of approximately 6.5 cm above the bottom of the PP containers and approximately 2.5 cm above the bottom of the beakers (at the 200 mL mark). Furthermore, the pH and DO probes were gently moved with a stirring motion, according to manufacturer's instructions, when measurements were being collected. Conversely, the  $\text{Cl}^-$  probe remained stationary during the collection of measurements.

DO,  $\text{Cl}^-$  concentration, temperature, and pH measurements were also collected from a control solution of each of the three solution types. Again, the concentration of Isopac and Alum used for the control solutions were 0.010 and 0.017 volume %, respectively. DIUF volume, coagulant volume, and total solution volume for each control solution are listed in Table 3-7. The data collected from the three control solutions could be compared to the data from each corrosion cell of the same electrolyte in order to determine if any radical changes were observed over the 28 day test period due to corrosion. Additionally, the control solutions were prepared using the same methods and equipment as the corrosion cell electrolytes. Furthermore, the control solutions were each held in a 1000 mL beaker.

Table 3-7: Volume of control solutions.

Control Solution	DIUF Volume [mL]	Coagulant Addition [ $\mu$ L]	Total Volume [mL]
Isopac	800.0	80.0	800.1
Alum	800.0	136.0	800.1
DIUF	800.0	N/A	800.0

N/A: Not Applicable

While out of solution, one coupon per alloy and solution combination (twelve coupons in total) were photographed in order to record any noticeable changes to the coupon surfaces, as well as to identify any corrosion products that had formed during the test. Further information on the coupon photography is provided in Section 3.2.1.

Due to the removal of coupons from solution to measure the four parameters, as well as to take photographs, minor solution mass losses had occurred from both solution evaporation and due to the removal of the corrosion coupons. The solution mass loss was measured to be less than 4% of the total solution volume. Moreover, each coupon was in solution for approximately 28 days. Due to the coupons being removed, the coupons were not in solution for 28 days in total. The average plus/minus two-sided 95% confidence interval of the total amount of time the photographed and non-photographed coupons were out of solution during the experiment were 2 hours and 23 minutes  $\pm$  13 minutes ( $n = 12$ ) and 48 minutes  $\pm$  5 minutes ( $n = 24$ ), respectively.

### 3.2 Coupon Characterization

Several characterization methods were performed on the coupons in order to qualify and possibly quantify the extent of corrosion damage that occurred due to exposure of the three test solutions. Both macro photography and stereo microscopy were performed on the coupons, and information regarding both methods is provide in Sections 3.2.1 and 3.2.2, respectively. Next, the deposits formed underneath or adjacent to the crevice former were further analyzed with three techniques, specifically: energy dispersive x-ray (EDX) spectroscopy, x-ray

diffraction (XRD), and Fourier transform infrared (FTIR) spectroscopy. Information on each technique, including how the technique was performed and the equipment used, are individually discussed in the sub-sections of Section 3.2.3. Quantification of any corrosion damage was determined through coupon mass changes. Further information on the coupon mass measurements is provided in Section 3.2.4. Finally, after the immersion testing was completed but prior to the examination and testing listed in Section 3.2, the coupons were stored in a desiccator.

### 3.2.1 Macro Photography

Visual evidence of changes to the coupon surfaces from immersion testing, and subsequent identification of deposits, was recorded via macro photography. The coupons were photographed before, during (for only twelve coupons), and after the 28 day immersion test.

In order to minimize any contamination from handling the coupons either before, during, or after the immersion testing, a special photography/light table was created, which allowed for adjustable suspension and rotation of the coupons while photos were taken. This table, as well as the position of the lights, camera, and coupon is illustrated in Figure 3-4.

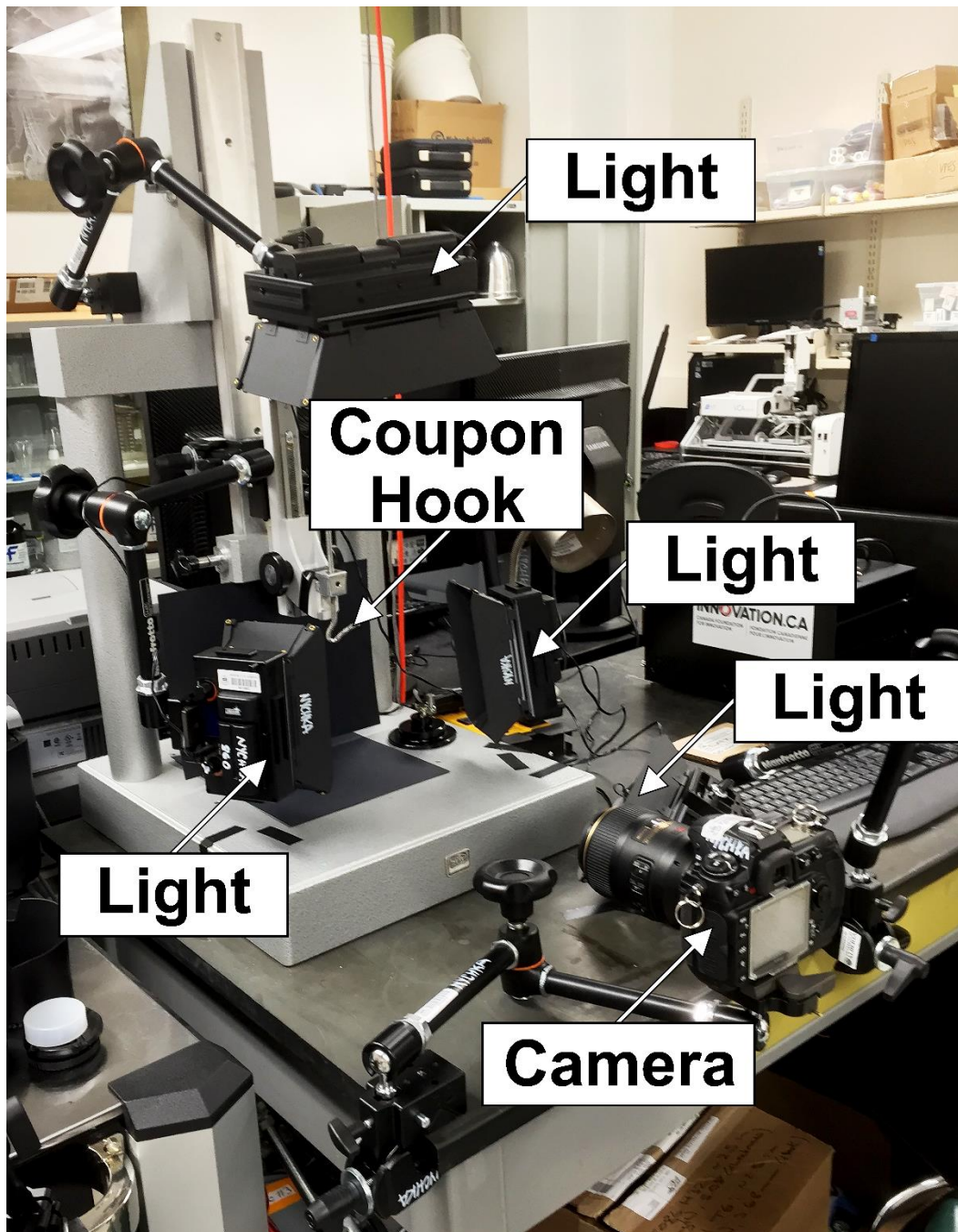


Figure 3-4: Macro photography set-up (nylon hook suspended from light table adjustable metal hook; camera lens focuses on coupon; LED lights are fully adjustable, and their orientation relative to the coupon are changed in order to allow for proper oblique lighting).

A digital single lens reflex camera (D300s, Nikon Corp., Tokyo, Japan) equipped with a 105 mm lens (AF-S Micro Nikkor 105 mm f2.8GED, Nikon Corp., Tokyo, Japan), and operated in manual mode, was used to capture the photos. Three

small light emitting diode (LED) lights (LD17DS, Lumahawk, NADEL Enterprises Inc., Toronto, ON, Canada) and one large LED light (LD312DS LED, Lumahawk, NADEL Enterprises Inc., Toronto, ON, Canada) were used to provide oblique lighting to the coupon surface. The camera and all four LED lights were individually mounted and positioned using adjustable, variable friction arms (Model 244 Magic Arm with Super Clamp, Manfrotto, Lino Manfrotto & Co., Cassola, VI, Italy).

For imaging of the coupons throughout the immersion testing (before, during, and after), the following camera and LED light settings were applied for all photographs. The white balance was set via selection of the colour temperature on both the camera and lights, which were 5560 K and 5600 K, respectively. The camera aperture was set to f13 and an ISO of 200 was selected. Finally, the shutter speed and exposure compensation was varied depending on the coupon orientation as well as the variation in lighting power and position.

Due to the different coupon's reflectivity (due to surface finish and alloy chemistry), size and orientation, the position and orientation of the lights and their intensities were adjusted in order to achieve adequate oblique lighting conditions. The light orientations and intensities were changed for each of the four alloys, except for the 5086 and 6061 tubes which had the same light orientations and intensities. Additionally, the subject to lens distance varied due to the position of the specimen surface and crevice former being imaged. Hence, the magnification had to be adjusted for each coupon. Contrarily, the working distance between the camera lens and the suspended corrosion coupon (specifically from the center of the metal hook on the light stand) was approximately 16 inches.

Photographs were taken of two sides of each coupon, none of which were the coupon edges. Next, the images were adjusted using Adobe Photoshop (CC, Adobe Systems Incorporated, San Jose, CA, USA). The specific adjustments implemented to each image were: brightness, contrast, exposure, and white balance.

Finally, Photoshop was also used to crop the photos to the necessary size and to add scale bars.

### 3.2.2 Stereo Microscopy

Images of the coupon surface beneath and immediately adjacent to the crevice former were collected using two, manual stereo microscopes. For lower and higher magnifications, the EZ4 HD (Leica Microsystems, Wetzlar, Germany) and M125 (Leica Microsystems, Wetzlar, Germany) stereo microscopes were used, respectively. Images from both stereo microscopes were collected from only one location on one side of the coupon, in oblique lighting conditions. Moreover, any three dimensional reconstructions created, or scale bars added, using the M125 stereo microscope were done using Leica imaging software (Leica Application Suite, Leica Microsystems, Wetzlar, Germany). Finally, any image editing, including: brightness, contrast, exposure, white balance, and cropping were also performed using Photoshop.

### 3.2.3 Deposit Characterization

This section is comprised of three sub-sections, each of which contains the necessary information regarding each technique. Again, the chemical characterization methods (namely EDX, XRD, and FTIR) were only conducted on deposits formed underneath or adjacent to the crevice former. These deposits were believed to be corrosion products.

#### *3.2.3.1 Energy Dispersive X-ray (EDX) Spectroscopy*

EDX was performed in order to qualitatively or semi-quantitatively (at best) determine the elemental composition of the deposits. A scanning electron microscope (SEM) (Evo MA 15, Carl Zeiss Inc., Toronto, ON, Canada) with an

energy dispersive X-ray (EDX) spectrometer (Silicon Drift Detector, Bruker, East Milton, ON, Canada) was used.

Due to the amount of deposit present as well as the size of the coupons, two methods were used to prepare the deposit specimens for analysis. For the tube coupons, the deposit specimens were removed from the coupon surface, via scraping with folded weigh paper (Low-Nitrogen Weighing Paper, Fisher Scientific, Edmonton, AB, Canada), and mounted on pins with double-sided carbon tape. These specimens were then stored in a desiccator cabinet (Secador, Fisher Scientific, Ottawa, ON, Canada). Prior to testing, the specimens were carbon coated using a carbon evaporator (EM SD005, Leica, Richmond Hill, ON, Canada). Conversely, deposits on the sheet coupons were directly analyzed in the SEM, and were not carbon coated. Only one side of the sheet coupons was analyzed.

While collecting the element data, the SEM was operated in backscattered electron (BSE) mode with a LaB<sub>6</sub> filament functioning at an accelerating voltage of 20 kV. Moreover, the aperture was set at 30 microns, and all specimens (both deposits on pins or directly on the coupon) tested were orientated at a tilt angle of 0 degrees. Due to the nature of EDX, as well as the variability observed in the different locations of the specimens, compositional data were reported for three points within each specimen.

#### *3.2.3.2 X-ray Diffraction (XRD)*

XRD was performed on the deposits in order to identify the presence of any crystalline corrosion products. An XRD machine (Rigaku Ultima IV XRD System, Rigaku, ON, Canada) was used to collect the data from the deposit specimens. The subsequent patterns were solved with Jade 9.1 software (Jade 9.1, Materials Data Inc, Livermore, CA, USA).

Deposit was removed directly from the coupons onto zero background slides (zero background specimen holder, Rigaku, ON, Canada) by gently scraping with folded weigh paper. To help the small amount of deposit collected adhere to the zero background plates, one to two small drops of American Chemical Society (ACS) reagent grade methanol was placed on the plates to wet the surface. Aluminum hydroxide and aluminum oxide are insoluble in methanol [17,18]. Meanwhile, stainless steel corrosion products including: iron (II) oxide, iron (II,III) oxide, iron (III) oxide, iron (II) hydroxide, and iron (III) hydroxide are also insoluble in methanol [18,19]. Prior to analyzing the specimens, the methanol was allowed to air dry (leading to natural evaporation of the methanol).

The XRD machine was operated in continuous reflective XRD mode, in which the 2 theta angle was scanned between 5 and 90 degrees at a rate of 2 degrees per minute. Additionally, the machine employed a Co anode operated at 38 kV and 38 mA. Furthermore, the system utilized a curved graphite monochromator, and the system was configured in the focused beam geometry. An automated 10 position stage was used to expedite the analysis (ASC-10 Stage, Rigaku, ON, Canada).

### *3.2.3.3 Fourier Transform Infrared (FTIR) Spectroscopy*

FTIR was performed on the deposits in order to identify the presence of any amorphous corrosion products (through identification of chemical bonds). As with EDX, due to the amount of deposit present as well as the size of the coupons, two methods were used to prepare the deposit specimens for analysis. For the tube coupons, the deposit was removed using a stainless steel scraper. The deposit specimens were each mechanically pulverized and mixed with potassium bromide (KBr) powder (International Crystal Labs, Garfield, NJ, USA). Then, the powder mixtures were compressed into spherical pellets. The KBr pellets were tested using a Fourier transform infrared spectrometer (FTIR) (Thermo Nicolet 8700 FTIR Spectrometer, Thermo Scientific, Newington, NH, USA) with a deuterated triglycine sulfate (DTGS) detector (Thermo Scientific, Newington, NH, USA) and

a spectral range of 7800 to 350  $\text{cm}^{-1}$ . The spectrometer was operated in transmittance mode with 32 scans and a resolution of 4  $\text{cm}^{-1}$ . The spectra for each pellet were collected between 400  $\text{cm}^{-1}$  and 4000  $\text{cm}^{-1}$ . Finally, the collected data were processed using Omnic 8.3 software (Omnic 8.3, Thermo Scientific, Newington, NH, USA).

Conversely, deposits on the sheet coupons were directly analyzed using a FTIR microscope (Nicolet Continuum FTIR Microscope, Thermo Scientific, Newington, NH, USA), which was connected to the same FTIR spectrometer used for the KBr pellets. The microscope was operated in reflectance mode (near normal reflection and absorption). The spectra were collected between 650  $\text{cm}^{-1}$  and 4000  $\text{cm}^{-1}$ , and the samples were run with 128 scans and a resolution of 4  $\text{cm}^{-1}$ . Finally, only one side of the sheet coupons was analyzed, and the collected data were also processed using Omnic 8.3 software.

### 3.2.4 Mass Change Measurements

In order to quantify (if any) the corrosion damage, mass measurements were collected from each of the coupons before (more specifically, before installation of the crevice former(s) and after initial cleaning) and after (specifically after removal of the crevice formers and cleaning) the 28 day immersion experiment.

After the immersion testing, as well as collection and testing of deposits and removal of crevice formers, cleaning of the coupons was performed as per ASTM G1 [12], ASTM G31 [1], and ISO 8047 [20]. As in Section 3.1.1, the following cleaning procedure was performed on individual coupons; one coupon at a time. First, the coupon was submerged in a room temperature solution of 5 g corrosion inhibited cleaning powder (Alconox®) dissolved in 200 mL DIUF for one minute. Next, the coupon was scrubbed with a toothbrush for one minute, followed by rinsing in tap water while scrubbing with the same toothbrush for an additional minute. The coupon was then rinsed in tap water, followed by being placed in a

beaker filled with ethanol, which was subsequently placed in an ultrasonic bath (3510DTH, Branson, Emerson Electric Co., St. Louis, MO, USA) for five minutes. These five steps were repeated five times before the coupon was dried with a hot air gun. Afterwards, the coupon was placed on a bench top (with weigh paper between the coupon and the bench top surface) and allowed to air cool.

The mass of each coupon was measured to the nearest 0.1 mg as per ASTM G31 [1], using an analytical balance (Pinnacle P-114, Sartorius (formerly Denver Instrument), Bohemia, NY, USA). Additionally, the coupons were handled with nitrile gloves during both cleaning and weighing steps.

The mass change of each coupon was calculated by taking the difference in coupon mass before the immersion test and after the fifth interval of cleaning. Using the same statistical analysis performed in Section 3.1.1, the average and 95% confidence interval mass change was calculated for each of the twelve alloy and solution combinations, using the three coupons from each set.

### **3.3 References**

- [1] NACE/ASTM G31, Standard Guide for Laboratory Immersion Corrosion Testing of Metals, West Conshohocken, PA, 2013. doi:10.1520/G0031-12A.
- [2] ISO 11845, Corrosion of metals and alloys - General principles for corrosion testing, Geneva, Switzerland, 1995. www.iso.org.
- [3] J.R. Davis, ed., Corrosion of Aluminum and Aluminum Alloys, ASM International, Materials Park, OH, 1999. doi:10.1361/caaa1999.
- [4] J.S. Pavelich, J.A. Nychka, Preliminary Findings Report: Visual Inspection and Corrosion Assessment of the EPCOR Borealis Waste Water Treatment Plant, Edmonton, AB, 2013.
- [5] J.S. Pavelich, J.A. Nychka, Additional Inspection Report: Additional Visual Inspection and Corrosion Assessment of the EPCOR Borealis Wastewater Treatment Plant, Edmonton, AB, 2014.

- [6] C. Vargel, Corrosion of Aluminium, Elsevier Ltd, Kidlington, UK, 2004.
- [7] S. Gustafsson, Corrosion properties of aluminium alloys and surface treated alloys in tap water, Uppsala University, 2011.
- [8] J.R. Davis, ed., Corrosion: Understanding the Basics, ASM International, Materials Park, OH, 2000.
- [9] NACE Standard RP0497, Field Corrosion Evaluation Using Metallic Test Specimens, Houston, TX, 2004. [www.nace.org](http://www.nace.org).
- [10] ASTM G78, Standard Guide for Crevice Corrosion Testing of Iron-Base and Nickel-Base Stainless Alloys in Seawater and Other Chloride-Containing Aqueous Environments, West Conshohocken, PA, 2012. doi:10.1520/G0078-01R12.
- [11] D.C. Montgomery, G.C. Runger, Applied Statistics and Probability for Engineers, 3rd ed., John Wiley & Sons, Inc., New York, NY, 2003.
- [12] ASTM G1, Standard Practice for Preparing, Cleaning, and Evaluating Corrosion Test Specimens, West Conshohocken, PA, 2011. doi:10.1520/G0001-03R11.
- [13] A.W. Zeuthen, R.M. Kain, Crevice Corrosion Testing of Austenitic, Superaustenitic, Superferritic, and Superduplex Stainless Type Alloys in Seawater, in: R.M. Kain, W.T. Young (Eds.), ASTM STP 1300 Corros. Test. Nat. Waters Second Vol., ASTM International, West Conshohocken, PA, 1997: pp. 91–108.
- [14] HACH Company, User Manual Luminescent Dissolved Oxygen Probe: Model LDO10101, LDO10103, LDO10105, LDO10110, LDO10115, or LDO10130, (2013). <http://www.hach.com/intellical-ldo101-standard-luminescent-optical-dissolved-oxygen-ldo-probe-1-meter-cable/product-downloads?id=7640489854&callback=qs>.
- [15] HACH Company, User Manual Refillable pH Probe: Model PHC30101 or PHC30103, (2013). <http://www.hach.com/intellical-phc301-standard-refillable-ph-electrode-1-meter-cable/product-downloads?id=7640512232>.
- [16] HACH Company, User Manual Chloride Probe: Model ISECl18101 or ISECl18103, (2013). <http://www.hach.com/intellical-isecl181-chloride-ion-selective-electrode-ise-1-meter-cable/product-downloads?id=7640513801&callback=qs>.
- [17] R.C. Weast, ed., CRC Handbook of Chemistry and Physics, 59th ed., CRC Press, West Palm Beach, FL, 1978.

- [18] D.L. Perry, Handbook of Inorganic Compounds, 2nd ed., CRC Press, Boca Raton, FL, 2011.
- [19] D.R. Lide, ed., CRC Handbook of Chemistry and Physics, 84th ed., CRC Press, Boca Raton, FL, 2004.
- [20] ISO 8047, Corrosion of metals and alloys - Removal of corrosion products from corrosion test specimens, Geneva, Switzerland, 2009. [www.iso.org](http://www.iso.org).

# Chapter 4 – Results and Discussion

## 4.1 Coupon Characterization

The modes of corrosion observed on the various alloys tested in the three electrolytes are summarized in Table 4-1. All of the modes listed were identified with stereo microscopy (Section 4.1.2), except for the intergranular corrosion (IGC) observed on the Isopac-5086/5083 combination which was identified via scanning electron microscopy (SEM; Section 4.1.3.1).

Table 4-1: Modes of corrosion identified on the corrosion coupons immersed in the three electrolytes tested in this study.

Alloy	Electrolyte		
	Isopac	Alum	DIUF
5086	<ul style="list-style-type: none"> <li>• Pitting</li> <li>• Crevice Corrosion</li> </ul>	<ul style="list-style-type: none"> <li>• Pitting</li> <li>• Crevice Corrosion</li> </ul>	<ul style="list-style-type: none"> <li>• Pitting</li> <li>• Crevice Corrosion</li> </ul>
6061	<ul style="list-style-type: none"> <li>• Pitting</li> <li>• Crevice Corrosion</li> <li>• IGC</li> </ul>	<ul style="list-style-type: none"> <li>• Pitting</li> <li>• Crevice Corrosion</li> </ul>	<ul style="list-style-type: none"> <li>• Pitting</li> <li>• Crevice Corrosion</li> </ul>
5086/5083	<ul style="list-style-type: none"> <li>• Pitting</li> <li>• Crevice Corrosion</li> </ul>	<ul style="list-style-type: none"> <li>• Pitting</li> <li>• Crevice Corrosion</li> <li>• IGC</li> </ul>	<ul style="list-style-type: none"> <li>• Pitting</li> <li>• Crevice Corrosion</li> </ul>
304	<ul style="list-style-type: none"> <li>• N/A</li> </ul>	<ul style="list-style-type: none"> <li>• N/A</li> </ul>	<ul style="list-style-type: none"> <li>• N/A</li> </ul>

N/A: Not Applicable

From the information in Table 4-1, it can be claimed that corrosion was observed on the aluminum alloy coupons tested in all three electrolytes. Moreover, no corrosion was identified on the 304 stainless steel coupons in any of the electrolytes. Further information and discussion on the identification and evaluation of the above-mentioned modes of corrosion are presented in the following subsections.

### 4.1.1 Macro Photography

Throughout and upon completion of the immersion testing, the corrosion coupons were photographed in order to capture any visual information of corrosion. This information is comprised of two pieces of evidence: the presence of any deposit, which would have been formed either directly from or as a by-product from a corrosion reaction; and metal loss, which is due to anodic dissolution in the corrosion reaction. Identification of either deposit or metal loss on the coupons is further explored in the remainder of this section. To aid in the examination, the coupon surface was separated into two locations: the exposed surface (absence of crevice former) or underneath the crevice former (henceforth known as the crevice surface). Examination of the ends/edges of the coupons and inner circumference of the tubular coupons were not investigated.

Figure 4-1 contains representative before and after images of one side, from one of three corrosion coupons, from each of the twelve electrolyte-alloy combinations. These images were collected after the coupons were removed from the immersion cells, air dried, and after the crevice formers were removed from the coupon surfaces. All other sides of each of the three coupons per each electrolyte-alloy combination are provided in Appendix D. Also included in this figure are representative images of each of the four alloy surfaces before testing. It should be noted that the crevice former from one of the 6061 alloy coupons in DIUF had changed position during the test. More specifically, the crevice former was shifted on the fourteenth day of testing, while the coupon was being removed from the beaker. The crevice former was shifted back into position and, upon completion of relevant measurements, was placed back into solution.

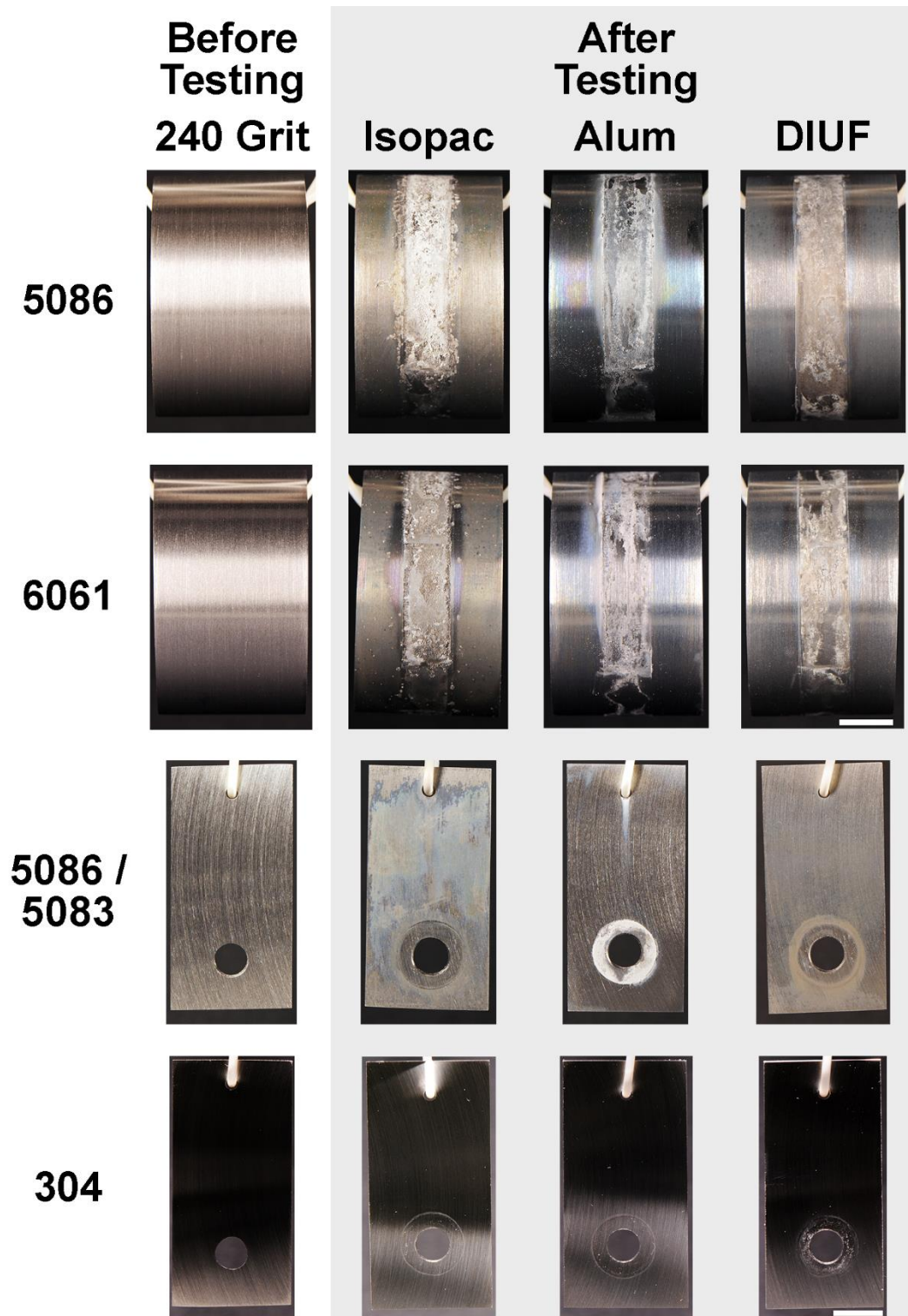


Figure 4-1: Representative images of corrosion coupons, before and after the 28-day immersion testing, from the twelve electrolyte-alloy combinations. Both scale bars are 1 cm.

Comparing the different electrolyte-alloy combinations after immersion testing to before testing, all aluminum alloy coupons appeared to have varying amounts of deposit present on both the exposed and crevice surfaces. The deposit on the exposed surfaces appeared to be a tarnish, whose colour and amount of surface area coverage varied between the coupons. Conversely, the 304 stainless steel coupons appeared to only have deposit present on or immediately adjacent to the crevice surface. The buildup of tarnish on the aluminum alloy coupons and lack of tarnish formation on the 304 coupons is shown in Figures 4-2 and 4-3, respectively.

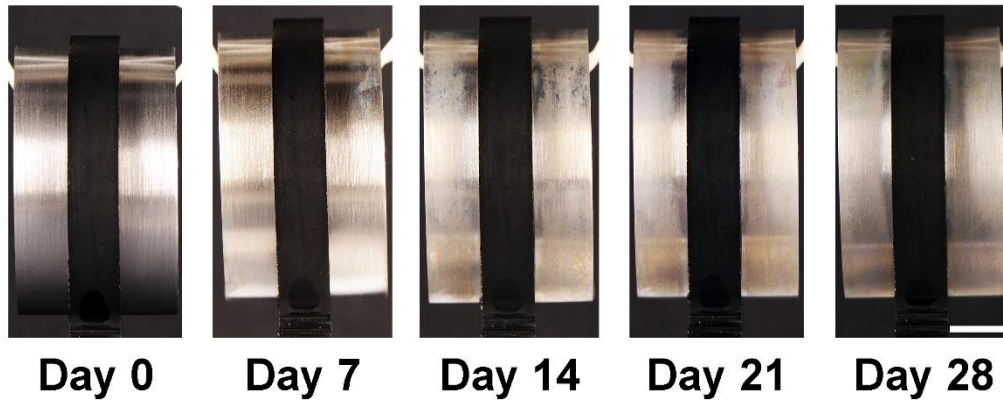


Figure 4-2: Representative image of tarnish build-up on the aluminum alloy coupons throughout the 28-day immersion testing. Electrolyte-alloy combination presented is Isopac-5086. The coupon was still wet and the scale bar is 1 cm.

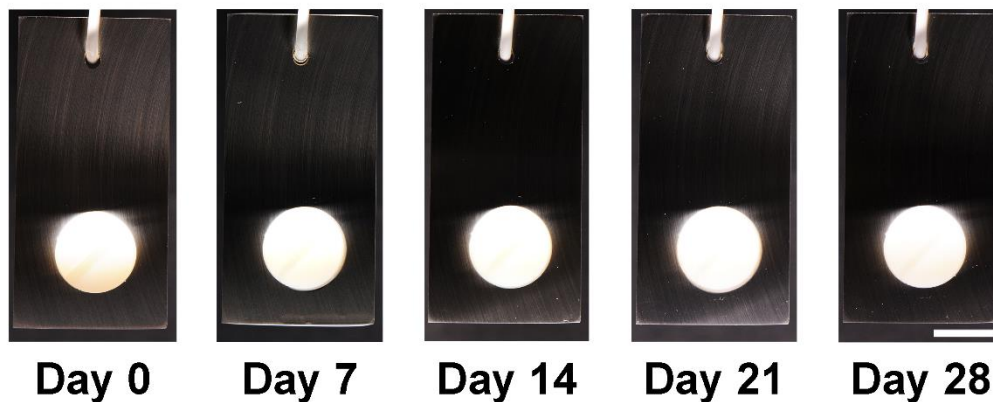


Figure 4-3: Representative image of the lack of tarnish build-up on the stainless steel coupons throughout the 28-day immersion testing. The coupon was still wet (and in this image, exposed to Isopac) and the scale bar is 1 cm.

The deposit on and adjacent to the crevice surfaces of all the alloys appeared creamy white in colour. The amount of deposit varied among each combination; yet, for the 5086 and 6061 alloys, the presence of deposit was most prominent on the coupons in the Isopac solution, followed by Alum, then DIUF. Regarding the 5086/5083 alloy, deposit was consistently present on and adjacent to the crevice surfaces of the coupons in the Alum solution. Moreover, deposit also appeared to be originating from the hook hole. There was little deposit present on the 5086/5083 coupons in DIUF and Isopac solutions; however, one side from one of the three coupons per combination appeared to have deposit (Figure 4-4). Regarding the other surfaces of the remaining two coupons per combination, all surfaces appeared relatively similar. There were some differences in the amount of deposit present on the crevice surface; however, this difference is believed to have occurred due to the inherent variability of deposit precipitating out of solution, or the unwanted dislodgement of deposit when the crevice formers were removed. Finally, all 304 coupons exhibited small amounts of deposit on and adjacent to the crevice surface.

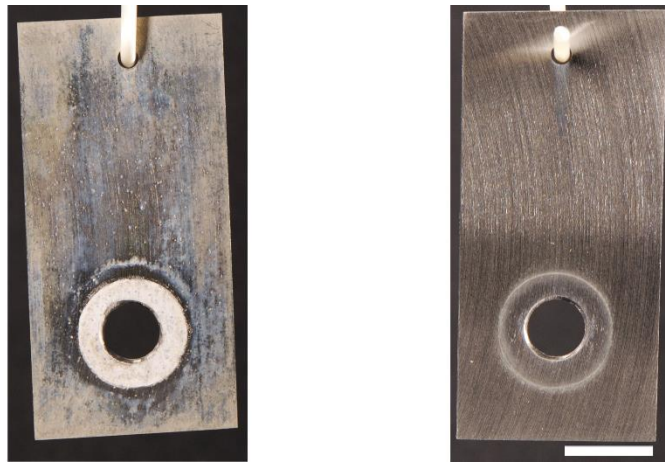


Figure 4-4: 5086/5083 coupons which exhibited deposit on and adjacent to the crevice surface. The coupon on the left was in Isopac solution, while the coupon on the right was in DIUF. Scale bar is 1 cm.

Also observed on the 6061 coupons in Isopac solution was the presence of creamy white tubercles. These tubercles (large spots) were easy to distinguish in the photographs and are believed to be locations of pitting corrosion.

The cause of the tarnish could be from several sources, such as: the contents of the electrolyte (DIUF and selected coagulants); any trace methanol or acetone staining produced from insufficient cleaning of the coupons; any degradation of the nylon crevice formers; and any corrosion products, either directly from the exposed surface or which migrated out from between the crevice surface and former. The composition, structure, or thickness of the tarnishes observed were not studied. Nevertheless, the tarnish had formed on the coupons from being subjected to the different electrolytes as substantiated by comparing the before and after images of the coupons in Figure 4-1.

The creamy white deposit on and adjacent to the crevice surface of the aluminum alloy coupons is indicative of aluminum hydroxide corrosion products [1]. Moreover, the formation of deposit is most likely due to the presence of all the necessary components of a corrosion cell, and a crevice that leads to the creation of a more corrosive localized environment (i.e., a differential aeration cell) – indicative of crevice corrosion. The same rationale can be applied to the white tubercles on the 6061 coupons in Isopac solution. However, to definitively confirm whether any of the deposit is in fact corrosion products, further chemical analysis was required (provided in Section 4.1.3). Even more conclusive in confirming whether corrosion had indeed occurred would be detection of any metal loss. Metal loss could not be detected visually from macro photography, so further examination at higher magnification of the coupons was conducted (Section 4.1.2) to visualize any metal loss.

#### 4.1.2 Stereo Microscopy

Stereo microscopy imaging allowed for examination of both the exposed and crevice surfaces; particularly in the crevice surface where metal loss was most likely to occur. Representative, higher magnification images were taken of one coupon from each of the twelve electrolyte-alloy combinations. As with the macro

photography, examination of the ends/edges of the coupons and inner circumference of the tubular coupons was not conducted.

Examination of the exposed surfaces revealed small tubercles on the aluminum alloys in all three electrolytes. A representative image of a tubercle, as well as the underlying pit, can be observed in Figure 4-5. No tubercles or pits were found on the exposed surfaces of the 304 stainless steel coupons in any of the three electrolytes. The presence of both tubercles and pits indicate that pitting had occurred on the exposed surfaces of the aluminum alloys in all three electrolytes.

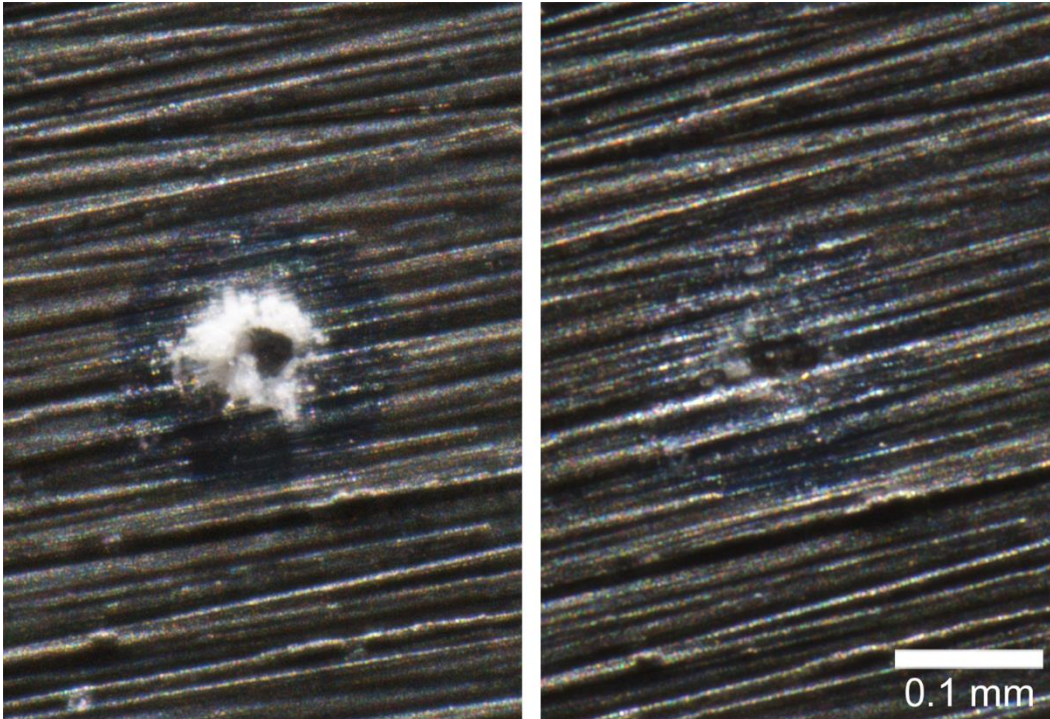


Figure 4-5: Representative image of a tubercle on a 5086/5083 coupon in DIUF, before (left photo) and after (right photo) removal. A small, round-shaped pit can be observed beneath the removed tubercle.

IGC was also observed on the Isopac-6061 combination, which is shown in Figure 4-6. No other electrolyte-alloy combination exhibited indications of IGC during *stereo microscopic examination*.

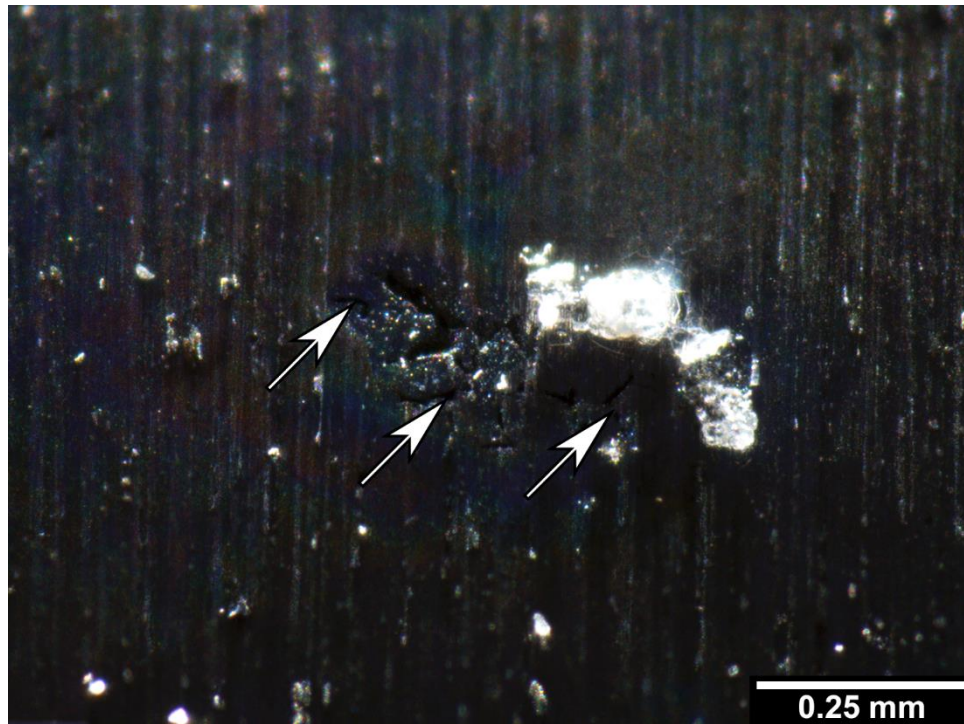


Figure 4-6: IGC (white arrows) identified on the surface of a 6061 coupon that was exposed to Isopac.

No further examination was performed on the exposed surfaces, or where tubercles were present. Although it is possible that the small tubercles would be covering pits of varying depth – which signifies varying amounts of metal loss – there is a higher likelihood of identifying metal loss in the crevice surface. Additionally, the observed IGC on the Isopac-6061 combination appeared only superficial in depth, and there were no signs that grains had “dropped out” of the coupon’s surface. Hence, for this study, further examination and images are only presented for the crevice surface.

Figures 4-7 to 4-12, 4-14 to 4-18, and 4-19 to 4-23 contain images of each of the four alloys that were exposed to Isopac, Alum, and DIUF, respectively. It should be noted that some of the images in Figures 4-7, 4-14, and 4-19 contain both exposed and crevice surfaces; therefore, the images are orientated so the crevice surface is above (top of the picture) the exposed surface (bottom of the picture). Also included in the figures are images of the coupon surfaces before immersion testing, after the testing and before cleaning, and after the testing and after cleaning.

As with the macro photography pictures, varying amounts of creamy white deposit appeared around and adjacent to the crevice surface on each of the coupons. Metal loss was identified on the aluminum alloy coupons in the “After Testing, After Cleaning” images. This metal loss appeared as pits – of various shapes and sizes – which resulted in discontinuities in the 240 grit machining marks. The pit openings were described using the guidelines provided in ASTM G46 [2]. The machining marks were oriented parallel to the tube coupons’ circumference and varied in orientation for the sheet coupons. Additionally, tarnish remained on the coupon surface, even after cleaning. No metal loss was observed on the 304 stainless steel coupons upon cleaning of their surfaces.

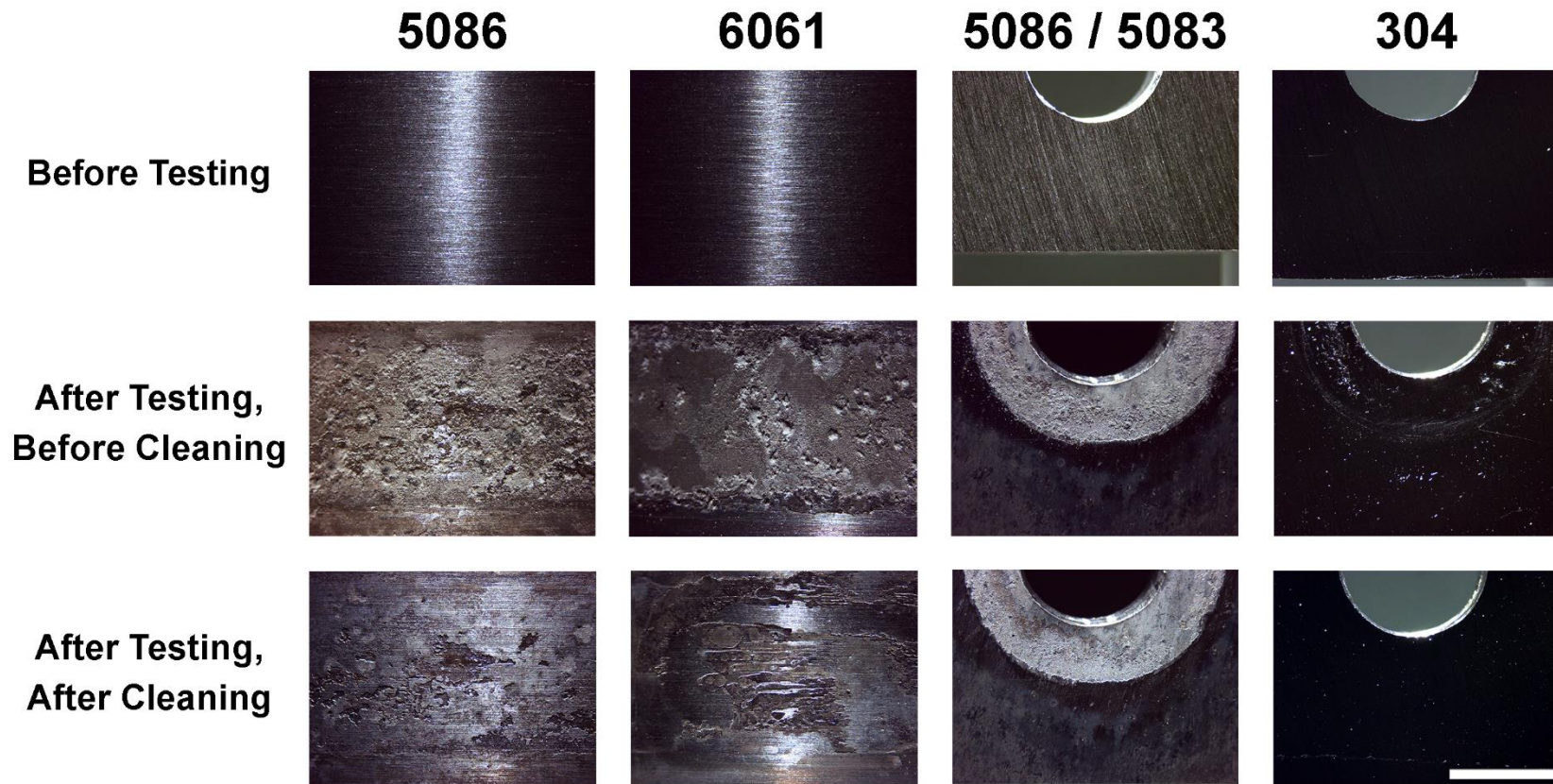


Figure 4-7: Composite images of four alloys before and after being immersed in Isopac solution, as well as after cleaning. Metal loss can be identified in the “After Testing, After Cleaning” images, and it appears as pits. Scale bar is 5 mm.

Higher magnification images of the coupon surfaces illustrates the morphology of the corrosion damage. Unless otherwise indicated, the following images were taken of the coupon surface before cleaning. Figures 4-8 and 4-9 show metal loss on the crevice surface of the 5086 alloy. The damage in Figure 4-8 looked somewhat round or elongated in shape – with no directionality. Meanwhile, the damage in Figure 4-9 was irregular in shape and appeared to have initiated in the grooves formed from the 240 grit surface finish. These oriented grooves appear to eventually consolidate into wide and shallow metal loss. Whichever way the metal loss initiates and subsequently propagates, this damage signifies that crevice corrosion had occurred.

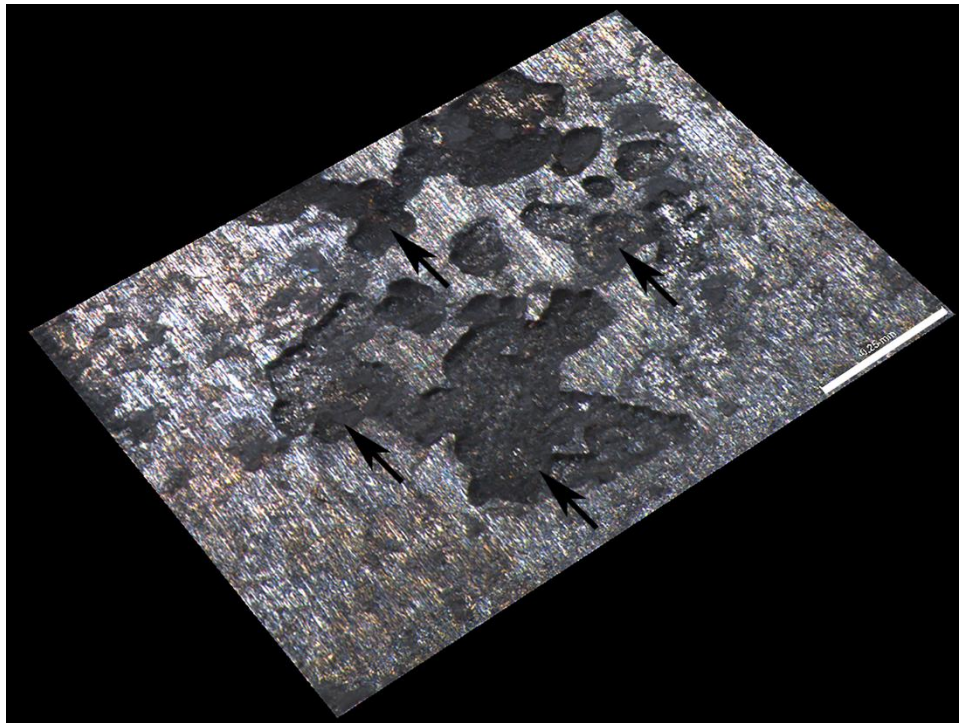


Figure 4-8: Corrosion (black arrows) on the crevice surface of 5086 alloy in Isopac solution. This metal loss signifies that crevice corrosion has occurred. Arrows are also oriented parallel to the grinding marks. Scale bar is 0.25 mm.

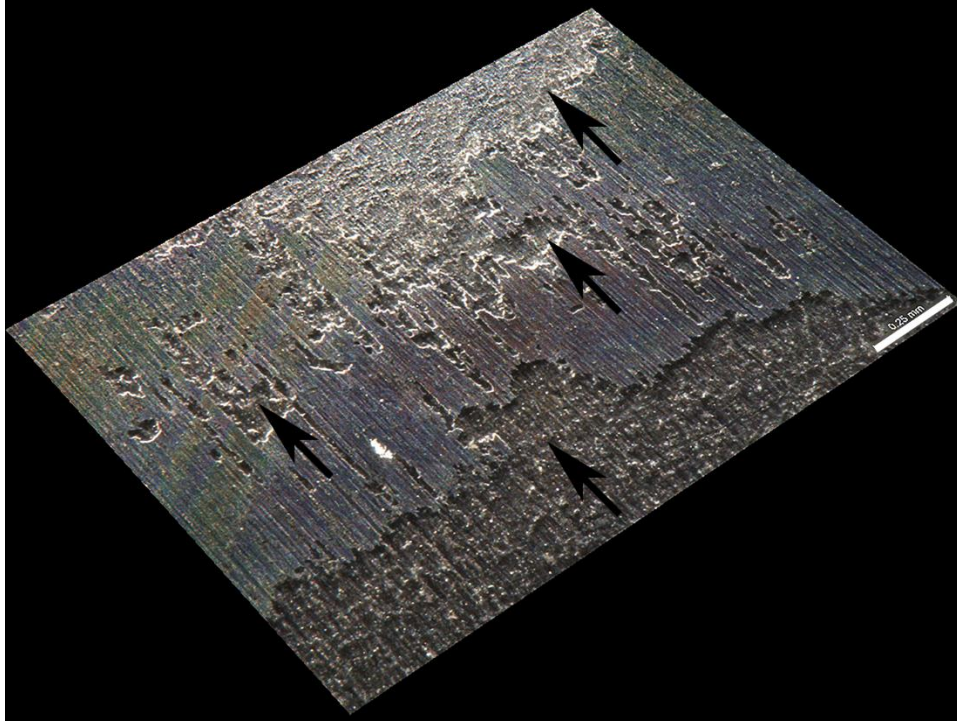


Figure 4-9: Additional image of corrosion (black arrows) on the crevice surface of 5086 alloy in Isopac solution. Again, crevice corrosion has occurred. Arrows are also oriented parallel to the grinding marks. Scale bar is 0.25 mm.

Varying amounts of corrosion damage can also be seen on the 6061 (Figure 4-10) and 5086/5083 (Figure 4-11) crevice surfaces. The metal loss appeared to be more wide and shallow, with no preferential orientation. Again, the presence of metal loss indicates that crevice corrosion had occurred. Meanwhile, no corrosion damage could be identified on the crevice surface of the 304 alloy (Figure 4-12). Deposit in and adjacent to the crevice surface can be observed in the figure; however, at higher magnifications, metal loss could not be observed.

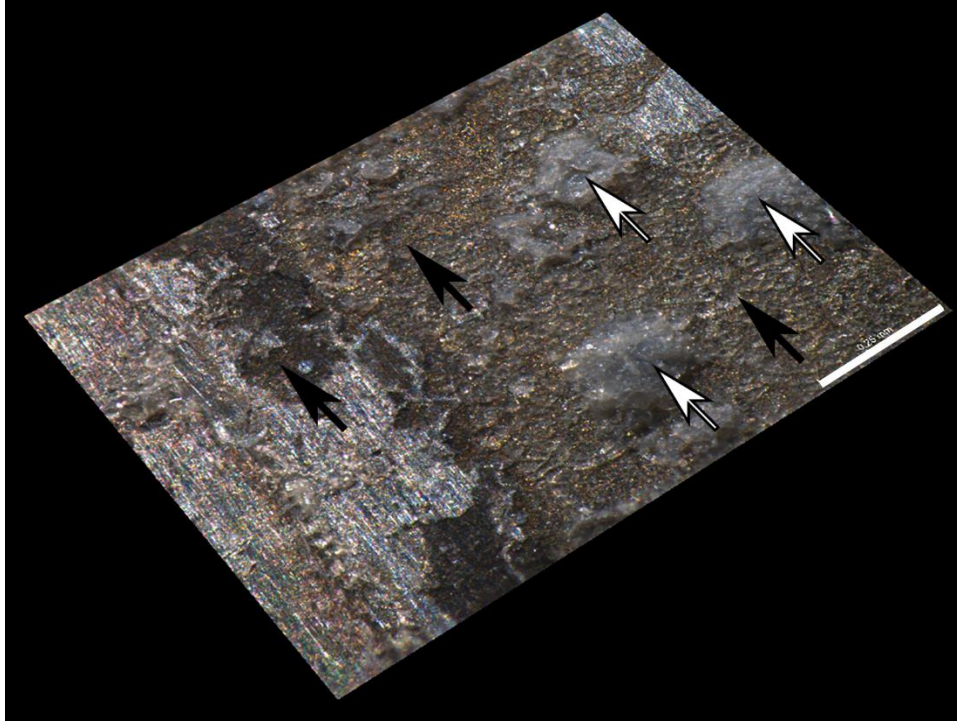


Figure 4-10: Corrosion (black arrows) on the crevice surface of 6061 alloy in Isopac solution. Deposit is also observed on the surface (white arrows). Arrows are also oriented parallel to the grinding marks. Scale bar is 0.25 mm.



Figure 4-11: 5086/5083 alloy in Isopac solution; both of the exposed and crevice surfaces (top and bottom of picture, respectively). Deposit (white arrows) and corrosion damage (black arrows) is also observed.

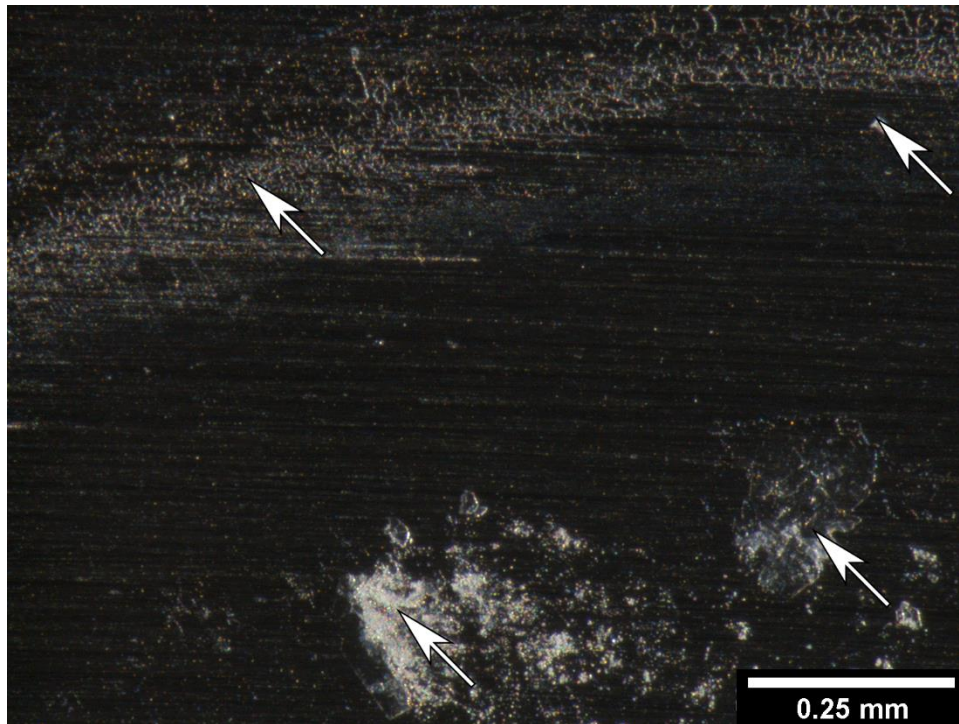


Figure 4-12: 304 alloy in Isopac solution; both of the exposed (top of picture) and crevice (bottom of picture) surfaces. Deposit is also observed on the surfaces (white arrows).

Gouging marks (Figure 4-13) were also observed on the 5086 and 6061 surfaces; in all three electrolytes. It is believed that these marks were formed during the machining of the tube coupons, and were either caused by chattering of the lathe or by larger SiC grit particles catching on the surface. Additionally, these marks may act as anodic sites (such as crevices or due to large amounts of plastic deformation with high dislocation density), which could result in preferential, localized corrosion. Though the occurrence of such gouging was not common, care should be taken when using a lathe to prepare the surfaces of the coupons for testing.

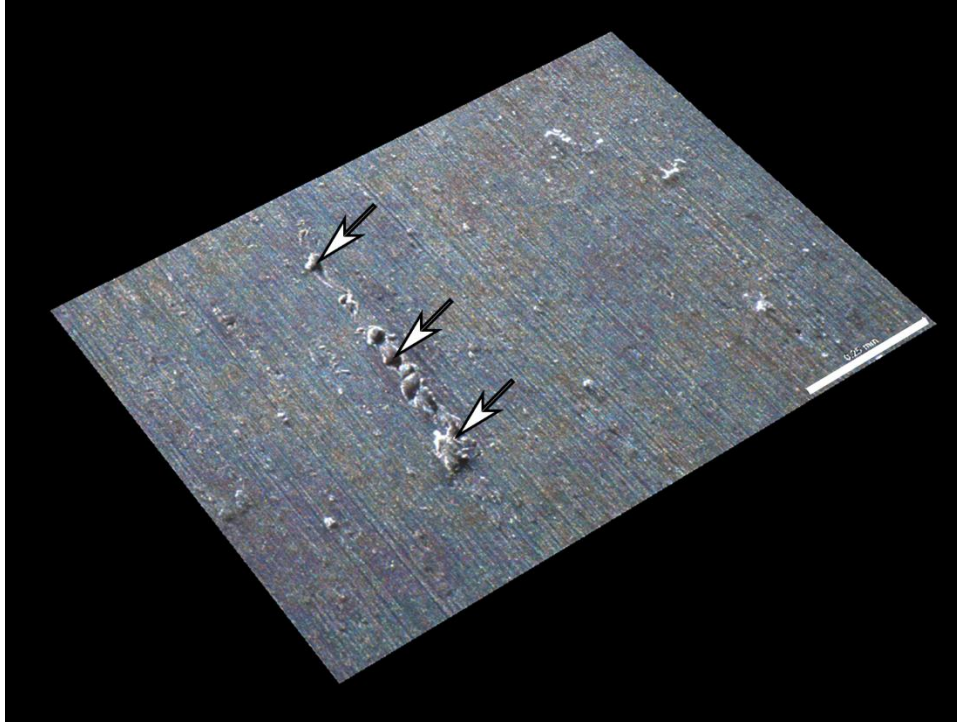


Figure 4-13: Representative image of gouging (white arrows) on the 5086 and 6061 alloy coupons, in all electrolytes, due to surface preparation using a lathe. Scale bar is 0.25 mm.

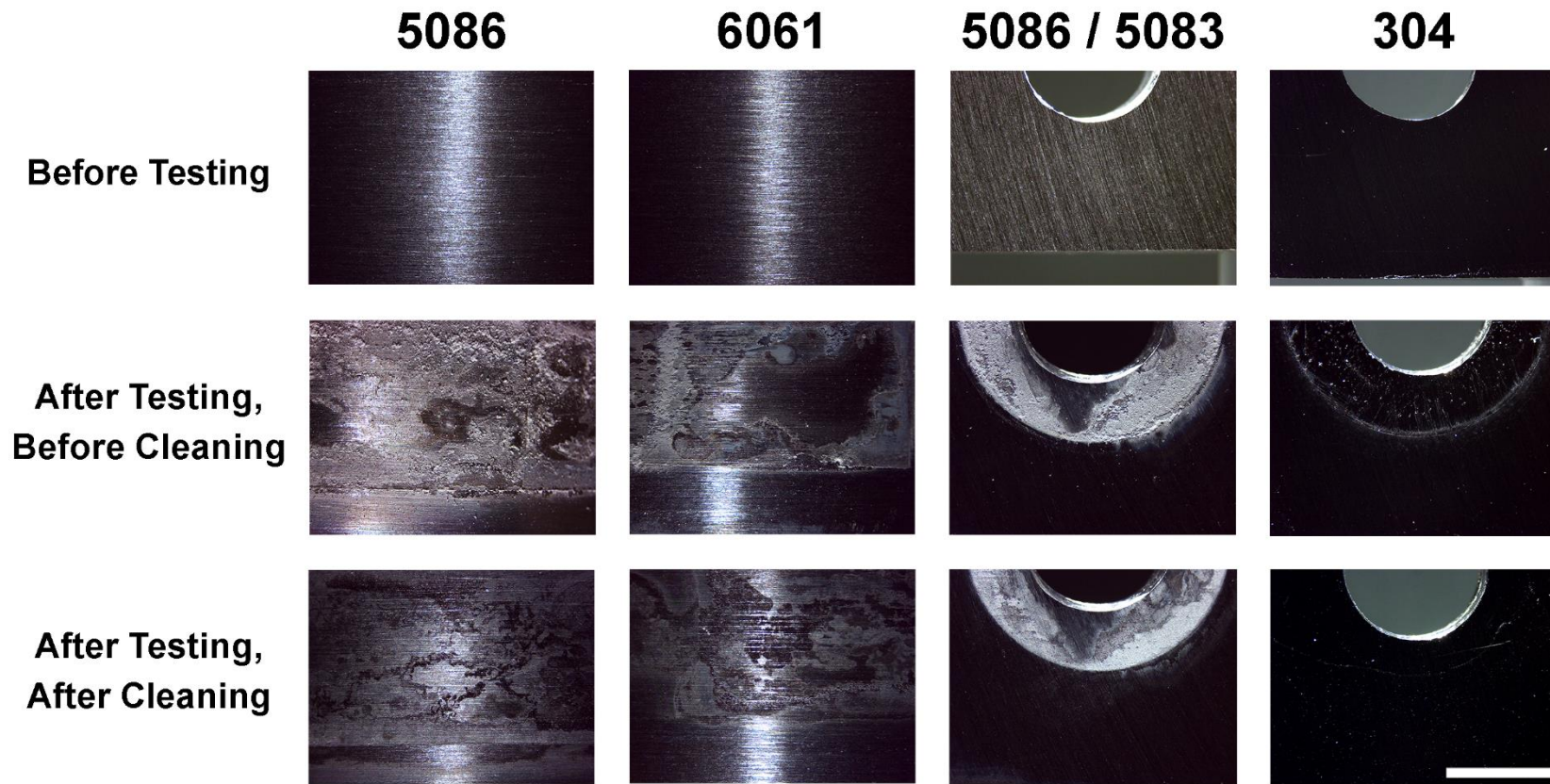


Figure 4-14: Composite images of alloys before and after being immersed in Alum solution, as well as after cleaning. Metal loss can be identified in the “After Testing, After Cleaning” images, and it appears as pits. Scale bar is 5 mm.

Small amounts of corrosion damage and deposit were observed on the crevice surfaces of the 5086 (Figure 4-15), 6061 (Figure 4-16), and 5086/5083 (Figure 4-17) alloys, which were exposed to Alum. Again, all images were taken after testing but before cleaning. The morphology of the damage appeared to vary between the alloys, which include round, elongated, and irregular pit openings. Nevertheless, crevice corrosion occurred on all three aluminum alloys. Meanwhile, no corrosion damage was identified on the crevice surface of the 304 alloy (Figure 4-18). As with the 304 coupons in Isopac solution, deposit was observed in Figure 4-18; however, at higher magnifications, metal loss could not be identified.

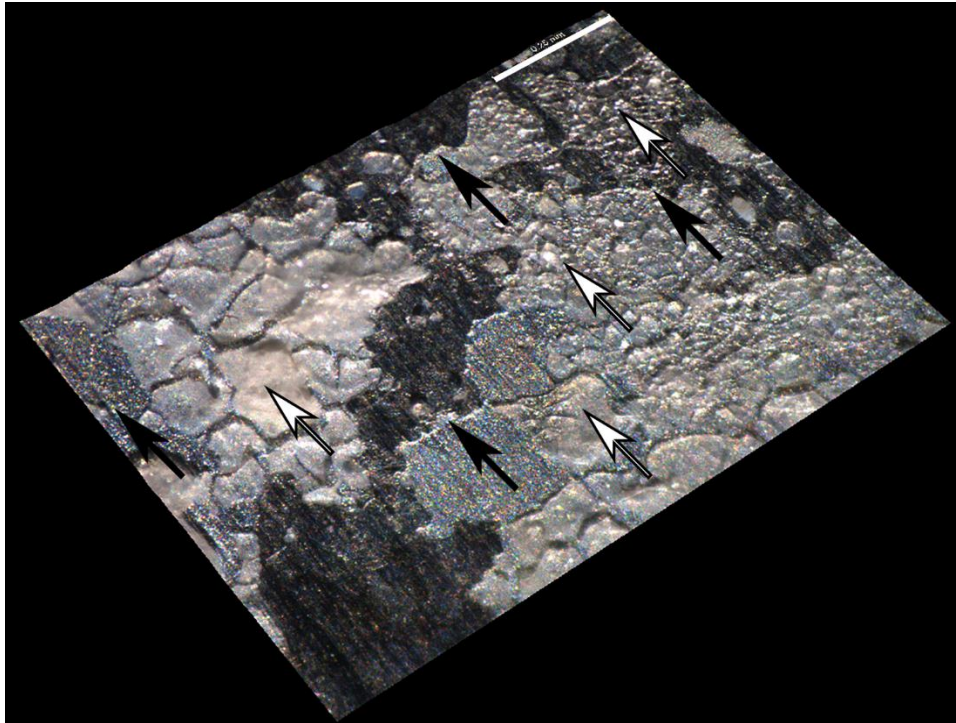


Figure 4-15: Corrosion damage (black arrows) and deposit (white arrows) on the 5086 alloy crevice surface in Alum solution. Arrows are also oriented parallel to the grinding marks. Scale bar is 0.25 mm.

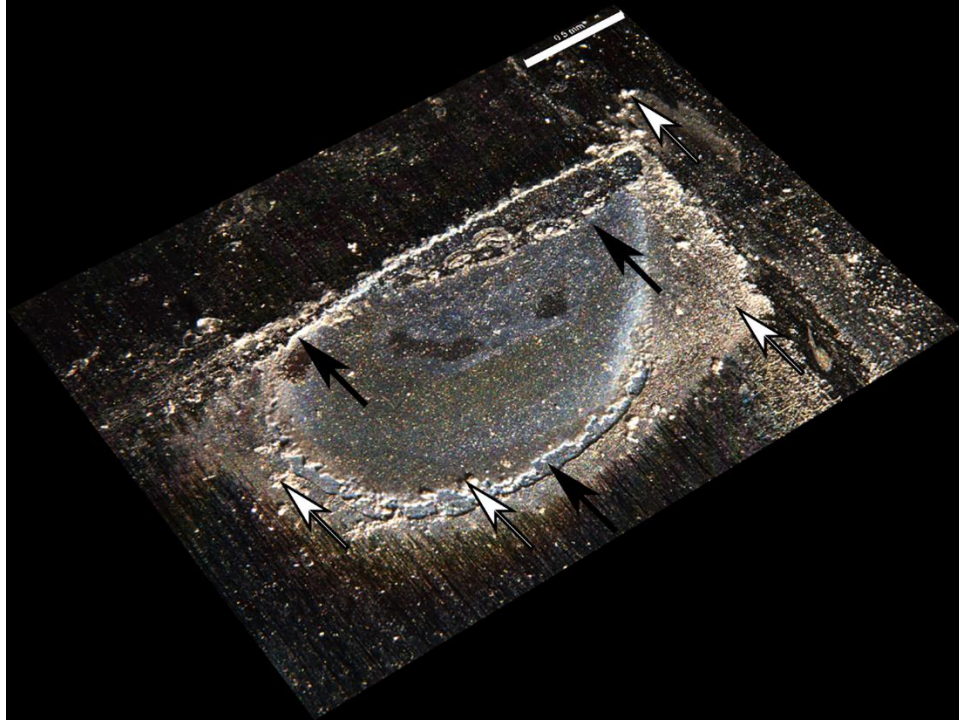


Figure 4-16: Corrosion damage (black arrows) and deposit (white arrows) on the 6061 alloy crevice surface in Alum solution. Arrows are also oriented parallel to the grinding marks. Scale bar is 0.5 mm.

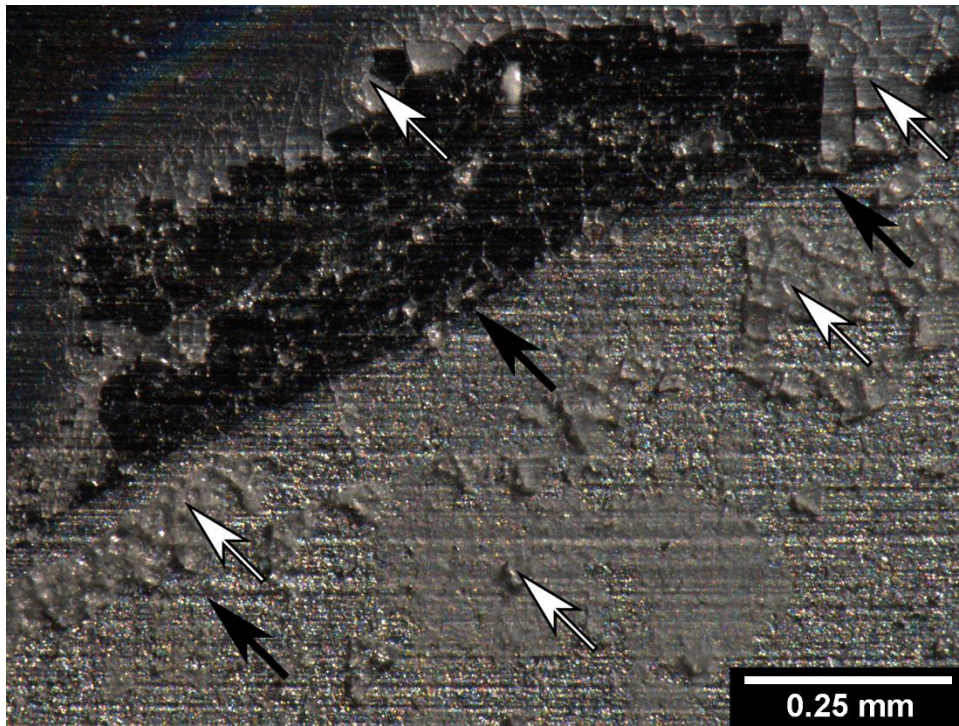


Figure 4-17: Corrosion damage (black arrows) and deposit (white arrows) on the 5086/5083 alloy crevice surface (bottom of picture) in Alum solution. Deposit (top white arrows) can also be observed on the exposed surface (top of picture).

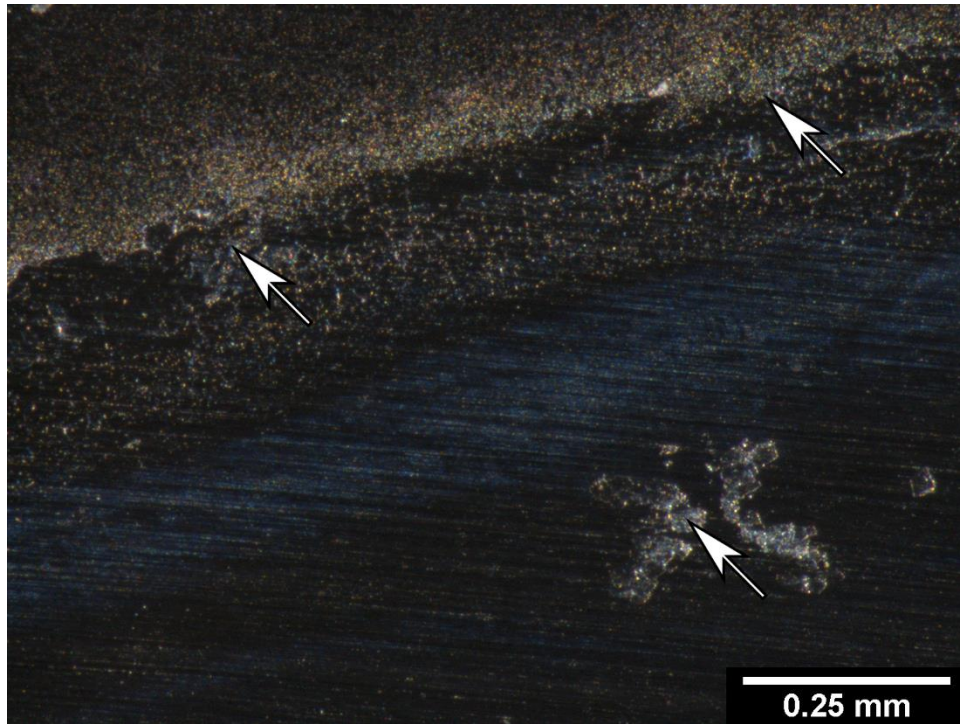


Figure 4-18: 304 alloy in Alum solution; both of the exposed (top of picture) and crevice (bottom of picture) surfaces. Deposit is also observed on both surfaces (white arrows).

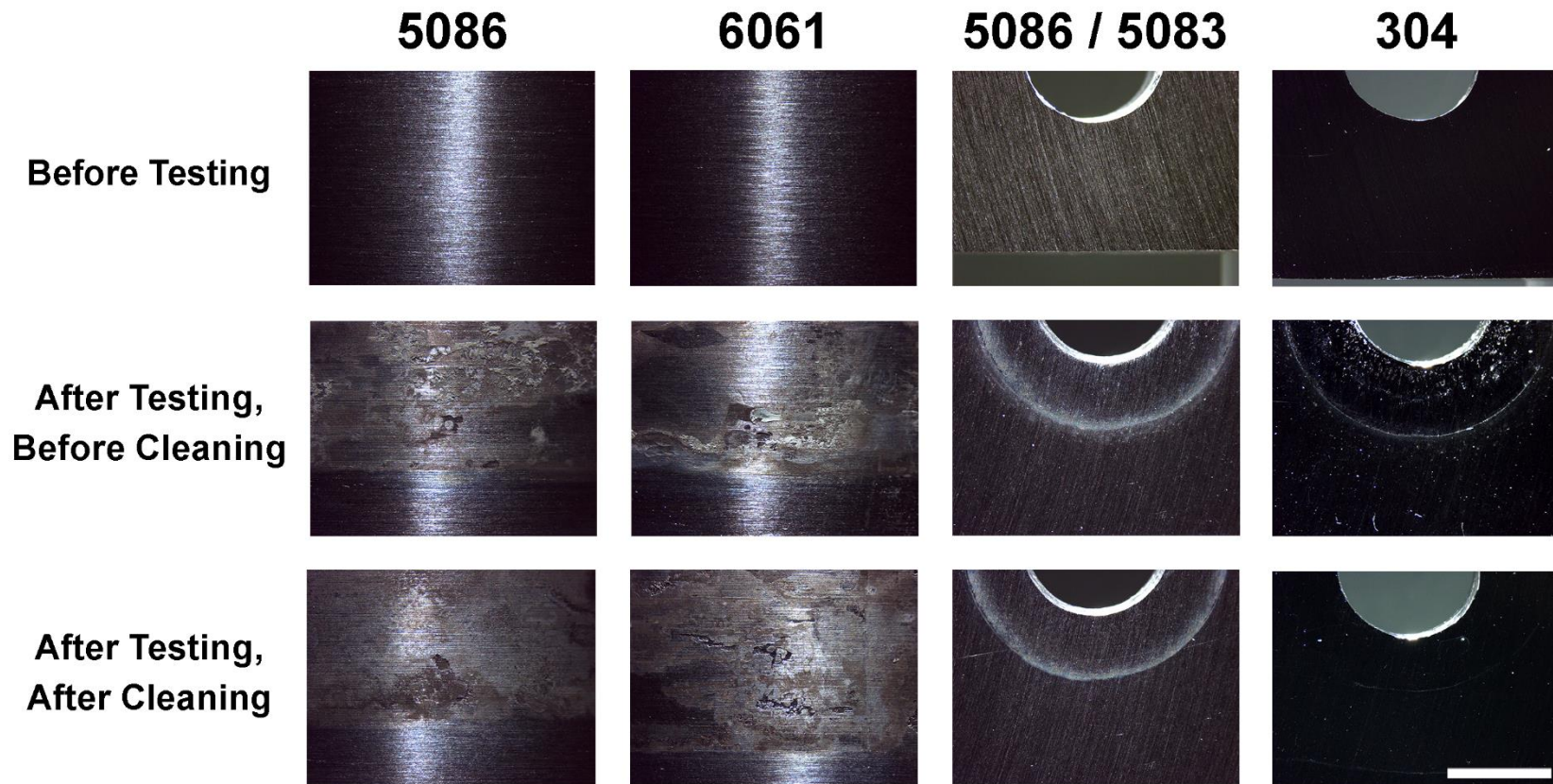


Figure 4-19: Composite images of alloys before and after being immersed in DIUF, as well as after cleaning. Metal loss can be identified in the “After Testing, After Cleaning” images, and it appears as pits. Scale bar is 5 mm.

Similarly to the alloys in the coagulant solutions, trace amounts of corrosion damage and deposit were observed on the crevice surfaces of the 5086 (Figure 4-20), 6061 (Figure 4-21), and 5086/5083 (Figure 4-22) alloys, which were exposed to DIUF. Again, all images were taken after testing but before cleaning. The morphology of the damage appeared to vary between the alloys, which include round, elongated, and irregular pit openings. Nevertheless, crevice corrosion occurred on all three aluminum alloys. Meanwhile, no corrosion damage could be identified on the crevice surface of the 304 alloy (Figure 4-23). As with the 304 coupons in the coagulant solutions, deposit can be observed in Figure 4-23; however, at higher magnifications, metal loss could not be identified.



Figure 4-20: Corrosion damage (black arrows) and deposit (white arrows) on the 5086 alloy crevice surface in DIUF.



Figure 4-21: Corrosion damage (black arrows) and deposit (white arrows) on the 6061 alloy crevice surface in DIUF.

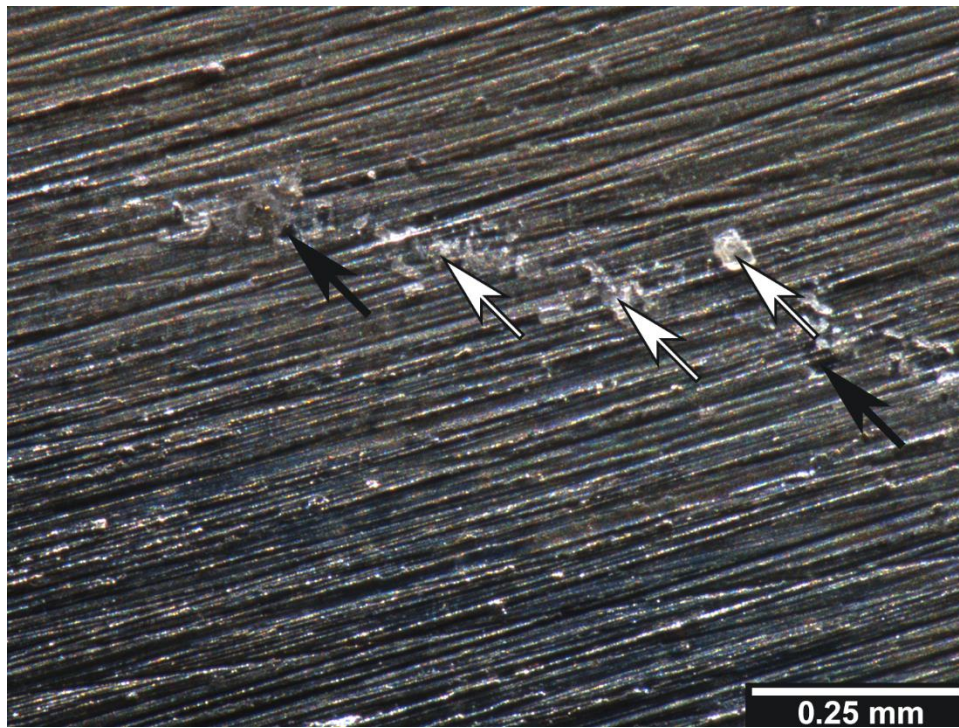


Figure 4-22: Corrosion damage (black arrows) and deposit (white arrows) on the 5086/5083 alloy crevice surface in DIUF. Above the deposit (top of image) is the exposed surface, while below the deposit (bottom of image) is the crevice surface.

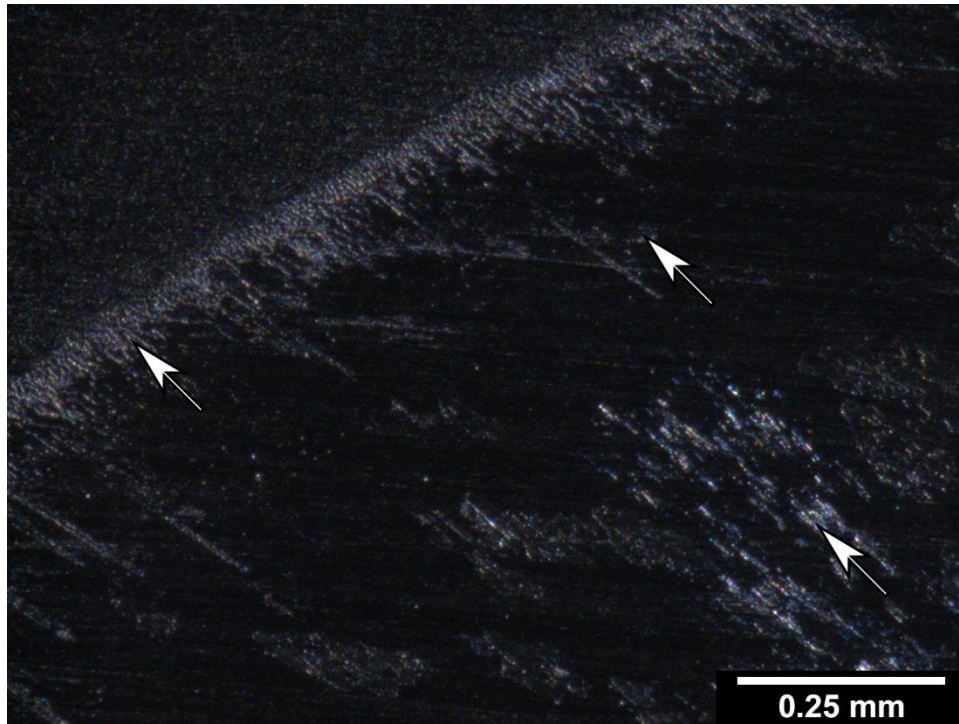


Figure 4-23: 304 alloy in Alum solution; both of the exposed (top of picture) and crevice (bottom of picture) surfaces. Deposit is also observed on the surface (white arrows). Scale bar is 0.25 mm.

The “After Testing, After Cleaning” stereo micrographs from Figures 4-7, 4-14, and 4-19 were organized based off their respective electrolyte-alloy combination. These images are presented below in Figure 4-24. At this magnification ( $\sim 8\times$ ), the shape of the pit openings, on the crevice surfaces, appear irregular and elongated for both the 5086 and 6061 coupons in all three electrolytes. The corrosion damage on the 5086/5083 coupons in both Isopac and Alum look more wide and shallow, and irregular in shape. Conversely, at this magnification, it is difficult to identify the morphology of the corrosion damage on the 5086/5083 coupons in DIUF. At higher magnification, the small pit openings are round in shape (as shown in Figure 4-22). Ultimately, crevice corrosion was identified on all of the aluminum alloys tested in the Isopac, Alum, and DIUF electrolytes. Moreover, the crevice corrosion appeared more pronounced on the aluminum alloys exposed to Isopac, followed by Alum then DIUF. Regarding the depth of metal loss, the crevice corrosion on all of the aluminum alloys in the

aforementioned electrolytes appeared to be superficial. This assessment in depth is only qualitative; no depth measurements were performed in this study.

As opposed to the three aluminum alloys, no crevice corrosion was observed on the 304 stainless steel in any of the above-mentioned electrolytes. Deposit was identified on the stainless steel in each of the three electrolytes; however, no metal loss could be found – even during inspection at higher magnifications.

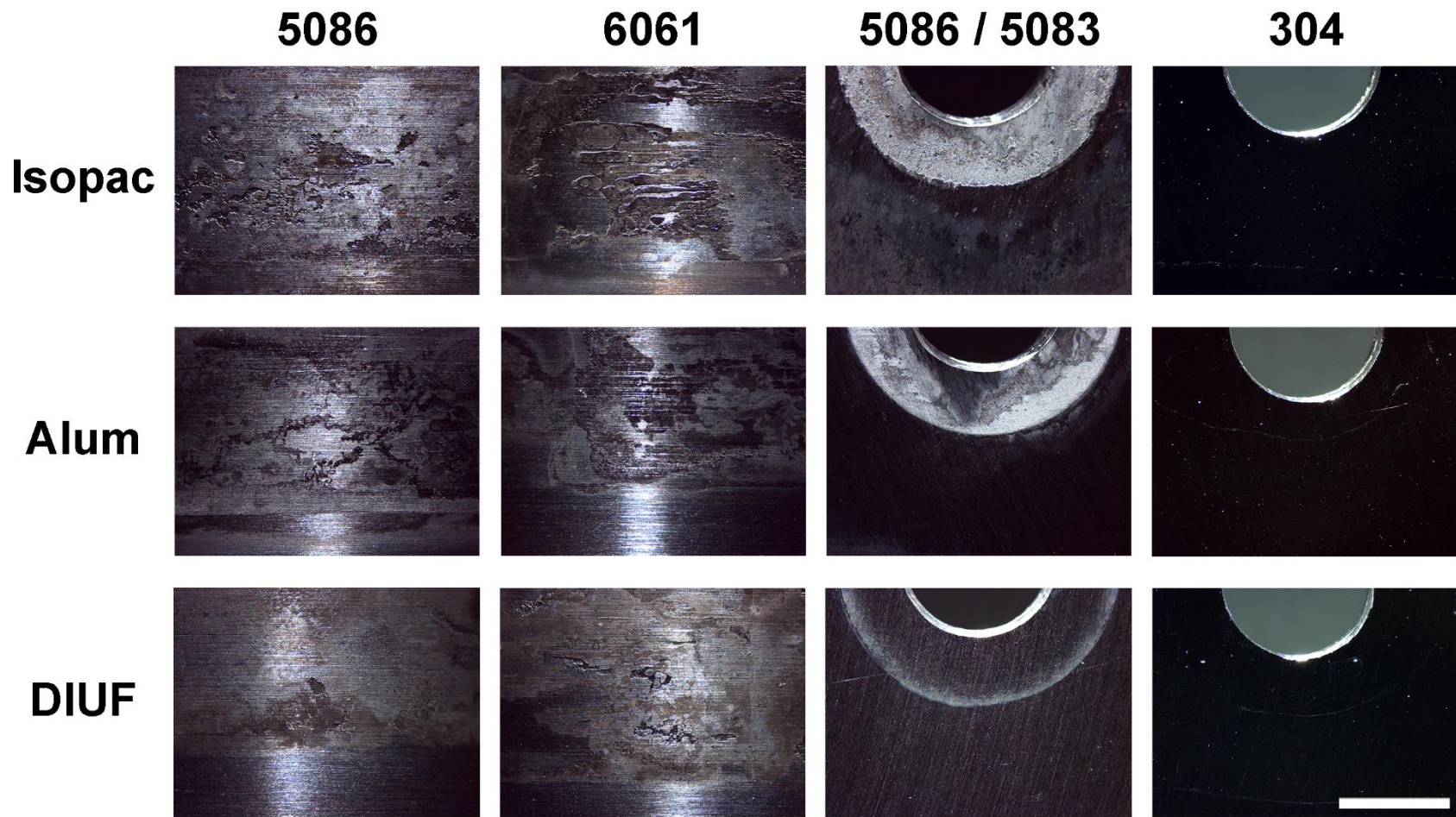


Figure 4-24: Composite images of all twelve electrolyte-alloy combinations after immersion and cleaning. Scale bar is 5 mm.

### 4.1.3 Deposit Characterization

As mentioned in Chapter 3, deposit was removed from the crevice surface of each electrolyte-alloy combination in order to determine its chemical composition and structure. Due to the small amounts of deposit present on the coupons, one characterization technique (namely: EDX, XRD, or FTIR) was performed on only one of the three coupons, of the twelve electrolyte-alloy combinations. With triplicate coupons of the same alloy being exposed to the same electrolyte, it was assumed that the composition and structure of the three coupons' deposits are the same. Only deposit in the crevice surface was tested.

#### *4.1.3.1 Energy Dispersive X-ray (EDX) Spectroscopy*

The purpose of the EDX examination was to determine the elemental composition of the deposit formed on the corrosion coupons, post immersion testing. Figure 4-25 is a representative, backscattered electron (BSE) image of deposit collected from a tube coupon (either 5086 or 6061 alloys), which was examined while being mounted on a pin and carbon tape. Deposit in Figure 4-25 is from the Isopac-5086 combination. Conversely, Figure 4-26 is a representative, BSE image of deposit that was directly examined on the surface of a sheet coupon (either 5086/5083 or 304 alloys). IGC can also be identified on the coupon surface – specifically the crevice surface – in Figure 4-26. The electrolyte-alloy combination presented in Figure 4-26 is Alum-5086/5083. From a qualitative assessment, the IGC appeared to be superficial; no attempt was made to quantify the depth. Furthermore, no grains appeared to have “dropped out” of the coupon's surface. Inspection of the remaining sheet coupon, electrolyte-alloy combinations revealed no signs of IGC. Moreover, no SEM imaging (either secondary electron (SE) or BSE) was performed on any of the tube coupons.

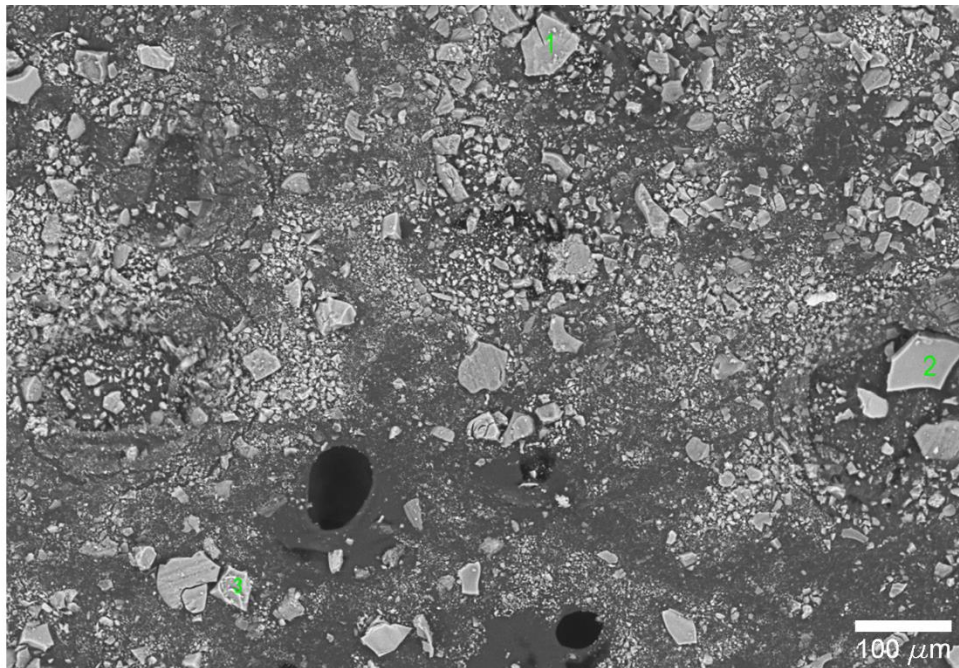


Figure 4-25: Representative BSE image of deposit collected from tube coupons. The three green numbers cover the locations where EDX data was acquired. Image taken at a 20 kV accelerating voltage and a 7 mm working distance.

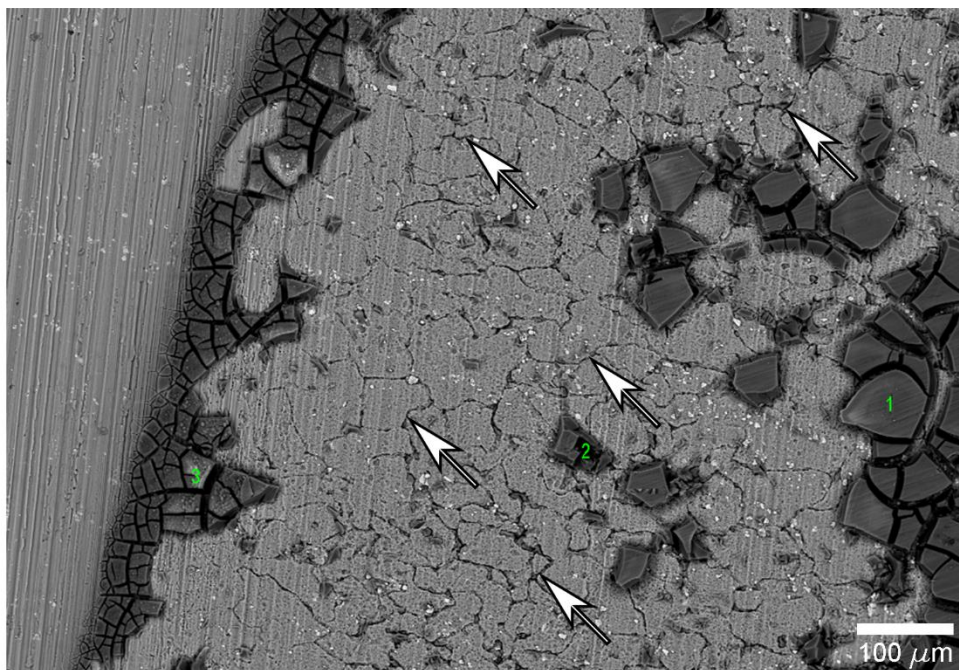


Figure 4-26: Representative BSE image of deposit collected from sheet coupons. The three green numbers cover the locations where EDX data was acquired. IGC (white arrows) can be identified on the crevice surface (right side of image; exposed surface is on the left side of the image, beyond the deposit). Image taken at a 20 kV accelerating voltage and a 11 mm working distance.

The composition of the deposits from the four alloys tested in Isopac, Alum, and DIUF solutions are listed in Tables 4-2, 4-3, and 4-4, respectively. It should be noted that the compositional data collected from EDX is to be regarded as qualitative to semi-quantitative (at best) in nature. Moreover, for the deposits examined directly on the sheet coupons (5086/5083 and 304 alloys), the carbon weight percentage values were kept since these deposits were not carbon coated. It is emphasized that even though carbon values were kept, the potentially numerous sources of carbon and its relatively low atomic weight make the measured values only qualitative. Conversely, the carbon weight percentage values were removed from the deposits of the tube coupons (5086 and 6061 alloys).

Table 4-2: Representative elemental data collected from deposit removed or found on each of the four alloys tested in Isopac solution.

Alloy	Pt	Element [Normalized Weight %]										
		Al	O	Si	C	S	Cl	Mg	Fe	Cr	Ni	N
5086	1	37.0	53.2				8.9	0.8				
	2	32.0	57.4				7.8	2.8				
	3	34.8	55.5				9.0	0.7				
6061	1	31.7	54.8				13.5					
	2	45.8	53.7					0.5				
	3	27.5	54.3				18.2					
5086 / 5083	1	30.5	42.4		17.7		8.5	0.8				
	2	46.7	45.2		6.1		0.7	1.3				
	3	52.0	39.6		6.6			1.8				
304	1	0.2	7.2	0.2	57.9				21.3	5.6	2.2	5.4
	2		6.0	0.2	54.0				25.5	6.4	2.5	5.3
	3		3.4	0.3	32.8				43.8	11.1	4.9	3.8

Table 4-3: Representative elemental data collected from deposit removed or found on each of the four alloys tested in Alum solution.

Alloy	Pt	Element [Normalized Weight %]										
		Al	O	Si	C	S	Cl	Mg	Fe	Cr	Ni	N
5086	1	23.7	64.4			12.0						
	2	26.2	62.6			11.2						
	3	27.4	61.6			11.1						
6061	1	26.7	61.2	0.9		11.2						
	2	28.6	61.0	1.9		8.6						
	3	30.1	59.1	1.2		9.6						
5086 / 5083	1	21.2	64.3		2.9	11.6						
	2	6.3	17.5		65.8	2.9						7.6
	3	25.4	65.3			9.3						
304	1		7.0	0.2	59.6				19.8	5.1	2.1	6.2
	2		4.9	0.3	45.3				33.1	8.2	3.6	4.7
	3		4.3	0.3	40.5				37.5	9.4	4.0	4.1

Table 4-4: Representative elemental data collected from deposit removed or found on each of the four alloys tested in DIUF.

Alloy	Pt	Element [Normalized Weight %]										
		Al	O	Si	C	S	Cl	Mg	Fe	Cr	Ni	N
5086	1	39.5	60.0	0.5								
	2	88.7	7.3					4.0				
	3	32.6	62.6	4.1				0.7				
6061	1	37.2	62.8									
	2	66.0	32.8	0.6				0.6				
	3	41.1	57.5	1.2				0.2				
5086 / 5083	1	24.7	5.1		63.6			1.0				5.6
	2	24.4	5.3		63.6			1.1				5.6
	3	27.7	4.6		61.4			1.2				5.2
304	1		5.2	0.2	51.0				28.5	7.3	2.8	5.0
	2		5.9	0.1	59.2				21.5	5.6	2.1	5.6
	3		4.1	0.3	37.5				39.9	9.9	4.5	3.9

Large quantities of aluminum and oxygen were present (in varying stoichiometric amounts), in all deposits examined from nearly all of the aluminum alloy coupons in each of the three electrolytes. The DIUF-5086/5083 combination had an especially low amount of oxygen present in its examined deposit. The presence of these elements is consistent with aluminum corrosion products. Since hydrogen is below the detectability of the EDX detector (beryllium – atomic number of 4 – is the lower limit of detectability), it cannot be determined whether the deposit is hydrated or not. Next, the presence of either magnesium or silicon in the deposits can be credited to the fact that both elements are alloying elements in

the three aluminum alloys tested. Also measured in some of the deposits formed in the Isopac and Alum solutions are chlorine and sulphur. The occurrence of these elements can be attributed to their existence in the Isopac and Alum solutions, with chlorine and sulphur only being found in deposits from Isopac and Alum solutions, respectively. Additionally, neither chlorine nor sulphur are present in the deposits formed on the aluminum alloy coupons in DIUF. Finally, the presence of carbon in the 5086/5083 sheet coupon deposit is believed to have occurred due to the nylon washers, or – in the case of the 5086/5083 alloy in Isopac solution – Isopac itself. The belief that nylon transfer had occurred on the 5086/5083 coupons is further substantiated due to the identification of nitrogen in several locations of the deposits tested. Nylon (also known as polyamide) contains amines, which are organic functional groups that contain a nitrogen atom [3]. Moreover, the low and high amounts of oxygen and carbon, respectively, measured in the DIUF-5086/5083 combination deposit suggests that nylon is present instead of aluminum corrosion products.

Chromium, nickel, and iron were all found in the deposits of the 304 stainless steel alloy, in each of the three electrolytes; however, such presence is likely due to technique, not corrosion. The presence of these elements might suggest that corrosion occurred; however, from the stereo microscopy images, no metal loss could be identified. Moreover, there are very small amounts of oxygen present in the deposits, which doesn't support the existence of chromium, nickel, or iron oxide (or hydroxide) corrosion products. Furthermore, the EDX data was collected from deposits which were analyzed *directly* on the surface of the coupon. Therefore, detection of metals in the deposit is due to the fact that the interaction volume during EDX penetrated through the deposit into the metal immediately below; indicating the presence of the 304 alloying elements (including silicon). Due to the high amount of carbon, and varying amounts of nitrogen, the deposits on the 304 coupons are believed to have been caused by nylon transfer during installation and removal of the nylon washers (i.e., crevice formers). This transfer of material may also have occurred on the 5086/5083 coupons (as shown by the presence of

carbon and nitrogen in the deposit formed in the DIUF solution). Furthermore, this material transfer suggests that the nylon washers on the sheet coupons were more tightly joined to the coupons than the nylon hose clamps. The torque applied to the sheet coupon crevice formers was quantified to 1 N•m, whereas the force (and subsequent stress) could not be quantified on the tube coupons.

#### *4.1.3.2 X-ray Diffraction (XRD)*

XRD was performed on the coupon deposits from each electrolyte-alloy combination in order to identify any known, crystalline corrosion compounds. The resulting patterns from the testing are presented below in Figure 4-27. Due to the trace amounts of deposit found on all of the 304 coupons (in all three electrolytes) as well as the 5086/5083 alloy coupons in DIUF, no testing could be performed on those electrolyte-alloy combinations.

All XRD patterns did not exhibit any combination of peaks of known crystalline compounds. There appears to be some noise in the patterns (in the form of many small peaks), as well as a broad peak between 10 and 15°. This broad peak corresponds to the quartz of the zero background slide used for holding the deposit specimen during testing. The lack of any crystalline compounds suggests that there are only amorphous compounds present in the deposit, or there is not enough crystalline material to meet the minimum volume percent required for detection. Further analysis of the deposits using FTIR was performed to substantiate the former.

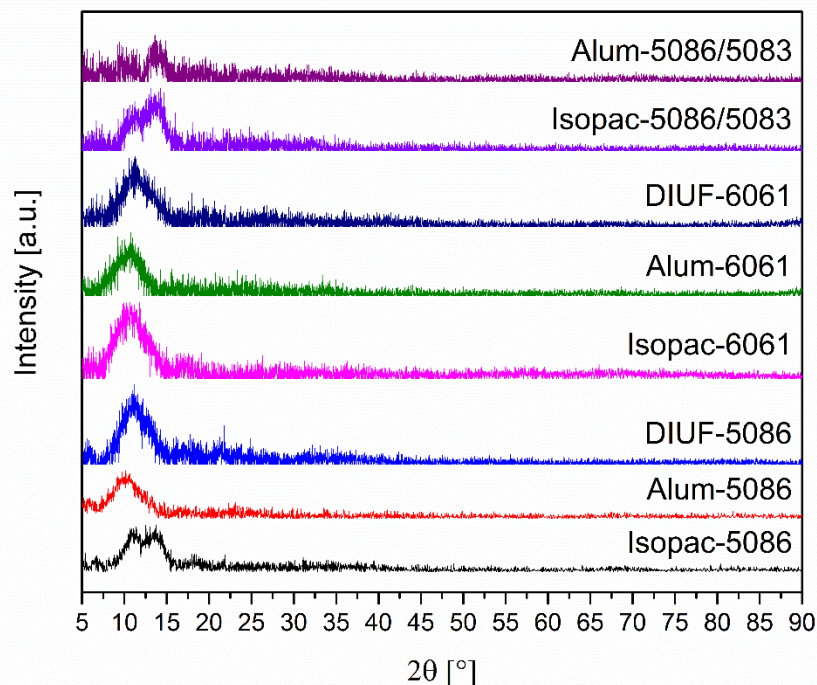


Figure 4-27: Representative XRD patterns of deposit collected from eight of the twelve electrolyte-alloy combinations.

#### 4.1.3.3 Fourier Transform Infrared (FTIR) Spectroscopy

FTIR was performed on the coupon deposits from each electrolyte-alloy combination in order to identify any known, amorphous corrosion compounds. The collected spectra of all three aluminum alloys are presented in Figures 4-28 and 4-29 for Isopac and Alum solutions, respectively. The characteristic peaks of each spectrum were compared to peaks of the following oxides and hydroxides (whose data can be found in Appendix E): gibbsite, bayerite, boehmite, diaspore, and corundum.

There are similarities between the spectra collected from all three aluminum alloys in both Isopac and Alum. Strong peaks around  $3500\text{ cm}^{-1}$  and  $1000\text{ cm}^{-1}$  suggest the presence of either bayerite or gibbsite [4–6]. Moreover, the peaks between  $1500$  and  $1700\text{ cm}^{-1}$  indicate either the presence of aluminum oxide ( $\text{Al}_2\text{O}_3$ ) [6] or water (through a peak produced by HOH bending) [5]. There are, however, some issues with the aforementioned assessments of the collected

characteristic peaks. First, there consistently appears to be a mismatch with either the number of characteristic peaks present, or the location of the peaks, between the collected deposit spectra and the peaks listed in the Appendix E literature. (On another note, there are discrepancies in the characteristic peak data, between the references provide in Appendix E.) Normally, this mismatch in data would suggest that any of the previously listed oxides and hydroxides are not present in the deposits. However, the deposits on the aluminum alloy coupons were formed in solutions that were not solely comprised of water, but also small amounts of coagulant. The presence of either Isopac or Alum (as confirmed by the presence of either chlorine or sulphur via EDX) could alter the chemistry and structure of the deposit, leading to changes in position of the characteristic peaks of the oxides and hydroxides. Additionally, the presence of these elements may also lead to an increase in the number of characteristic peaks, due to the increase in number of potential bond wavenumbers between the various elements.

Second, because of the broad (wide) peaks in the collected spectra, it makes matching the identified characteristic peak wavenumbers to compound data in literature more difficult. Moreover, peak wavenumbers in the fingerprint region (wavenumber less than  $1500\text{ cm}^{-1}$ ) are more difficult to discern and match to values in literature [7].

Third, and finally, additional discrepancies between the collected and referenced spectra are due to how FTIR is used to identify compounds. The potential presence of other elements in the deposits makes it incredibly difficult to identify compounds of interest, by solely comparing the collected deposit spectra to select, pure compound spectra. Therefore, it is entirely possible that amorphous aluminum oxides and hydroxides are present in the deposits formed on the aluminum alloys in either Isopac or Alum solutions. Furthermore, FTIR may not be the best method to determine the presence of amorphous corrosion products.

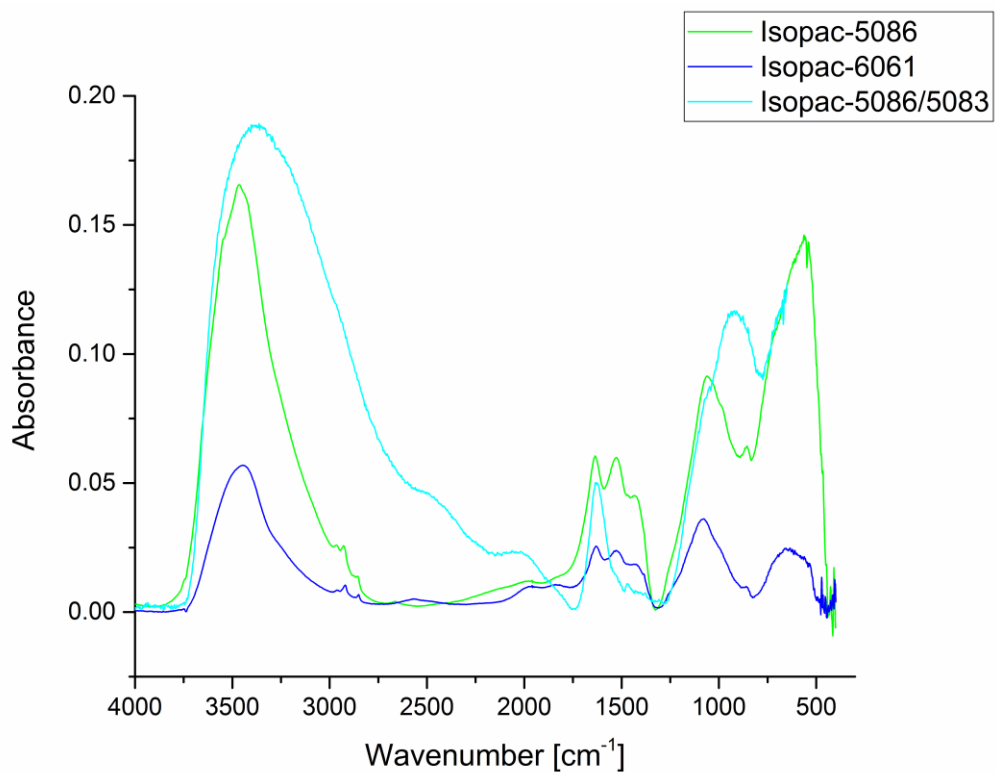


Figure 4-28: Representative FTIR spectra of 5086, 6061, and 5086/5083 alloys in Isopac solution.

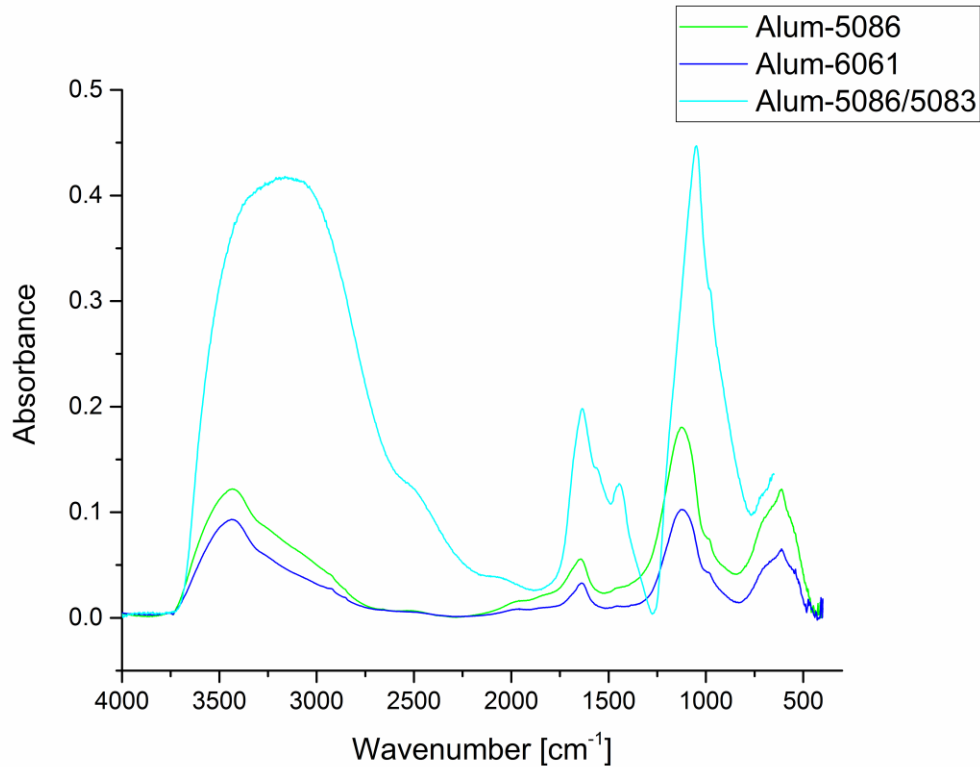


Figure 4-29: Representative FTIR spectra of 5086, 6061, and 5086/5083 alloys in Alum solution.

The collected spectra of the deposits from 5086 and 6061 alloys in DIUF are displayed in Figure 4-30. As with the aluminum alloys in coagulant solutions, strong peaks identified around  $3500\text{ cm}^{-1}$  and  $1000\text{ cm}^{-1}$  suggest the presence of either bayerite or gibbsite [4–6]. The peaks between  $1500$  and  $1700\text{ cm}^{-1}$  also indicate either the presence of aluminum oxide ( $\text{Al}_2\text{O}_3$ ) [6] or water (through a peak produced by HOH bending) [5]. However, there are discrepancies between the collected spectra and the peak wavenumber data provided in Appendix E. Again, it is entirely possible that amorphous aluminum oxides and hydroxides are present in the deposits formed on either the 5086 or 6061 alloys; however, it cannot be definitively confirmed.

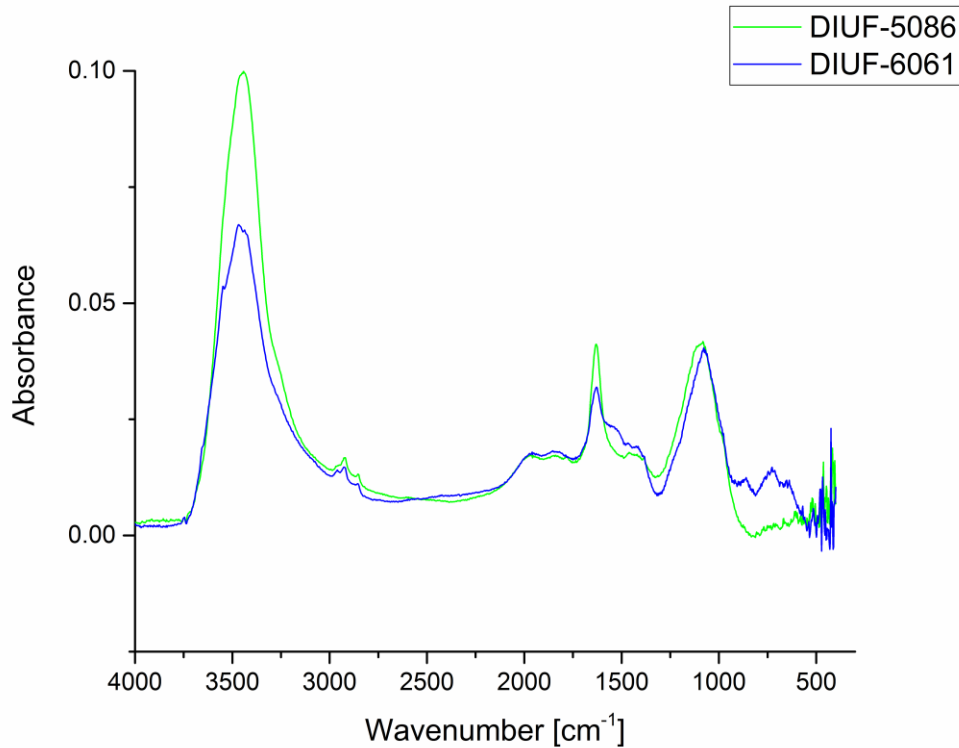


Figure 4-30: Representative FTIR spectra of 5086 and 6061 alloys in DIUF.

Spectra measured from the deposit on alloys 5086 and 6061 appear to be similar to each other, in each of the three electrolytes; indicating that deposit formed on both alloys were the same. Conversely, the spectra from deposit formed on the 5086/5083 alloy in either Isopac or Alum solutions were different than those formed on the other two aluminum alloys in the same electrolytes. This discrepancy between deposits on the tube and sheet coupons may be due to the crevice formers used, and the localized environment that was subsequently produced. Ultimately, there were similarities in strong peaks around  $3500\text{ cm}^{-1}$  and  $1000\text{ cm}^{-1}$ , and between  $1500$  and  $1700\text{ cm}^{-1}$  for all of the above-mentioned electrolyte-alloy combinations. No further examination was conducted into the similarities and differences between the deposits formed on the tube and sheet aluminum alloy coupons, in any of the three electrolytes.

Spectra from deposits present on the 304 sheet coupons, in all three electrolytes, are provided in Figure 4-31. All three electrolyte-alloy deposits were

found to match the spectra of the nylon 6,6 washers used as crevice formers. Both the FTIR spectra and EDX compositional data confirm that the deposit produced on the 304 stainless steel alloys in all three electrolytes is indeed nylon. This information further indicates that nylon was transferred onto the surfaces of the coupons during installation and possibly removal of the crevice formers.

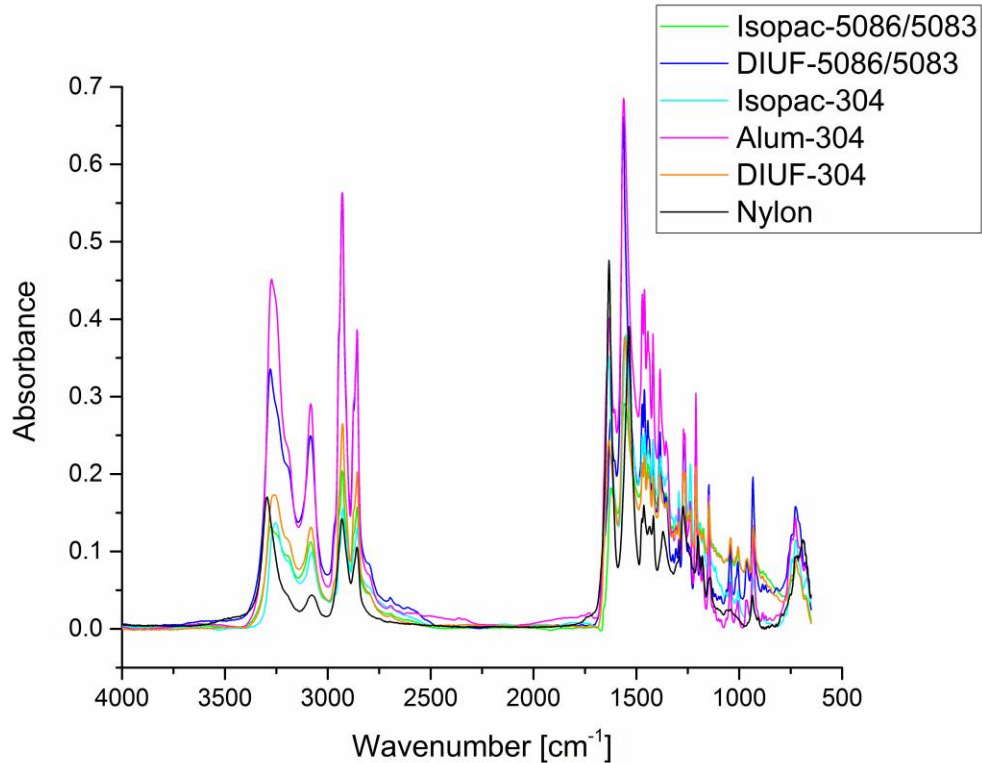


Figure 4-31: Representative FTIR spectra of nylon present in the deposits of the 304 alloy in all three electrolytes, and on the 5086/5083 alloy in both Isopac solution and DIUF.

Also included in Figure 4-31 is nylon deposit which was found on the crevice surface of the 5086/5083 alloy in Isopac solution and DIUF. The presence of two different spectra collected from the 5086/5083 alloy in Isopac solution indicates that both corrosion products had formed and nylon transfer had occurred. Meanwhile, the presence of nylon on the 5086/5083 alloy in DIUF indicates that only nylon transfer had occurred. This point is supported by the previously collected EDX data, which contains both large amounts of carbon and nitrogen.

However, small amounts of metal loss can be observed on the 5086/5083 alloy surface in DIUF as shown in Figure 4-22 (Section 4.1.2). Next, no nylon was detected in the deposit formed on the 5086/5083 alloy in Alum solution; yet one point analyzed with EDX (Point 2 of the 5086/5083 alloy in Table 4-3; Section 4.1.3.1) also contains large amounts of carbon and nitrogen. Moreover, metal loss could also be observed on the alloy surface in the Alum solution (Figure 4-17; Section 4.1.2). Therefore, it is believed that both nylon transfer had occurred and corrosion product had formed on the 5086/5083 coupons in all three electrolytes.

#### 4.1.4 Mass Change Measurements

The mass change measurements (between coupon mass before corrosion testing and after cleaning) of the corrosion coupons are presented below in Figure 4-27. More specifically, the average mass loss and error bars (from the calculated confidence interval;  $n = 3$ ) for each of the twelve combinations is plotted in Figure 4-32.

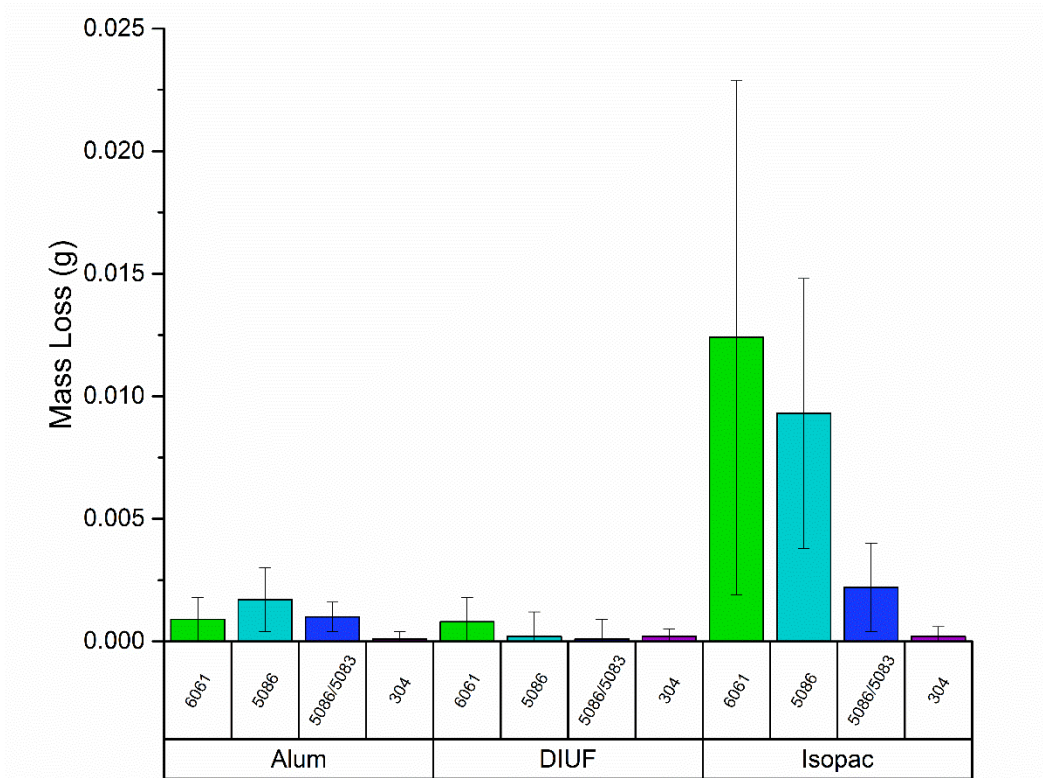


Figure 4-32: Average mass loss measurements for the twelve electrolyte-alloy combinations used in immersion testing.

All of the aluminum alloys in Isopac solution had relevant mass loss, whereas only 5086 and 5086/5083 alloys in Alum solution had mass loss measurements which were relevant. Relevance is judged based on the lower bound of the mass loss confidence interval being greater than zero. If this lower bound is greater than zero, then the mass loss is said to be relevant, and vice versa. Conversely, the calculated mass loss for the 304 stainless steel in all three electrolytes, the aluminum alloys in DIUF, and 6061 in Alum were negligible. Even though the average measurements were greater than zero, the corresponding confidence intervals rendered said measurements irrelevant.

Prior to performing the immersion studies, relevant mass loss was believed to occur in all aluminum alloys exposed to either Isopac or Alum; especially since artificial crevices were installed to induce an environment conducive to crevice corrosion. Moreover, both coagulants were stated to be corrosive to aluminum, as

per their respective material safety data sheets [8,9]. This statement was confirmed true for all of the aluminum alloys in either Isopac or Alum, except for 6061 in Alum (which was deemed negligible). Regarding the aluminum alloys in DIUF, even with the crevice former present, relevant corrosion was thought **not** to occur. Finally, no mass loss was believed to occur on the 304 stainless steel in any of the three electrolytes. Both of these statements were confirmed as per the mass loss data – particularly the lower bound of the confidence interval being equal to or less than zero – in Figure 4-32.

The highest mass loss was for the aluminum alloys in the Isopac solution, followed by the aluminum alloys in the Alum solution. The order from highest to lowest metal loss, for the electrolyte-alloy combinations, are as follows: Isopac-6061 ( $0.0124 \pm 0.0105$  g), Isopac-5086 ( $0.0093 \pm 0.0055$  g), Isopac-5086/5083 ( $0.0022 \pm 0.0018$  g), Alum-5086 ( $0.0017 \pm 0.0013$  g), Alum-5086/5083 ( $0.0010 \pm 0.0006$  g), and Alum-6061 ( $0.0009 \pm 0.0009$  g).

Four key points can be made regarding these mass loss measurements. First, based solely on the mass loss measurements, Isopac appears to be the most corrosive to all three aluminum alloys, followed by Alum then DIUF. Meanwhile, Isopac, Alum, or DIUF do not appear to cause any relevant mass loss to the 304 stainless steel. Second, even though no relevant mass loss had occurred on the aluminum alloys in DIUF, or 6061 in Alum, stereo microscopy images presented in Section 4.1.2 show small amounts of localized metal loss. This amount may be low enough that it could not be detected (to a relevant quantity) by the analytical balance used to perform the measurements. The measurement uncertainty of the analytical balance was determined to be  $\pm 0.0003$  g. Third, even after cleaning the coupons using the procedure outlined in Chapter 3, tarnish is still present on the coupon surfaces (refer to Figures 4-7, 4-14, and 4-19 in Section 4.1.2). Additional chemical cleaning as per either ASTM G1 [10] or ISO 8047 [11] could be used to remove said tarnish or adherent corrosion deposit; consequently leading to higher mass loss measurements. However, for the purposes of this study, this aggressive

cleaning was not performed so as to not exacerbate the localized corrosion damage. The forth (and final) point, is that the error bars are quite large – even for the Isopac-6061 and Isopac-5086 combinations. This wide range of potential metal loss values (for each individual electrolyte-alloy combination) is most likely due to the localized attack observed on the crevice surface, and the passive nature of all four alloys used in the immersion testing. For these four points, the comparison of solution corrosivity using only mass loss measurements may be misleading. Therefore, mass loss measurements should be collected in conjunction with visual examination – at various length scales – of the corrosion coupons' surfaces.

Regarding the 6061 alloy coupon in DIUF that had its crevice former moved during the immersion testing, the calculated average mass loss and confidence interval for the DIUF-6061 combination presented in Figure 4-32 could be changed. The value presented in the figure ( $0.0008 \pm 0.0010$  g) includes the mass loss measurements for all three coupons in the DIUF-6061 set. If it is assumed that the mass measurement of the disturbed coupon is invalid, the average mass loss and confidence interval for the DIUF-6061 combination, using the remaining two coupons, would be  $0.0010 \pm 0.0025$  g. Therefore, even with the coupon removed, the mass loss measurement for this combination would be irrelevant.

## 4.2 In Situ Monitoring Results

The temperature (T), dissolved oxygen concentration (DO), pH, and chloride concentration ( $[Cl^-]$ ) were measured in all thirty six immersion cells, throughout the 28-day test. The four parameters are presented in Figures 4-33 through 4-36, and are compared to the parameters measured of the relevant control solution. The T, DO, and pH are plotted as average values of the triplicate coupons tested. The confidence interval ( $n = 3$ ) was used for the error bars of the pH values, whereas the accuracy of the DO probe ( $\pm 0.3$  °C for T;  $\pm 0.1$  mg/L for DO between 0 and equal to 8 mg/L, and  $\pm 0.2$  mg/L for DO greater than 8 mg/L) was used as the error bars for the T and DO values. (It should be noted that the error associated with

the accuracy of both the T and DO measurements was greater than the calculated, respective confidence intervals; hence, the accuracy values were used instead.) Meanwhile, the  $[Cl^-]$  is plotted as the average of three measurements taken of the single coupon (per combination) tested, with the resulting confidence interval ( $n = 3$ ) as the error bars. These parameters are segregated based off of solution, and are plotted as functions of both day of measurement and alloy. All parameters for each of the three coupons, in each of the twelve electrolyte-alloy combinations, can be found in Appendix F. It should be noted that the DO and T measurements were not collected on day 14 of the DIUF control, and the  $[Cl^-]$  measurement was not collected on day 7 of the DIUF control.

The T and DO measurements for all electrolyte-alloy combinations and control solutions appear constant over the 28-day test. There are a few degrees in variation between the T measurements of the different electrolyte-alloy combinations. At these low temperatures, it is generally accepted that increasing the solution temperature leads to an increase in both the corrosion reaction and mass transport kinetics [12–14]; resulting in an increase in rate of corrosion. However, since the temperatures are different by only a couple of degrees, the effects of temperature cannot be used to explain the differences in mass loss measured between the electrolyte-alloy combinations. Concerning the DO, all measurements appear the same for the twelve electrolyte-alloy combinations and the control solutions. These constant measurements make sense since there was a large volume of oxygen available in the head-space of the corrosion cells (between the top of the solution and the Parafilm® cover). Moreover, the air in the head-space got replenished whenever the Parafilm® cover was removed for both the macrophotography and parameter measurements. Therefore, the effects of DO also cannot explain the differences in mass loss measured.

The pH measurements of the Isopac and Alum combinations and controls appear to vary over the duration of the experiment. Yet, due to the large error bars, no trend can be extracted from the measurements. While the coagulant solution pH

measurements vary around 4.5, the DIUF combinations and control measurements fluctuate greatly; both at the start and throughout the experiment. The error bars of the DIUF pH measurements are even larger than those of the other two solutions; again, no trend could be extracted from the measurements. At present, it is believed that the large pH fluctuations observed in both the immersion cells and controls are from the sensitivity of the probe.

Lower pH measurements in both the coagulant solutions explain the greater mass loss measurements of the aluminum alloys. For some instances during the experiment, the pH measurements fell below the lower threshold of the passive range of aluminum. As mentioned in Chapter 2, the passive pH range of aluminum is 4 to 9 [1,12,14–17]. However, the pH measurements were collected from the bulk solution of each immersion cell, and not from underneath the coupon crevice formers. This local pH, as well as local DO and  $[Cl^-]$ , could not be measured. Hence, from the corrosion observed underneath the crevices (i.e., the crevice surface) of the aluminum alloys, it is suspected that the local pH beneath the crevices was less than 4. This lower pH in the crevice is supported by the acidification of the local electrolyte, as per the propagation stage described to occur in crevice corrosion [12,13,18,19].

The  $[Cl^-]$  of both the Isopac combinations and control appear to slightly decrease over the duration of the experiment. Moreover, the combination and control  $[Cl^-]$  were the same or slightly different on each day measured. This downward trend in both the control and immersion cells'  $[Cl^-]$  is believed to be from the sensitivity of the probe, and the lack of ISA pillows used when taking the measurement – both leading to inaccurate measurements. An argument could be made that chlorides are being consumed in corrosion-related reactions during the experiment, subsequently leading to a decrease in concentration in the immersion cells. However, the Isopac control  $[Cl^-]$  decreased during the testing. Moreover, the  $[Cl^-]$  of the 304 stainless steel in Isopac, which exhibited no visible signs of corrosion or relevant mass loss, also decreased through the duration of the test. The

MSDS for Isopac states that the compound is completely soluble in water [8]; indicating that the Isopac molecule completely dissociates – freeing up the bonded chlorides. Hence, the Isopac control's  $[Cl^-]$  shouldn't continue to change (or decrease in this case) after the Isopac was added to the deionized water. Therefore, based off of the decrease in  $[Cl^-]$  in the immersion cells, it cannot be definitively stated that chlorides were consumed in reactions associated with corrosion during the course of the 28-day test. (Even though it is highly likely that the chlorides were consumed since the greatest mass loss was found to have occurred on the aluminum alloys in Isopac solution.)

Opposed to the Isopac  $[Cl^-]$ , the  $[Cl^-]$  of the Alum solution and DIUF are at the detection limit (0.1 mg/L) of the chloride probe, throughout the immersion testing. Therefore, both solutions'  $[Cl^-]$  are deemed negligible.

As previously mentioned in Section 4.1.4, the largest mass loss measurements were recorded in the aluminum alloys that were exposed to Isopac solution. This fact is substantiated by the presence of the corrosive chlorides present in the Isopac solution. The next largest mass loss measurements were found in the aluminum alloys that were exposed to Alum solution; indicating that the sulphate in the Alum solution is also corrosive. No measurements of the sulphate ion were performed in this study; yet, the higher mass loss measurements suggest that sulphate had participated in the corrosion of the aluminum alloys. Additionally, both chloride [1,17,20] and sulphate [1,17,21] are known to cause depassivation in aluminum. Hence, both coagulant solutions in trace quantities (0.010 vol% Isopac and 0.017 vol% Alum, respectively), are corrosive to the aluminum alloys, with artificial crevice formers, tested in this study. Conversely, the 304 stainless steel appears immune to corrosion damage, even with the installed artificial crevice formers.

Regarding whether the parameters measured within the immersion cells were within the operational range of the aeration tank, only the temperature measurements of the immersion cells were found to be consistently within range.

The aeration tank operating data for T (17.8 to 27.4 °C), DO (0.10 to 6.10 mg/L), pH (5.8 to 7.8), and  $[Cl^-]$  ( $190 \pm 17$  mg/L) can be found in Appendix C. The DO measurements in the immersion cells were above the operating range of the tank. The lower aeration tank DO is most likely due to the DO actively being consumed by biological oxidation. Since oxygen is a strong oxidizing agent, the higher DO in the immersion cells should lead to greater amounts of corrosion than what is observed in the aeration tank. However, more severe corrosion damage was witnessed in the aeration tank (likely due to longer exposure times and other compounding factors such as the possibility of microbiologically influenced corrosion (MIC)).

Next, the  $[Cl^-]$  in the aeration tank was multiple times larger than that of the Isopac immersion cells. This difference is believable since the aeration tank would contain many more sources of chlorides than what is present in any of the solutions used in this study. These other sources include: urine, table salt (NaCl), and countless other chloride-containing compounds that could naturally be present in wastewater. The greater the  $[Cl^-]$ , the greater amount of corrosion should occur [1]; corroborated by the severe corrosion witnessed in the aeration tank, as well as the greatest mass loss measurements recorded in the aluminum alloys exposed to Isopac solution (the chloride-containing coagulant).

Finally, the Alum and Isopac solution pH measurements were below the aeration tank operating range, while the DIUF pH measurements were within the aeration tank operating range. When the pH measurements in the Alum and Isopac solutions were lower than the passive range for aluminum, the aluminum alloys could succumb to depassivation and anodic dissolution.

With the variations between the pH, DO, and  $[Cl^-]$  of the immersion cells and the aeration tank, the immersion cells used in this study cannot be deemed fully representative of the aeration tank. Besides the differences in the aforementioned parameters, there are many other confirmed factors and operational conditions in

the aeration tank that could lead to the severe amounts of corrosion present. These include: presence of microorganisms (potential for MIC), forced aeration and fluid motion, transient process fluid composition, dissimilar metal contact, and the formation of deposit on any surfaces exposed to the process fluid. Even with the presence of artificial crevice formers on the coupons, the conditions in the aeration tank could not be simulated. Ultimately, the aeration tank conditions could be deemed more corrosive than those of any of the immersion cells, and their respective electrolyte compositions, and an *in situ* corrosion test would be preferred. Furthermore, it would be incorrect to assume that corrosion would only occur in the aeration tank due to the application of either coagulant.

It is important to mention that the laboratory scale corrosion cells still provided valuable insight into the corrosivity of either coagulant on the four alloys tested with artificial crevice formers. Even though the laboratory scale tests did not replicate the aeration tank parameters measured, the corrosion testing did allow for the study of the isolated effects of either coagulant. Moreover, due to the complexity of the environment observed in the aeration tank, it would have been impossible to predict and quantify the sole effects of either coagulant on the selected alloys, under crevice former conditions.

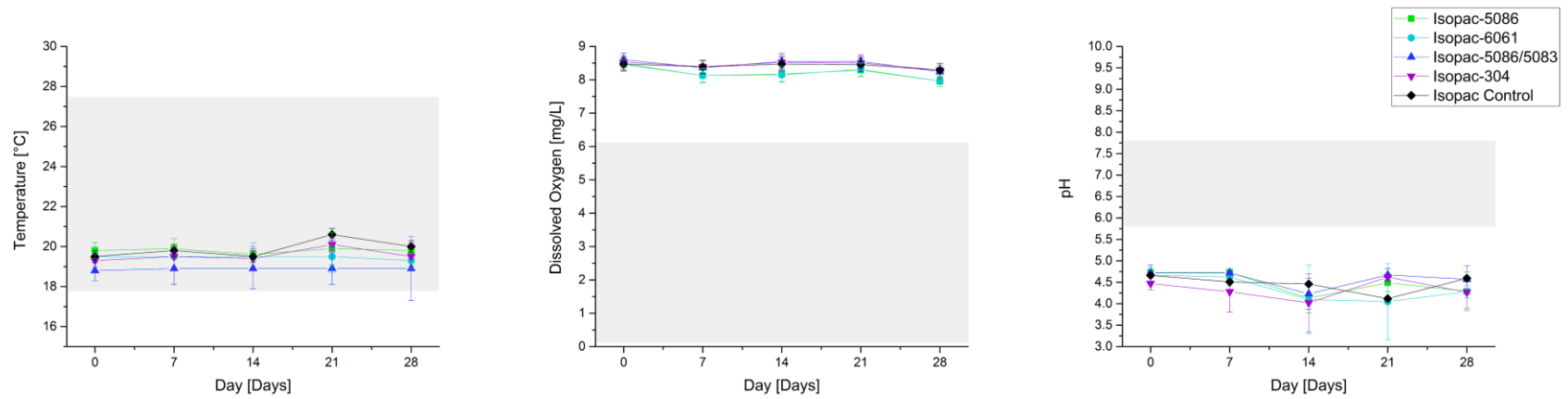


Figure 4-33: Average T, DO, and pH measurements for the four alloys in Isopac solution compared to the Isopac solution control. The shaded region in each graph is the operating range of the aeration tank.

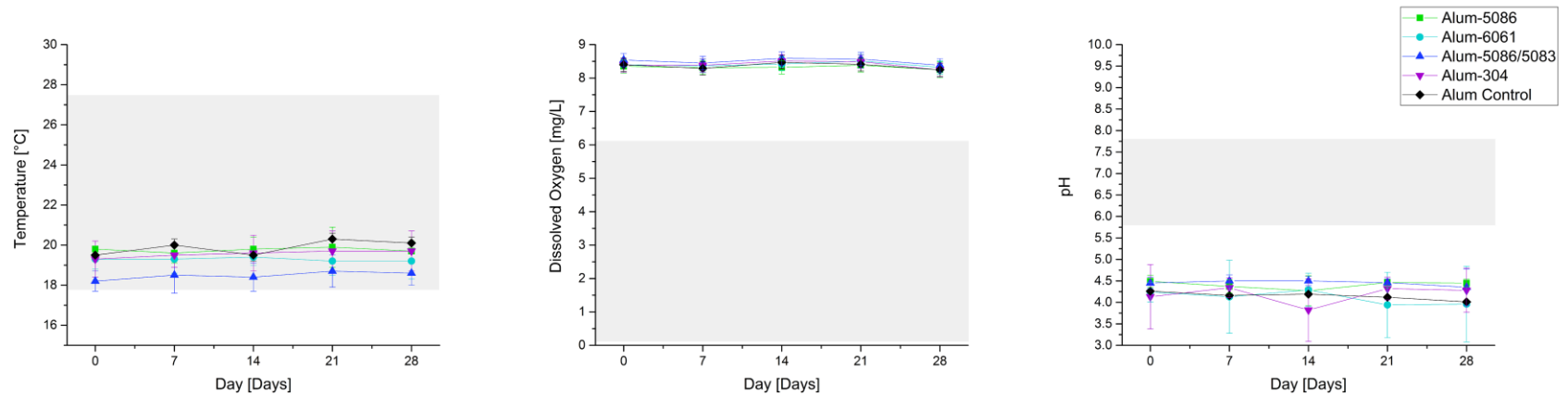


Figure 4-34: Average T, DO, and pH measurements for the four alloys in Alum solution compared to the Alum solution control. The shaded region in each graph is the operating range of the aeration tank.

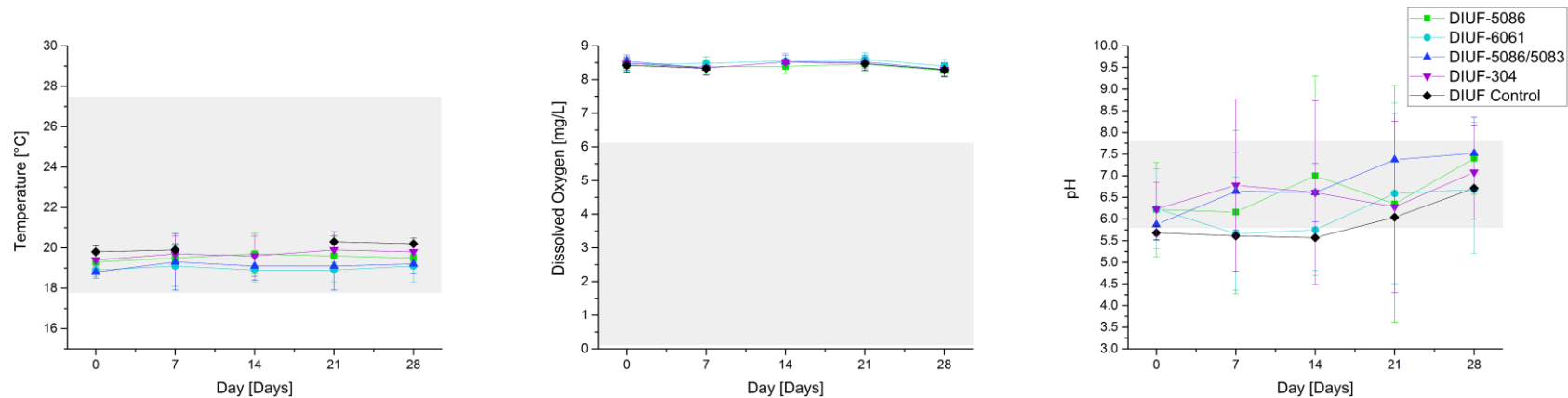


Figure 4-35: Average T, DO, and pH measurements for the four alloys in DIUF compared to the DIUF control. The shaded region in each graph is the operating range of the aeration tank.

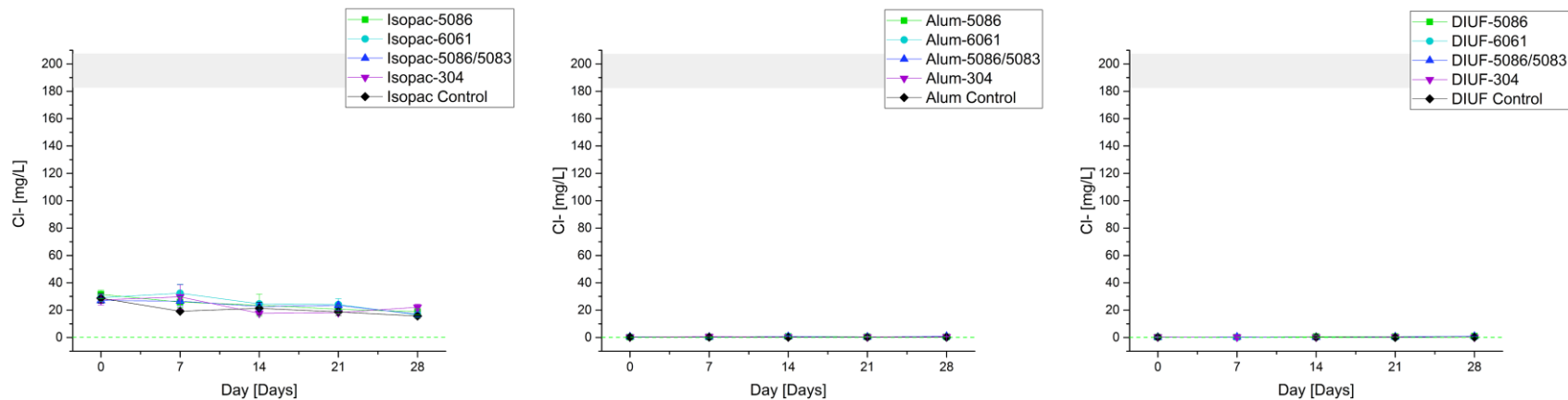


Figure 4-36: Average  $\text{Cl}^-$  measurements for select immersion cells compared to relevant control solution. The shaded region in each graph is the operating range of the aeration tank, while the green dashed line is the detectability limit of the  $\text{Cl}^-$  probe (at 0.1 mg/L).

### 4.3 Summary

- Localized corrosion, in the form of pitting and crevice corrosion, was identified visually on all of the aluminum alloys immersed in either Isopac, Alum, or DIUF electrolytes. Metal loss appeared the most prominent on the aluminum alloys exposed to Isopac, followed by Alum, then DIUF. Both localized modes of corrosion were observed throughout the damaged aeration tank (all surfaces in the aeration tank were covered by a naturally occurring crevice former).
- IGC was also identified visually, but only on the exposed surface of the Isopac-6061 combination and the crevice surface of the Alum-5086/5083 combination. Regarding the damaged aeration tank, IGC was only observed on the 6061 tubular ties (again, which were covered by a naturally occurring crevice former).
- Deposits collected and analyzed from the aluminum alloys in all three electrolytes – except the DIUF-5086/5083 combination – were indicative of aluminum corrosion products. Both the EDX data and FTIR spectra identified aluminum oxides or aluminum hydroxides; however, neither technique could confirm the exact chemistry and structure of the corrosion product(s). Aluminum corrosion products were also identified in the deposits collected from the damaged aeration tank.
- Neither metal loss (induced by any mode of corrosion) nor corrosion deposit was identified on the 304 stainless steels alloys in any of the three electrolytes tested. As with the aeration tank, no corrosion was observed on the stainless steel components.
- Relevant mass loss was determined for only aluminum alloys in Isopac and Alum (except the Alum-6061 combination), with the aluminum alloys

exhibiting the most mass loss in Isopac, followed by Alum. Ultimately, mass loss measurements should be collected in conjunction with visual examination – at various length scales – of the corrosion coupons' surfaces.

- Both coagulant solutions in quantities (0.010 vol% Isopac and 0.017 vol% Alum, respectively) administered in the aeration tank are corrosive to the aluminum alloys, with artificial crevice formers, tested in this study. Hence, neither coagulant should be used in aeration tanks constructed of aluminum alloys: 5086, 6061, or dual certified 5086/5083, which may be shielded by either artificial or naturally occurring crevice formers.
- The T and DO measurements for all electrolyte-alloy combinations and control solutions were constant over the 28-day test, whereas, the pH and  $[Cl^-]$  measurement fluctuated and decreased, respectively. Both the pH and  $[Cl^-]$  values are questionable due to their respective probe's sensitivity and – for the  $[Cl^-]$  – the measurement procedure used in this study.
- The corrosion cell T was within the operating range of the aeration tank, while the DO and  $[Cl^-]$  were above and below, respectively, the tank operating range. Moreover, the pH of the corrosion cells were either below (for Isopac and Alum) or within (for DIUF) the operating range of the aeration tank. These variations in parameters indicate that the immersion cells used in this study did not replicate the conditions in the aeration tank, at least based on the previously mentioned four parameters.
- Ultimately, the aeration tank conditions could be deemed more corrosive than those of any of the immersion cells, and their respective electrolyte compositions, and an *in situ* corrosion test would be preferred over a bench scale test such as that performed in this work.

- The corrosion testing allowed for the study of the isolated effects of either coagulant, under artificial crevice former conditions.

#### 4.4 References

- [1] C. Vargel, Corrosion of Aluminium, Elsevier Ltd, Kidlington, UK, 2004.
- [2] ASTM G46, Standard Guide for Examination and Evaluation of Pitting Corrosion, West Conshohocken, PA, 2013. doi:10.1520/G0046-94R13.
- [3] P.A. Schweitzer, Corrosion of Polymers and Elastomers, 2nd ed., CRC Press, Boca Raton, FL, 2006.
- [4] K. Wefers, C. Misra, Oxides and Hydroxides of Aluminum, 1987.
- [5] R.S. Alwitt, The Aluminum-Water System, in: J.W. Diggle, A.K. Vijh (Eds.), Oxides Oxide Film., Volume 4, Marcel Dekker, Inc., New York, NY, 1976: pp. 169–254.
- [6] S. Gustafsson, Corrosion properties of aluminium alloys and surface treated alloys in tap water, Uppsala University, 2011.
- [7] P.R. Griffiths, J.A. de Haseth, Fourier Transform Infrared Spectrometry, 2nd ed., John Wiley & Sons, Inc., Hoboken, NJ, 2007.
- [8] Klearwater Equipment & Technologies Corp., Isopac Solution MSDS, (2012). <http://www.klearwater.ca/page3.html>.
- [9] ClearTech Industries Inc., Aluminum Sulphate Solution MSDS, (2015). <http://www.cleartech.ca/msds/alumsulphateliq.pdf>.
- [10] ASTM G1, Standard Practice for Preparing, Cleaning, and Evaluating Corrosion Test Specimens, West Conshohocken, PA, 2011. doi:10.1520/G0001-03R11.
- [11] ISO 8047, Corrosion of metals and alloys - Removal of corrosion products from corrosion test specimens, Geneva, Switzerland, 2009. [www.iso.org](http://www.iso.org).
- [12] J.R. Davis, ed., Corrosion: Understanding the Basics, ASM International, Materials Park, OH, 2000.
- [13] M.G. Fontana, Corrosion Engineering, 3rd ed., McGraw Hill Book Company, New York, NY, 1987.

- [14] R.W. Revie, ed., *Uhlig's Corrosion Handbook*, 3rd ed., John Wiley & Sons, Inc., Hoboken, NJ, 2011.
- [15] D.C. Bennett, R.A. Nixon, *Corrosion and Materials Fundamentals for Engineers in Wastewater Treatment Plants & Collection Systems*, 3rd ed., NACE International, Houston, TX, 2016.
- [16] M. Pourbaix, *Atlas of Electrochemical Equilibria in Aqueous Solutions*, 2nd ed., NACE International, Houston, TX, 1974.
- [17] J.R. Davis, ed., *Corrosion of Aluminum and Aluminum Alloys*, ASM International, Materials Park, OH, 1999. doi:10.1361/caaa1999.
- [18] E.E. Stansbury, R.A. Buchanan, *Fundamentals of Electrochemical Corrosion*, ASM International, Materials Park, OH, 2000.
- [19] E. McCafferty, *Introduction to Corrosion Science*, Springer, New York, NY, 2010. doi:10.1007/978-1-4419-0455-3.
- [20] J.R. Galvele, Present State of Understanding of the Breakdown of Passivity and Repassivation, in: R.P. Frankenthal, J. Kruger (Eds.), *Passiv. Met.*, The Electrochemical Society, Princeton, NJ, 1978: pp. 285–327.
- [21] H.P. Godard, E.G. Torrible, The Effect of Chloride and Sulphate Ions on Oxide Film Growth on Al Immersed in Aqueous Solutions at 25°C, *Corros. Sci.* 10 (1970) 135–142.

# Chapter 5 – Conclusions and Future Work

## 5.1 Conclusions

As listed in the introduction chapter of this thesis, there were three objectives for the corrosion experiments performed in this study. The first was to design laboratory scale immersion corrosion cells which assess the corrosivity of the coagulants under artificial crevice former conditions. The addition of artificial crevice formers to the corrosion coupons, and the measured temperature (T) of the corrosion cells, were representative of the actual aeration tank. Again, the additional, confirmed factors present in the aeration tank, including: presence of microorganisms (potential for microbiologically influenced corrosion; MIC), forced aeration and fluid motion, transient process fluid composition, dissimilar metal contact, and the formation of deposit on any surfaces exposed to the process fluid were chosen not to be simulated in the laboratory scale immersion corrosion cells used in this study.

Only the corrosion cells' T was within the operating range of the aeration tank. Meanwhile, the dissolved oxygen concentration (DO), and chloride concentration ( $[Cl^-]$ ) of the corrosion cells were outside of the aeration tank operating range. More specifically, the DO and  $[Cl^-]$  were above and below, respectively, the tank operating range. The pH of the corrosion cells were either below (for Isopac and Alum) or within (for DIUF) the operating range of the aeration tank. These variations in parameters further indicate that the immersion cells used in this study could not replicate all the conditions in the aeration tank.

Even though the laboratory scale corrosion cells were not representative of the aeration tank, they still allowed for the study of the individual, corrosive effects of either Isopac or Alum. With the additional aforementioned factors present in the

aeration tank – and without performing the laboratory immersion testing – it would have been impossible to predict and quantify the sole effects of either coagulant on the selected alloys, under crevice former conditions. Therefore, the laboratory scale immersion testing could still be deemed relevant – at least in providing insight into the corrosivity of the coagulants on the four alloys tested with artificial crevice formers.

The second objective of this study was to determine the corrosivity of the individual wastewater treatment plant (WWTP) coagulants (Isopac and Alum), as well as de-ionized ultra-filtered (DIUF) water (the control solution), on the metal alloys identified in the corroded aeration tank. Results from the 28-day, laboratory scale immersion corrosion testing revealed that both coagulants – in very small quantities in solution; 0.010 vol% Isopac and 0.017 vol% Alum, respectively – led to localized corrosion of all three aluminum alloys tested with artificial crevice formers, as did DIUF water. Conversely, no corrosion was identified on the 304 grade stainless steel alloy, with artificial crevice formers, exposed to any of the aforementioned three solutions.

In order to assess the corrosion observed on the aluminum alloys, a combination of: visual examination, chemical analysis of formed deposits, and mass changes measurements were required. Both pitting and crevice corrosion were identified visually on all three aluminum alloys immersed in either Isopac, Alum, or DIUF solutions (electrolytes). From a qualitative assessment, the localized metal loss appeared the most prominent on the aluminum alloys exposed to Isopac, followed by Alum, then DIUF. Intergranular corrosion (IGC) was also identified, but only on two of the twelve electrolyte-alloy combinations. These combinations, as well as where the IGC was identified, were: on the exposed surface of aluminum alloy grade 6061, which was immersed in Isopac (1); and the crevice surface of the dual certified 5086/5083 aluminum alloy, which was immersed in Alum (2). None of the previously-mentioned three modes of corrosion – or any metal loss – could

be identified on the grade 304 stainless steel alloy, in any of the three electrolytes tested.

Next, deposits collected and chemically analyzed from the aluminum alloys in all three electrolytes – except the DIUF-5086/5083 combination – were indicative of aluminum corrosion products. These corrosion products were identified as either aluminum oxides or aluminum hydroxides, via energy dispersive x-ray (EDX) spectroscopy and Fourier transform infrared (FTIR) spectroscopy. No corrosion deposits were identified on the 304 stainless steel, in any of the three electrolytes tested.

Relevant mass loss was determined for only the aluminum alloys in Isopac and Alum – except for the Alum-6061 combination. Furthermore, the aluminum alloys in Isopac, followed by Alum, were measured to have the most mass loss. Meanwhile, no relevant mass loss was measured for any of the electrolyte-stainless steel combinations; confirming the lack of both visually discernable metal loss and corrosion deposits.

Ultimately, visual examination – at various length scales – of the corrosion coupons' surfaces, chemical analysis of formed deposits, and mass loss measurements were necessary in assessing the corrosivity of the coagulants and DIUF to the four metal alloys tested in this study. It can be concluded that neither Isopac nor Alum (even in very low volume percentages) should be used in aeration tanks constructed of aluminum alloys: 5086, 6061, or dual certified 5086/5083, which may be shielded by either artificial or naturally occurring crevice formers. Conversely, both coagulants – at the volume percentages used in this study – may be used in aeration tanks constructed from grade 304 stainless steel.

The third, and final, objective of this study was to determine if the conditions in the aeration tank would be more or less corrosive than those of the laboratory scale corrosion cells. The modes of corrosion observed on the aluminum

alloy coupons in the immersion testing (pitting, crevice corrosion, and in some instances IGC) were also identified in the aluminum alloy, aeration tank components (IGC was found only on the tubular ties). Additionally, aluminum corrosion products were identified in nearly all of the electrolyte-aluminum alloy combination deposits and the deposits collected from the damaged aeration tank. However, the extent of damage observed in the corrosion testing was nowhere near as severe as the damage measured in the aeration tank. Besides the duration of the immersion testing being only 28 days, and the aeration tank being in service for approximately 20 months, there is another key difference between the aeration tank and the laboratory immersion testing. (A common occurrence between both the aeration tank and the laboratory testing was the lack of corrosion identified on 304 grade stainless steel.) This difference is that there are several other factors present in the aeration tank – which were mentioned previously in this chapter – that could lead to, or exacerbate the corrosion observed in the tank. Hence, it would be incorrect to assume that corrosion would *only* occur due to the use of either coagulant in the aeration tank.

The individual presence of either coagulant was enough to cause corrosion in the aluminum alloys within 28 days of exposure. If the isolated chemical effects of either coagulant can induce corrosion, then the combination of additional factors and use of either coagulant should create a more aggressive environment in the aeration tank. Ultimately, it can be concluded that the aeration tank conditions could be deemed more corrosive than those of any of the immersion cells, and their respective electrolyte compositions.

## **5.2 Future Work**

The following list provides the items that could be considered for future work in this study.

1. Perform *in situ* corrosion testing in an active aeration tank using the same alloys as tested above in the laboratory scale corrosion tests. A field test would be the most representative test for assessing the corrosion resistance of the various alloys to the process fluid. Moreover, an *in situ* test would allow for the assessment of all factors in the aeration tank to be tested simultaneously.
2. Perform microbiological assessments and testing of the aeration tank process fluid. The purpose of this work is to determine whether the microbiology within the aeration tank had contributed to the identified corrosion damage; subsequently allowing for the confirmation or elimination of MIC. If *in situ* testing is performed, it would also be very important to perform biological assessments on the *in situ* corrosion coupons immediately after testing.

# Bibliography

## Chapter 1

- [1] J.S. Pavelich, J.A. Nychka, Preliminary Findings Report: Visual Inspection and Corrosion Assessment of the EPCOR Borealis Waste Water Treatment Plant, Edmonton, AB, 2013.
- [2] J.S. Pavelich, J.A. Nychka, Additional Inspection Report: Additional Visual Inspection and Corrosion Assessment of the EPCOR Borealis Wastewater Treatment Plant, Edmonton, AB, 2014.
- [3] C. Vargel, Corrosion of Aluminium, Elsevier Ltd, Kidlington, UK, 2004.
- [4] J.R. Davis, ed., Corrosion of Aluminum and Aluminum Alloys, ASM International, Materials Park, OH, 1999. doi:10.1361/caaa1999.
- [5] B.J. Little, J.S. Lee, Microbiologically Influenced Corrosion, John Wiley & Sons, Inc., Hoboken, NJ, 2007.
- [6] L. Metcalf, H.P. Eddy, eds., Wastwater Engineering Treatment and Resource Recovery, 5th ed., McGraw-Hill Education, New York, NY, 2014.

## Chapter 2

- [1] L. Metcalf, H.P. Eddy, eds., Wastwater Engineering Treatment and Resource Recovery, 5th ed., McGraw-Hill Education, New York, NY, 2014.
- [2] F.R. Spellman, Handbook of Water and Wastewater Treatment Plant Operations, Lewis Publishers, New York, NY, 2003.
- [3] M.L. Davis, Water and Wastewater Engineering Design Principles and Practice, McGraw Hill, New York, NY, 2010.
- [4] G. Bitton, Wastewater Microbiology, 3rd ed., John Wiley & Sons, Inc., Hoboken, NJ, 2005.
- [5] Design of Municipal Wastewater Treatment Plants: WEF Manual of Practice No. 8 ASCE Manuals and Reports on Engineering Practice No. 76, 5th ed., McGraw-Hill Professional, 2010.

- [6] R.Y. Surampalli, S.K. Brar, M. Verma, R.D. Tyagi, Wasterwater Treatment, in: *Encycl. Chem. Process.*, Taylor and Francis, New York, NY, 2007: pp. 1–14. doi:10.1081/E-ECHP-120008009.
- [7] J.-Q. Jiang, Development of Coagulation Theory and Pre-Polymerized Coagulants for Water Treatment, *Sep. Purif. Methods.* 30 (2001) 127–141. doi:10.1081/SPM-100102986.
- [8] H. Tang, F. Xiao, D. Wang, Speciation, stability, and coagulation mechanisms of hydroxyl aluminum clusters formed by PACl and alum: A critical review, *Adv. Colloid Interface Sci.* 226 (2015) 78–85. doi:10.1016/j.cis.2015.09.002.
- [9] ClearTech Industries Inc., Aluminum Sulphate Solution MSDS, (2015). <http://www.cleartech.ca/msds/alumsulphateliq.pdf>.
- [10] Klearwater Equipment & Technologies Corp., Isopac Solution MSDS, (2012). <http://www.klearwater.ca/page3.html>.
- [11] J.S. Pavelich, J.A. Nychka, Preliminary Findings Report: Visual Inspection and Corrosion Assessment of the EPCOR Borealis Waste Water Treatment Plant, Edmonton, AB, 2013.
- [12] J.S. Pavelich, J.A. Nychka, Additional Inspection Report: Additional Visual Inspection and Corrosion Assessment of the EPCOR Borealis Wastewater Treatment Plant, Edmonton, AB, 2014.
- [13] D.C. Bennett, R.A. Nixon, Corrosion and Materials Fundamentals for Engineers in Wastewater Treatment Plants & Collection Systems, 3rd ed., NACE International, Houston, TX, 2016.
- [14] Aluminum Company of America, Sewage Works Equipment and Supplies, *Sewage Work. J.* 16 (1944) 1040–1042.
- [15] The Aluminum Association, Aluminum the modern metal for sewage treatment equipment and plants, 1970.
- [16] E.R. Stowell, Corrosion in Sewage Works, *Sewage Ind. Waste.* 28 (1956) 328–330. <http://www.jstor.org/stable/25033027>.
- [17] W.H. Ailor, Metals in Wastewater Treatment, *J. Environ. Eng. Div.* 4 (1974) 295–309.
- [18] A. Kumar, L.D. Stephenson, Emerging Corrosion Prevention and Control Technologies for Wastewater Treatment Plants, in: *Corrosion, NACE*, 2005: p. 13.

- [19] A.H. Tuthill, Stainless Steel in Wastewater Treatment Plants, *Water Eng. Manag.* 137 (1990) 31–34.
- [20] G.E. Englert, I.L. Muller, The Corrosion Behaviour of Mild Steel and Type 304 Stainless Steel in Media from an Anaerobic Biodigestor, *Int. Biodeterior. Biodegradation.* 37 (1996) 173–180. doi:10.1016/S0964-8305(96)00019-4.
- [21] A. Iversen, MIC on Stainless Steels in Wastewater Treatment Plants, in: *Corrosion, NACE, 1999*: p. 12.  
<http://www.onepetro.org/mslib/servlet/onepetropreview?id=NACE-99171>.
- [22] A. Iversen, MIC on Stainless Steels in Wastewater Treatment Plants Field Tests and a Risk Assessment, in: *Corrosion, NACE, 2002*: p. 14.
- [23] A. Iversen, MIC on Stainless Steels in Wastewater Treatment - Anaerobic and Aerobic Treatments Influence on Ennoblement and the Passive Surface, in: *Corrosion, NACE, 2003*: p. 17.
- [24] C.W. Kovach, N. Kinsman, A. Iversen, Service Experience with High Performance Stainless Steels in Aggressive Fresh Waters, in: *Corrosion, NACE, 2002*: p. 14.
- [25] T. Mathiesen, E. Rislund, T.S. Nielsen, J.E. Frantsen, U. Tornaes, H.G. Pedersen, P. Nielsen, M.B. Petersen, MIC of Stainless Steel Pipes in Sewage Treatment Plants, in: *Corrosion, NACE, 2003*: p. 21.
- [26] J.S. Pavelich, J.A. Nychka, Preliminary Findings Report: Visual Inspection and Corrosion Assessment of the EPCOR Steepbank Waste Water Treatment Plant, Edmonton, AB, 2014.
- [27] ADI Water Solutions Ltd., (n.d.).  
<http://www.adewater.com/index.php/2015-10-16-16-28-28/membrane-bioreactor> (accessed October 31, 2016).
- [28] NatureClean, (n.d.). <http://www.natureclean.com/alibmod.html> (accessed October 31, 2016).
- [29] CORIX, (n.d.).  
[http://ywaterworks.com/documents/CWS\\_BRO'11\\_MBR.pdf](http://ywaterworks.com/documents/CWS_BRO'11_MBR.pdf) (accessed October 31, 2016).
- [30] NACE/ASTM G193, Standard Terminology and Acronyms Relating to Corrosion, West Conshohocken, PA, 2013. doi:10.1520/G0193-12D.

- [31] ISO 8044, Corrosion of metals and alloys - Basic terms and definitions, Geneva, Switzerland, 2015. [www.iso.org](http://www.iso.org).
- [32] E.E. Stansbury, R.A. Buchanan, Fundamentals of Electrochemical Corrosion, ASM International, Materials Park, OH, 2000.
- [33] J.R. Davis, ed., Corrosion: Understanding the Basics, ASM International, Materials Park, OH, 2000.
- [34] M.G. Fontana, Corrosion Engineering, 3rd ed., McGraw Hill Book Company, New York, NY, 1987.
- [35] E. McCafferty, Introduction to Corrosion Science, Springer, New York, NY, 2010. doi:10.1007/978-1-4419-0455-3.
- [36] R.W. Revie, ed., Uhlig's Corrosion Handbook, 3rd ed., John Wiley & Sons, Inc., Hoboken, NJ, 2011.
- [37] P.R. Roberge, Corrosion Engineering Principles and Practice, McGraw Hill Book Company, New York, NY, 2008. doi:10.1036/0071482431.
- [38] R.W. Revie, H.H. Uhlig, Corrosion and Corrosion Control: An Introduction to Corrosion Science and Engineering, 4th ed., John Wiley & Sons, Inc., Hoboken, NJ, 2008.
- [39] M. Pourbaix, Atlas of Electrochemical Equilibria in Aqueous Solutions, 2nd ed., NACE International, Houston, TX, 1974.
- [40] R.G. Kelly, J.R. Scully, D.W. Shoesmith, R.G. Buchheit, Electrochemical Techniques in Corrosion Science and Engineering, Marcel Dekker, Inc., New York, NY, 2002.
- [41] NACE/ASTM G31, Standard Guide for Laboratory Immersion Corrosion Testing of Metals, West Conshohocken, PA, 2013. doi:10.1520/G0031-12A.
- [42] ISO 11845, Corrosion of metals and alloys - General principles for corrosion testing, Geneva, Switzerland, 1995. [www.iso.org](http://www.iso.org).
- [43] ASTM G4, Standard Guide for Conducting Corrosion Tests in Field Applications, West Conshohocken, PA, 2008. doi:10.1520/G0004-01R08.
- [44] NACE Standard RP0497, Field Corrosion Evaluation Using Metallic Test Specimens, Houston, TX, 2004. [www.nace.org](http://www.nace.org).

- [45] C.P. Dillon, *Forms of Corrosion: Recognition and Prevention*, NACE International, Houston, TX, 1982.
- [46] P.R. Roberge, *Handbook of Corrosion Engineering*, McGraw Hill, New York, NY, 2000.
- [47] C. Vargel, *Corrosion of Aluminium*, Elsevier Ltd, Kidlington, UK, 2004.
- [48] J.R. Davis, ed., *Corrosion of Aluminum and Aluminum Alloys*, ASM International, Materials Park, OH, 1999. doi:10.1361/caaa1999.
- [49] ASTM G46, *Standard Guide for Examination and Evaluation of Pitting Corrosion*, West Conshohocken, PA, 2013. doi:10.1520/G0046-94R13.
- [50] ISO 11463, *Corrosion of metals and alloys - Evaluation of pitting corrosion*, Geneva, Switzerland, 1995. www.iso.org.
- [51] T.H. Orem, Influence of Crystallographic Orientation on the Corrosion Rate of Aluminum in Acids and Alkalies, *J. Res. Natl. Bur. Stand.* (1934). 58 (1957) 157–167.  
[http://nvlpubs.nist.gov/nistpubs/jres/58/jresv58n3p157\\_A1b.pdf](http://nvlpubs.nist.gov/nistpubs/jres/58/jresv58n3p157_A1b.pdf).
- [52] M. Baumgärtner, H. Kaesche, Aluminum pitting in chloride solutions: morphology and pit growth kinetics, *Corros. Sci.* 31 (1990) 231–236.
- [53] H. Kaesche, Pitting Corrosion of Aluminum, and Intergranular Corrosion of Aluminum Alloys, in: R.W. Staehle, B.F. Brown, J. Kruger, A. Agrawal (Eds.), *NACE-3*, NACE, 1974: pp. 516–525.
- [54] G.C. Wood, W.H. Sutton, J.A. Richardson, T.N.K. Riley, A.G. Malherbe, The Mechanism of Pitting of Aluminum and its Alloys, in: R.W. Staehle, B.F. Brown, J. Kruger, A. Agrawal (Eds.), *NACE-3*, NACE, 1974: pp. 526–539.
- [55] R. Baboian, ed., *NACE Corrosion Engineer's Reference Book*, 3rd ed., NACE International, Houston, TX, 2002.
- [56] J. Soltis, Passivity breakdown, pit initiation and propagation of pits in metallic materials - Review, *Corros. Sci.* 90 (2015) 5–22.  
doi:10.1016/j.corsci.2014.10.006.
- [57] M.C. Reboul, B. Baroux, Metallurgical aspects of corrosion resistance of aluminium alloys, *Mater. Corros.* 62 (2011) 215–233.  
doi:10.1002/maco.201005650.

- [58] M.C. Reboul, T.J. Warner, H. Mayet, B. Baroux, A ten-step mechanism for the pitting corrosion of aluminium, *Mater. Sci. Forum.* 217–222 (1996) 1553–1558. doi:10.1515/CORRREV.1997.15.3-4.471.
- [59] E. McCafferty, Sequence of steps in the pitting of aluminum by chloride ions, *Corros. Sci.* 45 (2003) 1421–1438. doi:10.1016/S0010-938X(02)00231-7.
- [60] R.T. Foley, Localized Corrosion of Aluminum Alloys—A Review, *Corrosion.* 42 (1986) 277–288. doi:10.5006/1.3584905.
- [61] J.M. Kolotyrkin, Pitting Corrosion of Metals, *Corrosion.* 19 (1963) 261t–268t. <http://www.corrosionjournal.org/doi/pdf/10.5006/0010-9312-19.8.261>.
- [62] G.S. Frankel, Pitting Corrosion of Metals A Review of the Critical Factors, *J. Electrochem. Soc.* 145 (1998) 2186–2198.
- [63] G.S. Frankel, The Effects of Microstructure and Composition on Al Alloy Corrosion, *Corrosion.* 71 (2015) 1308–1320.
- [64] J.R. Galvele, Transport Processes and the Mechanism of Pitting of Metals, *J. Electrochem. Soc.* 123 (1976) 464–474. doi:10.1149/1.2132857.
- [65] Z. Szklarska-Smialowska, Insight into the Pitting Corrosion Behavior of Aluminum Alloys, *Corros. Sci.* 33 (1992) 1193–1202.
- [66] Z. Szklarska-Smialowska, Pitting corrosion of aluminum, *Corros. Sci.* 41 (1999) 1743–1767. doi:10.1016/S0010-938X(99)00012-8.
- [67] Z. Szklarska-Smialowska, Review of Literature on Pitting Corrosion Published Since 1960, *Corrosion.* 27 (1971) 223–233. doi:10.5006/0010-9312-27.6.223.
- [68] H. Bohni, Breakdown of Passivity and Localized Corrosion Processes, *Langmuir.* 3 (1987) 924–930. doi:10.1021/la00078a010.
- [69] K. Wefers, C. Misra, *Oxides and Hydroxides of Aluminum*, 1987.
- [70] R.S. Alwitt, The Aluminum-Water System, in: J.W. Diggle, A.K. Vijh (Eds.), *Oxides Oxide Film.*, Volume 4, Marcel Dekker, Inc., New York, NY, 1976: pp. 169–254.
- [71] G.T. Chandler, R.L. Sindelar, P.S. Lam, Evaluation of Water Chemistry on the Pitting Susceptibility of Aluminum, in: *Corrosion*, 1997: p. 14.

- [72] H.P. Godard, The Corrosion Behavior of Aluminum in Natural Waters, *Can. J. Chem. Eng.* 38 (1960) 167–173. doi:10.1002/cjce.5450380507.
- [73] H.P. Godard, An Insight Into the Corrosion Behavior of Aluminum, *Mater. Perform.* (1981) 9–15.
- [74] P.M. Aziz, H.P. Godard, Pitting Corrosion Characteristics of Aluminum Influence of Magnesium and Manganese, *Ind. Eng. Chem. Res.* 44 (1952) 1791–1795. doi:10.1021/ie50512a028.
- [75] ASTM G78, Standard Guide for Crevice Corrosion Testing of Iron-Base and Nickel-Base Stainless Alloys in Seawater and Other Chloride-Containing Aqueous Environments, West Conshohocken, PA, 2012. doi:10.1520/G0078-01R12.
- [76] S.W. Borenstein, *Microbiologically influenced corrosion handbook*, Woodhead Publishing Ltd, Cambridge, England, 1994.
- [77] B.J. Little, J.S. Lee, *Microbiologically Influenced Corrosion*, John Wiley & Sons, Inc., Hoboken, NJ, 2007.
- [78] R.A. Lane, Under the Microscope: Understanding, Detecting, and Preventing Microbiologically Influenced Corrosion, *J. Fail. Anal. Prev.* 5 (2005) 10–38. doi:10.1361/154770205X65891.
- [79] A.K. Tiller, G.H. Booth, Anaerobic Corrosion of Aluminium by Sulphate-Reducing Bacteria, *Corros. Sci.* 8 (1968) 549–555.
- [80] A. Rajasekar, Y.-P. Ting, Microbial Corrosion of Aluminum 2024 Aeronautical Alloy by Hydrocarbon Degrading Bacteria *Bacillus cereus* ACE4 and *Serratia marcescens* ACE2, *Ind. Eng. Chem. Res.* 49 (2010) 6054–6061. doi:10.1021/ie100078u.
- [81] D. Walsh, D. Pope, M. Danford, T. Huff, The Effect of Microstructure on Microbiologically Influenced Corrosion, *J. Miner. Met. Mater. Soc.* 45 (1993) 22–30. doi:10.1007/BF03222429.
- [82] F. Mansfeld, The interaction of bacteria and metal surfaces, *Electrochim. Acta.* 52 (2007) 7670–7680. doi:10.1016/j.electacta.2007.05.006.
- [83] B.J. Little, J.S. Lee, Microbiologically influenced corrosion: an update, *Int. Mater. Rev.* 59 (2014) 384–393. doi:10.1179/1743280414Y.0000000035.
- [84] B.J. Little, P. Wagner, F. Mansfeld, An Overview of Microbiologically Influenced Corrosion, *Electrochim. Acta.* 37 (1992) 2185–2194.

- [85] B.J. Little, J.S. Lee, R.I. Ray, Diagnosing Microbiologically Influenced Corrosion: A State-of-the-Art Review, *Corrosion*. 62 (2006) 1006–1017. doi:10.5006/1.3278228.
- [86] B. Little, P. Wagner, F. Mansfeld, Microbiologically influenced corrosion of metals and alloys, *Int. Mater. Rev.* 36 (1991) 253–272. doi:10.1179/imr.1991.36.1.253.
- [87] R.C. Salvarezza, M.F.L. de Mele, H.A. Videla, Mechanisms of the Microbial Corrosion of Aluminum Alloys, *Corrosion*. 39 (1983) 26–32. doi:10.5006/1.3580810.
- [88] H.A. Videla, Microbially Induced Corrosion: an Updated Overview, *Int. Biodeterior. Biodegrad.* 48 (2001) 176–201. doi:10.1016/S0964-8305(01)00081-6.
- [89] ASTM G48, Standard Test Methods for Pitting and Crevice Corrosion Resistance of Stainless Steels and Related Alloys by Use of Ferric Chloride Solution, West Conshohocken, PA, 2011. doi:10.1520/G0048-11.
- [90] B. De Force, H. Pickering, A Clearer View of How Crevice Corrosion Occurs, *J. Miner. Met. Mater. Soc.* 47 (1995) 22–27. doi:10.1007/BF03221250.
- [91] I.L. Rosenfeld, Crevice Corrosion of Metals and Alloys, in: R.W. Staehle, B.F. Brown, J. Kruger, A. Agrawal (Eds.), *NACE-3, NACE*, 1974: pp. 373–398.
- [92] B.A. Shaw, M.M. McCosby, A.M. Abdullah, H.W. Pickering, The Localized Corrosion of Al 6XXX Alloys, *J. Miner. Met. Mater. Soc.* 53 (2001) 42–46. doi:10.1007/s11837-001-0087-7.
- [93] M. Pourbaix, Applications of electrochemistry in corrosion science and in practice, *Corros. Sci.* 14 (1974) 25–82.
- [94] ASTM G82, Standard Guide for Development and Use of a Galvanic Series for Predicting Galvanic Corrosion Performance, West Conshohocken, PA, 2014. doi:10.1520/G0082-98R14.
- [95] ASTM G71, Standard Guide for Conducting and Evaluating Galvanic Corrosion Tests in Electrolytes, West Conshohocken, PA, 2014. doi:10.1520/G0071-81R14.
- [96] ASTM G69, Standard Test Method for Measurement of Corrosion Potentials of Aluminum Alloys, West Conshohocken, PA, 2012. doi:10.1520/G0069-12.

- [97] T.D. Burleigh, R.C. Rennick, F.S. Bovard, Corrosion Potential for Aluminum Alloys Measured by ASTM G 69, *Corrosion*. 49 (1993) 683–685. doi:10.5006/1.3316100.
- [98] M.L.C. Lim, R.G. Kelly, J.R. Scully, Overview of Intergranular Corrosion Mechanisms, Phenomenological Observations, and Modeling of AA5083, *Corrosion*. 72 (2016) 198–220. doi:10.5006/1818.
- [99] R. Zhang, R.K. Gupta, C.H.J. Davies, A.M. Hodge, M. Tort, K. Xia, N. Birbilis, The Influence of Grain Size and Grain Orientation on Sensitization in AA5083, *Corrosion*. 72 (2016) 160–168. doi:10.5006/1703.
- [100] R. Zhang, S.P. Knight, R.L. Holtz, R. Goswami, C.H.J. Davies, N. Birbilis, A Survey of Sensitization in 5xxx Series Aluminum Alloys, *Corrosion*. 72 (2016) 144–159. doi:10.5006/1787.
- [101] T. Minoda, H. Yoshida, Effect of Grain Boundary Characteristics on Intergranular Corrosion Resistance of 6061 Aluminum Alloy Extrusion, *Metall. Mater. Trans. A*. 33 (2002) 2891–2898. doi:10.1007/s11661-002-0274-3.
- [102] ASTM G67, Standard Test Method for Determining the Susceptibility to Intergranular Corrosion of 5XXX Series Aluminum Alloys by Mass Loss After Exposure to Nitric Acid (NAMLT Test), West Conshohocken, PA, 2013. doi:10.1520/G0067-13.
- [103] ASTM G110, Standard Practice for Evaluating Intergranular Corrosion Resistance of Heat Treatable Aluminum Alloys by Immersion in Sodium Chloride + Hydrogen Peroxide Solution, West Conshohocken, PA, 2009. doi:10.1520/G0110-92R09.
- [104] ISO 11846, Corrosion of metals and alloys - Determination of resistance to intergranular corrosion of solution heat-treatable aluminium alloys, Geneva, Switzerland, 1995.
- [105] H. Kaesche, *Die Korrosion der Metalle*, 3rd ed., Springer, Berlin, Germany, 1990.
- [106] J.R. Galvele, Present State of Understanding of the Breakdown of Passivity and Repassivation, in: R.P. Frankenthal, J. Kruger (Eds.), *Passiv. Met.*, The Electrochemical Society, Princeton, NJ, 1978: pp. 285–327.
- [107] H.P. Godard, E.G. Torrible, The Effect of Chloride and Sulphate Ions on Oxide Film Growth on Al Immersed in Aqueous Solutions at 25°C, *Corros. Sci.* 10 (1970) 135–142.

- [108] A. Groysman, *Corrosion for Everybody*, Springer, New York, NY, 2010. doi:10.1007/978-90-481-3477-9.
- [109] A.W. Zeuthen, R.M. Kain, *Crevice Corrosion Testing of Austenitic, Superaustenitic, Superferritic, and Superduplex Stainless Type Alloys in Seawater*, in: R.M. Kain, W.T. Young (Eds.), *ASTM STP 1300 Corros. Test. Nat. Waters Second Vol.*, ASTM International, West Conshohocken, PA, 1997: pp. 91–108.
- [110] S.D. Cramer, B.S. Covino, eds., *ASM Handbook Volume 13B Corrosion: Materials*, ASM International, Materials Park, OH, 2005.
- [111] A. Iversen, B. Leffler, 3.04 – *Aqueous Corrosion of Stainless Steels*, in: B. Cottis, M. Graham, R. Lindsay, S. Lyon, T. Richardson, D. Scantlebury, H. Stott (Eds.), *Shreir’s Corros.*, Elsevier, Oxford, UK, 2010: pp. 1802–1878. doi:10.1016/B978-044452787-5.00091-3.

### Chapter 3

- [1] NACE/ASTM G31, *Standard Guide for Laboratory Immersion Corrosion Testing of Metals*, West Conshohocken, PA, 2013. doi:10.1520/G0031-12A.
- [2] ISO 11845, *Corrosion of metals and alloys - General principles for corrosion testing*, Geneva, Switzerland, 1995. www.iso.org.
- [3] J.R. Davis, ed., *Corrosion of Aluminum and Aluminum Alloys*, ASM International, Materials Park, OH, 1999. doi:10.1361/caaa1999.
- [4] J.S. Pavelich, J.A. Nychka, *Preliminary Findings Report: Visual Inspection and Corrosion Assessment of the EPCOR Borealis Waste Water Treatment Plant*, Edmonton, AB, 2013.
- [5] J.S. Pavelich, J.A. Nychka, *Additional Inspection Report: Additional Visual Inspection and Corrosion Assessment of the EPCOR Borealis Wastewater Treatment Plant*, Edmonton, AB, 2014.
- [6] C. Vargel, *Corrosion of Aluminium*, Elsevier Ltd, Kidlington, UK, 2004.
- [7] S. Gustafsson, *Corrosion properties of aluminium alloys and surface treated alloys in tap water*, Uppsala University, 2011.
- [8] J.R. Davis, ed., *Corrosion: Understanding the Basics*, ASM International, Materials Park, OH, 2000.

- [9] NACE Standard RP0497, Field Corrosion Evaluation Using Metallic Test Specimens, Houston, TX, 2004. [www.nace.org](http://www.nace.org).
- [10] ASTM G78, Standard Guide for Crevice Corrosion Testing of Iron-Base and Nickel-Base Stainless Alloys in Seawater and Other Chloride-Containing Aqueous Environments, West Conshohocken, PA, 2012. doi:10.1520/G0078-01R12.
- [11] D.C. Montgomery, G.C. Runger, Applied Statistics and Probability for Engineers, 3rd ed., John Wiley & Sons, Inc., New York, NY, 2003.
- [12] ASTM G1, Standard Practice for Preparing, Cleaning, and Evaluating Corrosion Test Specimens, West Conshohocken, PA, 2011. doi:10.1520/G0001-03R11.
- [13] A.W. Zeuthen, R.M. Kain, Crevice Corrosion Testing of Austenitic, Superaustenitic, Superferritic, and Superduplex Stainless Type Alloys in Seawater, in: R.M. Kain, W.T. Young (Eds.), ASTM STP 1300 Corros. Test. Nat. Waters Second Vol., ASTM International, West Conshohocken, PA, 1997: pp. 91–108.
- [14] HACH Company, User Manual Luminescent Dissolved Oxygen Probe: Model LDO10101, LDO10103, LDO10105, LDO10110, LDO10115, or LDO10130, (2013). <http://www.hach.com/intellical-ldo101-standard-luminescent-optical-dissolved-oxygen-ldo-probe-1-meter-cable/product-downloads?id=7640489854&callback=qs>.
- [15] HACH Company, User Manual Refillable pH Probe: Model PHC30101 or PHC30103, (2013). <http://www.hach.com/intellical-phc301-standard-refillable-ph-electrode-1-meter-cable/product-downloads?id=7640512232>.
- [16] HACH Company, User Manual Chloride Probe: Model ISECl18101 or ISECl18103, (2013). <http://www.hach.com/intellical-isecl181-chloride-ion-selective-electrode-ise-1-meter-cable/product-downloads?id=7640513801&callback=qs>.
- [17] R.C. Weast, ed., CRC Handbook of Chemistry and Physics, 59th ed., CRC Press, West Palm Beach, FL, 1978.
- [18] D.L. Perry, Handbook of Inorganic Compounds, 2nd ed., CRC Press, Boca Raton, FL, 2011.
- [19] D.R. Lide, ed., CRC Handbook of Chemistry and Physics, 84th ed., CRC Press, Boca Raton, FL, 2004.

- [20] ISO 8047, Corrosion of metals and alloys - Removal of corrosion products from corrosion test specimens, Geneva, Switzerland, 2009. [www.iso.org](http://www.iso.org).

## Chapter 4

- [1] C. Vargel, Corrosion of Aluminium, Elsevier Ltd, Kidlington, UK, 2004.
- [2] ASTM G46, Standard Guide for Examination and Evaluation of Pitting Corrosion, West Conshohocken, PA, 2013. doi:10.1520/G0046-94R13.
- [3] P.A. Schweitzer, Corrosion of Polymers and Elastomers, 2nd ed., CRC Press, Boca Raton, FL, 2006.
- [4] K. Wefers, C. Misra, Oxides and Hydroxides of Aluminum, 1987.
- [5] R.S. Alwitt, The Aluminum-Water System, in: J.W. Diggle, A.K. Vijh (Eds.), Oxides Oxide Film., Volume 4, Marcel Dekker, Inc., New York, NY, 1976: pp. 169–254.
- [6] S. Gustafsson, Corrosion properties of aluminium alloys and surface treated alloys in tap water, Uppsala University, 2011.
- [7] P.R. Griffiths, J.A. de Haseth, Fourier Transform Infrared Spectrometry, 2nd ed., John Wiley & Sons, Inc., Hoboken, NJ, 2007.
- [8] Klearwater Equipment & Technologies Corp., Isopac Solution MSDS, (2012). <http://www.klearwater.ca/page3.html>.
- [9] ClearTech Industries Inc., Aluminum Sulphate Solution MSDS, (2015). <http://www.cleartech.ca/msds/alumsulphateliq.pdf>.
- [10] ASTM G1, Standard Practice for Preparing, Cleaning, and Evaluating Corrosion Test Specimens, West Conshohocken, PA, 2011. doi:10.1520/G0001-03R11.
- [11] ISO 8047, Corrosion of metals and alloys - Removal of corrosion products from corrosion test specimens, Geneva, Switzerland, 2009. [www.iso.org](http://www.iso.org).
- [12] J.R. Davis, ed., Corrosion: Understanding the Basics, ASM International, Materials Park, OH, 2000.
- [13] M.G. Fontana, Corrosion Engineering, 3rd ed., McGraw Hill Book Company, New York, NY, 1987.

- [14] R.W. Revie, ed., Uhlig's Corrosion Handbook, 3rd ed., John Wiley & Sons, Inc., Hoboken, NJ, 2011.
- [15] D.C. Bennett, R.A. Nixon, Corrosion and Materials Fundamentals for Engineers in Wastewater Treatment Plants & Collection Systems, 3rd ed., NACE International, Houston, TX, 2016.
- [16] M. Pourbaix, Atlas of Electrochemical Equilibria in Aqueous Solutions, 2nd ed., NACE International, Houston, TX, 1974.
- [17] J.R. Davis, ed., Corrosion of Aluminum and Aluminum Alloys, ASM International, Materials Park, OH, 1999. doi:10.1361/caaa1999.
- [18] E.E. Stansbury, R.A. Buchanan, Fundamentals of Electrochemical Corrosion, ASM International, Materials Park, OH, 2000.
- [19] E. McCafferty, Introduction to Corrosion Science, Springer, New York, NY, 2010. doi:10.1007/978-1-4419-0455-3.
- [20] J.R. Galvele, Present State of Understanding of the Breakdown of Passivity and Repassivation, in: R.P. Frankenthal, J. Kruger (Eds.), Passiv. Met., The Electrochemical Society, Princeton, NJ, 1978: pp. 285–327.
- [21] H.P. Godard, E.G. Torrible, The Effect of Chloride and Sulphate Ions on Oxide Film Growth on Al Immersed in Aqueous Solutions at 25°C, Corros. Sci. 10 (1970) 135–142.

## **Appendix A**

- [1] J.S. Pavelich, J.A. Nychka, Preliminary Findings Report: Visual Inspection and Corrosion Assessment of the EPCOR Borealis Waste Water Treatment Plant, Edmonton, AB, 2013.
- [2] J.S. Pavelich, J.A. Nychka, Additional Inspection Report: Additional Visual Inspection and Corrosion Assessment of the EPCOR Borealis Wastewater Treatment Plant, Edmonton, AB, 2014.
- [3] C. Vargel, Corrosion of Aluminium, Elsevier Ltd, Kidlington, UK, 2004.
- [4] J.R. Davis, ed., Corrosion of Aluminum and Aluminum Alloys, ASM International, Materials Park, OH, 1999. doi:10.1361/caaa1999.
- [5] ASTM B928, Standard Specification for High Magnesium Aluminum-Alloy Sheet and Plate for Marine Service and Similar Environments, West Conshohocken, PA, 2013. doi:10.1520/B0928\_B0928M-13.

- [6] ASTM G46, Standard Guide for Examination and Evaluation of Pitting Corrosion, West Conshohocken, PA, 2013. doi:10.1520/G0046-94R13.
- [7] R.W. Revie, ed., Uhlig's Corrosion Handbook, 3rd ed., John Wiley & Sons, Inc., Hoboken, NJ, 2011.
- [8] D.C. Bennett, R.A. Nixon, Corrosion and Materials Fundamentals for Engineers in Wastewater Treatment Plants & Collection Systems, 3rd ed., NACE International, Houston, TX, 2016.
- [9] J.R. Davis, ed., Corrosion: Understanding the Basics, ASM International, Materials Park, OH, 2000.
- [10] E.E. Stansbury, R.A. Buchanan, Fundamentals of Electrochemical Corrosion, ASM International, Materials Park, OH, 2000.
- [11] The Aluminum Association, International Alloy Designations and Chemical Composition Limits for Wrought Aluminum and Wrought Aluminum Alloys, Regist. Rec. Ser. Teal Sheets. (2015).  
[http://www.aluminum.org/sites/default/files/TEAL\\_1\\_OL\\_2015.pdf](http://www.aluminum.org/sites/default/files/TEAL_1_OL_2015.pdf)  
(accessed November 15, 2016).
- [12] P.R. Griffiths, J.A. de Haseth, Fourier Transform Infrared Spectrometry, 2nd ed., John Wiley & Sons, Inc., Hoboken, NJ, 2007.
- [13] J.I. Goldstein, C.E. Lyman, D.E. Newbury, E. Lifshin, P. Echlin, L. Sawyer, D.C. Joy, J.R. Michael, Scanning Electron Microscopy and X-Ray Microanalysis, 3rd ed., Springer, New York, NY, 2007.
- [14] L. Metcalf, H.P. Eddy, eds., Wastewater Engineering Treatment and Resource Recovery, 5th ed., McGraw-Hill Education, New York, NY, 2014.
- [15] ASTM E407, Standard Practice for Microetching Metals and Alloys, West Conshohocken, PA, 2007. doi:10.1520/E0407-07.
- [16] J.G. Kaufman, Introduction to Aluminum Alloys and Tempers, ASM International, Materials Park, OH, 2000.
- [17] J.E. Hatch, ed., Aluminum Properties and Physical Metallurgy, ASM International, Materials Park, OH, 1984.
- [18] L.F. Mondolfo, Aluminum Alloys Structure & Properties, Butterworth & Co. Ltd., London, UK, 1976.

- [19] ASM Handbook Volume 9 Metallography and Microstructures, ASM International, Materials Park, OH, 1985.
- [20] ASM Handbook Volume 2 Properties and Selection: Nonferrous Alloys and Special-Purpose Materials, ASM International, Materials Park, OH, 1990.
- [21] J.C. Free, P.T. Summers, B.Y. Lattimer, S.W. Case, Mechanical Properties of 5000 Series Aluminum Alloys Following Fire Exposure, in: TMS2016 Annu. Meet. Suppl. Process., The Minerals, Metals, and Materials Society, 2016: pp. 657–664.
- [22] B.D. Cullity, Elements of X-Ray Diffraction, Addison-Wesley Publishing Company, Inc., Reading, MA, 1956.
- [23] C.R. Schmitt, Anomalous Microbiological Tuberculation and Aluminum Pitting Corrosion - Case Histories, in: NACE-8, NACE, 1985: pp. 69–75.
- [24] M. Baumgärtner, H. Kaesche, Aluminum pitting in chloride solutions: morphology and pit growth kinetics, Corros. Sci. 31 (1990) 231–236.
- [25] B.A. Shaw, M.M. McCosby, A.M. Abdullah, H.W. Pickering, The Localized Corrosion of Al 6XXX Alloys, J. Miner. Met. Mater. Soc. 53 (2001) 42–46. doi:10.1007/s11837-001-0087-7.
- [26] T. Minoda, H. Yoshida, Effect of Grain Boundary Characteristics on Intergranular Corrosion Resistance of 6061 Aluminum Alloy Extrusion, Metall. Mater. Trans. A. 33 (2002) 2891–2898. doi:10.1007/s11661-002-0274-3.
- [27] B.J. Little, J.S. Lee, Microbiologically Influenced Corrosion, John Wiley & Sons, Inc., Hoboken, NJ, 2007.
- [28] D.C. Montgomery, G.C. Runger, Applied Statistics and Probability for Engineers, 3rd ed., John Wiley & Sons, Inc., New York, NY, 2003.

## **Appendix B**

- [1] J.S. Pavelich, J.A. Nychka, Preliminary Findings Report: Visual Inspection and Corrosion Assessment of the EPCOR Borealis Waste Water Treatment Plant, Edmonton, AB, 2013.
- [2] J.S. Pavelich, J.A. Nychka, Additional Inspection Report: Additional Visual Inspection and Corrosion Assessment of the EPCOR Borealis Wastewater Treatment Plant, Edmonton, AB, 2014.

- [3] Had2Know, (n.d.). <http://www.had2know.com/academics/spherical-cap-volume-surface-area-calculator.html> (accessed December 1, 2016).

## Appendix E

- [1] K. Wefers and C. Misra, "Oxides and Hydroxides of Aluminum," 1987.
- [2] S. Gustafsson, "Corrosion properties of aluminium alloys and surface treated alloys in tap water," Uppsala University, 2011.
- [3] R. S. Alwitt, "The Aluminum-Water System," in *Oxides and Oxide Films*, Volume 4., J. W. Diggle and A. K. Vijh, Eds. New York, NY: Marcel Dekker, Inc., 1976, pp. 169–254.

# Appendix A – Examination of Aeration Tank Components<sup>1</sup>

## A-1.0 Introduction

### A-1.1 Background<sup>2</sup>

It was requested that Dr. John Nychka and Scott Pavelich conduct a visual inspection and damage assessment of the damaged aeration tank TK-3100-1. The aeration tank is a biological reactor, which removes organic constituents in wastewater using microorganisms and injected air. This particular aeration tank is a critical process vessel in Train #1, which is further encompassed in the three-train, Borealis Expansion Wastewater Treatment Plant (WWTP). Table A-1 itemizes the contents of the visual inspection and damage assessments performed.

Table A-1: Inspection methods performed on aeration tank TK-3100-1 [1,2].

Equipment	Inspection/Test Methods Performed
<p style="text-align: center;"><b>Aeration Tank TK-3100-1</b></p>	<ul style="list-style-type: none"> <li>• External and internal visual inspection</li> <li>• Identify construction standards and material grades</li> <li>• Identification of grounding wires</li> <li>• Magnetic susceptibility of components, plates, and welds</li> <li>• Electrical resistance, voltage, and current measurements</li> <li>• Pit measurements: floor, wall, tooling marks, welds, and areas by air diffusers</li> <li>• Sample collection of large deposits (“sludge”<sup>†</sup>) from floor and brackets, and deposit samples from walls (including tooling marks and welds)</li> <li>• Sample collection of a portion of: tubular tie, floor, and wall, as well as an aeration piping bracket, washers, and bolts</li> </ul>

<sup>†</sup>: “Sludge” is termed deposits found within the aeration tank, whose origin is unknown. “Sludge” may include by-products of a damage mechanism or accumulation of solids from the process fluid.

<sup>1</sup> Portions of this Appendix were taken from previous reports written by the author. These reports include: *Preliminary Findings Report: Visual Inspection and Corrosion Assessment of the EPCOR Borealis Waste Water Treatment Plant* [1] and *Additional Inspection Report: Additional Visual Inspection and Corrosion Assessment of the EPCOR Borealis Wastewater Treatment Plant* [2].

<sup>2</sup> Significant portions of this subsection were taken from previous reports written by the author [1,2].

## A-1.2 Summary of Inspection Findings<sup>3</sup>

The following list summarizes key findings from the aforementioned inspections and assessments performed. Further information on these findings, as well as the locations where components and deposits were collected from the aeration tank can be found in reports written by the author [1,2].

- External visual inspection of aeration tank TK-3100-1 revealed no signs of visually apparent corrosion, or significant mechanical damage such as cracking [1].
- Significant localized corrosion damage was observed at various locations inside the aeration tank, with the most severe pitting identified on the tubular ties and floor [1]. The tubular ties found in close proximity to and in contact with the stainless steel aeration piping exhibited through wall pitting corrosion (Figure A-1) [1]. Moreover, pit measurements gathered from the tank floor, immediately adjacent to the aeration lines, measured up to approximately 4 mm deep (up to ~42% of wall thickness; Figure A-2) [1].
- Visual inspection of the 304/304L grade stainless steel aeration piping, in the tank, revealed no signs of corrosion or mechanical damage [1]. Portions of each of the nine air lines (including portions entering and travelling along the base of the tank) appeared discolored (below the water line) [1]. Additionally, some of these portions were covered in dried process fluid [1]. No visually observable signs of damage were identified on the aeration piping [1].
- Pitting damage appeared to be exacerbated by galvanic coupling through dissimilar metal interactions via direct electrical connection [1]. This coupling includes contact between: 304/304L grade stainless steel aeration piping and

---

<sup>3</sup> Significant portions of this subsection were taken from previous reports written by the author [1,2].

brackets (Figure A-3) and/or pipe supports (Figure A-4); aeration piping and tank walls (Figure A-5) and/or floor (Figure A-6); aeration piping and tubular ties (Figure A-1); and, finally, bolting (nuts, bolts, and washers) and aeration piping brackets (Figure A-3) [1].

- Artificial or naturally occurring crevice formers were involved in all forms of corrosion damage found within the aeration tank [1,2]. Artificial crevices include: tooling or grinding marks, points of physical contact between components (such as between aeration piping and tubular ties, and between aeration piping and brackets), and in some positions at the welds (such as weld toes, gaps between beads and start-stop locations) [1]. Naturally occurring crevice formers can be separated into two categories: (1) crevices formed by fluid constituents coming out of solution and attaching to, or settling on, the surface of the metal, and (2) crevices formed by precipitated corrosion reaction products. Examples of the first kind of naturally occurring crevice formers include insoluble deposits (such as solids and sludge found on the floor) or thin films of solids which adhere to materials submerged in the process fluid (such as the process fluid coating the walls and tubular ties) [1,2]. An example of the second kind of naturally occurring crevice former is the tubercles found along the walls [1,2]. Ultimately, both types of naturally occurring crevice formers can lead to under-deposit corrosion (a form of crevice corrosion) [1,2].
- Two kinds of deposit were present in the aeration tank [1]. The first type was a sludge-like deposit (identified as “sludge” deposit), which was found on: aeration piping brackets, floor, and floor welds [1]. This deposit was large and globular in shape, brown and grey in colour, friable, and was easily removed from surfaces [1]. Finally, multiple small pits were encapsulated in wider area pits under this kind of deposit [1]. This first kind of deposit is illustrated in Figures A-6 and A-7. The second type was a “crusty top hat” deposit, which was found on: walls (including welds and tooling marks) and the floor [1]. This deposit was cylindrical in shape, creamy light grey in colour, hard and rigid in

texture, and was difficult to remove from surfaces (very adherent) [1]. Finally, multiple small pits were found under this kind of deposit [1]. This second kind of deposit is illustrated in Figures A-5, A-8, A-9, and A-10.

- From pitting observed on grinding and tooling marks, as well as on portions of the weld profiles, construction or assembly flaws may have contributed to corrosion on the walls, floor, tubular ties, and linking welds of the aeration tank [1]. Therefore, questions can be raised whether assembly and installation of the aeration tank was performed according to appropriate design or inspection criteria.
- From the numerous findings, including: electrical resistance, voltage, and current measurements between components within the aeration tank as well as the aeration tank with the surrounding plant equipment (such as the aeration tank being connected to 304 stainless steel piping, both upstream and downstream) [1,2]; the lack of gasket or dielectric material between the bases of the aeration tanks and the steel floor [1,2]; the various grounding wires which were connected to all three aeration tanks and the steel floor [1,2]; and the lack of grounding wires on the WWTP buildings [2], it appeared as if everything (such as the aeration tank walls, floors, aeration lines, piping, etc.) was electrically connected to each other [1,2].
- Several specimens were collected from the aeration tank for further materials characterization to be performed. These included: a large portion of tubular tie; one aeration piping bracket and associated hardware (nuts, bolts, and washers); a portion of the floor (Figure A-11) and wall (Figure A-12); and varying amounts of sludge and “crusty top hat” deposits from the tank floor, walls, and brackets.

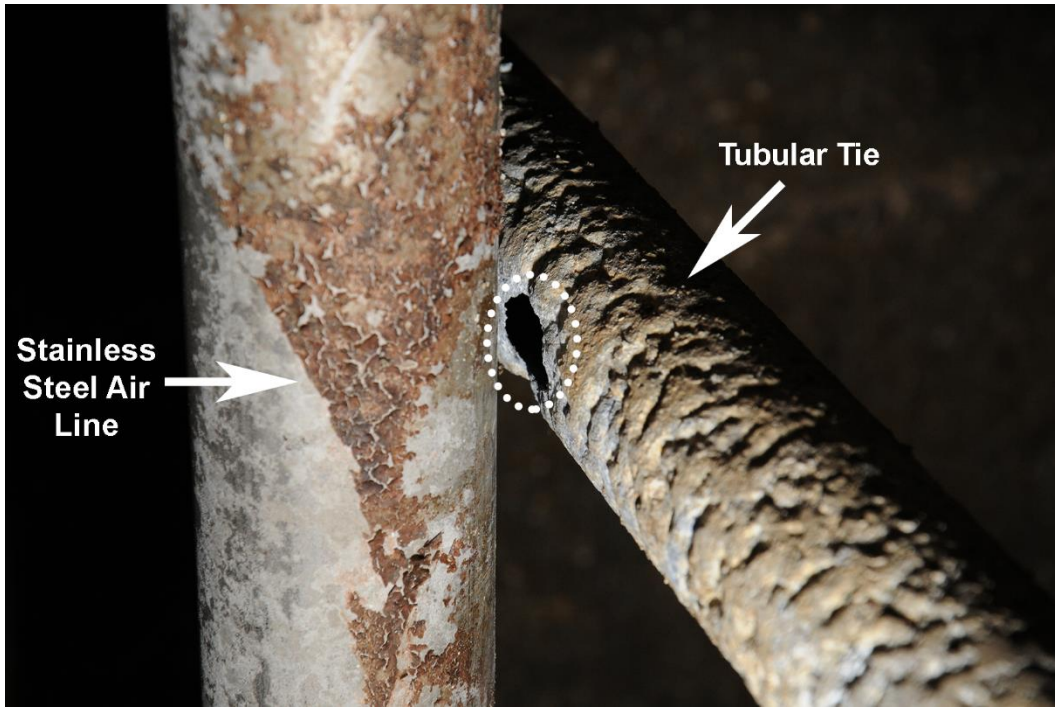


Figure A-1: Through wall corrosion (indicated by the dotted oval) of a tubular tie immediately adjacent to aeration piping [1].



Figure A-2: “Pit measurements taken from the deepest identified pit on the floor of the aeration tank. After brushing deposits clear.” [1] The gauge indicates that the pit is ~4 mm deep (~42% of the thickness assuming 9.53 mm / 0.375 inch thickness) [1].



Figure A-3: Localized corrosion on brackets, shown with direct (left) and oblique (right) lighting [1].



Figure A-4: Pipe support under brackets of an aeration line [1]. Pipe support exposed to both direct (left) and oblique (right) lighting conditions [1].

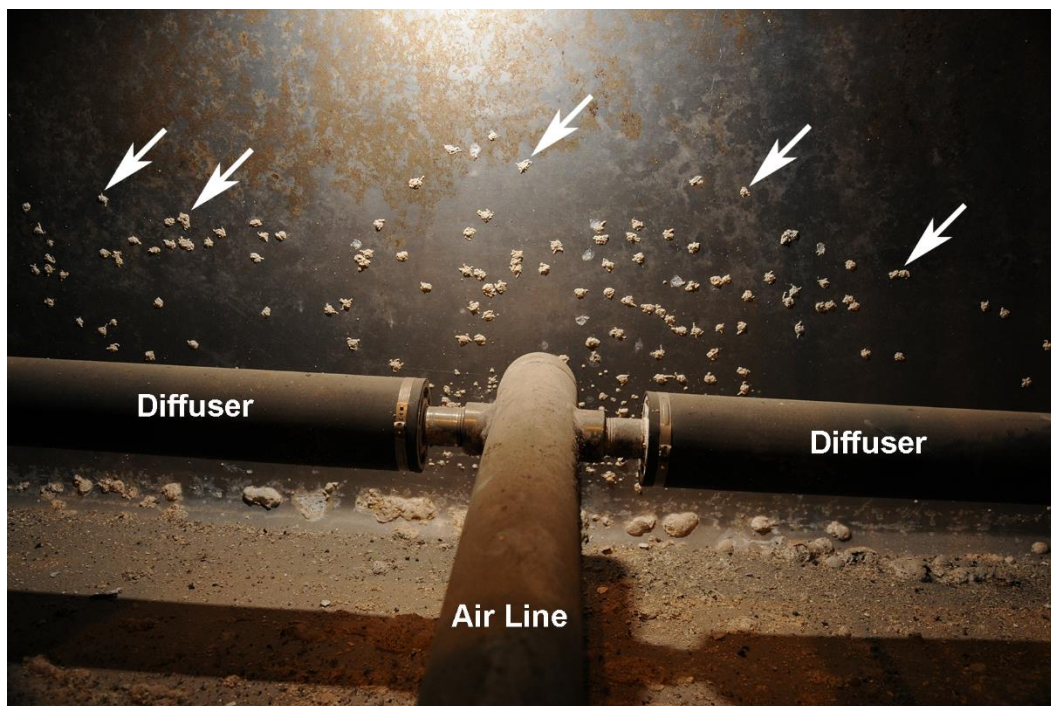


Figure A-5: "Crusty top hat" deposits (white arrows) on the tank wall in close proximity to the end of an aeration line and diffusers [1].

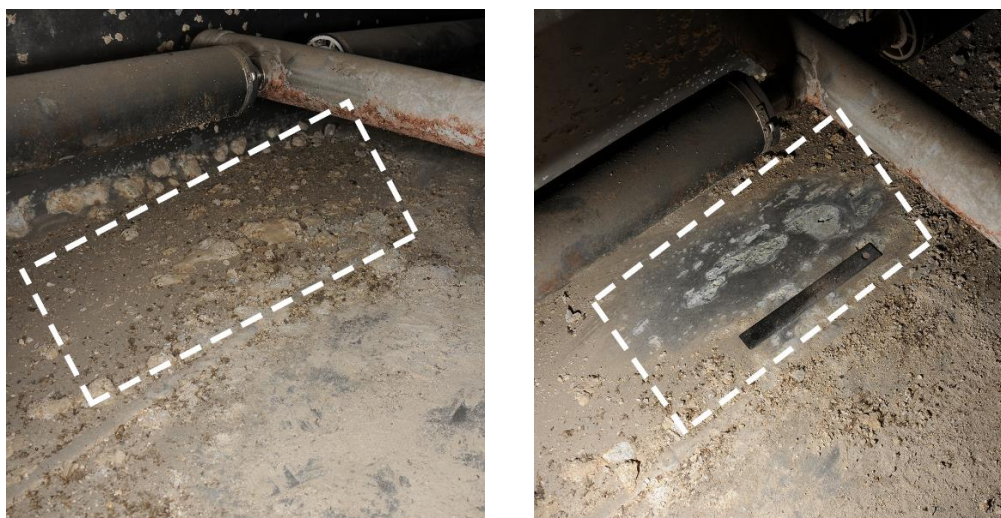


Figure A-6: Before (left) and after (right) removal of “sludge” deposits (dashed rectangle) from the aeration tank floor [1].

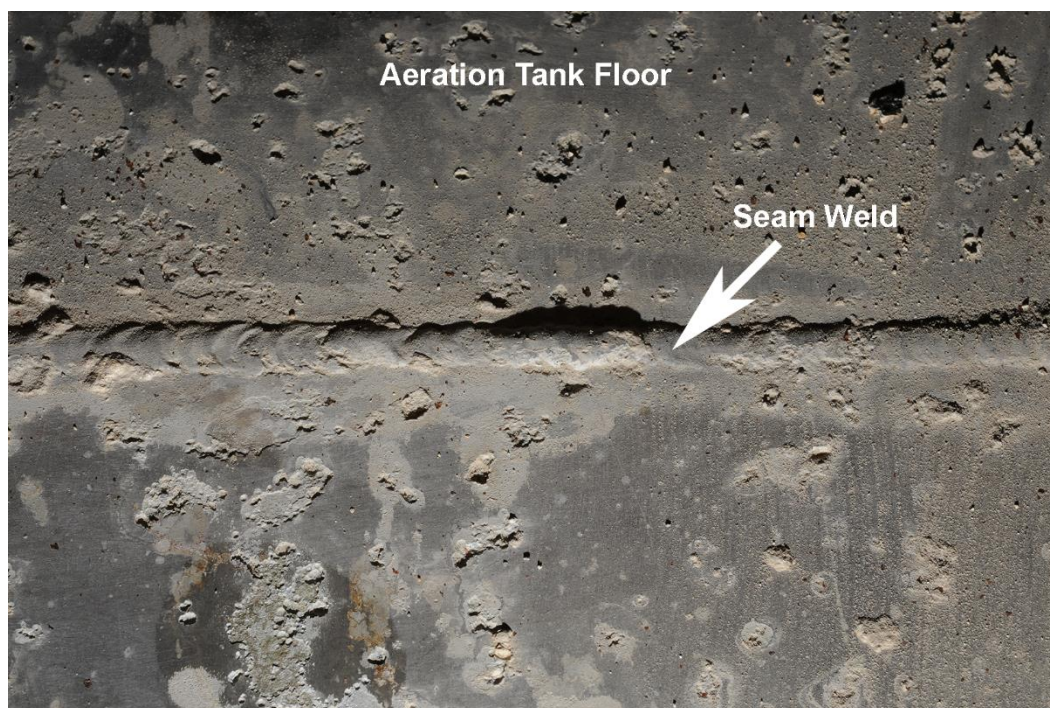


Figure A-7: First type of under-deposit corrosion identified on the floor and welds of the aeration tank (after brushing off the deposits) [1].

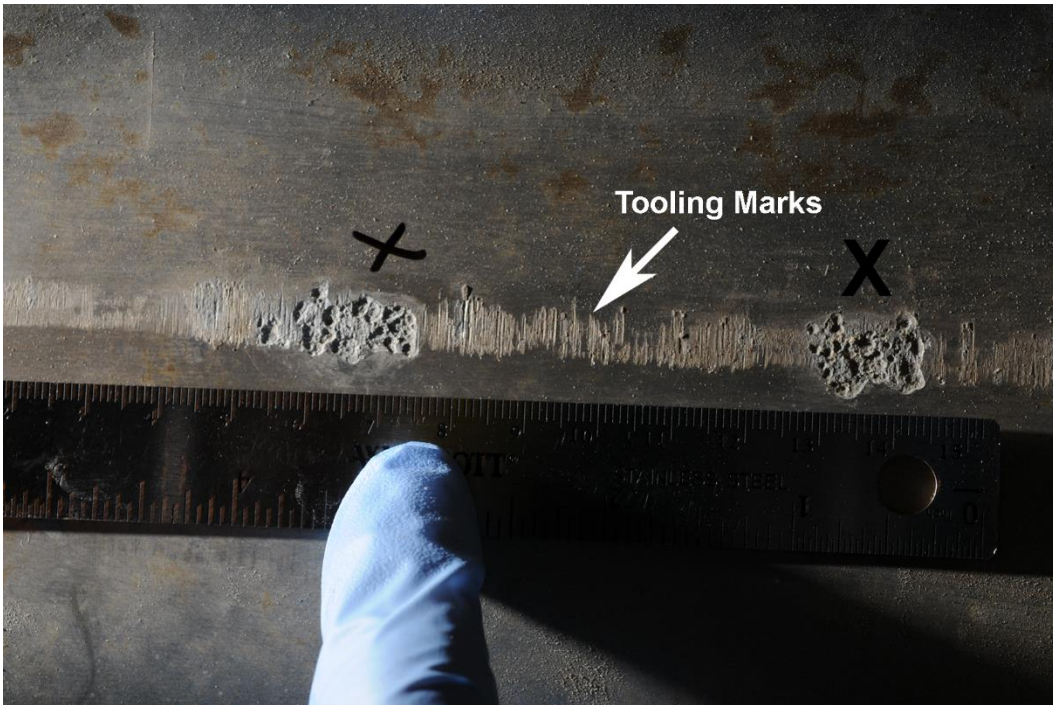


Figure A-8: Second type of under-deposit corrosion identified on tooling marks along a wall of the aeration tank (after brushing off the deposits) [1]. “Regions directly below “X” are pitting damage, showing multiple pits within pits. Vertical striations are the tooling damage discussed throughout.” [1]

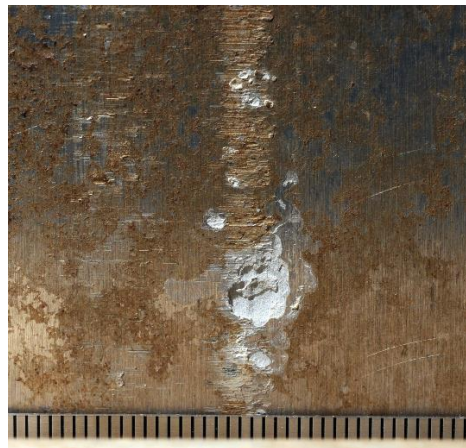


Figure A-9: “Crusty top hat” deposit on tooling marks located on vertical wall of gusset plates [1]. Images taken before (left) and after (right) removal of the deposit [1]. 1 mm divisions on the ruler in the right image [1].

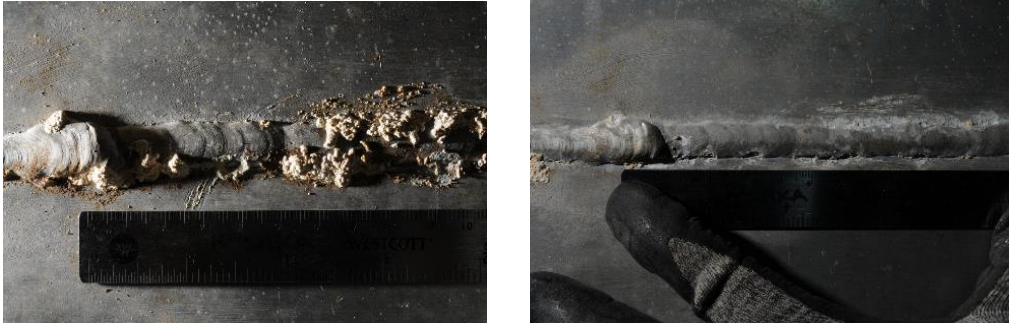


Figure A-10: Before (left) and after (right) removal of “crusty top hat” deposits from horizontal wall welds [1].

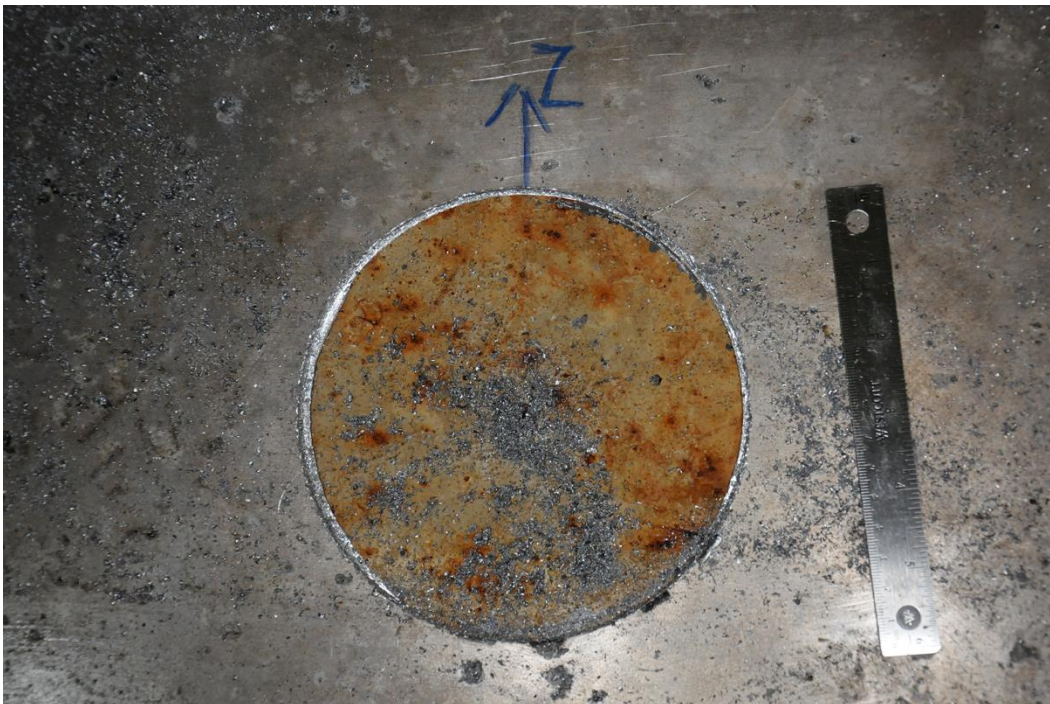


Figure A-11: Circular floor section removed from TK-3100-1 (arrow in the photo points north) [2].

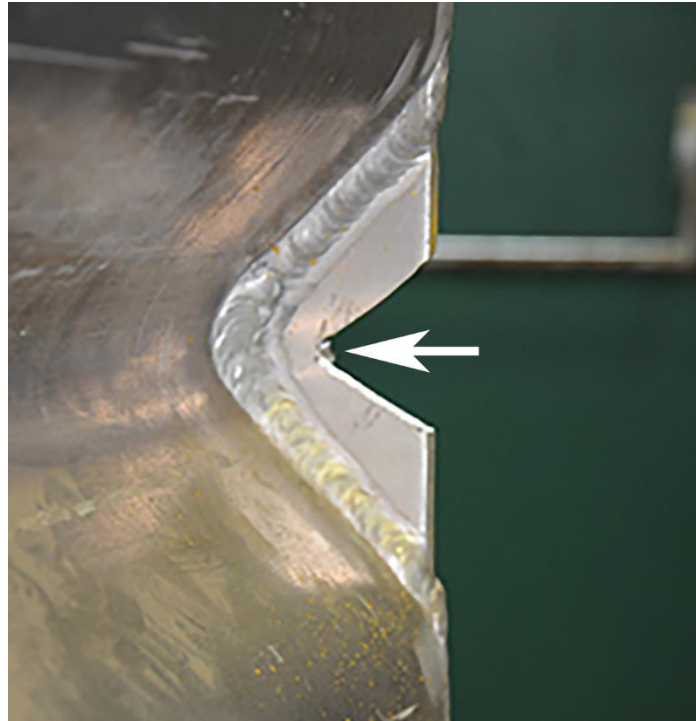


Figure A-12: “Section of webbing cut from northwest corner, bottom horizontal bend of TK-3100-1; section tip (white arrow) was notched to prevent crack formation/propagation.” [2]

### A-1.3 Scope

From previous inspections, samples were collected from the aeration tank in order for further examination and testing to be performed. Table A-2 lists the selected laboratory tests and analyses methods, which were conducted on these samples in order to carry out the necessary investigation. Their results are presented throughout the contents of this appendix (Appendix A).

It should be noted that due to the lack of corrosion damage, as well as the stamps on the bolts, no microstructural or mechanical property evaluations were performed on any of the bolts, nuts, or washers.

Table A-2: Laboratory tests and analysis work performed on samples.

Sample	Analysis / Test Method	Purpose of Test
<b>Wall Section</b>	<ol style="list-style-type: none"> <li>1. Inductively coupled plasma (ICP) mass spectroscopy (ICP-MS) and optical emission spectroscopy (ICP-OES)</li> <li>2. Metallography - imaging via optical microscopy (OM)</li> <li>3. Vickers microhardness testing (HT)</li> </ol>	<ol style="list-style-type: none"> <li>1. Determine elemental composition</li> <li>2. Microstructural examination</li> <li>3. Determine hardness and any gradients in mechanical properties</li> </ol>
<b>Floor Section</b>	<ol style="list-style-type: none"> <li>1. Visual inspection and pit depth measurements</li> <li>2. ICP-MS and ICP-OES</li> <li>3. Metallography - imaging via OM and scanning electron microscopy (SEM)</li> <li>4. Energy dispersive X-ray spectroscopy (EDX)</li> <li>5. X-Ray diffraction (XRD) analysis</li> <li>6. Fourier Transform Infrared Spectroscopy (FTIR)</li> <li>7. HT</li> </ol>	<ol style="list-style-type: none"> <li>1. Identify modes and causes of damage, and quantify pitting</li> <li>2. Determine elemental composition</li> <li>3. Microstructural examination</li> <li>4. Semi-quantitatively determine elemental composition of deposits and select microstructural features</li> <li>5. Identify crystalline corrosion products</li> <li>6. Identify amorphous corrosion products (through identification of chemical bonds)</li> <li>7. Determine hardness and any gradients in mechanical properties</li> </ol>
<b>Tubular Tie</b>	<ol style="list-style-type: none"> <li>1. Visual inspection and pit depth measurements</li> <li>2. ICP-MS and ICP-OES</li> <li>3. Metallography - imaging via OM and SEM</li> <li>4. EDX</li> <li>5. XRD</li> <li>6. FTIR</li> <li>7. HT</li> </ol>	<ol style="list-style-type: none"> <li>1. Identify modes and causes of damage, and quantify pitting</li> <li>2. Determine elemental composition</li> <li>3. Microstructural examination</li> <li>4. Semi-quantitatively determine elemental composition of deposits and select microstructural features</li> <li>5. Identify crystalline corrosion products</li> <li>6. Identify amorphous corrosion products (through identification of chemical bonds)</li> </ol>

		7. Determine hardness and any gradients in mechanical properties
<b>Aeration Line Bracket</b>	<ol style="list-style-type: none"> <li>1. Visual inspection and pit depth measurements</li> <li>2. ICP-MS and ICP-OES</li> <li>3. Metallography - imaging via OM and SEM</li> <li>4. EDX</li> <li>5. XRD</li> <li>6. FTIR</li> <li>7. HT</li> </ol>	<ol style="list-style-type: none"> <li>1. Identify modes and causes of damage, and quantify pitting</li> <li>2. Determine elemental composition</li> <li>3. Microstructural examination</li> <li>4. Semi-quantitatively determine elemental composition of deposits and select microstructural features</li> <li>5. Identify crystalline corrosion products</li> <li>6. Identify amorphous corrosion products (through identification of chemical bonds)</li> <li>7. Determine hardness and any gradients in mechanical properties</li> </ol>
<b>Corrosion Deposit or “Sludge”<sup>†</sup> Samples</b>	<ol style="list-style-type: none"> <li>1. ICP-MS</li> <li>2. SEM</li> <li>3. EDX</li> <li>4. XRD</li> <li>5. FTIR</li> </ol>	<ol style="list-style-type: none"> <li>1. Determine elemental composition</li> <li>2. Examine morphology of deposits</li> <li>3. Semi-quantitatively determine elemental composition of deposits and select microstructural features</li> <li>4. Identify crystalline corrosion products</li> <li>5. Identify amorphous corrosion products (through identification of chemical bonds)</li> </ol>

<sup>†</sup>: “Sludge” is termed deposits found within the aeration tank, whose origin is unknown. “Sludge” may include by-products of a damage mechanism or accumulation of solids from the process fluid.

#### A-1.4 Summary of Failure Investigation

The following section provides a high level summary of the findings acquired from the examinations and failure analyses performed on the collected aeration tank components and samples. An exhibit containing images which present

some of the observed findings is provided below in Figure A-13. Further information can be found in the remaining sections of this Appendix.

- Four modes of corrosion were identified on the examined components, with three on the tank floor and bracket being pitting, crevice, and galvanic corrosion. In addition to those three corrosion modes, IGC was also identified on the tubular tie.
- Overall, all corrosion was found to be *underneath* either artificial and/or naturally occurring crevice formers (also known as under-deposit corrosion).
- Pitting damage appeared to be exacerbated by dissimilar metal interactions, through direct electrical connections between the stainless steel aeration piping and various aeration tank components.
- Chlorine, sulphur, copper, nickel, and lead were identified in some deposits and examined cross-sections. These elements are known to be causes of corrosion in aluminum and aluminum alloys [3,4].
- The presence of elemental aluminum, oxygen, known crystalline aluminum hydroxides – as well as the general appearance and morphology – of the collected deposits (throughout the aeration tank), suggest that they contained aluminum corrosion products.
- The wall, floor, and bracket chemistries were within the specified range of elemental composition for 5086 and 5083 grade aluminum. Conversely, the chemistry of the tubular tie was within the stated range for 6061 grade aluminum.

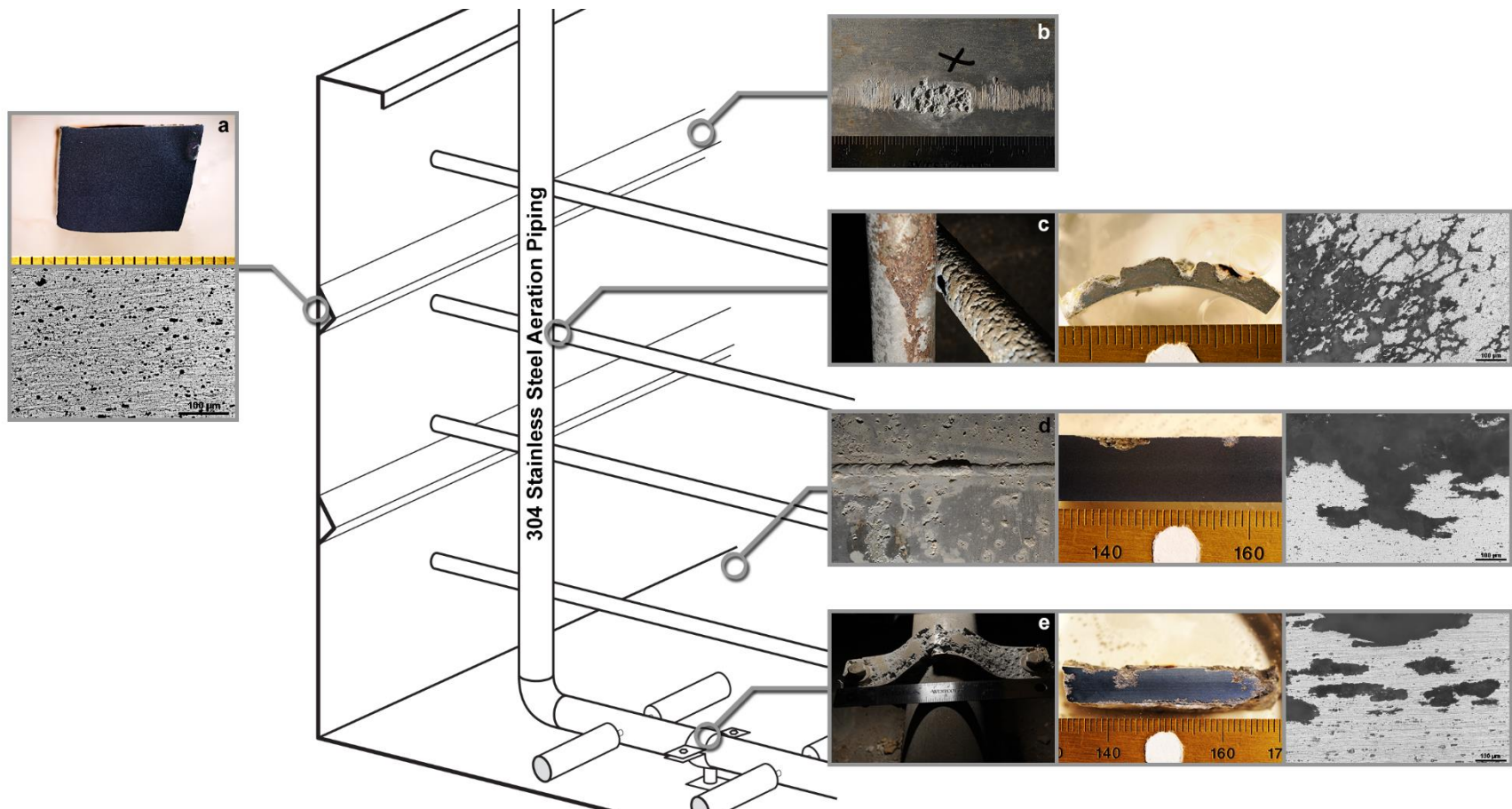


Figure A-13: Partial schematic of the aeration tank, along with images (including macrophotographs, cross-sections, and micrographs) acquired from key locations/aluminum alloy components, namely: collected wall cross-section (a), pitting on wall tooling marks (b), tubular tie in contact with aeration piping (c), tank floor (d), and an aeration piping bracket (e). Four modes of corrosion (pitting, crevice, galvanic, and IGC) were identified. Deposit(s) were removed to aid in the macrophotography. Scale on ruler is in mm.

- It appears that the environment (i.e., process fluid) and its composition may be the “main” causes of corrosion for the components in question. Moreover, the observed corrosion may have been induced from a biological origin; however, further biological assessments and testing are required in order to confirm any microbial involvement.

## **A-2.0 Investigation**

### **A-2.1 Visual and Non-destructive Examination**

The following section will be divided into subsections comprised of the individual, metallic, aeration tank components collected, namely: wall, floor, tubular tie, and aeration line bracket.

#### *A-2.1.1 Wall*

A small section of webbing (Figure A-14) was cut from the northwest corner of the aeration tank TK-3100-1. More specifically, the webbing was removed from the bottom horizontal bend of the external northwest corner. Examination of the wall section revealed no signs of visually apparent corrosion, or significant mechanical damage such as cracking, denting, or gouging.

From the internal visual inspection, the south wall was stamped *Dual Certified 5086 5083 H116 Novelis 0.375 Ticket 03077-1 ASTM B928-04* [1]. It was suspected that the other tank walls were constructed of the same grade and temper of aluminum alloy; however, no material stamps were found on the north, west, or east walls – partially due to inaccessibility.

Surface fabrication markings (longitudinal lines) were observed on the surface of the wall specimen. The orientation of the surface fabrication markings were parallel to the “up arrow” (pointing towards the top of the tank), and believed

to be in parallel to the rolling direction of the overall wall sheet (i.e., surface markings were indicative of rolling marks).

Wall thickness measurements were collected and listed below in Table A-3. The average measurement ( $9.21 \pm 0.06$  mm;  $n = 3$ ) was slightly below the thickness listed in the stamp (9.53 mm); however, there are no dimensional tolerances specified in the ASTM B928 standard [5].



Figure A-14: Wall section collected from aeration tank. Scale is in mm.

Table A-3: Wall thickness measurements

Specimen	Thickness [inch (mm)]	
	Measurements	Average $\pm$ CI
Wall	0.363 (9.22) 0.362 (9.19) 0.364 (9.23)	$0.363 \pm 0.002$ ( $9.21 \pm 0.06$ )
<b>ASTM B928-04 5086/5083 H116</b>	-	<b>0.375 (9.53)</b>

CI: 95% Confidence Interval; refer to Section 6.0 for sample calculation; shaded row is a reported material standard value

### *A-2.1.2 Floor*

A ~14.5 cm diameter floor section (Figure A-15) was removed from aeration tank TK-3100-1 for further examination. More specifically, the center of the circular section was approximately 6 m from the west wall and 99 cm from the south wall.

Several pits of varying diameter (Figures A-16 and A-17) were found on the top surface (exposed to process fluid) of the floor, with the largest diameter pit equaling approximately 5.1 cm (Figure A-16). Examination and description of the pit openings and cross-sections – in this section and throughout Appendix A – follow the guidelines provided in ASTM G46 [6]. The pits appeared to have a wide, shallow opening with multiple smaller pits encapsulated within them. The smaller pits were elliptical in shape, deeper, and also exhibited signs of undercutting (Figures A-16 through A-18). There also appeared to be alignment of the rolling direction with some features in the pits (Figure A-18). In most locations, within the pits, there appeared to be small amounts of creamy white deposit. Attempts were made to remove the deposit from inside the pits, unfortunately trace amounts were collected. Meanwhile, in areas of pits absent of white deposit, there appeared to be either exposed metal or dark, brown deposit. This deposit is believed to be from exposure to the wastewater process fluid.

Also observed on the top surface of the floor specimen were surface fabrication markings (longitudinal lines), which were oriented perpendicular to the north arrow (pointing towards the north wall), and believed to be in parallel to the rolling direction of the overall floor sheet. Finally, light scratches were identified on the material surface due to the removal process of collecting the floor specimen, as well as trying to collect deposit from within pits.

Pit measurements were collected from the top surface of the floor specimen. The location of pits measured, as well as their depths can be found in Figure A-19

and Table A-4, respectively. Note that a digital pit gauge with a fine tip needle was used. Moreover, the pit depths were measured to the deepest part of the pit (perpendicular to the surface), as per ASTM G46 [6]. From the measurements, the average pit depth was calculated to be  $1.03 \pm 0.33$  mm ( $n = 13$ ).

On the opposite side of the floor specimen (bottom surface; in contact with the steel floor) orange and white deposits were also observed (Figure A-20). The orange deposit appeared to be iron oxide corrosion product from the steel floor (Figure A-12). Meanwhile, the shallow pits were found within and adjacent to the white deposits (Figures A-21 and A-22). These pits had irregular openings. At present, there is no evidence available to suggest that both the deposits and pits were incurred due to leaking of the aeration tank. There are several possible sources of moisture (that could have led to corrosion), which include: being trapped upon installation, collected from fluid spilling over the side and wicking inward (beneath the tank), or collected via washing of the floors or equipment. Conversely, it could be possible that the atmosphere itself had induced the corrosion. Nevertheless, whichever the cause of corrosion, there is no evidence to suggest that the aeration tank floor is or is not leaking.

Finally, surface fabrication markings (longitudinal lines) were also identified on the bottom surface – oriented perpendicular to the north arrow – and believed to be in parallel to the rolling direction of the overall floor sheet.

Floor thickness measurements were collected and listed in Table 5. Note that the floor thickness measurements were taken between 1.9 and 2.5 cm away from the cut edges. Furthermore, thickness measurements were acquired with a digital micrometer at locations where original, undamaged material was present. The average floor thickness was calculated to be  $9.28 \pm 0.04$  mm ( $n = 4$ ).

No standard specification or material grade stamp was identified on the floor; however, it is suspected that the floor was manufactured from a similar grade

of aluminum alloy as the walls (a 5086 or 5083 grade of aluminum alloy). Additionally, no comparisons could be made between the collected thickness measurements and any dimensional tolerances that may be listed in a material standard.



Figure A-15: As collected cut-out of floor section. Note the pits still contain metal shavings/other debris produced during removal the section from the aeration tank. (Blue arrow points north). Hole in the center is due to the hole saw used to extract the disc. Scale is in mm.



Figure A-16: Close-up of large pit. Round pits within pits and undercutting (white arrows) can be observed. Scale is in mm.



Figure A-17: Close-up of small pits. Scale is in mm.

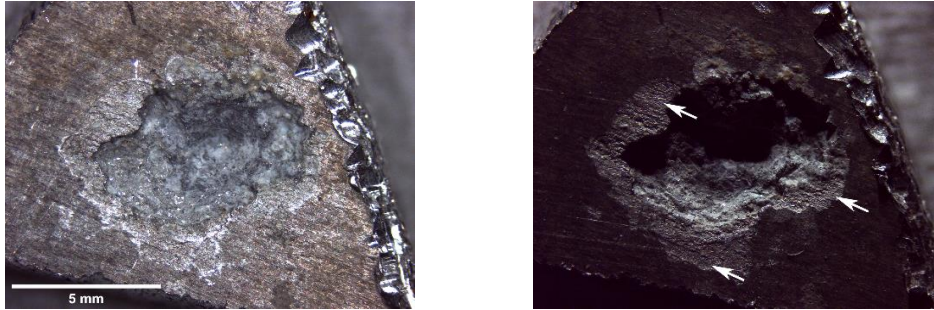


Figure A-18: Stereomicroscope images of small floor pit, with varying amounts of indirect lighting. Alignment of the rolling direction with some features in the pits (white arrows; parallel to rolling direction) can also be observed.



Figure A-19: Location of pit depth measurements. Scale is in mm.

Table A-4: Floor pit depth measurements

Pit Number	Depth Measurements	
	[inch]	[mm]
1	0.076	1.94
2	0.040	1.01
3	0.019	0.47
4	0.011	0.29
5	0.054	1.38
6	0.021	0.54
7	0.050	1.26
8	0.020	0.52
9	0.070	1.77
10	0.024	0.60
11	0.057	1.44
12	0.060	1.52
13	0.025	0.64
<b>Average ± CI</b>	0.041 ± 0.013	1.03 ± 0.33

CI: 95% Confidence Interval



Figure A-20: Bottom surface of collected cut-out of floor section. Scale is in mm.

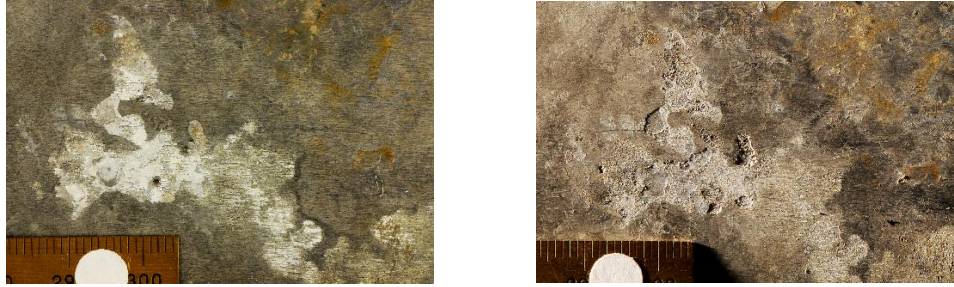


Figure A-21: Corrosion (as small, irregular shaped pits) on the bottom of the aeration tank floor. Images collected with varying amounts of indirect lighting. Scale is in mm.



Figure A-22: Corrosion (as small, irregular shaped pits) on the bottom of the aeration tank floor. Images collected with varying amounts of indirect lighting. Scale is in mm.

Table A-5: Floor thickness measurements

Thickness [inch (mm)]	
Measurements	Average $\pm$ CI
0.365 (9.27)	0.365 $\pm$ 0.002 (9.28 $\pm$ 0.04)
0.365 (9.27)	
0.367 (9.32)	
0.365 (9.27)	

CI: 95% Confidence Interval

### A-2.1.3 Tubular Tie

The top tubular tie on row 7 (adjacent to aeration line #3) was removed from the aeration tank for further examination and laboratory testing. During removal, the tie was cut into two sections, the first being 61 cm in length (north section; Figure A-23) and the second being 2.13 m in length (south section; Figure A-24). Both sections exhibited varying amounts of corrosion damage, with the most severe

damage (i.e. through-wall pitting) identified on the north section where the tie was immediately adjacent to the stainless steel aeration piping (Figure A-25).

The size of the elliptical hole on the north section was approximately 3.0 cm (minor axis) by 4.4 cm (major axis). The hole was located at the 9 o'clock position on the tie (clock face facing towards the north tank wall; top of tie being the 12 o'clock position). Surrounding the hole, deep pits were found, with the deepest pits observed immediately adjacent to the hole (Figures A-25 and A-26). These pits exhibited a range of different opening shapes, including round, elongated, and irregular. Additionally, away from the through-hole, the pitting appeared to be fairly uniform in distribution around the circumference, and was observed along the length of the north section. Moreover, regarding the entire length of the tie (both north and south sections), the pitting areal density appeared to decrease moving from the south end of the north section to the south end of the south section.

Deposits were found throughout the length of the tie north section, including – but not limited to – in pits, on or near remaining outer-diameter wall material (Figure A-27), and on the inner diameter of the tie (Figure A-25). The colour of deposits varied, with colours such as grey, creamy white, yellow, and brown being present across the length of the north section. However, under higher magnification, deposits within pits appeared to be creamy white in colour (Figure A-28). The other coloured deposits are believed to be formed from exposure to the wastewater process fluid. Additionally, what appeared to be fabrication marks – from either the drawing or extrusion process – were observed on the non-corroded, outer diameter material of the tie north section (Figure A-28).

Pitting was observed along the length of the south section of the tubular tie. The pitting on the southern-most end of the tubular tie was similar in opening shape to the pits observed on the north section; however, the pits were visually less pronounced in size, depth, and proportion of the surface covered (Figures A-29

through A-32). Moreover, the pitting on the south section appeared to be less uniform and more random in distribution around the tie circumference than the north section.

Similar to the north section, deposits were found throughout the length of the tie south section. The locations of deposit included (but were not limited to) in pits, on or near remaining outer-diameter wall material (Figures A-30 and A-32), and on the tie inner diameter. The colour of deposits varied similar to what was observed on the north section of the tubular tie. Furthermore (as what was also distinguished on the north section), under higher magnification, deposits within pits appeared to be creamy white in colour (Figures A-30 and A-32). The other coloured deposits are believed to be formed from exposure to the wastewater process fluid. Fabrication marks – from either the drawing or extrusion process – were also observed on the non-corroded, outer diameter material of the tie south section (Figures A-31 and A-32).

Across the entire length of the tie (both north and south sections) there appeared to be a wide variation in pit depth. Depths ranged from through-wall pitting near the north end of the tie (Figures A-25 and A-27), to very shallow, near superficial pits on the south end (Figures A-29 and A-31). Hence, pit depth measurements were not collected for the tubular tie. Additionally, it is believed that galvanic effects from the proximity of the stainless steel aeration piping were exacerbating corrosion damage observed on the north section. This corrosion damage was especially apparent in material which was immediately adjacent to, or in physical contact with, the aeration piping.

Tie thickness and diameter measurements were collected and listed in Tables A-6 and A-7, respectively. Note that the tie thickness measurements were collected using a caliper. Moreover, these measurements were taken from locations where original, undamaged, outer and inner diameter material was present. From the collected measurements, the average tie thickness was calculated to be  $3.68 \pm$

0.04 mm ( $n = 3$ ) for the north end of the north section and  $3.61 \pm 0.21$  mm ( $n = 3$ ) for the south end of the south section. Conversely, the average diameter measurement was approximately 48 mm.

No standard specification or material grade stamp was identified on any section of the tubular tie; however, it was suspected that the tie was constructed of a grade of aluminum alloy. Additionally, no comparisons could be made between the collected thickness or diameter measurements and any dimensional tolerances that may be listed in a material standard or drawing package.



Figure A-23: As collected north section of removed tubular tie. Arrow points north and scale is 300 mm.



Figure A-24: As collected south section of removed tubular tie. Arrow points north and scale is 300 mm.

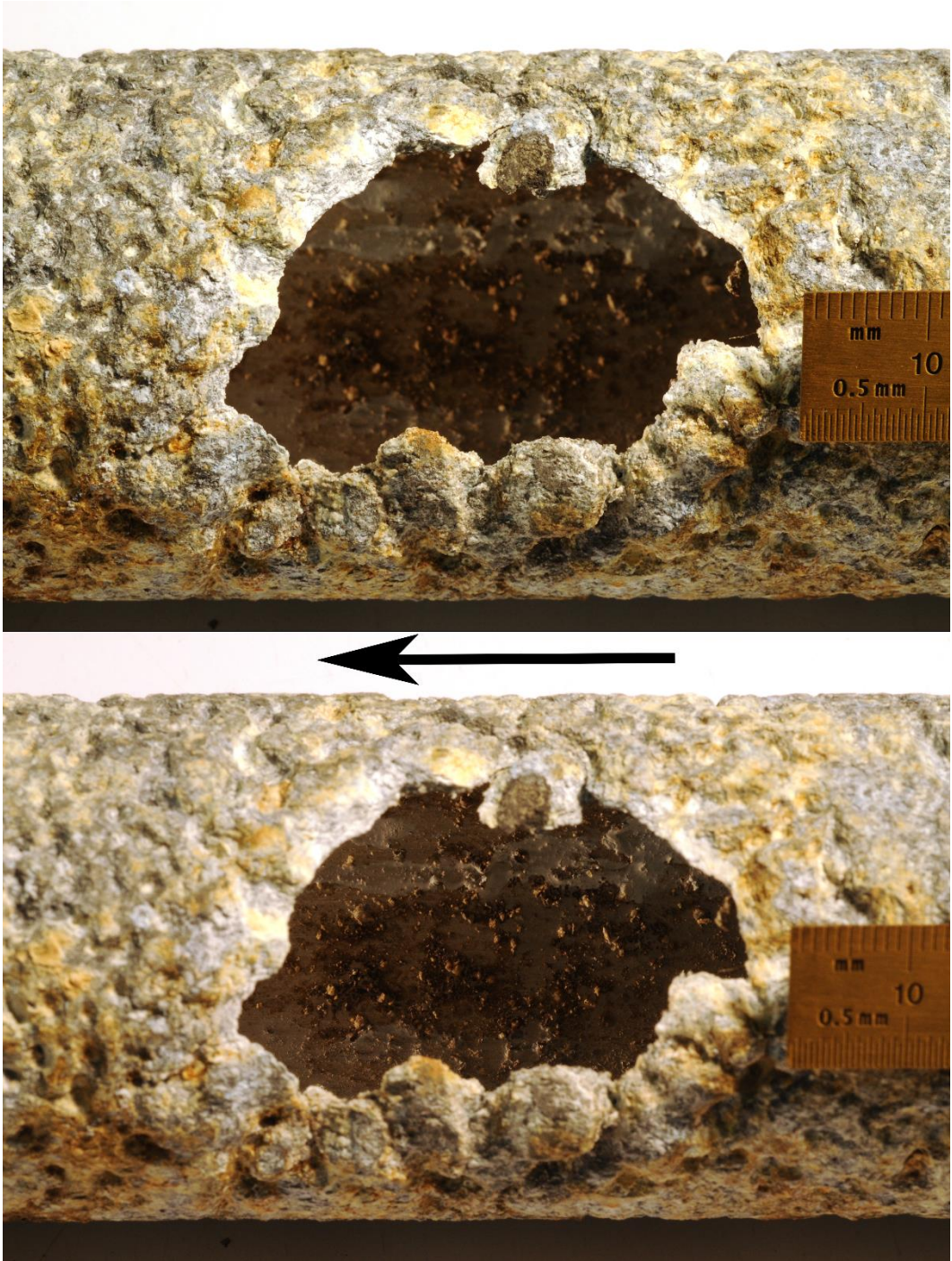


Figure A-25: Hole in north section of tubular tie. Composite image with focus on the outside (top image) and inside (bottom image) of the tie. Arrow points north. Scale is in mm.



Figure A-26: Pits on opposite side of through-wall hole. Images collected with varying amounts of indirect lighting. Scale is in mm.

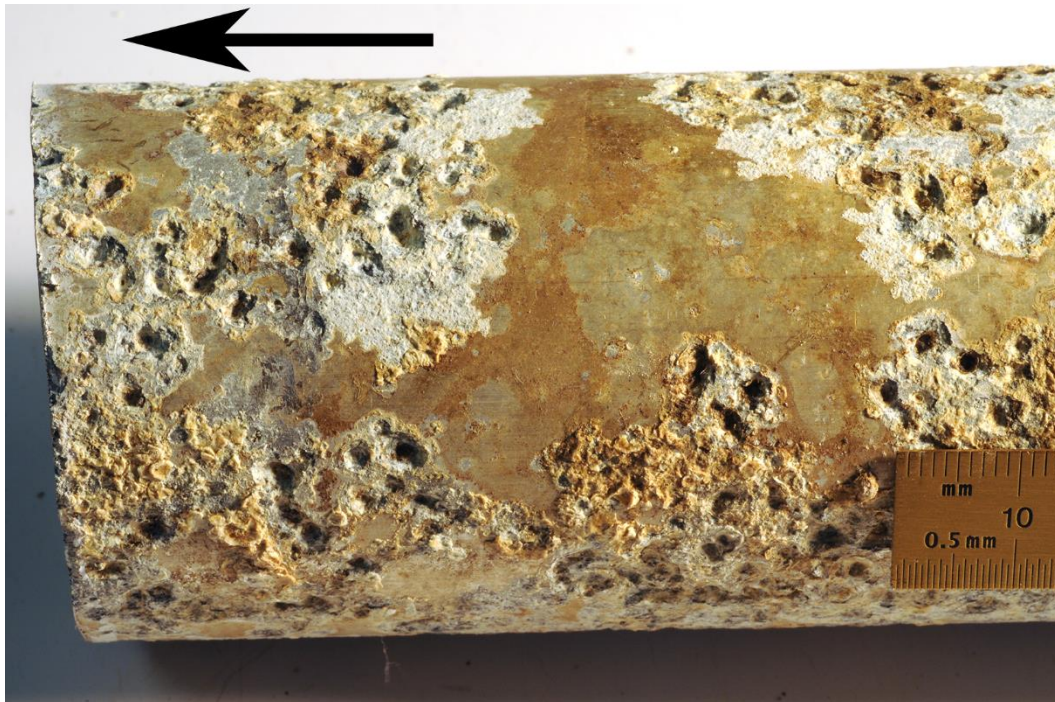


Figure A-27: North end of north section of the tubular tie. Arrow points north. Scale is in mm.

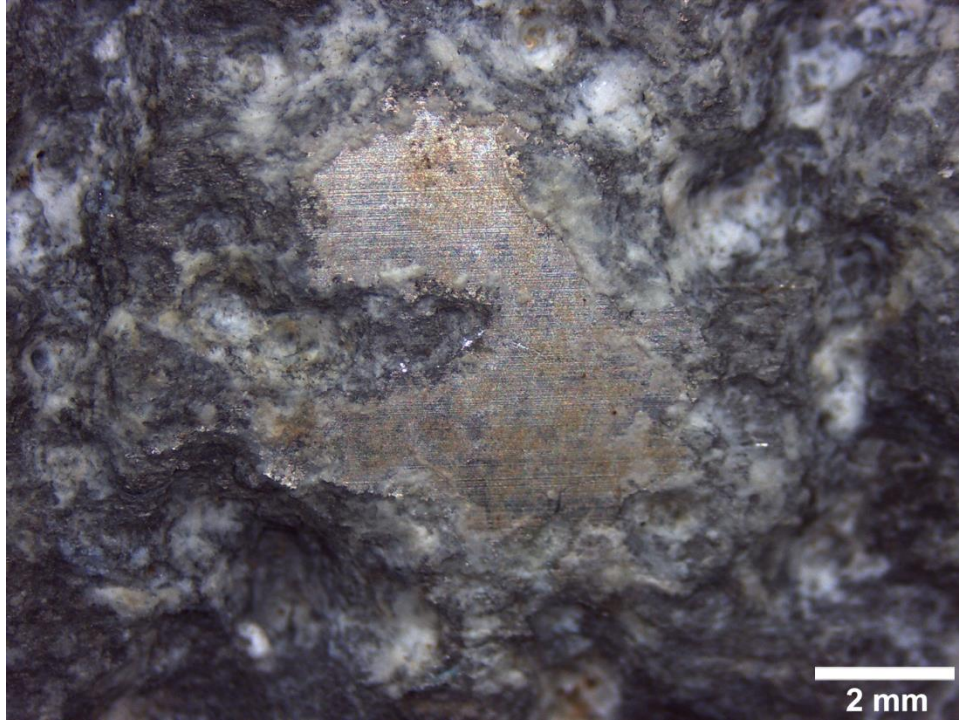


Figure A-28: Original outer diameter material near the hole in the north section of the tubular tie.

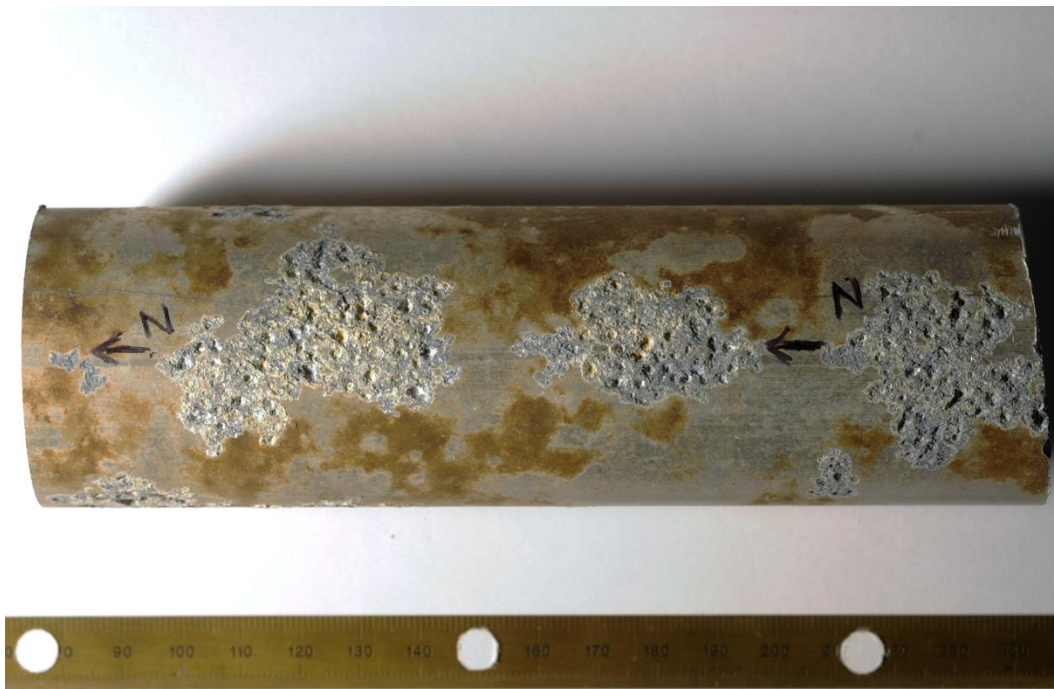


Figure A-29: South end of south portion of the tubular tie. Arrows written on the tie point north. Scale is in mm.

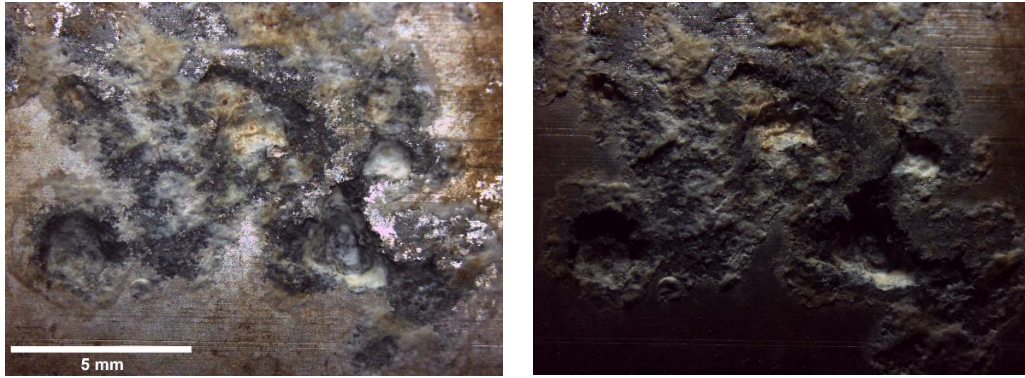


Figure A-30: Pits in south section of tubular tie. Images collected with varying amounts of indirect lighting.

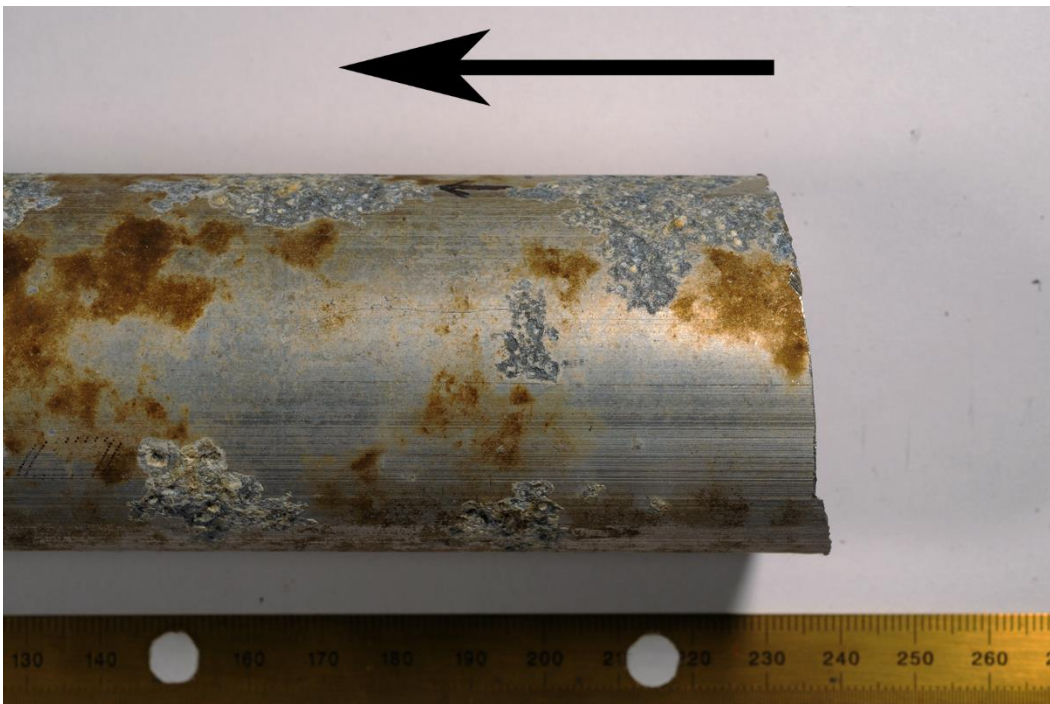


Figure A-31: South-most section of south portion of the tubular tie. Arrow points north. Scale is in mm.

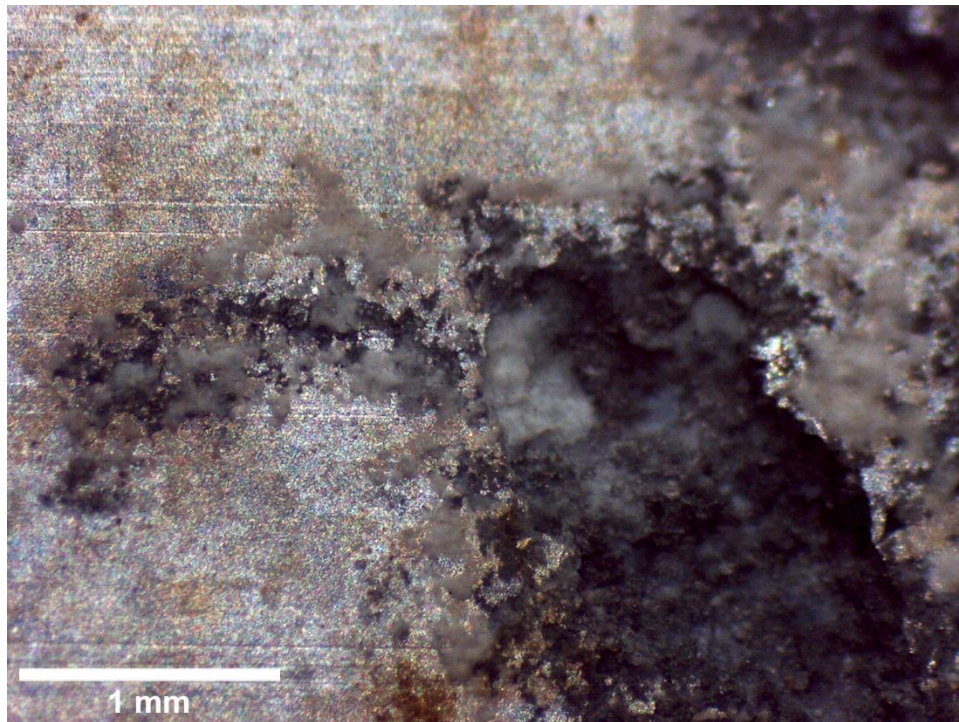


Figure A-32: Close-up of small pits (from above composite images).

Table A-6: Tie thickness measurements

Location	Thickness [inch (mm)]	
	Measurements	Average $\pm$ CI
North End of North Section	0.146 (3.70)	0.145 $\pm$ 0.002 (3.68 $\pm$ 0.04)
	0.144 (3.66)	
	0.145 (3.69)	
South End of South Section	0.139 (3.54)	0.142 $\pm$ 0.008 (3.61 $\pm$ 0.21)
	0.146 (3.71)	
	0.141 (3.59)	

CI: 95% Confidence Interval

Table A-7: Tie diameter measurements

Location / Clock Position		Diameter [inch (mm)]	
Tie End	Orientation	Measurements	Average ± CI
North <sup>†</sup>	12-6	1.890 (48.01)	1.893 ± 0.005 (48.07 ± 0.14)
		1.894 (48.11)	
		1.894 (48.09)	
	3-9	1.901 (48.29)	1.904 ± 0.008 (48.35 ± 0.19)
1.903 (48.34)			
1.907 (48.44)			
South <sup>‡</sup>	12-6	1.896 (48.16)	1.895 ± 0.008 (48.12 ± 0.20)
		1.897 (48.18)	
		1.891 (48.03)	
	3-9	1.898 (48.21)	1.897 ± 0.002 (48.19 ± 0.05)
		1.898 (48.20)	
		1.897 (48.17)	

CI: 95% Confidence Interval; <sup>†</sup> north end of north section; <sup>‡</sup> south end of south section

*A-2.1.4 Aeration Line Bracket*

A bracket (and associated hardware including nuts, bolts, and washers) was removed from the south end of the western most aeration line (aeration line #1; ~ 0.78 m from the west wall) for further examination and laboratory testing (Figure A-33). Examination of the bracket revealed significant pitting damage and deposit buildup on all surfaces of the bracket (Figures A-33 through A-35). On surfaces directly exposed to the process fluid, the pitting appeared similar to what was observed on the aeration tank floor specimen.

Pits of varying diameter (Figure A-36) were found on the top bracket surface. The pits appeared to have a wide, shallow opening with multiple smaller pits encapsulated within them. The smaller pits were elliptical in shape, deeper, and also exhibited signs of undercutting (Figures A-36 through A-38). In most locations, within the pits, there appeared to be small amounts of creamy white deposit. Meanwhile, in areas of pits absent of white deposit, there appeared to be either exposed metal or grey, yellow, or dark brown deposit. This deposit is believed to be from exposure to the wastewater process fluid. Additionally, most areas where 304 stainless steel bolts and washers covered the bracket were found

to be undamaged (Figures A-33 and A-36). However, deep pits were identified immediately adjacent to or slightly below where the washers were installed (Figure A-38). It is believed that galvanic effects from the stainless steel bolts and washers were exacerbating the corrosion damage observed on the bracket; particularly in locations immediately adjacent to where the bolts and washers were installed.

Pitting was also observed on the sides and bottom of the bracket (Figures A-34, A-35, and A-39). The pitting size and morphology on the bottom of the bracket was similar to what was observed on the top of the bracket; however, the pits appeared to be shallower. Meanwhile, pits on the side of the bracket appeared to be smaller in area and had either a round or irregular opening.

A large amount of creamy white deposit was found on the bottom of the bracket (Figure A-35), where the bracket was in direct contact with a 304 stainless steel aeration line. In other locations, on the bottom of the bracket, there appeared to be either exposed metal or grey, yellow, or dark brown deposit. This deposit is believed to be from exposure to the wastewater process fluid. On the side of the bracket, within most pits, there appeared to be small amounts of creamy white deposit (Figure A-39). Meanwhile, in other locations or areas of pits absent of white deposit, there appeared to be either exposed metal or grey, yellow, or dark brown deposit (Figure A-34). This deposit is also believed to be from exposure to the wastewater process fluid.

Pit measurements were collected from the top, bottom and one side of the bracket. The location of pits measured, as well as their depths, can be found in the following figures and tables: Figure A-40 and Table A-8 for the top of the bracket; Figure A-41 and Table A-9 for the bottom of the bracket; and Figure A-42 and Table A-10 for the side of the bracket. As previously noted in Section 2.1.2, a digital pit gauge with a fine tip needle was used to collect the measurements. Moreover, the pit depths were measured to the deepest part of the pit (perpendicular to the surface), as per ASTM G46 [6]. Also, it was difficult to gather reliable

measurements from the bottom bracket pits. Comparing the average pit depths – from the three locations – the pitting was determined to be the worst on the top of the bracket ( $3.60 \pm 0.61$  mm;  $n = 16$ ), followed by the side ( $1.56 \pm 0.22$  mm;  $n = 4$ ), and finally the bottom ( $0.95 \pm 0.18$  mm;  $n = 7$ ).

Again, the bolting and associated hardware appeared intact with no apparent signs of corrosion or mechanical damage. Hence, no further examination was performed on the bolting or hardware (which includes nuts, bolts, and washers).

Also observed on the top surface of the bracket were surface fabrication markings (longitudinal lines); however, they appeared to have very little directionality (Figure A-37).

Bracket width and thickness measurements were collected and listed in Tables A-11 and A-12, respectively. Note that the thickness measurements were taken from locations where original, undamaged material was present. The average bracket width and thickness measurements were calculated to be  $38.64 \pm 0.25$  mm ( $n = 5$ ) and  $6.10 \pm 0.43$  mm ( $n = 4$ ), respectively.

No standard specification or material grade stamp was identified on the bracket; however, it was suspected that the bracket was constructed of a grade of aluminum alloy. Moreover, no comparisons could be made between the collected width or thickness measurements and any dimensional tolerances that may be listed in a material standard. The bolts used to fasten the clips around the air line were stamped A2 70, which is a grade of 304 stainless steel. No stamps were found on any of the collected nuts or washers.



Figure A-33: As collected photo of bracket, with nuts, washers, and bolts (hardware). Arrow on the bracket points towards the north wall of the aeration tank. Scale is in mm.



Figure A-34: As collected photo of bracket side, with hardware. Scale is in mm.



Figure A-35: Bottom of bracket with hardware removed. Scale is in mm.



Figure A-36: As collected photo of the top of the bracket, with hardware removed. Arrow on the bracket points towards the north wall of the aeration tank. Scale is in mm.

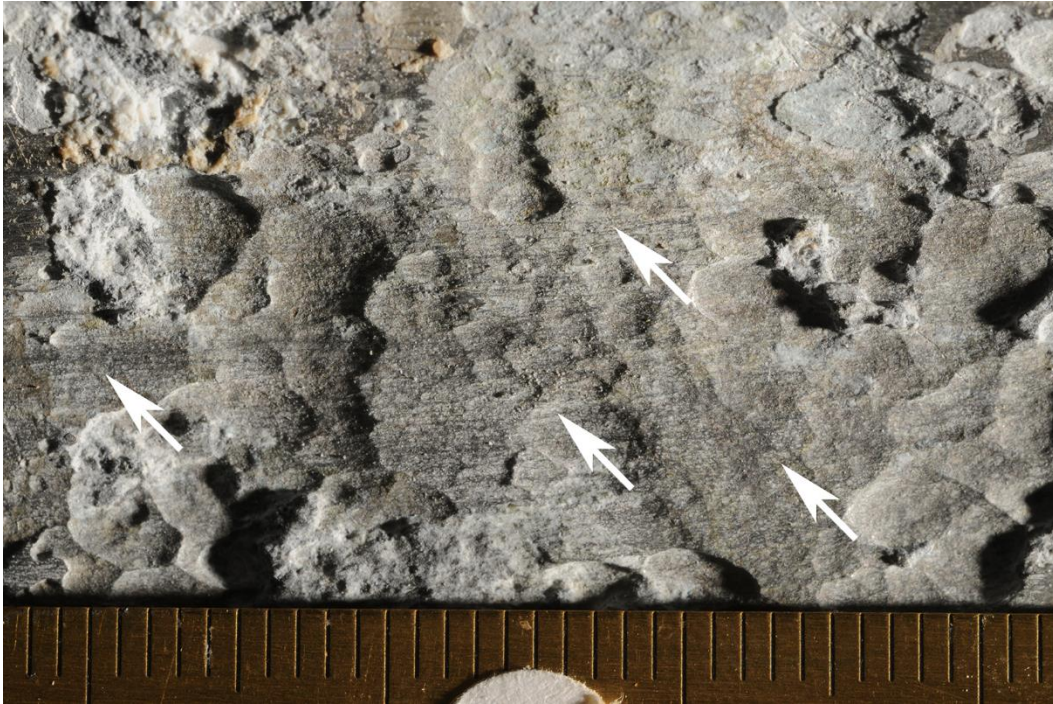


Figure A-37: Close-up on bracket pits and surface fabrication markings (white arrows). Scale is in mm.



Figure A-38: Deep pits found immediately adjacent to where washers were installed. Images collected with varying amounts of indirect lighting. Scale is in mm.



Figure A-39: Pitting identified on the side of the bracket. Images collected with varying amounts of indirect lighting. Scale is in mm.

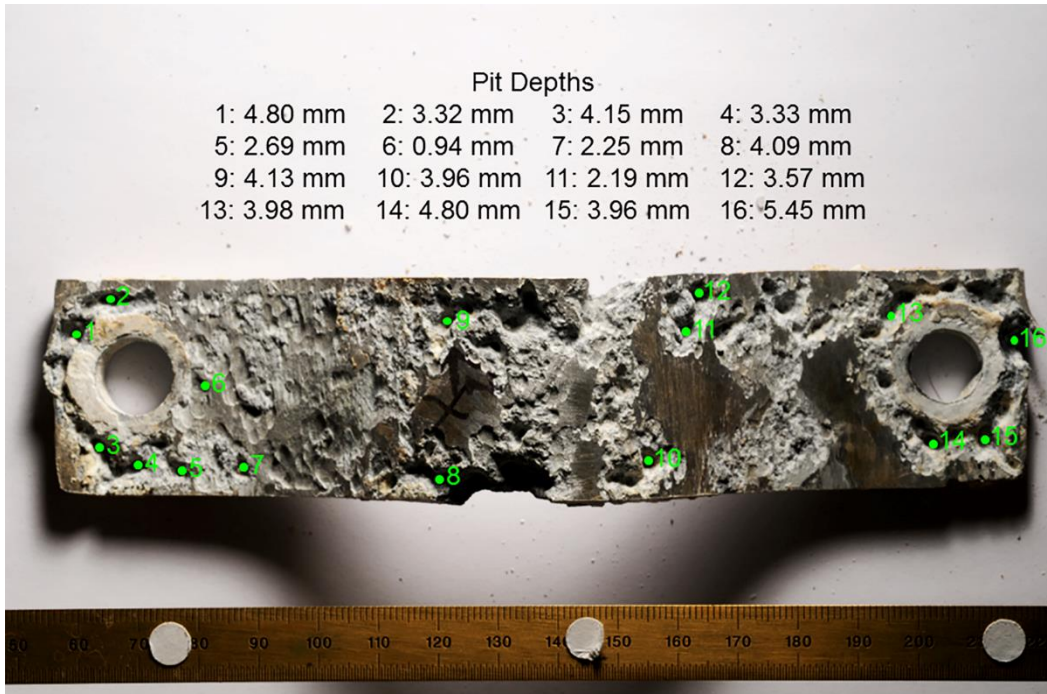


Figure A-40: Pit depths on the top of the bracket. Arrow on the bracket points towards the north wall of the aeration tank. Scale is in mm.

Table A-8: Top of bracket pit depth measurements

Pit Number	Depth Measurements	
	[inch]	[mm]
1	0.189	4.80
2	0.131	3.32
3	0.163	4.15
4	0.131	3.33
5	0.106	2.69
6	0.037	0.94
7	0.089	2.25
8	0.161	4.09
9	0.163	4.13
10	0.156	3.96
11	0.086	2.19
12	0.141	3.57
13	0.157	3.98
14	0.189	4.80
15	0.156	3.96
16	0.215	5.45
<b>Average ± CI</b>	0.142 ± 0.024	3.60 ± 0.61

CI: 95% Confidence Interval

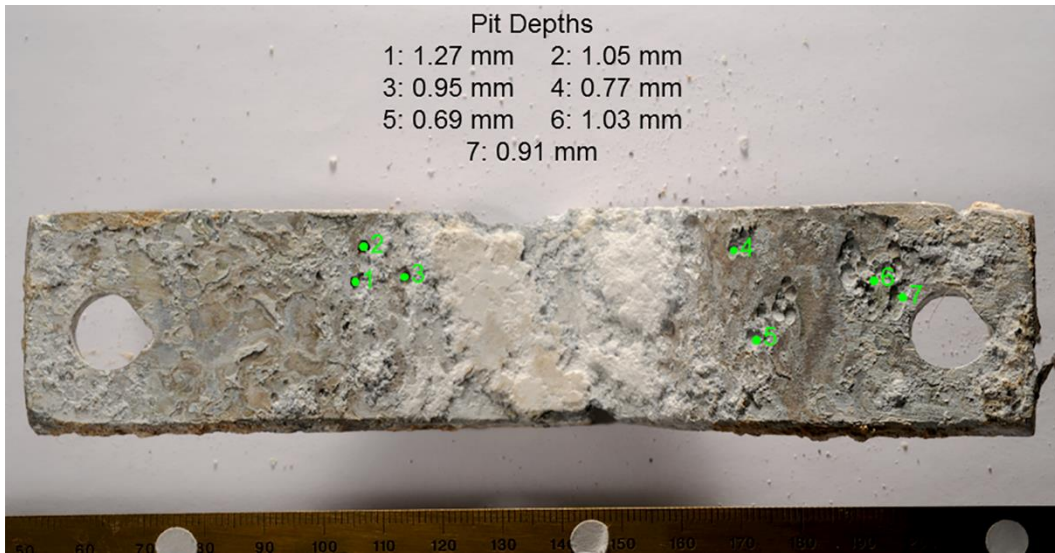


Figure A-41: Pit depths on the bottom of the bracket. Scale is in mm.

Table A-9: Bottom of bracket pit depth measurements

Pit Number	Depth Measurements	
	[inch]	[mm]
1	0.050	1.27
2	0.041	1.05
3	0.037	0.95
4	0.030	0.77
5	0.027	0.69
6	0.041	1.03
7	0.036	0.91
<b>Average ± CI</b>	<b>0.038 ± 0.007</b>	<b>0.95 ± 0.18</b>

CI: 95% Confidence Interval

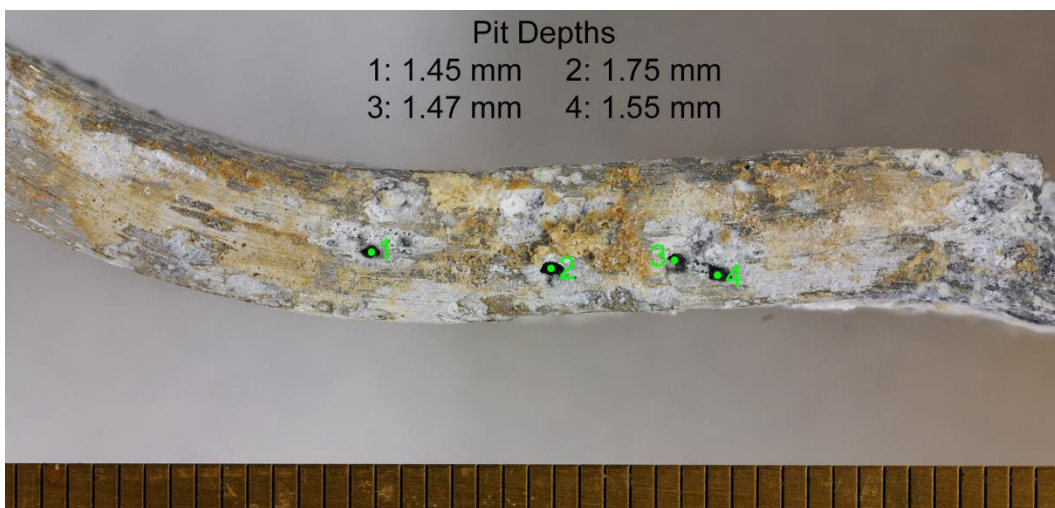


Figure A-42: Pit depths on the side of the bracket. Scale is in mm.

Table A-10: Bracket side pit depth measurements

Pit Number	Depth Measurements	
	[inch]	[mm]
1	0.057	1.45
2	0.069	1.75
3	0.058	1.47
4	0.061	1.55
<b>Average ± CI</b>	0.061 ± 0.009	1.56 ± 0.22

CI: 95% Confidence Interval

Table A-11: Bracket width measurements

Width [inch (mm)]	
Measurements	Average ± CI
1.512 (38.41)	1.521 ± 0.010 (38.64 ± 0.25)
1.526 (38.76)	
1.531 (38.89)	
1.515 (38.47)	
1.522 (38.65)	

CI: 95% Confidence Interval

Table A-12: Bracket thickness measurements

Thickness [inch (mm)]	
Measurements	Average ± CI
0.228 (5.79)	0.240 ± 0.017 (6.10 ± 0.43)
0.236 (5.99)	
0.252 (6.41)	
0.244 (6.21)	

CI: 95% Confidence Interval

## A-2.2 Chemical Analysis

The following section will be divided into subsections based on the analysis techniques performed on the collected specimens. Also, labels of the collected deposits, as well as brief descriptions and locations where they were collected, are provided in Table A-13.

Table A-13: Deposit labels and locations of collection

<b>Deposit Label</b>	<b>Description and Location</b>
<b>Bracket – Bottom</b>	Creamy white deposit collected from the bottom surface of the removed bracket.
<b>Bracket – Pits</b>	Creamy white deposit collected from multiple pits from the top surface of the removed bracket.
<b>Bracket/Air Line</b>	“Sludge” <sup>†</sup> deposit collected from between the north clip and third aeration line (relative to the west aeration tank wall).
<b>South Section End – Inside</b>	Creamy white deposit collected from the inner diameter of the south end of the south section of the removed tubular tie.
<b>North Section Hole – Inside</b>	Creamy white deposit collected from the inner diameter of the north end of the north section of the removed tubular tie. Deposit near the through-wall hole.
<b>North Section Hole – Pits</b>	Creamy white deposit collected from multiple pits adjacent to the through-wall hole on the north end of the north section of the removed tubular tie.
<b>Base Plate</b>	“Sludge” <sup>†</sup> deposit from base plate of an air line pipe support. Located below the south bracket on the first aeration line (relative to the west aeration tank wall).
<b>Floor Deposit #1</b>	“Sludge” <sup>†</sup> deposit located under the first row of diffusers, on the second aeration line (relative to the west aeration tank wall), near the south tank wall.
<b>Floor Deposit #2</b>	“Sludge” <sup>†</sup> deposit located under the first aeration line (relative to the west aeration tank wall), near the south tank wall.
<b>Floor – Pit Deposit</b>	Creamy white deposit collected from multiple pits from the top surface of the removed floor sample.
<b>Wall Horizontal Weld and Grind Marks</b>	“Crusty top hat” deposit from horizontal welds and buffing marks on the south tank wall. Deposit located between the second and third, as well as the third and fourth (bottom) rows of tubular ties.
<b>Wall Tooling Marks</b>	“Crusty top hat” deposit from tooling marks on the south aeration tank wall. Deposit located between the second and third, as well as the third and fourth (bottom) rows of tubular ties.

<sup>†</sup>: “Sludge” is termed deposits found within the aeration tank, whose origin is unknown. “Sludge” may include by-products of a damage mechanism or accumulation of solids from the process fluid.

*A-2.2.1 Inductively Coupled Plasma Mass Spectroscopy (ICP-MS) and ICP Optical Emission Spectroscopy (ICP-OES)*

ICP-MS and ICP-OES were performed on metallic samples cut from the wall, floor, tubular tie, and aeration piping bracket in order to determine their elemental compositions. The results are presented in Table A-14. Note that only the primary alloying elements' weight percentages are listed. Also presented in Table A-14 are the elemental compositions of the standard grades of aluminum alloys which match the compositions of the samples collected from each component. The tested components were made from the following aluminum alloy grades:

1. Tubular Tie: 6061
2. Floor: 5086 and 5083
3. Wall: 5086 and 5083
4. Bracket: 5086 and 5083

Note that the weight percentage for magnesium (Mg) in the floor sample (3.97 weight %) is slightly below the minimum Mg weight percentage for 5083 grade aluminum (4.0 weight %). However, upon rounding of the floor Mg weight percentage to appropriate significant figures – as used for the grade compositions – the floor meets the minimum Mg requirement to be classified as 5083 grade aluminum.

ICP-MS was performed on several samples from deposits collected from within the aeration tank. Their respective chemistries are listed below in Table A-15. Note that ICP-MS was only performed on collected samples with sufficient mass that could be destructively examined (i.e.,  $\geq 0.2$  g). All other deposits' elemental compositions were measured via energy dispersive x-ray spectroscopy (EDX), and provided in Section 2.3.4. From the collected data, all deposits appeared to be primarily comprised of aluminum. Additionally, nearly all elements surveyed were identified in the tested deposits. This survey included elements such as copper, nickel, and lead which are known to be causes of corrosion in aluminum and aluminum alloys [3,4,7–10].

Table A-14: Composition of components collected from aeration tank TK-3100-1.

Specimen	Element [Weight %]								
	Al	Cr	Fe	Cu	Mg	Mn	Ti	Zn	Si
<b>Tubular Tie</b>	Bal.	0.06	0.26	0.25	0.89	0.07	0.03	0.06	0.51
<b>6061 Grade Aluminum Alloy</b>	Bal.	0.04 – 0.35	Max 0.7	0.15 – 0.4	0.8 – 1.2	Max 0.15	Max 0.15	Max 0.25	0.4 – 0.8
<b>Floor</b>	Bal.	0.12	0.24	0.06	3.97	0.57	0.03	0.02	0.10
<b>Wall</b>	Bal.	0.11	0.33	0.04	4.48	0.67	0.02	0.01	0.12
<b>Bracket</b>	Bal.	0.19	0.32	0.04	4.44	0.50	0.01	0.01	0.09
<b>5083 Grade Aluminum Alloy</b>	Bal.	0.05 – 0.25	Max 0.4	Max 0.1	4.0 – 4.9	0.4 – 1.0	Max 0.15	Max 0.25	Max 0.4
<b>5086 Grade Aluminum Alloy</b>	Bal.	0.05 – 0.25	Max 0.5	Max 0.1	3.5 – 4.5	0.2 – 0.7	Max 0.15	Max 0.25	Max 0.4

Shaded rows are material standards, whose elemental composition is directly compared to the tank components [11].

Table A-15: Composition of deposits collected from aeration tank TK-3100-1.

Deposit	Element [ppm]									
	Li	Be	B	Na	Mg	Al	P	K	Ca	Ti
<b>Floor Deposit #2</b>	6.27	0.3	9	4139	796	216983	6084	3034	1180	554
<b>Base Plate</b>	6.48	0.3	6	4969	1023	186246	9256	4272	1430	663
<b>Bracket/Air Line</b>	1.02	<DL	12	737	408	202683	8450	623	222	228
<b>Detection Limits</b>	0.05	0.1	2	0.5	2	0.2	5	6	31	0.09

<b>Deposit</b>	<b>Fe</b>	<b>Cr</b>	<b>Ni</b>	<b>V</b>	<b>Mn</b>	<b>Co</b>	<b>Cu</b>	<b>Zn</b>	<b>Ga</b>	<b>As</b>
<b>Floor Deposit #2</b>	5425	326	163	35.1	77.6	2.99	204	69.0	22.2	0.80
<b>Base Plate</b>	3787	324	115	47.4	66.7	2.88	157	45.1	17.7	1.09
<b>Bracket/Air Line</b>	1363	687	17.5	32.5	39.0	0.57	72.3	18.0	8.48	0.67
<b>Detection Limits</b>	3.7	0.05	0.06	0.05	0.03	0.03	0.03	0.08	0.01	0.06
<b>Deposit</b>	<b>Se</b>	<b>Rb</b>	<b>Sr</b>	<b>Y</b>	<b>Zr</b>	<b>Nb</b>	<b>Mo</b>	<b>Pd</b>	<b>Ag</b>	<b>Cd</b>
<b>Floor Deposit #2</b>	0.9	6.75	29.2	1.50	27.8	4.29	14.2	1.03	0.57	0.13
<b>Base Plate</b>	0.9	8.91	24.0	1.37	28.5	2.02	10.1	1.01	0.35	0.14
<b>Bracket/Air Line</b>	0.5	1.26	2.65	0.24	20.9	0.59	4.77	0.66	0.19	<DL
<b>Detection Limits</b>	0.2	0.04	0.03	0.02	0.09	0.04	0.02	0.01	0.01	0.06
<b>Deposit</b>	<b>Sn</b>	<b>Sb</b>	<b>Cs</b>	<b>Ba</b>	<b>La</b>	<b>Ce</b>	<b>Pr</b>	<b>Nd</b>	<b>Sm</b>	<b>Eu</b>
<b>Floor Deposit #2</b>	7.98	1.84	0.19	189	6.74	12.6	1.20	4.20	0.62	0.19
<b>Base Plate</b>	8.77	2.03	0.22	174	3.75	7.78	0.86	3.29	0.58	0.19
<b>Bracket/Air Line</b>	5.91	2.01	<DL	19.4	0.75	1.56	0.16	0.60	0.11	<DL
<b>Detection Limits</b>	0.06	0.01	0.02	0.03	0.03	0.03	0.04	0.03	0.04	0.03
<b>Deposit</b>	<b>Gd</b>	<b>Dy</b>	<b>Er</b>	<b>Yb</b>	<b>Hf</b>	<b>Ta</b>	<b>W</b>	<b>Pb</b>	<b>Th</b>	<b>U</b>
<b>Floor Deposit #2</b>	0.55	0.40	0.21	0.19	0.86	0.29	2.25	13.9	0.70	0.73
<b>Base Plate</b>	0.48	0.40	0.21	0.20	1.11	0.34	5.26	28.4	0.83	0.62
<b>Bracket/Air Line</b>	<DL	<DL	<DL	<DL	1.00	0.13	1.36	3.09	0.20	0.54
<b>Detection Limits</b>	0.03	0.04	0.04	0.05	0.05	0.02	0.08	0.03	0.01	0.03

<DL: Bellow Detection Limit; shaded rows are the detection limits for each element

### A-2.2.2 *X-Ray Diffraction (XRD)*

XRD was performed on the deposits in order to identify the presence of any crystalline corrosion compounds. Prior to testing, the samples collected from the deposits were mechanically pulverized in order to aid in the analysis. The results are presented below in Table A-16. It should be noted that only qualitative information was collected. Additionally, a representative indexed XRD pattern (for the “North Section Hole – Inside” deposit) is provide below in Figure A-43.

Several minerals were identified in the deposits, including: quartz, albite, calcite, dolomite, anorthite, hematite, and gahnite. These minerals were believed to be from dirt, which is most likely a normal constituent in the wastewater process fluid. No further work was performed in determining the exact cause(s) or source(s) of the aforementioned minerals.

Next, aluminum was present in all of the deposits removed from the bracket and tubular tie. Besides both the bracket and tubular tie being made of aluminum, the presence of this element in the deposits is most likely due to the method in which a tungsten carbide scraper was used to scrape off the deposits for collection. Finally, diaspore, gibbsite, and corundum were present in select deposits. These compounds are minerals which may naturally occur. However, both diaspore and gibbsite are also known corrosion products of aluminum [3,4,7]. Additionally, corundum ( $\text{Al}_2\text{O}_3$ ) is also the naturally occurring passive film which is present on aluminum and all aluminum alloys [3,4,7].

Table A-16: XRD results on tested deposits

<b>Deposit</b>	<b>Compound / Chemical Formula</b>
<b>Bracket – Bottom</b>	1. Aluminum / Al
<b>Bracket – Pits</b>	1. Aluminum / Al 2. Quartz / SiO <sub>2</sub> 3. Albite / (Na,Ca)Al(Si,Al) <sub>3</sub> O <sub>8</sub>
<b>Bracket/Air Line</b>	1. Quartz / SiO <sub>2</sub> 2. Calcite / CaCO <sub>3</sub> 3. Diaspore / AlO(OH)
<b>South Section End – Inside</b>	1. Aluminum / Al 2. Gibbsite / Al(OH) <sub>3</sub>
<b>North Section Hole – Inside</b>	1. Aluminum / Al 2. Quartz / SiO <sub>2</sub> 3. Calcite / CaCO <sub>3</sub> 4. Gibbsite / Al(OH) <sub>3</sub>
<b>North Section Hole – Pits</b>	1. Aluminum / Al 2. Quartz / SiO <sub>2</sub> 3. Calcite / CaCO <sub>3</sub> 4. Dolomite / CaMg(CO <sub>3</sub> ) <sub>2</sub>
<b>Base Plate</b>	1. Quartz / SiO <sub>2</sub> 2. Calcite / CaCO <sub>3</sub> 3. Anorthite / (Ca,Na)(Al,Si) <sub>2</sub> Si <sub>2</sub> O <sub>8</sub>
<b>Floor Deposit #1</b>	1. Quartz / SiO <sub>2</sub> 2. Hematite / Fe <sub>2</sub> O <sub>3</sub>
<b>Floor Deposit #2</b>	1. Quartz / SiO <sub>2</sub> 2. Unnamed Calcite / (Mg <sub>0.1</sub> Cd <sub>0.9</sub> )CO <sub>3</sub> 3. Corundum / Al <sub>2</sub> O <sub>3</sub> 4. Albite / NaAlSi <sub>3</sub> O <sub>8</sub>
<b>Floor – Pit Deposit</b>	N/A <sup>†</sup>
<b>Wall Horizontal Weld and Grind Marks</b>	1. Quartz / SiO <sub>2</sub>
<b>Wall Tooling Marks</b>	1. Quartz / SiO <sub>2</sub> 2. Calcite / CaCO <sub>3</sub> 3. Albite / NaAlSi <sub>3</sub> O <sub>8</sub> 4. Gahnite / ZnAl <sub>2</sub> O <sub>4</sub>

<sup>†</sup> Not enough deposit available to perform XRD

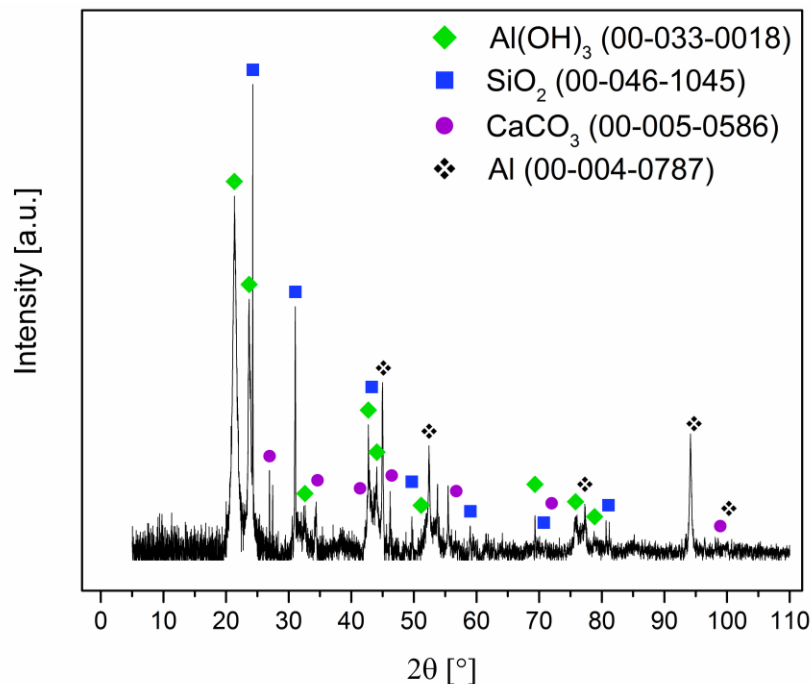


Figure A-43: Representative indexed XRD pattern for the “North Section Hole – Inside” deposit.

#### A-2.2.3 *Fourier Transform Infrared Spectroscopy (FTIR)*

FTIR was performed on all of the deposits collected. Prior to testing, the samples collected from the deposits were mechanically pulverized and mounted in potassium bromide (as a KBr pellet) in order to aid in the analysis. After testing, the collected spectra were compared to known FTIR spectra of aluminum oxides and hydroxides. This comparison was done in order to identify any amorphous or crystalline aluminum corrosion products. The collected spectra were only compared to characteristic peaks of the following oxides and hydroxides: gibbsite, bayerite, boehmite, diaspore, and corundum. No good fit was found between the collected deposit spectra and any of the characteristic peaks of the aforementioned aluminum oxides or hydroxides. Even though compounds such as diaspore, gibbsite, and corundum were identified with XRD, they may not be identified using FTIR. This discrepancy is due to how FTIR is used to identify compounds. It is believed that the potential presence of other organic or inorganic compounds (in the deposits) makes it incredibly difficult to identify compounds of interest, by

solely comparing the collected deposit spectra to select, pure compound spectra [12].

### A-2.3 Scanning Electron Microscopy (SEM)

The following section is separated into subsections based on component, as well as the specific specimen collected from the component for SEM examination. In the various subsections, some combination of imaging mode (i.e. secondary electron (SE) or backscattered electron (BSE)) and energy dispersive x-ray spectroscopy (EDX) were performed. Note that the compositional data collected from EDX is to be regarded as qualitative to semi-quantitative (at best) in nature. Moreover, all of the collected EDX weight percentage data was normalized to 100%, and any discrepancies due to rounding were corrected by adjusting the elemental oxygen weight percentage. Finally, carbon weight percentage values measured with EDX are unreliable [13]; therefore, carbon was subtracted from the EDX data.

#### A-2.3.1 *Floor*

The large, 5.1 cm diameter pit was cross-sectioned with a slow-speed saw and examined via SEM. Imaging and EDX analysis were both performed. The imaging and compositional data are presented in Sections 2.3.1.1 and 2.3.1.2, respectively. Note that the cut surface of the specimen was ground to a 1200 grit finish (preceded by a 240, 320, 400, 600, and 800 grit sequential wet-grinding procedure) and cleaned. Moreover, the cut surface was not etched, or carbon coated.

##### A-2.3.1.1 *Pit Cross-section*

The morphology of the large pit is shown below in Figures A-44 through A-46. Pits within pits could be observed. Moreover, deposit was found to be

covering the surface of the pits. Note that Figures A-44 through A-46 were tilted on the SEM stage 60 degrees.

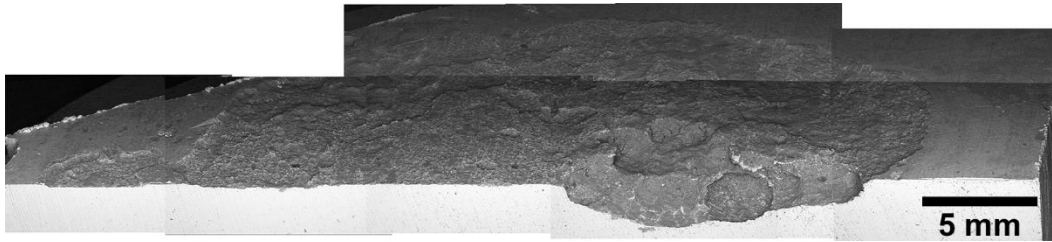


Figure A-44: Composite BSE image of the large 5.1 cm diameter pit. Able to discern pits within pits.

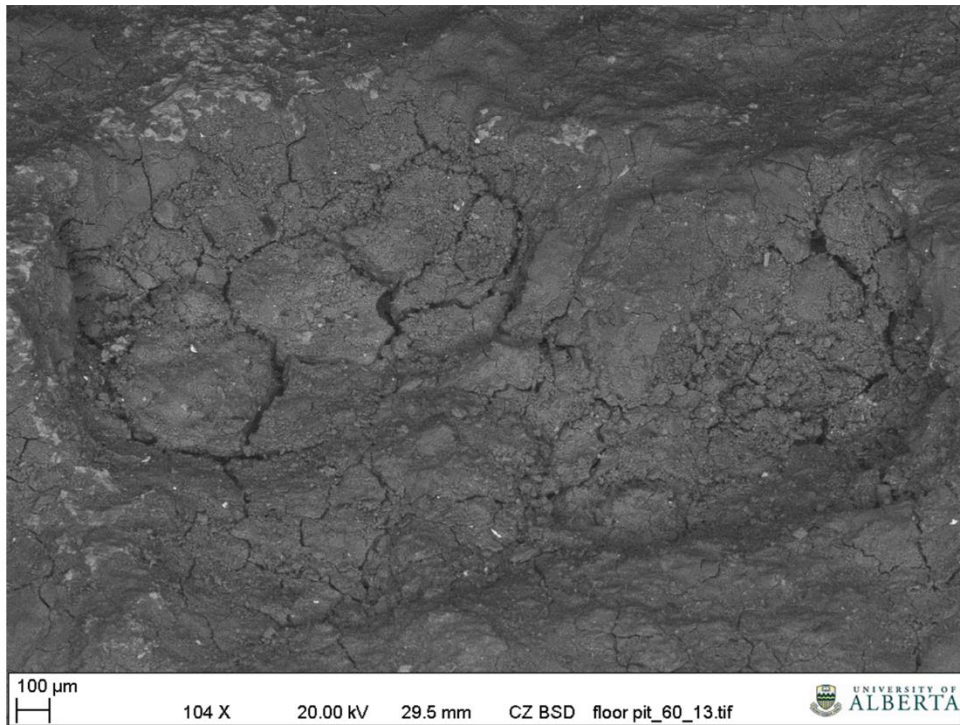


Figure A-45: Close-up of pits within pits (BSE image).

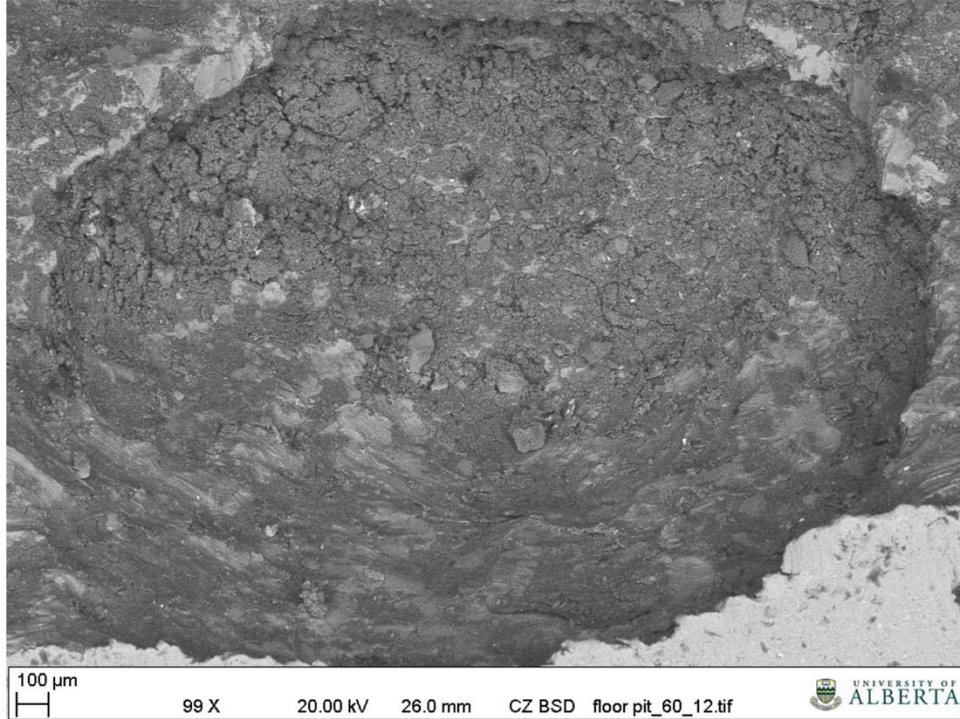


Figure A-46: Deposit within pits; image of the deepest pit (BSE image). Abrasion marks from handling can be seen in the foreground (bottom half of the image within the pit) as curved scatches.

#### A-2.3.1.2 Pit Deposit

EDX data was collected from four points within the large 5.1 cm pit. The locations of the points, as well as the compositional data are presented below in Figure A-47 and Table A-17, respectively.

High concentrations of aluminum and oxygen were present in each location; both of which are indicative of aluminum corrosion products [3,4,7]. Additionally, chlorine and sulphur were present in several locations. These elements either as ions (such as chloride) or as polyatomic anions (such as sulphate) are known to cause corrosion in aluminum and aluminum alloys [3,4]. The occurrence of both of these elements could be due to a number of different sources. These sources include: chemical constituents which may be naturally present in the wastewater (such as urine, table salt, or dissolved inorganic compounds [14]), compounds which are produced via metabolic processes of the microorganisms that are treating

the wastewater, or chemical additives (including coagulants) which aid in the treatment of wastewater (such as aluminum sulphate (Alum) or polyaluminum chloride (PACl; Isopac) [14]).

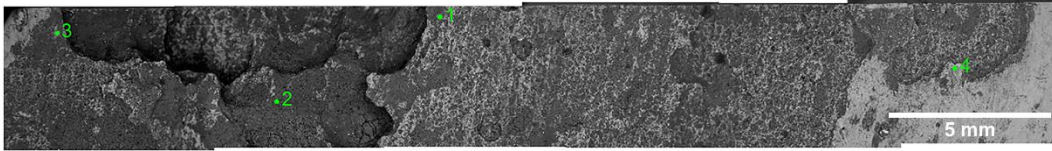


Figure A-47: Top overview image of large pit. Dots indicate where EDX data was collected (BSE image).

Table A-17: EDX data from points in Figure A-47

Point	Element [Normalized Weight %]								
	Al	O	Si	S	Cl	Na	Fe	Ca	Mg
1	26.9	64.0	0.3	7.1	0.4	0.4			0.9
2	30.5	56.9	2.9	5.5	0.8	0.4	0.8	1.5	0.7
3	37.5	53.0	1.0	5.1	0.6	0.6	0.3	0.8	1.1
4	72.6	23.8		1.5					2.1

#### A-2.3.2 Tubular Tie

A cross-section of the tubular tie was removed approximately 13.5 cm south (relative to the tie north end) of the through-wall hole and examined via SEM. Imaging as well as EDX analysis were performed. A portion of the cross-section was cold mounted in epoxy resin and examined (Section 2.3.2.2), while the remaining cross-section was examined unmounted (Section 2.3.2.1). EDX data was collected from deposits within pits in the mounted cross-section (Section 2.3.2.3). Finally, line scans were performed across grains in select portions of the mounted cross-section (Section 2.3.2.4).

##### A-2.3.2.1 Unmounted Cross-section

The morphology of the tie pits and buildup of deposit are shown below in Figures A-48 through A-53. In addition to pitting, intergranular corrosion (IGC) was observed both at and below the surface of the pits (Figures A-49 through A-

53) – identified by the morphology of material loss at grain boundaries. It appears that corrosion was occurring both in the grains and at the grain boundaries. Moreover, deposit appeared to be covering the surface of the pits, as well as corroded grain boundaries. It should be noted that Figures A-48 through A-53 were tilted on the SEM stage 50 degrees. Moreover, the cut surface of the specimen was ground to a 1200 grit finish (preceded by a 240, 320, 400, 600, and 800 grit sequential wet-grinding procedure), and was cleaned. Finally, the cut surface was not etched or carbon coated.

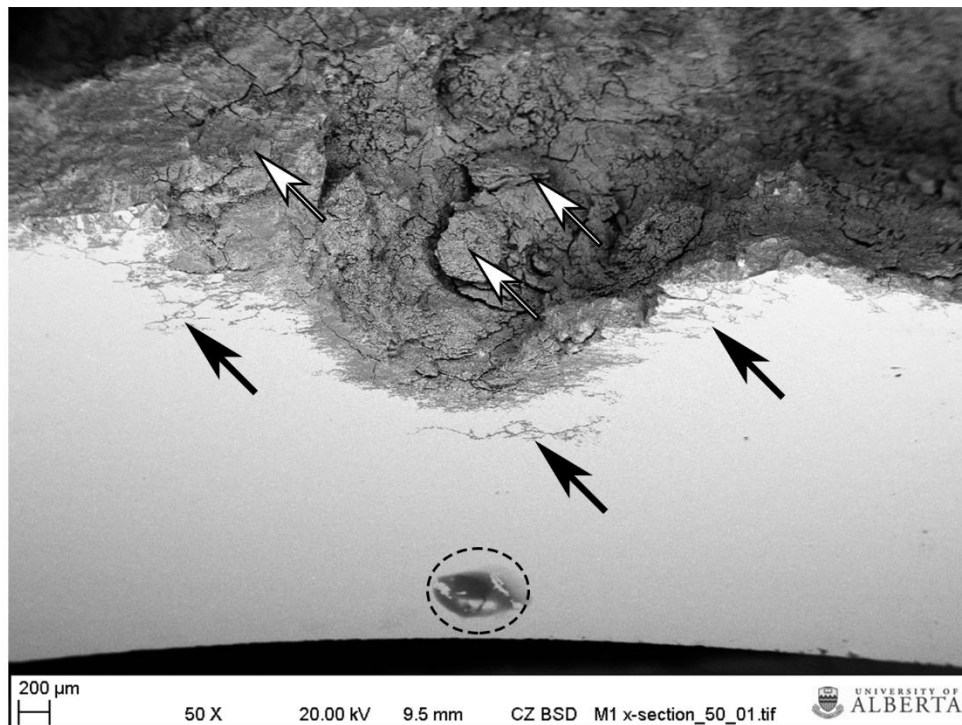


Figure A-48: BSE image of large pit on the outer circumference of the cross-section. Deposit (white arrows) and IGC (black arrows) are also present. Note the dot on the sectioned surface was made with a Sharpie® marker in order to identify location of interest (black dashed oval).

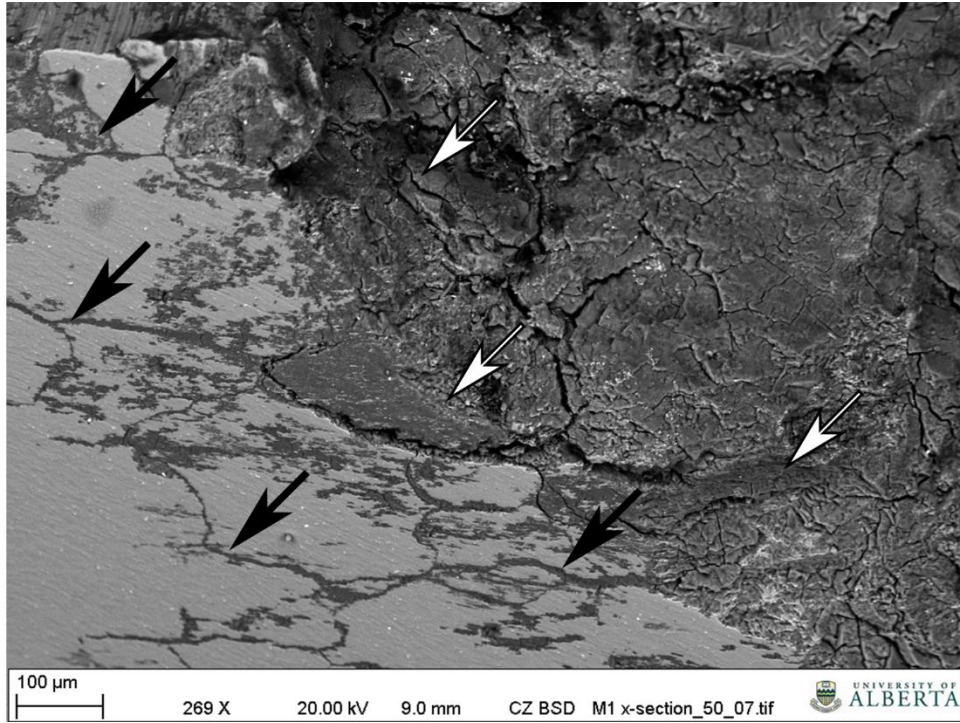


Figure A-49: Close-up on IGC (black arrows) and deposit (white arrows) at the large pit opening (BSE image).

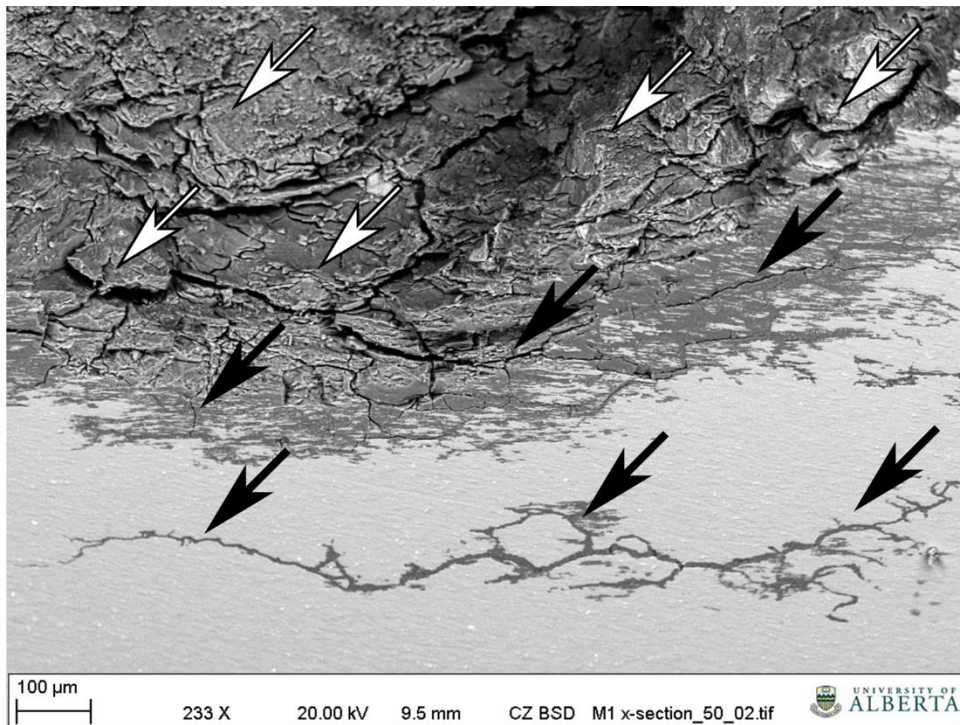


Figure A-50: Close-up BSE image of IGC (black arrows) and deposit (white arrows) at the bottom of the large pit opening.

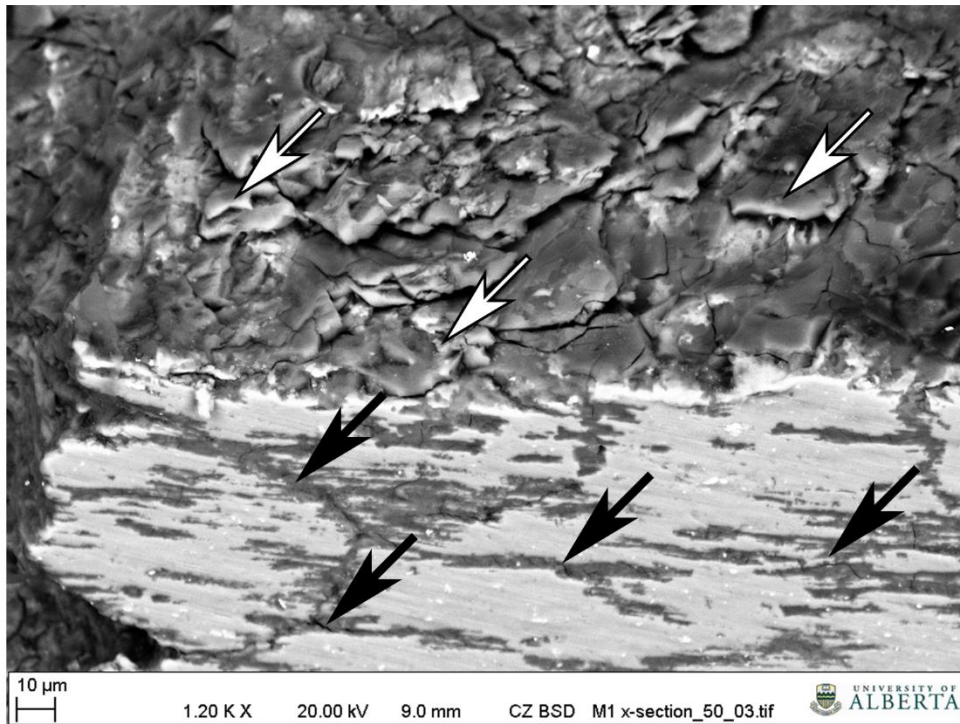


Figure A-51: Additional close-up BSE image of deposit (white arrows) on the pit surface, as well as IGC (black arrows).

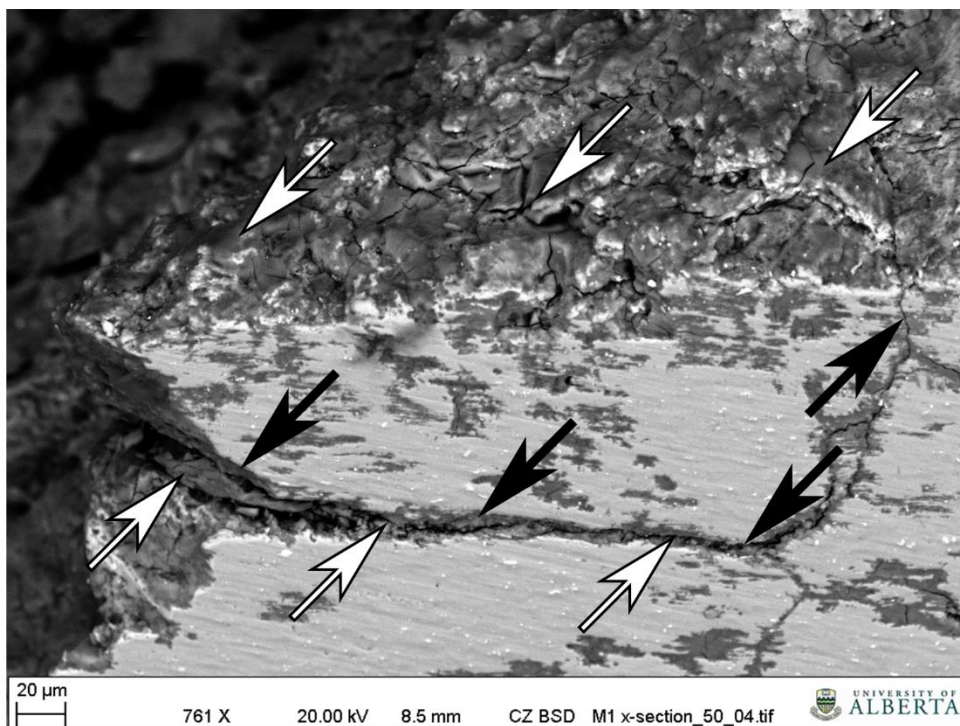


Figure A-52: Close-up BSE image of deposit (white arrows) on the pit surface, as well as IGC (black arrows) around an entire grain. There also appears to be deposit build-up between the grains (white arrows).

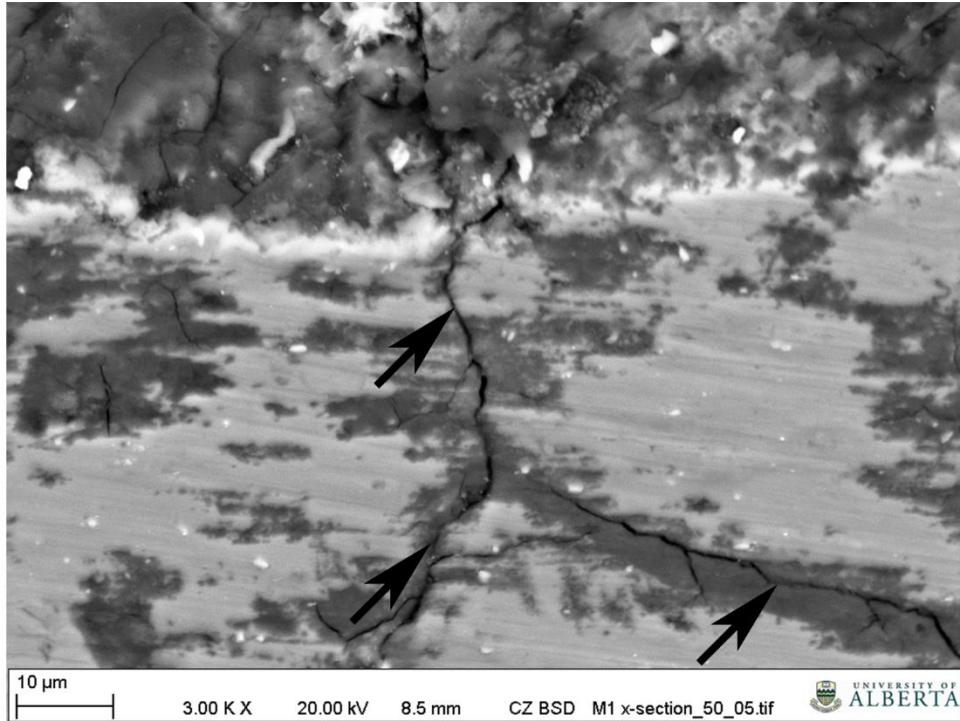


Figure A-53: Close-up on IGC (black arrows) in Figure A-52 (BSE image). Note the cracking within the corrosion product formed at metal grain boundaries.

#### A-2.3.2.2 *Mounted Cross-section*

The morphology of the tie pits is shown below in Figures A-54 through A-58. As with the unmounted cross-section, both pitting and IGC were observed (Figures A-54 through A-58). Moreover, it is suspected that after IGC occurs the grains may be able to drop out of the material (Figure A-58), which would result in high material loss rates. Deposit also appeared to be covering the surface of the pits (exposed to the process fluid), as well as corroded grain boundaries. It should be noted that the cut surface of the mounted specimen was polished to a 1 micron finish, followed by etching with a freshly prepared hot sodium hydroxide solution (etched for 30 s in 1.3 g NaOH and 100 mL de-ionized ultra-filtered water (DIUF) at 70 °C). The specific surface preparation achieved for the mounted cross-section (prior to etching) was performed as follows: 240, 320, 400, 600, 800, and 1200 grit sequential wet-grinding with silicon carbide grit paper, followed by 3 micron and 1 micron polishing with diamond suspension. After the cross-section was cleaned and etched, it was carbon coated.

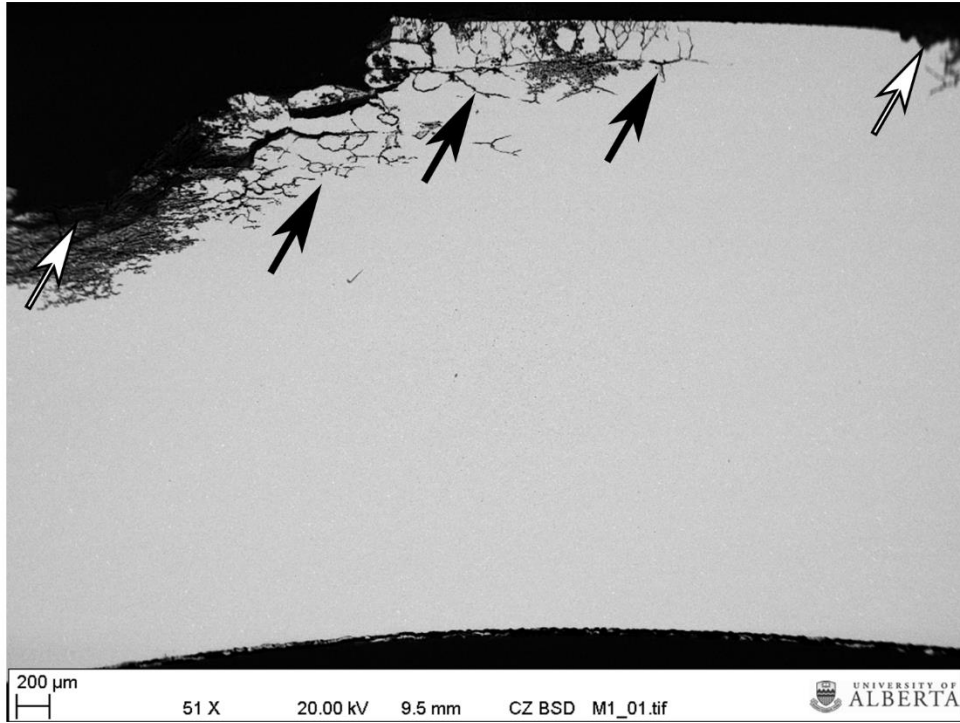


Figure A-54: BSE image of the mounted cross-section. Pitting (white arrows) and IGC (black arrows) observed on the outer circumference of the cross-section.

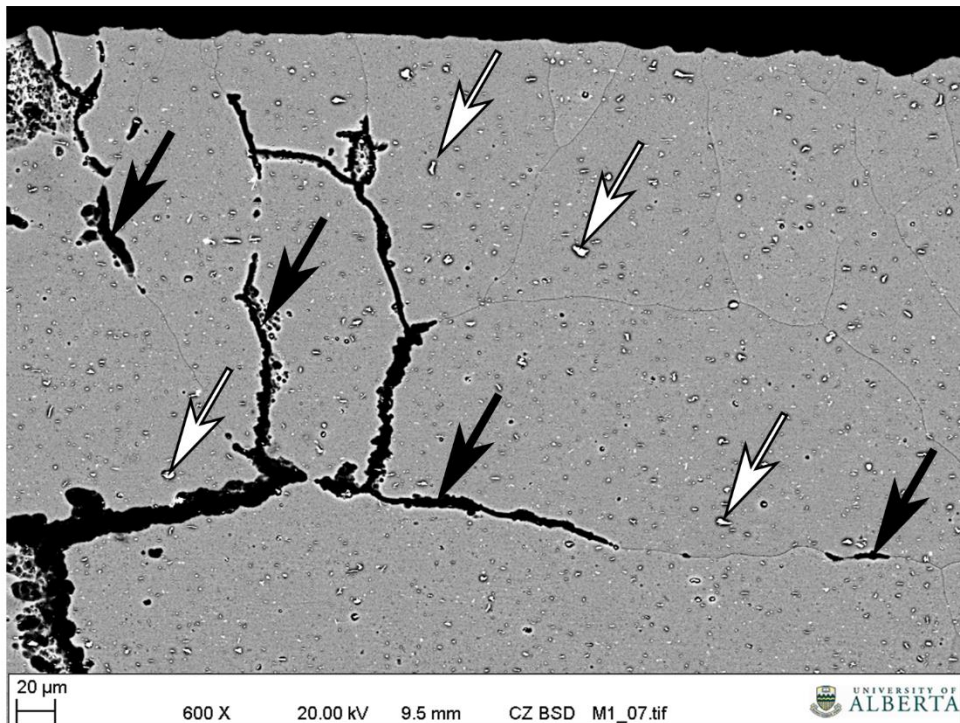


Figure A-55: Close-up on IGC (black arrows) at the tie surface (from Figure A-54; BSE image). Precipitates (white arrows) can also be observed.

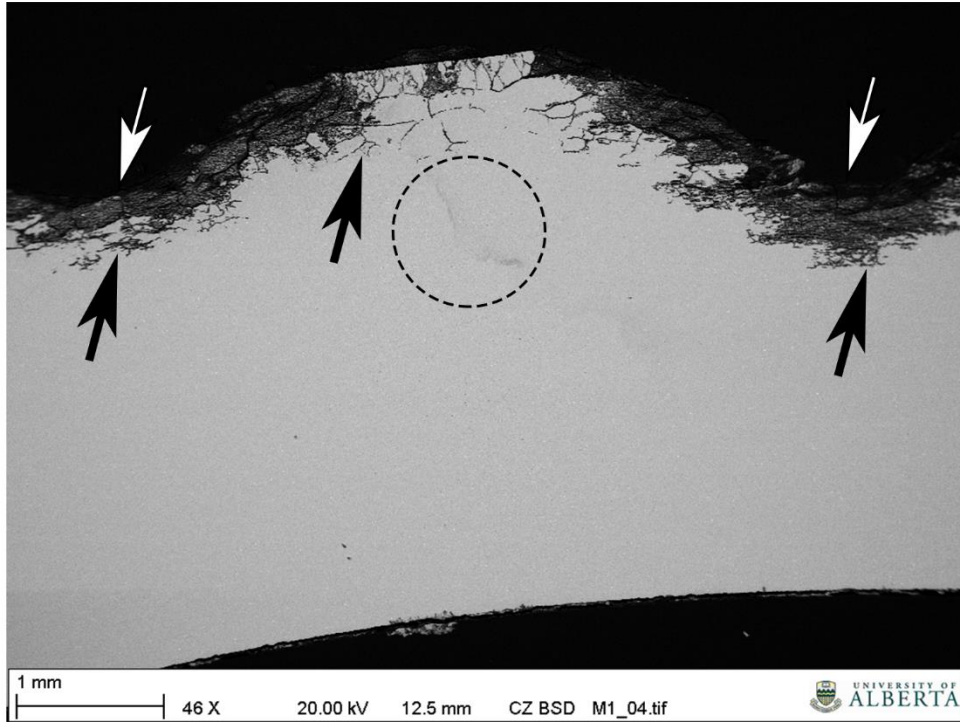


Figure A-56: BSE image of another location on the tubular tie exhibiting signs of pitting (white arrows) and IGC (black arrows). Some staining (black dashed oval) was found below the IGC. The staining is an artifact from the etching process.

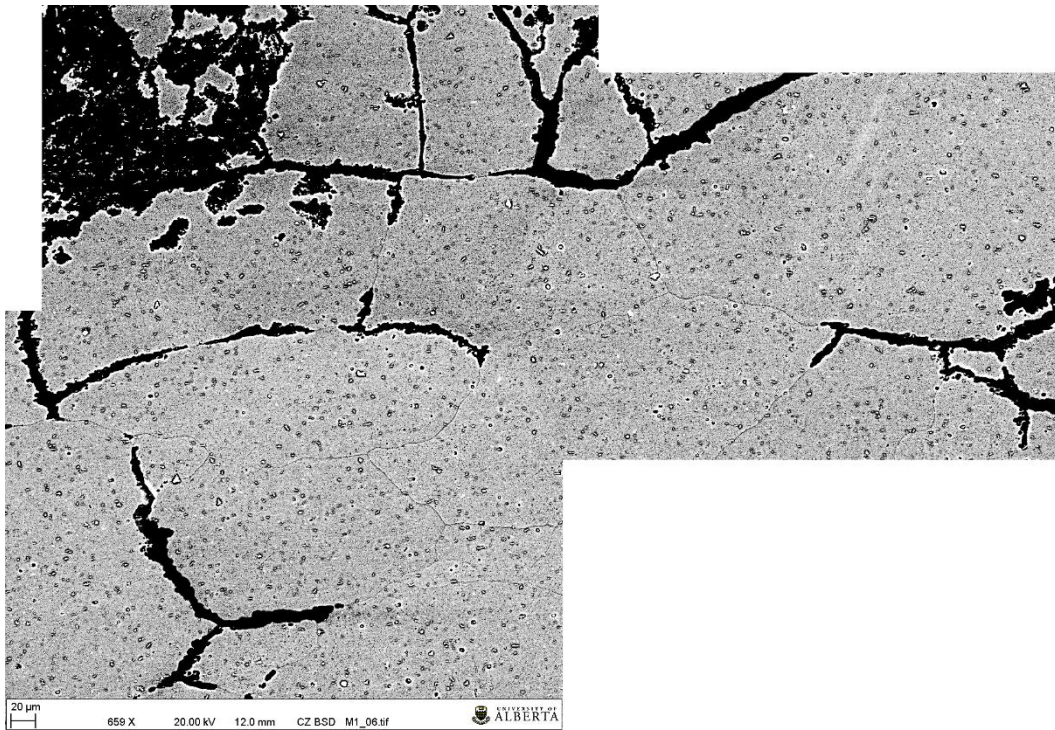


Figure A-57: Close-up BSE image of IGC (from Figure A-56).

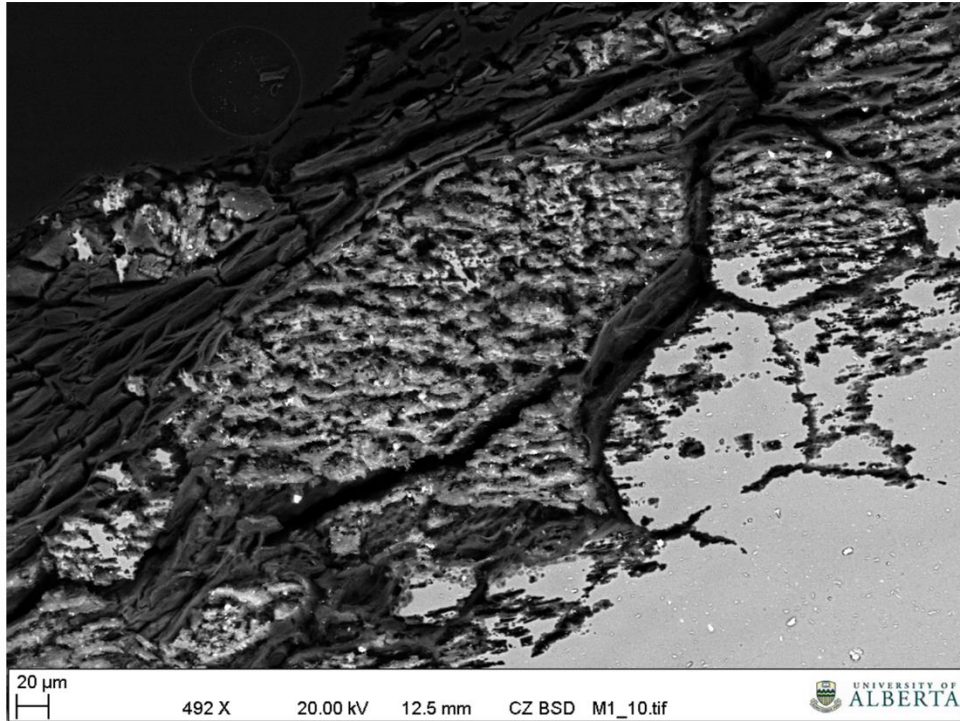


Figure A-58: Close-up BSE image of IGC and corroded grains (from Figure A-56). Figure demonstrates the progression of corrosion of the tie from initial IGC to entirely corroded grains which naturally drop out due to gravity or fluid motion.

#### A-2.3.2.3 *Pit Deposit*

EDX data was collected from multiple points within two large pits in the mounted tie cross-section. The locations of the points and pits, as well as the compositional data are presented below in Figures A-59 and A-60, and Tables A-18 and A-19, respectively.

As identified on the floor cross-section, high concentrations of aluminum and oxygen were present in the deposits; both of which are indicative of aluminum corrosion products [3,4,7]. Chlorine and sulphur were also found in several locations, and – as chloride and sulphate – cause corrosion in aluminum and aluminum alloys [3,4]. Additionally, copper was identified in several locations. Again, copper is known to cause corrosion in aluminum and aluminum alloys [3,4,7–10].

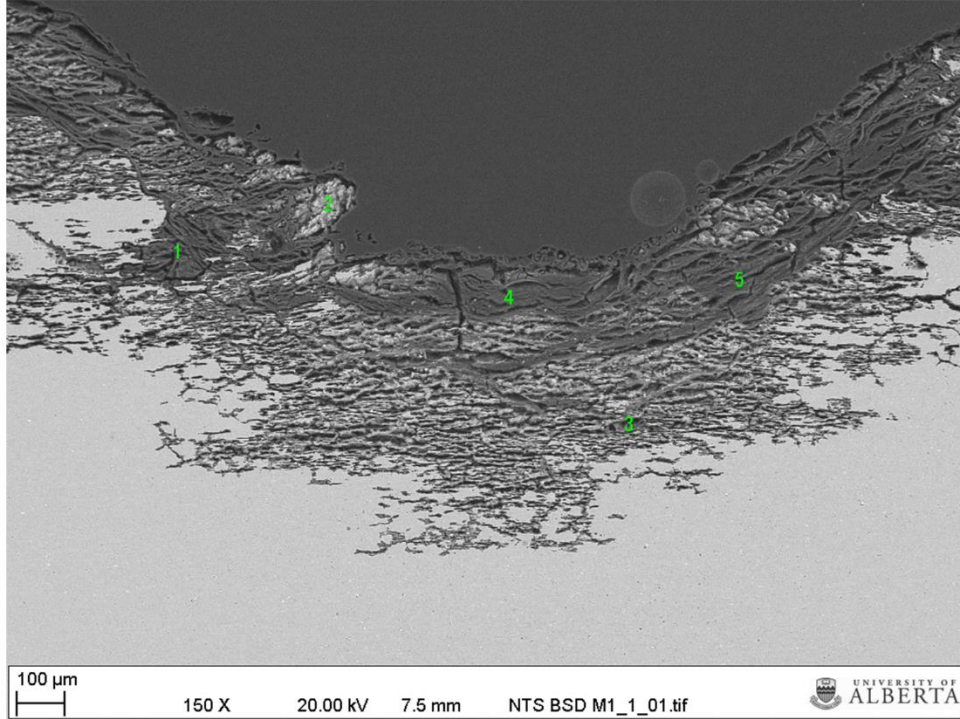


Figure A-59: BSE image of pit in mounted tie cross-section. Numbers indicate where EDX data was collected.

Table A-18: EDX data from numbers in Figure A-59

Point	Element [Normalized Weight %]									
	Al	O	Si	P	S	Cl	Na	Fe	Ca	Mg
1	30.2	53.8	2.9		4.0	2.3	0.4	2.7	3.7	
2	58.4	31.8	5.8						1.8	2.2
3	57.5	32.7	2.3		1.9	0.7		1.3	1.7	1.9
5	27.8	54.9	2.0	2.2	3.3	2.3	0.3		6.4	0.8

Note that the data from Point 4 is missing; hence, it is not present in the table.

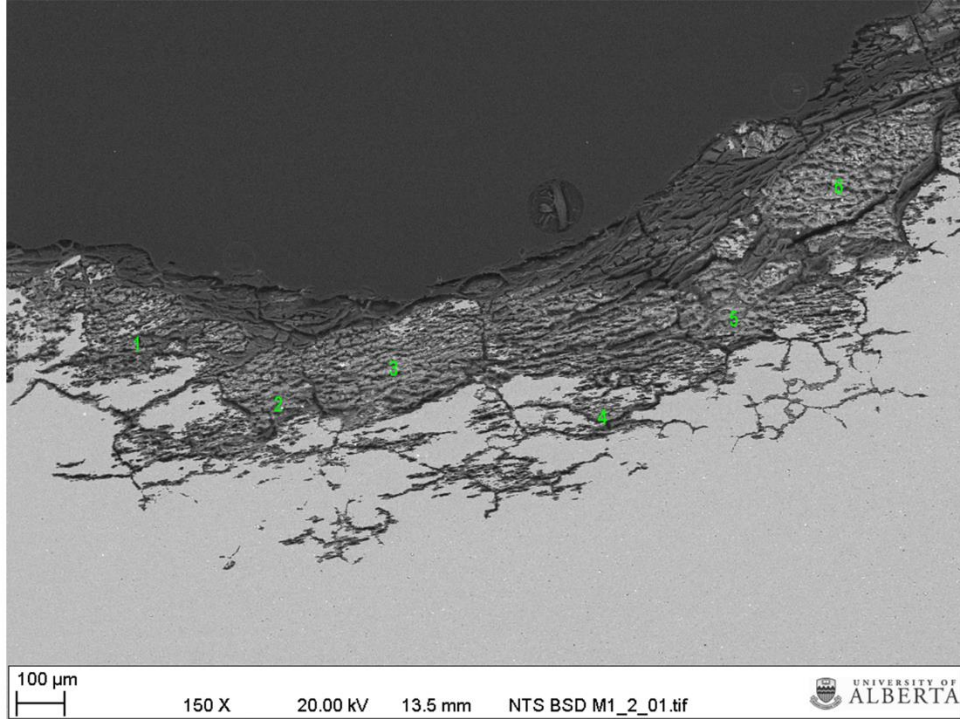


Figure A-60: BSE image of pit in mounted tie cross-section. Numbers indicate where EDX data was collected.

Table A-19: EDX data from numbers in Figure A-60

Point	Element [Normalized Weight %]							
	Al	O	Si	S	Fe	Ca	Cu	Mg
1	51.3	33.7	4.7	0.7	1.5	2.8	3.7	1.6
2	54.4	30.8	5.0	0.8	2.3	1.9	3.8	1.0
3	65.3	23.7	4.3		1.6	1.4	2.4	1.3
4	66.7	24.4	2.6		1.0	0.7	2.3	2.3
5	65.2	20.7	4.2	0.7	2.7	1.8	3.1	1.6
6	65.1	24.3	3.9	0.1	0.9	1.2	2.7	1.8

#### A-2.3.2.4 Grain Line Scans

Due to the presence of IGC, line scans were performed across grains throughout the mounted tie cross-section (Figures A-61 through A-64). These scans were done in order to assess whether there was any chemical anisotropy of the primary alloying elements (namely aluminum, magnesium, and silicon) as well as oxygen throughout the length, and across the boundaries, of the grains. Having grains with gradients in chemistry could lead to variations in passivation of the material (in addition to resulting in electrochemical potential differences),

subsequently leading to corrosion of the more anodic portion of the grain. Naturally, there are slight differences in potential at the grain boundary, relatively to the center of the grain. However, drastic differences in chemistry due to manufacturing of the material could lead to greater differences in potential, which could result in the exacerbation of corrosion that may naturally occur.

From the line scans, the grains examined appeared to be relatively uniform in composition throughout the length of the grain. Only relevant changes in composition appeared when line scans interacted with either secondary phases (such as  $Mg_2Si$  precipitates), impurities (such as oxide inclusions), or at the grain boundaries.

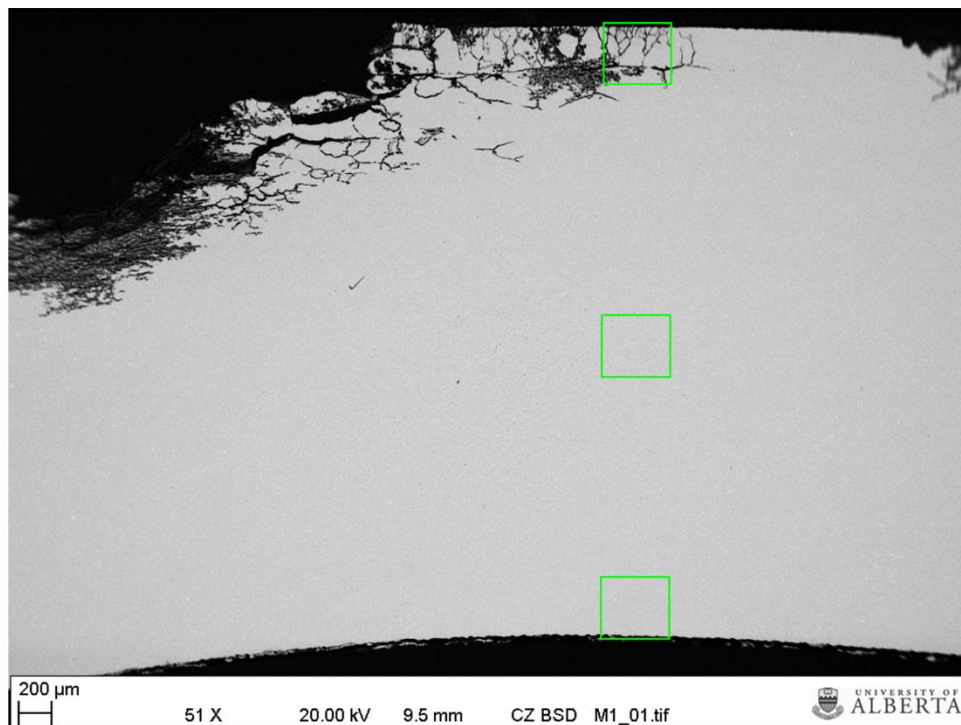


Figure A-61: BSE image of mounted tie cross-section. Boxes show locations where line scans were performed on grains.

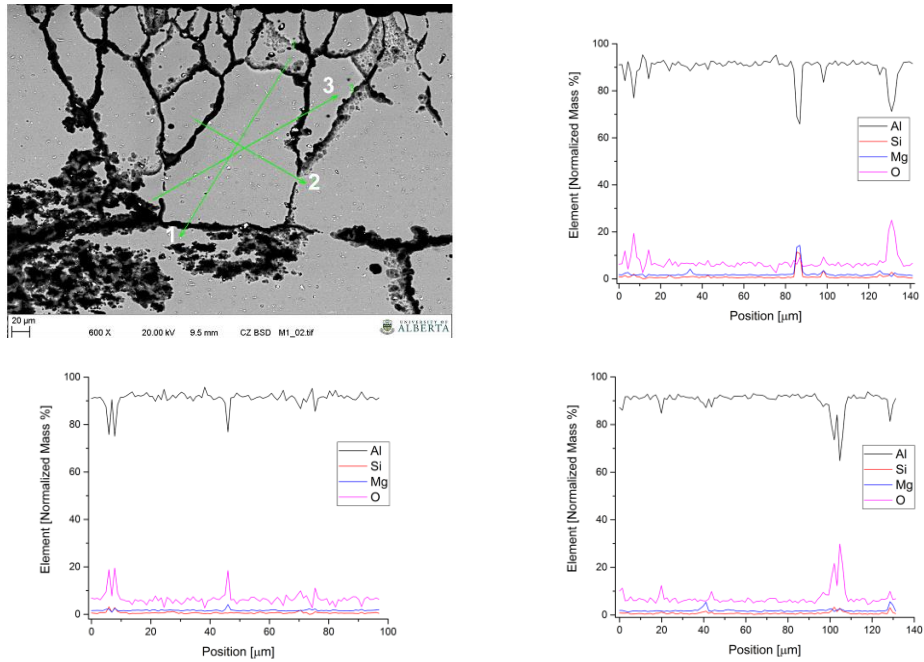


Figure A-62: BSE image of tie, near the outer circumference (Top left). Locations of line scans performed on a grain are shown. Graphs show EDX results for: Line 1 (Top Right), Line 2 (Bottom Left), and Line 3 (Bottom Right).

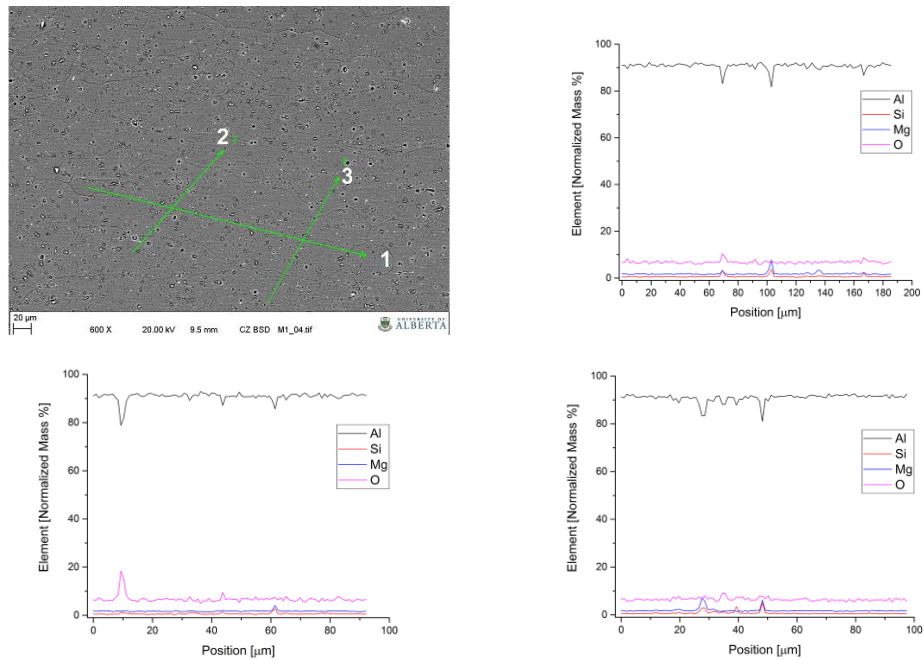


Figure A-63: BSE image of tie, near the center (mid thickness) (Top left). Locations of line scans performed on a grain are shown. Graphs show EDX results for: Line 1 (Top Right), Line 2 (Bottom Left), and Line 3 (Bottom Right).

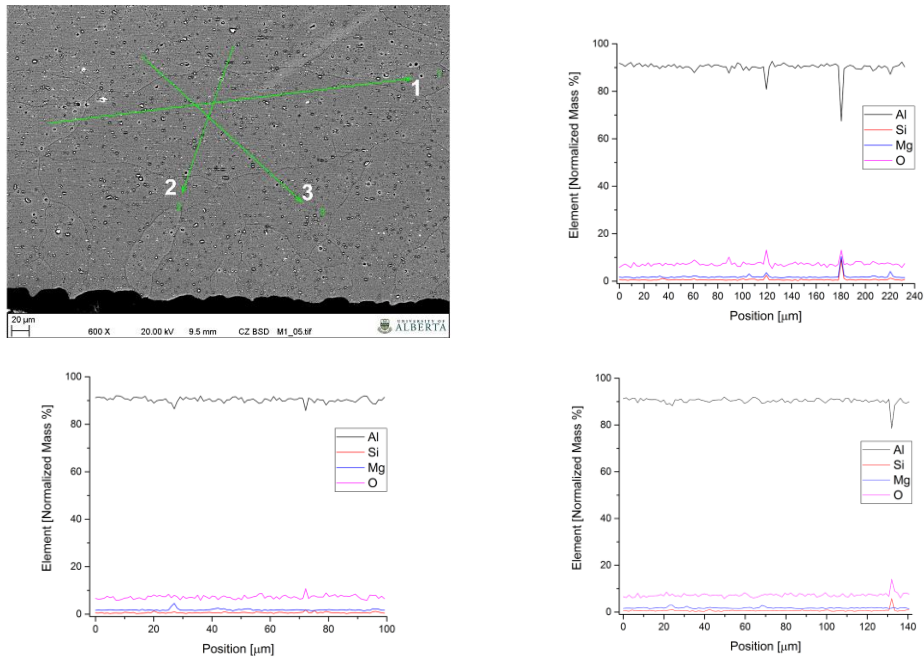


Figure A-64: BSE image of tie, near the inner circumference (Top left). Locations of line scans performed on a grain are shown. Graphs show EDX results for: Line 1 (Top Right), Line 2 (Bottom Left), and Line 3 (Bottom Right).

### A-2.3.3 Aeration Line Bracket

A cross-section of the aeration line bracket was made and examined via SEM. Imaging as well as EDX analysis was performed, and their results are presented in Section 2.3.3.1. The cross-section was cold mounted in epoxy resin and examined. EDX data was collected from deposits within pits in the mounted cross-section.

#### A-2.3.3.1 Mounted Cross-section and Pit Deposit

The morphology of the bracket pits is shown below in Figures A-65 through A-71. Moreover, severe tunnelling<sup>4</sup> was also observed both at and below the surface of the pits (Figures A-65 through A-71). At high magnification, crystallographic

<sup>4</sup> The word “tunneling” is not used in ASTM G46 [6]; however, the presence of tunnels starting at pit walls is a morphology of corrosion that suggests the presence of microbial action (as microbiologically influenced corrosion; MIC) [27].

pits (in the shape of cubes) were found on the walls of the pit tunnels (Figure A-71). Additionally, deposit appeared to be covering the surface of the pits (exposed to the process fluid), as well as in the tunnels. It should be noted that the cut surface of the mounted specimen was polished to a 1 micron finish. The specific surface preparation achieved for the mounted cross-section was performed as follows: 240, 320, 400, 600, 800, and 1200 grit sequential wet-grinding with silicon carbide grit paper, followed by 3 micron and 1 micron polishing with diamond suspension. The cross-section was then cleaned. Finally, the specimen was unetched and not carbon coated.

EDX data was collected from multiple points within the mounted tie cross-section. The locations of the points and pits, as well as the compositional data are presented below in Figures A-65 through A-67 and A-69, and Tables A-20 through A-23, respectively.

Again, high concentrations of aluminum and oxygen were present in the deposits; both of which are indicative of aluminum corrosion products [3,4,7]. Intermetallic precipitates or inclusions were also identified in some locations (Figures A-66 and A-67). These compounds – which, depending on the alloy chemistry and processing, may naturally be present in the material – can lead to the creation of a local galvanic cell between themselves and the surrounding matrix. Chlorine and sulphur were also found in several locations. Again, chloride and sulphate are known to cause corrosion in aluminum and aluminum alloys [3,4].

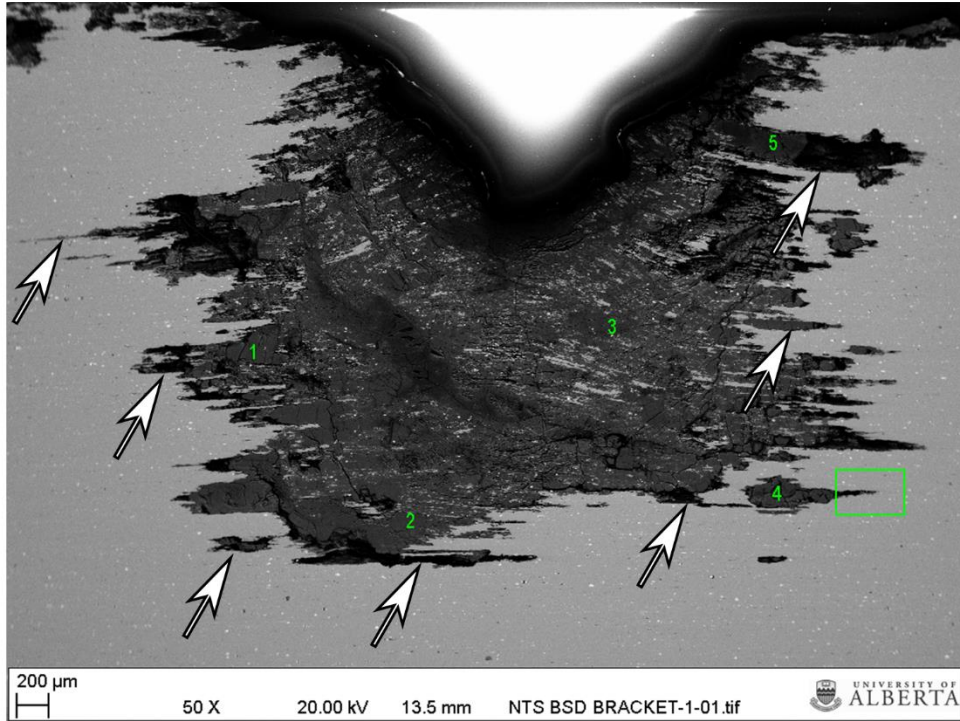


Figure A-65: BSE image of large pit on the top of the bracket. Numbers indicate where EDX data was collected. Tunnelling (white arrows) can also be observed. Green box is the location of Figure A-66.

Table A-20: EDX data from numbers in Figure A-65

Point	Element [Normalized Weight %]					
	Al	O	S	Cl	F	Mg
1	30.9	63.4	1.9		2.5	1.3
2	30.4	65.3	0.8		1.8	1.7
3	32.4	62.6	3.9			1.1
4	31.5	60.2	0.4		6.8	1.1
5	34.0	61.7	3.2	0.8		0.3

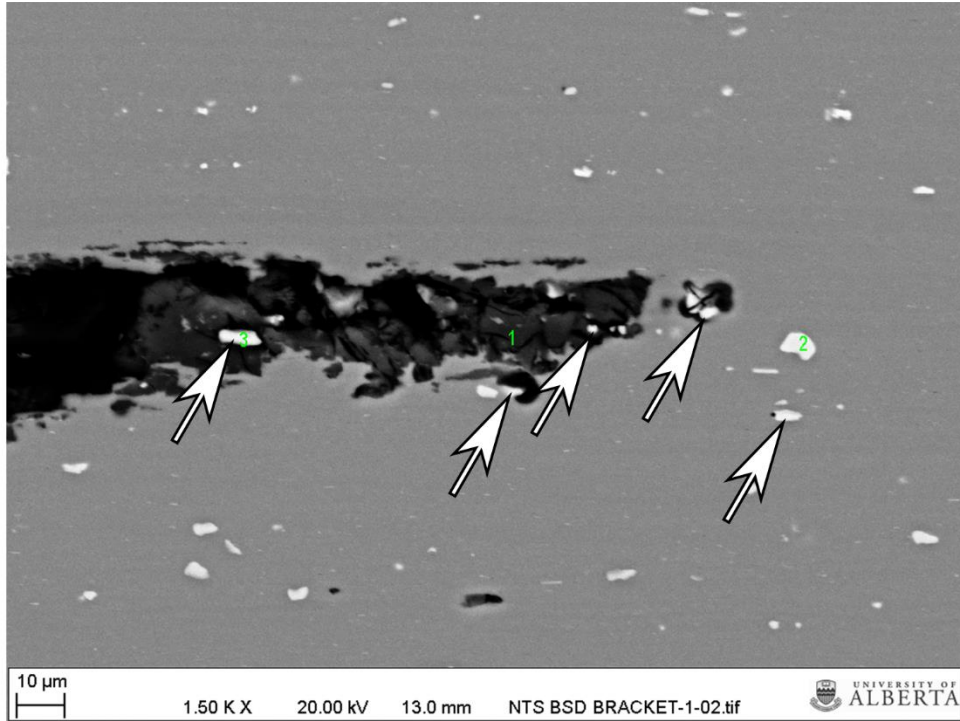


Figure A-66: Close-up on tunneling (from Figure A-65; BSE image). Numbers indicate where EDX data was collected. A local galvanic cell can be observed between the intermetallic inclusions (white arrows) and the surrounding matrix.

Table A-21: EDX data from numbers in Figure A-66

Point	Element [Normalized Weight %]									
	Al	O	Si	S	Cl	Cr	Fe	Mn	F	Mg
1	38.7	53.8		0.8	0.9				4.4	1.4
2	54.7		3.3			5.3	23.8	12.9		
3	61.6	13.1				1.2	16.0	7.6		0.5

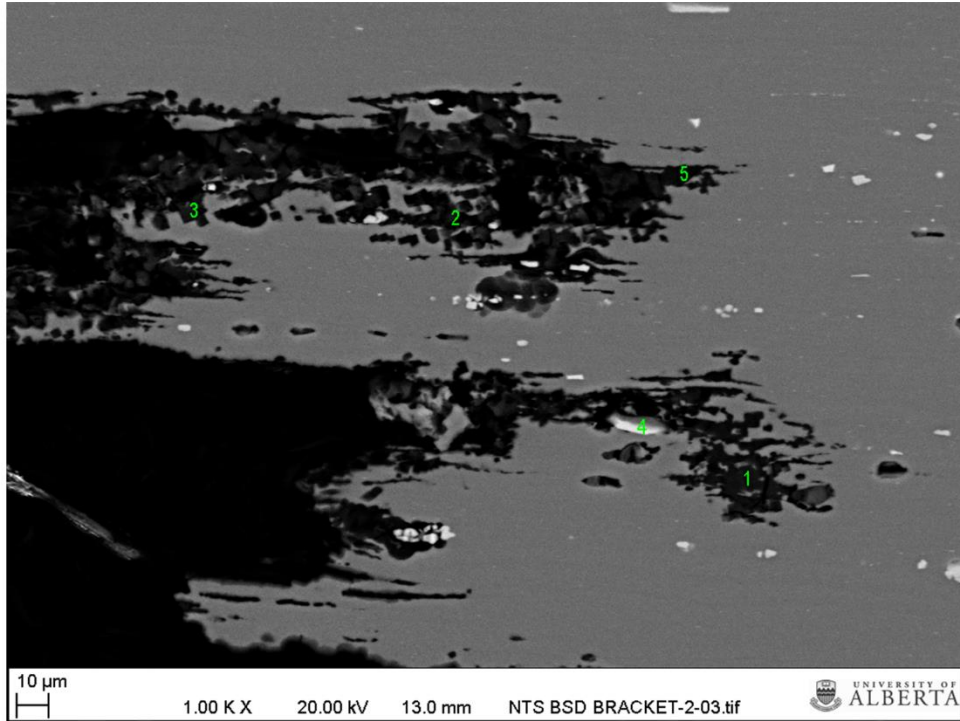


Figure A-67: Close-up on tunneling (from Figure A-65; BSE image). Numbers indicate where EDX data was collected.

Table A-22: EDX data from numbers in Figure A-67

Point	Element [Normalized Weight %]									
	Al	O	Si	Mn	S	Na	Fe	Cr	F	Mg
1	36.3	54.5	0.3		2.6	1.1			4.0	1.2
2	39.6	53.2	0.1		2.5	1.0			1.5	2.1
3	41.9	50.2	1.1		2.9	0.1			1.7	2.1
4	48.1	18.1	3.2	7.7			16.7	2.2	3.6	0.4
5	36.0	56.8			2.1	3.2				1.9

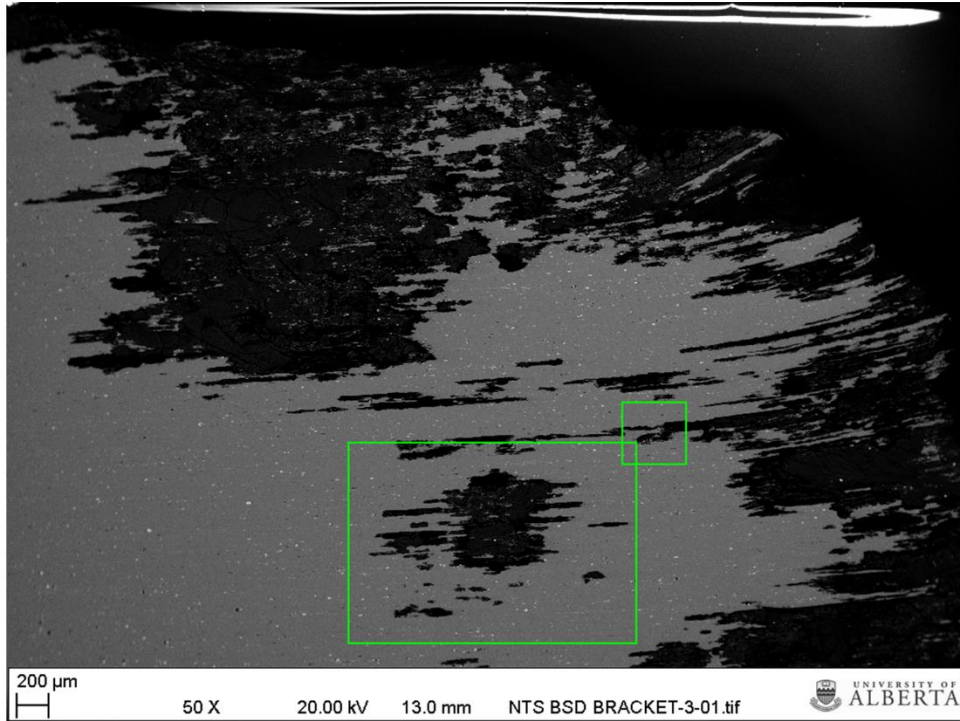


Figure A-68: BSE image of pitting and tunneling on the side of the bracket. The large green box is the location of Figure A-69, while the small green box is the location of Figure A-70.

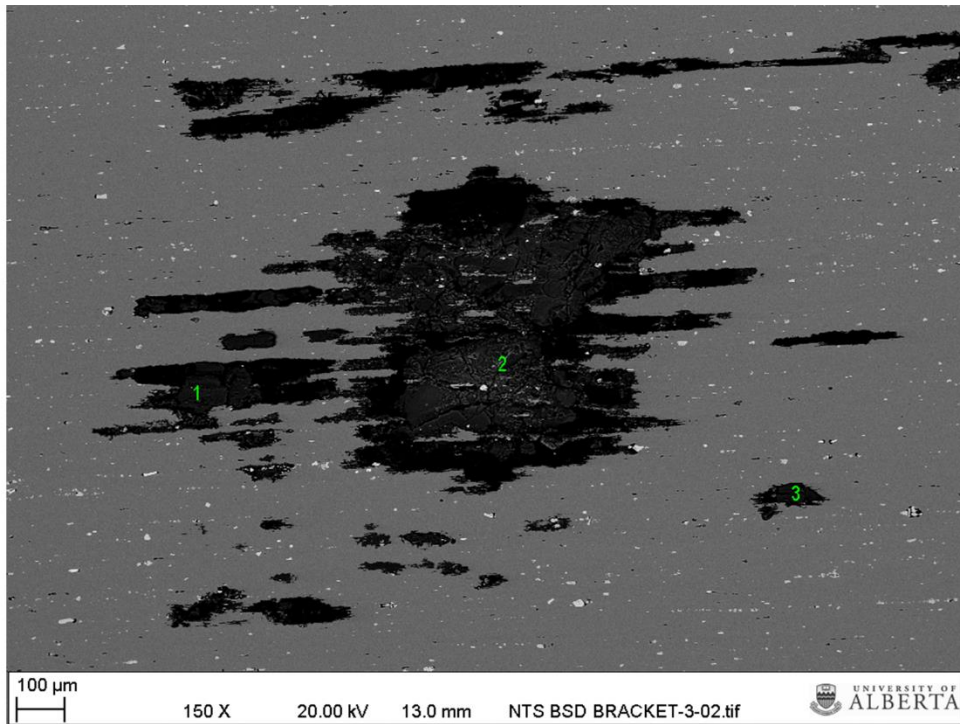


Figure A-69: Close-up on tunneling (from Figure A-68; BSE image). Numbers indicate where EDX data was collected.

Table A-23: EDX data from numbers in Figure A-69

Point	Element [Normalized Weight %]							
	Al	O	Si	S	Na	Ca	F	Mg
1	32.3	60.3	0.4	0.7	0.1	0.6	4.7	0.9
2	31.0	61.4	0.6	0.6		0.7	4.4	1.3
3	35.8	58.0	0.2	0.9	0.5	0.3	3.0	1.3

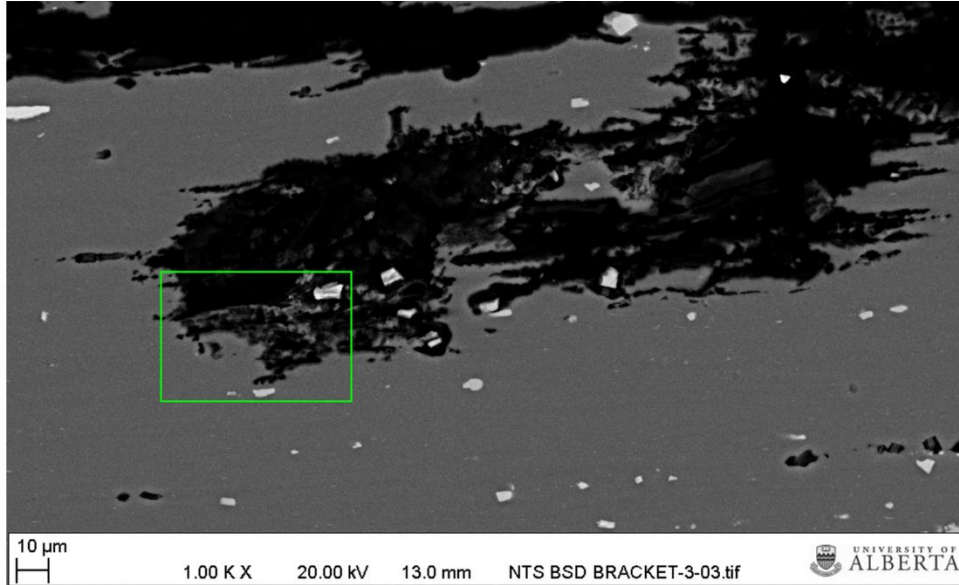


Figure A-70: Close-up on tunneling (from Figure A-68; BSE image). Green box is the location of Figure A-71.

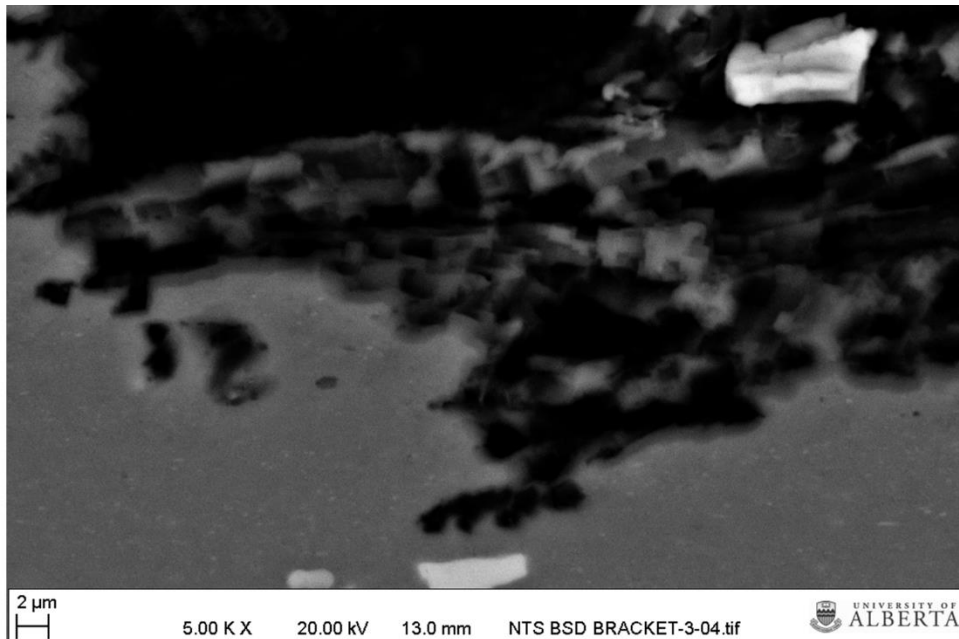


Figure A-71: Close-up of crystallographic pitting on the tunnel surfaces (from Figure A-70; BSE image).

#### *A-2.3.4 Deposit Compositions*

EDX analysis was performed on specimens from nearly all of the collected deposits. The specimens were prepared in the following manner before being analyzed. First, the samples were rinsed with acetone, followed by methanol. Then the specimens were allowed to dry in a desiccator for 24 hours. After drying, the specimens were mounted on pins with double-sided carbon tape, and carbon coated. Due to the nature of EDX, as well as the variability observed in the different locations of the specimens, compositional data was reported for three points within each specimen.

High concentrations of aluminum and oxygen were present in nearly all locations within the deposits. Both elements are indicative of aluminum corrosion products [3,4,7]. Chlorine and sulphur were also found in nearly all specimens tested. Again, chloride and sulphate are known to cause corrosion in aluminum and aluminum alloys [3,4]. Additionally, copper was identified in one location in the “Tie North Section Hole – Inside” specimen. This element is also known to be a cause of corrosion in aluminum and aluminum alloys [3,4,7–10].

Table A-24: EDX data from collected deposit specimens

		Element [Normalized Weight %]														
Deposit	Point	Al	O	Si	P	S	Cl	Mg	Cu	Fe	Cr	Mn	Mo	Na	Ca	K
Bracket – Bottom	1	92.5	3.3					4.2								
	2	34.7	56.9			1.9	6.0	0.5								
	3	27.7	56.1			1.4	14.3	0.5								
Bracket – Pits	1	24.3	52.1	0.9		7.0	0.8		13.0		1.9					
	2	92.3	3.7					4.0								
	3	35.2	56.6			3.7	4.4	0.1								
Bracket/Air Line	1	23.1	63.0	3.3	0.6	5.3	4.1			0.6						
	2	22.6	66.7	3.0	2.7	2.1	1.6			0.6					0.7	
	3	21.4	58.5	3.6	8.1	1.5	1.3			2.0		1.5			2.1	
Tie South Section End – Inside	1	84.8	14.2					1.0								
	2	37.0	61.7	0.3			0.9	0.1								
	3	33.8	65.8				0.2	0.2								
Tie North Section Hole – Inside	1	33.4	53.8	1.8		0.8	0.6	1.1	4.9	0.9					2.7	
	2	34.9	62.6				1.2							1.3		
	3	2.8	31.8	1.1		0.3		0.2		63.8						
Tie North Section Hole – Pits	1	18.4	65.4	2.3	6.3			0.5					2.3	0.4	4.4	
	2	6.6	50.2	5.4		0.3		0.5		36.1				0.3		0.6
	3	17.0	60.7	2.3	7.7	6.3	1.1							0.5	4.2	

Deposit	Point	Element [Normalized Weight %]														
		Al	O	Si	P	S	Cl	Mg	Cu	Fe	Cr	Mn	Mo	Na	Ca	K
Base Plate	1	24.8	58.3	6.7	1.0	8.0	1.2									
	2	19.9	58.7	13.1	0.6	3.8	0.7						3.2			
	3	23.6	63.8	0.4	3.9	6.3	1.0			0.6					0.4	
Floor Deposit #1	1	21.7	61.6	7.7	1.3	4.9	1.6			0.8					0.4	
	2	33.2	58.1			8.7										
	3	29.9	53.6	6.6	1.8	7.6				0.5						
Floor Deposit #2	1	20.9	55.6	13.2	0.9	6.6	1.6			0.6						0.6
	2	26.8	52.6	12.8	0.8	5.0	0.8			0.7						0.5
	3	10.7	39.2	34.6		0.9		1.4						5.2	8.0	
Wall Horizontal Weld and Grind Marks	1	29.8	61.0	0.8	2.0	4.2	1.6								0.6	
	2	26.2	62.1	1.4	1.7	6.8	1.4								0.4	
	3	41.8	41.0	4.7	1.2	3.5	7.1								0.7	
Wall Tooling Marks	1	28.0	57.6	4.6	2.7	3.6	2.3			0.5					0.7	
	2	10.5	47.3	29.7	1.0		0.5							1.5		9.5
	3	26.6	59.3	2.0	5.5	1.6	2.5	0.9		0.3					1.3	

## A-2.4 Metallographic Examination and Hardness Testing

The following section is broken down into subsections based on the component and specific specimen collected from the component for metallographic examination. All cross-sections were cold mounted in epoxy resin. The specific surface preparation achieved, prior to etching, was as follows: 240, 320, 400, 600, 800, and 1200 grit sequential wet-grinding with silicon carbide grit paper, followed by 3 micron and 1 micron polishing with diamond suspension. Etching of the wall, floor, and aeration line bracket cross-sections was done electrolytically with freshly prepared Barker's reagent (etched for 3 to 10 minutes in 5 mL fluoroboric acid ( $\text{HBF}_4$ ) and 200 mL DIUF at 30 V and 0.2 A). Meanwhile, the tubular tie cross-sections were etched with freshly prepared hot sodium hydroxide solution (as described in Section 2.3.2.2). All etchants and etching procedures allowed for the examination of the various samples' microstructure. For further information on etching, refer to ASTM E407 [15].

Due to the variability in pitting damage on the tubular tie, three cross-sections were removed and prepared for microstructural examination. Of the three, two cross-sections were removed from material adjacent to the through-wall hole on the north section of the tie. The first cross-section was in the radial direction (labelled "Hole Circumference"), and the second cross-section was in the axial direction (labelled "Hole Axial"). The third cross-section was removed from material near the south end of the tubular tie south section. This cross-section was in the radial direction (labelled "End Circumference").

Finally, the results of the hardness testing performed on each cross-section are provided in Section 2.4.2.

#### A-2.4.1 *Optical Microscopy (OM)*

##### A-2.4.1.1 *Wall Cross-section*

The wall cross-section and its microstructure are shown below in Figures A-72 and A-73, respectively. The orientation of the cross-section is perpendicular to both the wall surface fabrication markings and suspected rolling direction of the overall wall sheet. The microstructure was comprised primarily of flat, elongated aluminum grains. Also present were precipitates that were fairly uniformly distributed throughout the cross-section. These precipitates are believed to be magnesium aluminides ( $Mg_2Al_3$ ;  $\beta$  phase) and, to a lesser extent, magnesium silicides ( $Mg_2Si$ ). Finally, larger inclusions (believed to be intermetallics of varying composition) were identified throughout the cross-section. This microstructure appeared consistent with rolled 5086 or 5083 sheet [16–21].

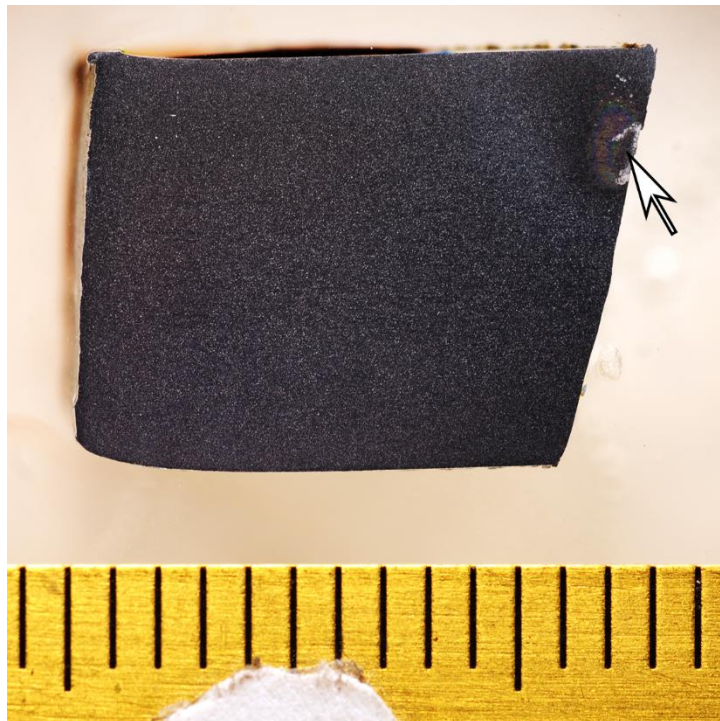


Figure A-72: Overall image of etched wall cross-section. The mark near the top right corner (white arrow) is an artifact from the etching process. Scale is in mm.

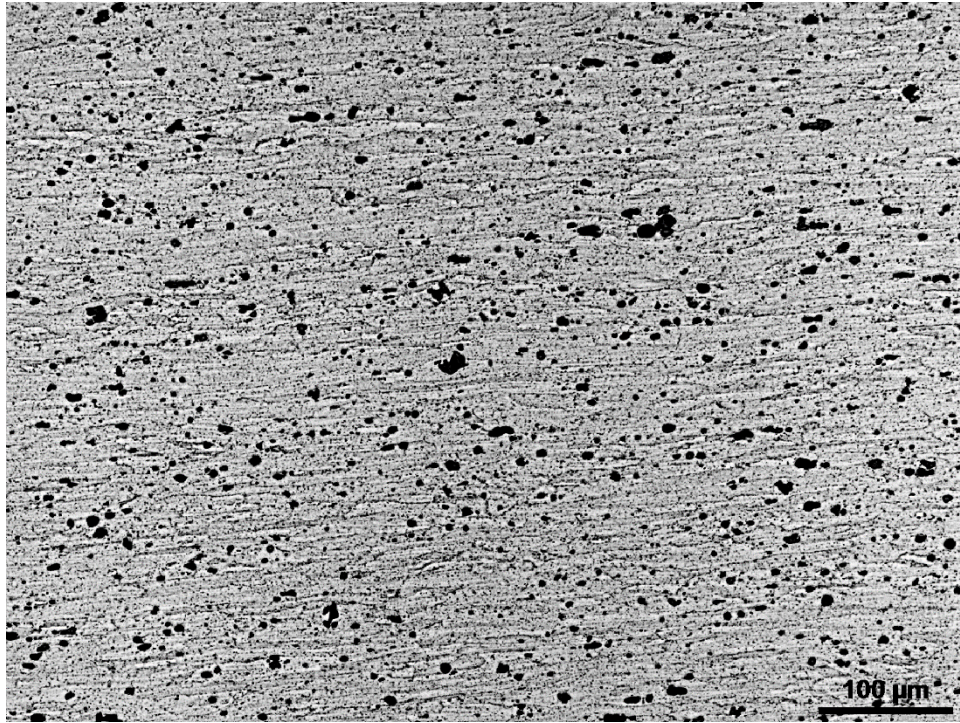


Figure A-73: Microstructure of the wall cross-section (center of specimen; from Figure A-72).

#### *A-2.4.1.2 Floor Pit Cross-section*

The floor cross-section and its microstructure are shown below in Figures A-74 through A-83. This cross-section (Figure A-74) is the other half of the large, 5.1 cm diameter pit, which was sectioned for SEM examination. The large pit appeared to have a wide, shallow opening with multiple smaller pits encapsulated within it (Figures A-75, A-78, and A-82). The smaller pits were elliptical in shape, deeper, and also exhibited signs of undercutting (Figures A-75 and A-78). At higher magnification, tunneling could be seen originating from and below pit surfaces (Figures A-76, A-78, A-79, and A-82). Finally, crystallographic pits (in the shape of cubes) were found on the walls of the pit tunnels (Figures A-77, A-80, A-81, and A-83). Due to the etching process, it becomes difficult to view the crystallographic pitting (loss of edge fidelity and resolution); therefore, both etched and un-etched images are provided where appropriate. Unless otherwise stated, all images are etched.

The microstructure was comprised primarily of flat, elongated aluminum grains. Also present were precipitates that were fairly uniformly distributed throughout the cross-section. The microstructure observed on the floor cross-section appeared to be the same as the wall cross-section, which was consistent with rolled 5086 or 5083 sheet [16–21]. Furthermore, preferential corrosion occurring with respect to the metallurgical grain structure could not be identified.



Figure A-74: Overall image of the etched floor cross-section. The mark near the bottom right corner (white arrow) is an artifact from the etching process. Scale is in mm.

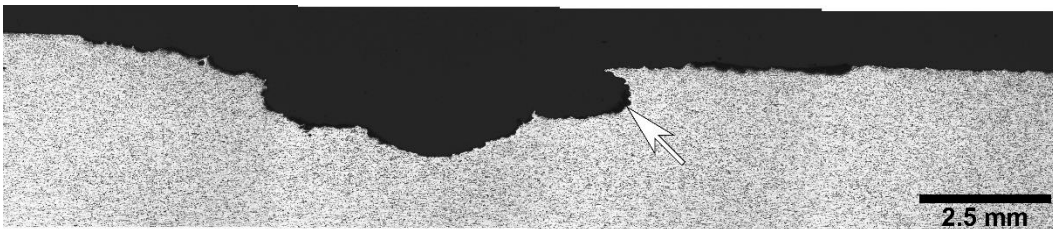


Figure A-75: Composite image of the deepest portion of the 5.1 cm pit. Undercutting (white arrow) can also be observed.

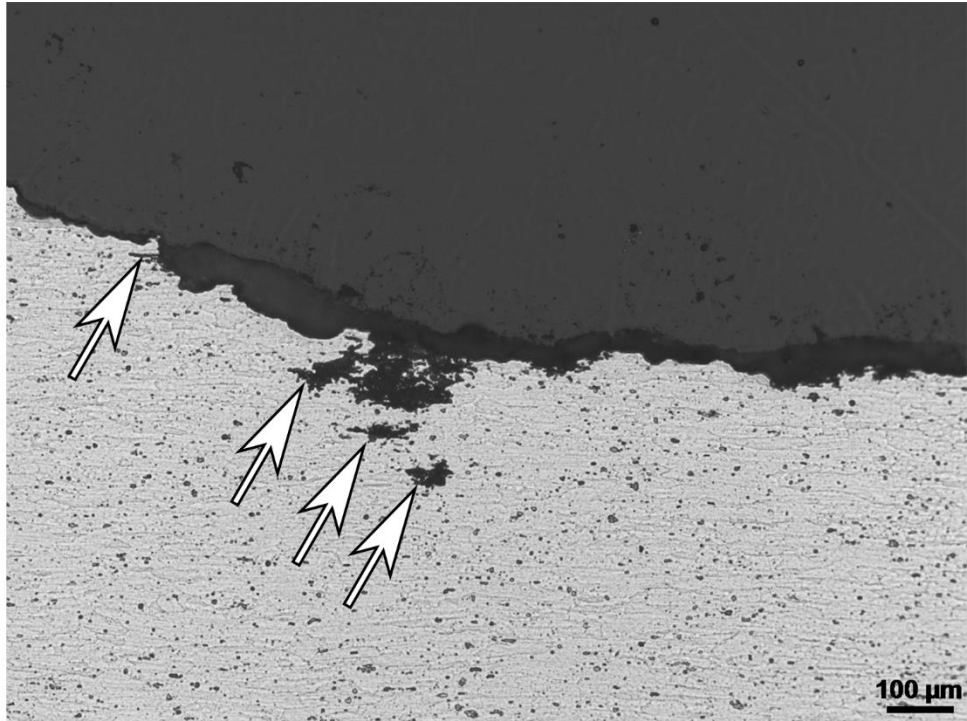


Figure A-76: Tunneling (white arrows) near the bottom of the deepest part of the pit (left of the deepest pit; from Figure A-75).

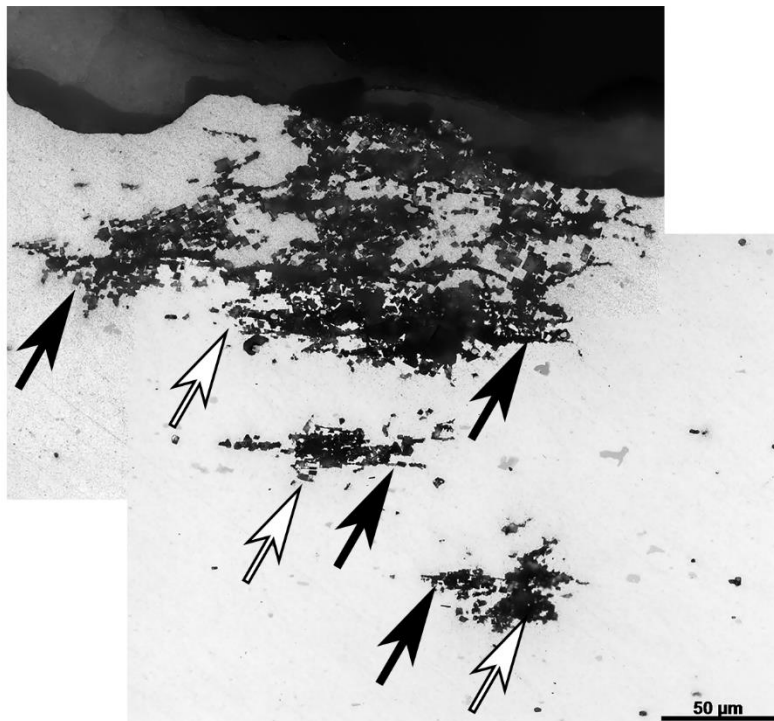


Figure A-77a: Close-up on tunneling (white arrows) and crystallographic pitting (black arrows). Figure A-77a is un-etched; from Figure A-76.

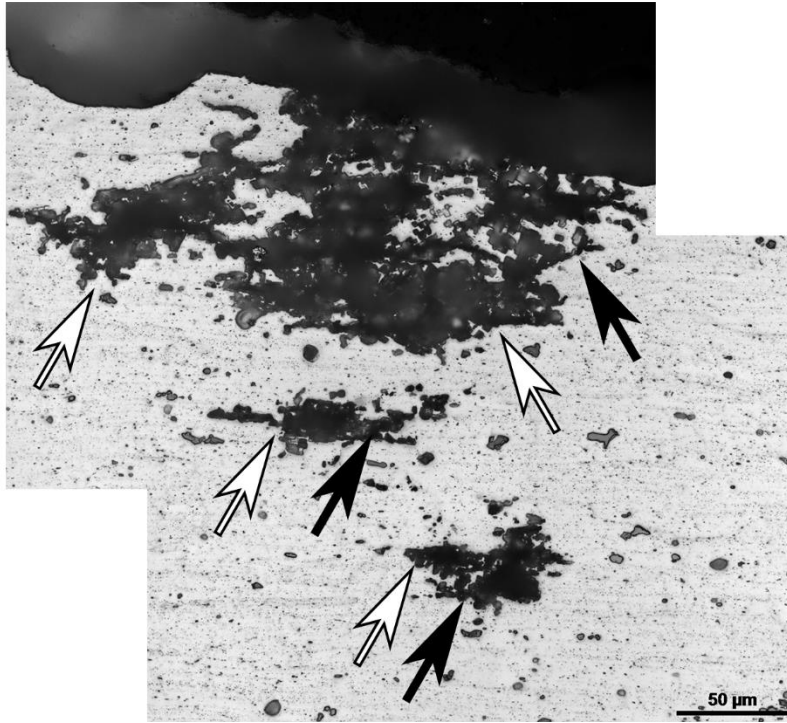


Figure A-77b: Close-up on tunneling (white arrows) and crystallographic pitting (black arrows) – after etching same region from Figure A-77a. Figure A-77b is etched; from Figure A-76.

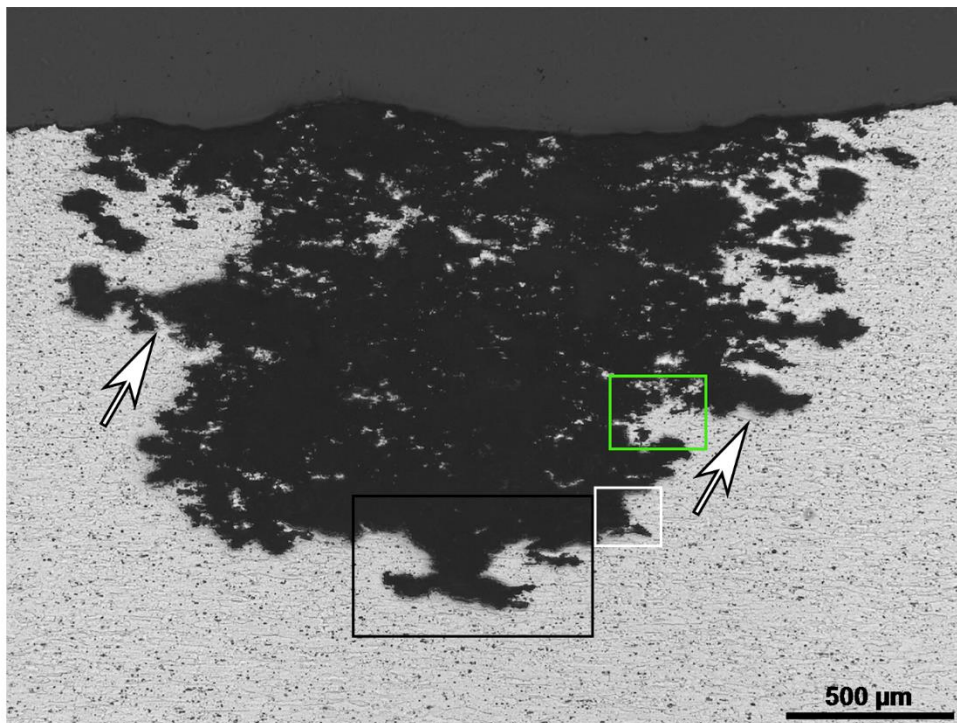


Figure A-78: Image of smaller pit (from Figure A-74). Tunnelling (white arrows) can also be observed. Black, white, and green boxes contain Figures A-79, A-80, and A-81, respectively. Tunneling is also observed in the black box.



Figure A-79: Tunneling at the bottom of the deepest part of the smaller pit (from Figure A-78).



Figure A-80: Close-up on tunneling (white arrows) and crystallographic pitting (black arrows) (from Figure A-78). The left image is un-etched while the right image is etched.

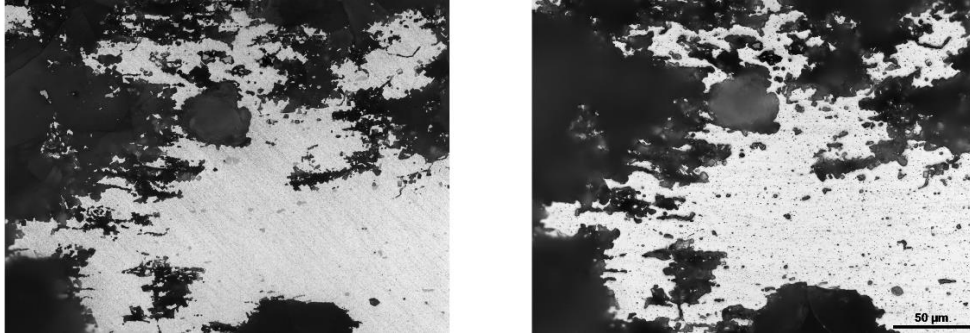


Figure A-81: Close-up on tunneling and crystallographic pitting (from Figure A-78). The left image is un-etched while the right image is etched.

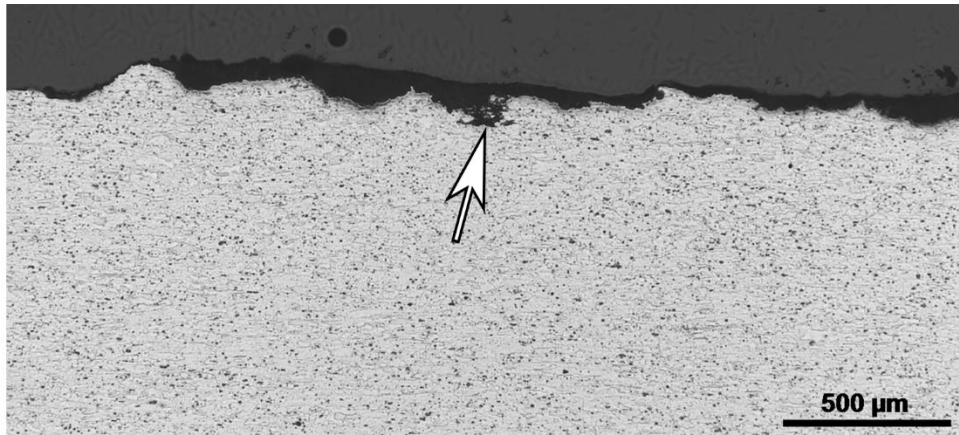


Figure A-82: Very small pit at the surface of the floor cross-section exhibiting tunneling (white arrow).

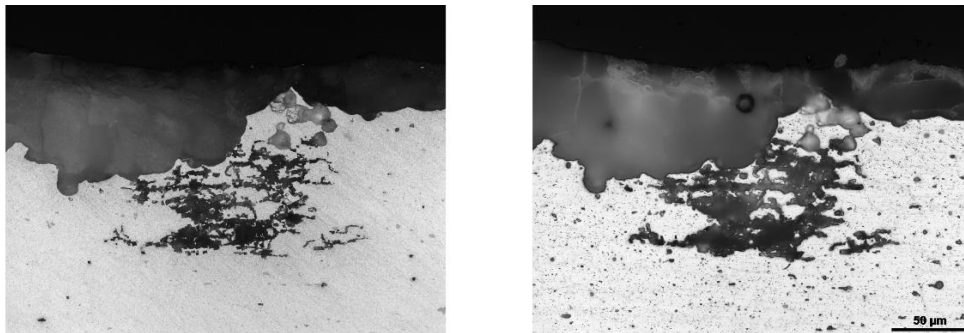


Figure A-83: Close-up on tunneling and crystallographic pitting (from Figure A-82). The left image is un-etched while the right image is etched.

#### A-2.4.1.3 Tubular Tie – Hole Circumference Cross-section

The first tie cross-section (in the radial direction; labelled “Hole Circumference”) and its microstructure are shown below in Figures A-84 through

A-93. Corrosion damage was found on all of the cross-section surfaces (Figures A-84, A-85, A-88, A-90, and A-93). Again, in addition to pitting, IGC was observed both at and below the surface of the pits (Figures A-86, A-87, A-89, A-91, and A-92) as well as on un-pitted surfaces (Figure A-93). As with the unmounted cross-section (Section 2.3.2.1), corrosion was found to have occurred both in the grains and at the grain boundaries (Figures A-87, A-89, A-91, and A-92). Moreover, the most severe damage was found on the portion of the cross-section which was immediately adjacent to the through-wall hole (Figures A-85 through A-87) and, consequently, the 304 stainless steel aeration piping.

The microstructure was comprised primarily of large, coarse aluminum grains. Also present were precipitates that were fairly uniformly distributed throughout the cross-section. These precipitates are believed to be magnesium silicides ( $Mg_2Si$ ). Finally, larger inclusions (believed to be intermetallics of varying composition) were identified throughout the cross-section. This microstructure appeared consistent with extruded 6061 tube [16–19].

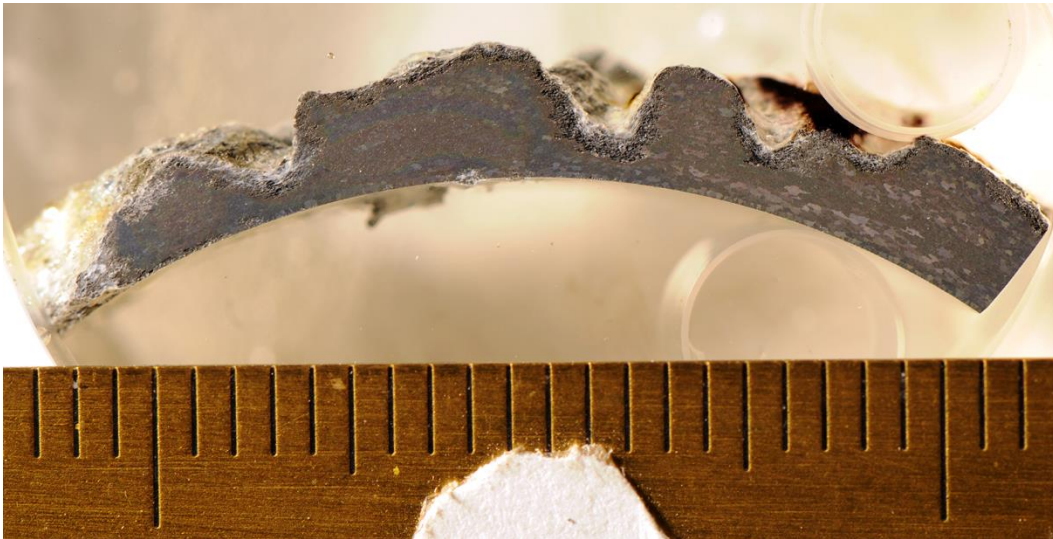


Figure A-84: Overall image of etched tubular tie cross-section (in the radial direction; labelled “Hole Circumference”). Scale is in mm.

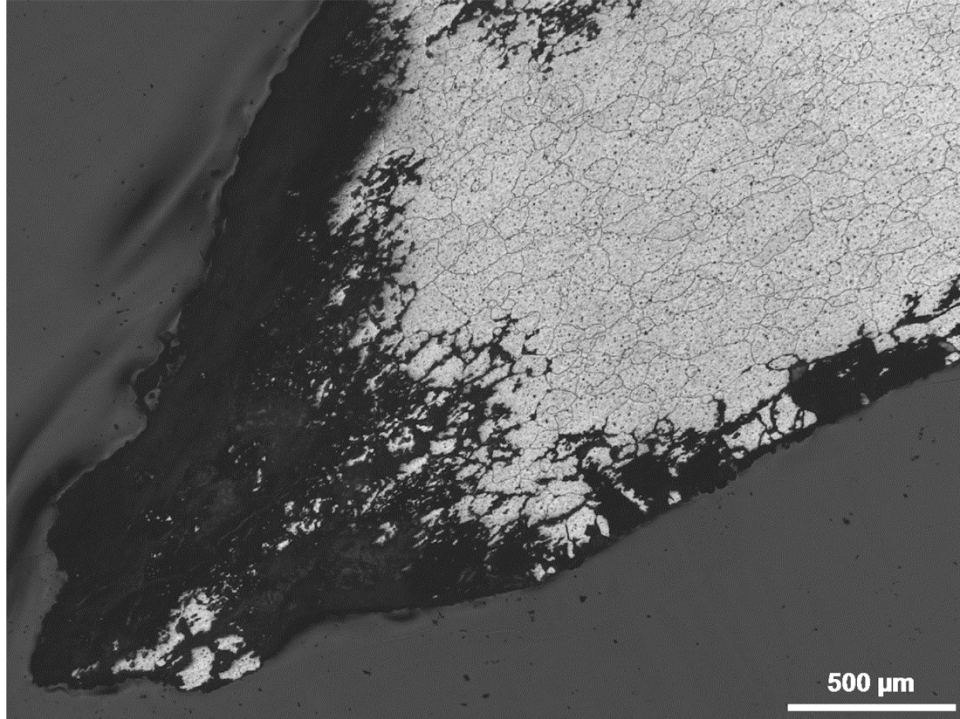


Figure A-85: Severe corrosion damage on portion of the tie immediately adjacent to the through-wall hole (from Figure A-84).

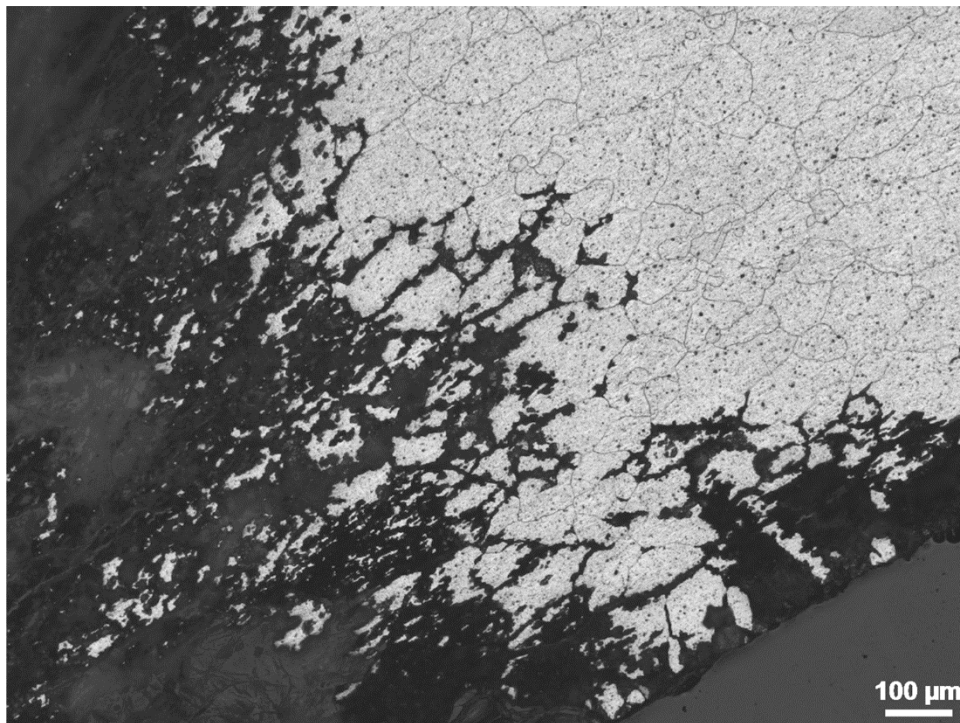


Figure A-86: IGC and pitting on portion of the tie immediately adjacent to the through-wall hole (from Figure A-85).

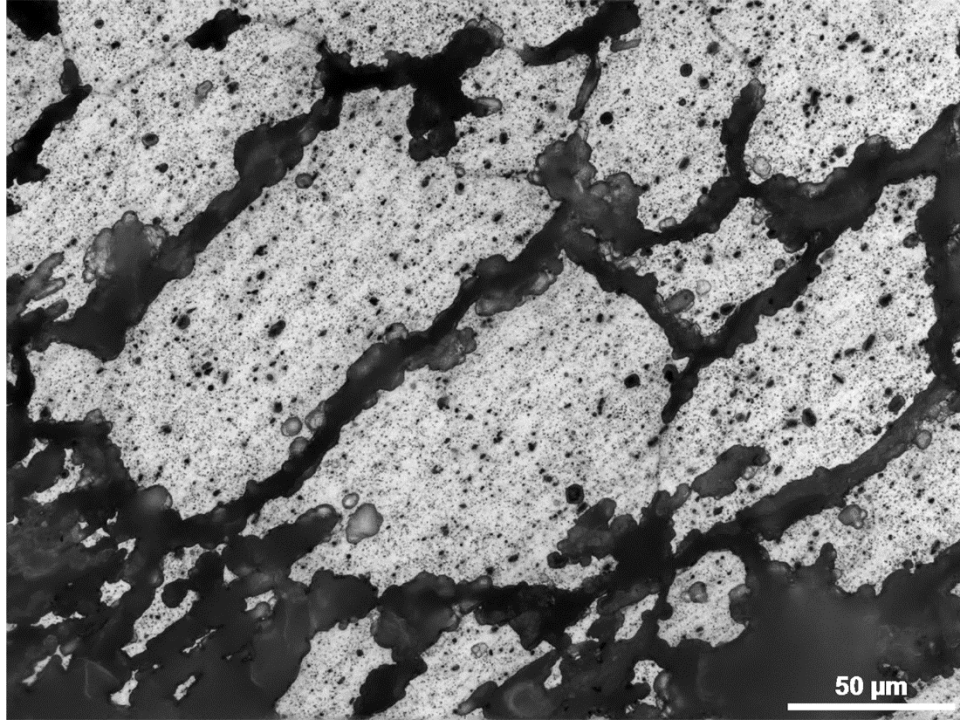


Figure A-87: Close-up on IGC and pitting (from Figure A-86).

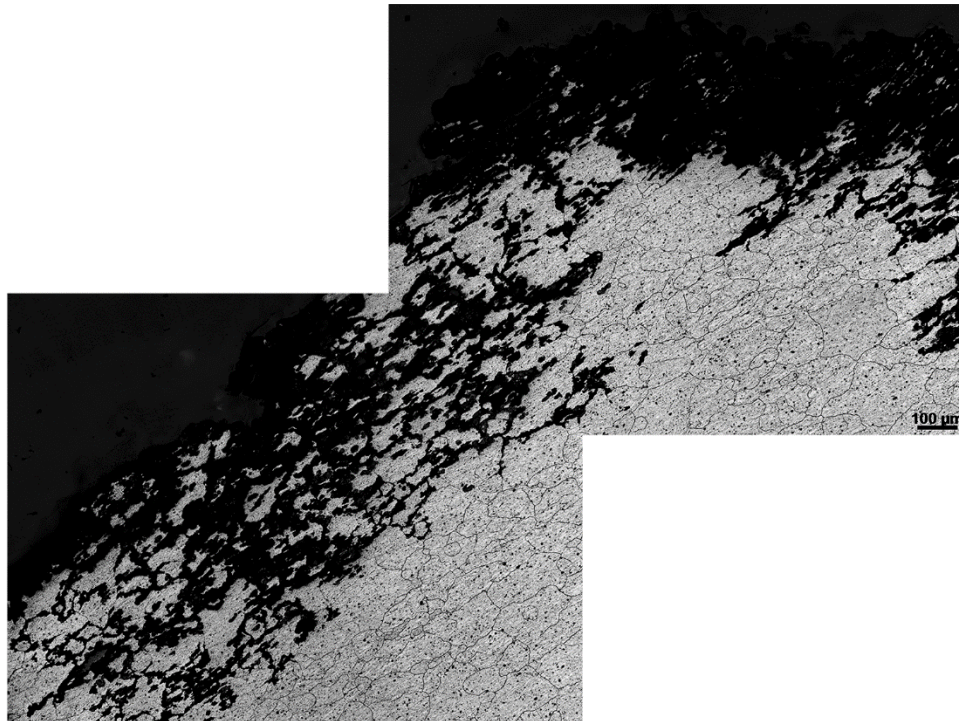


Figure A-88: IGC and pitting on the outer diameter of the tie cross-section (from Figure A-84).

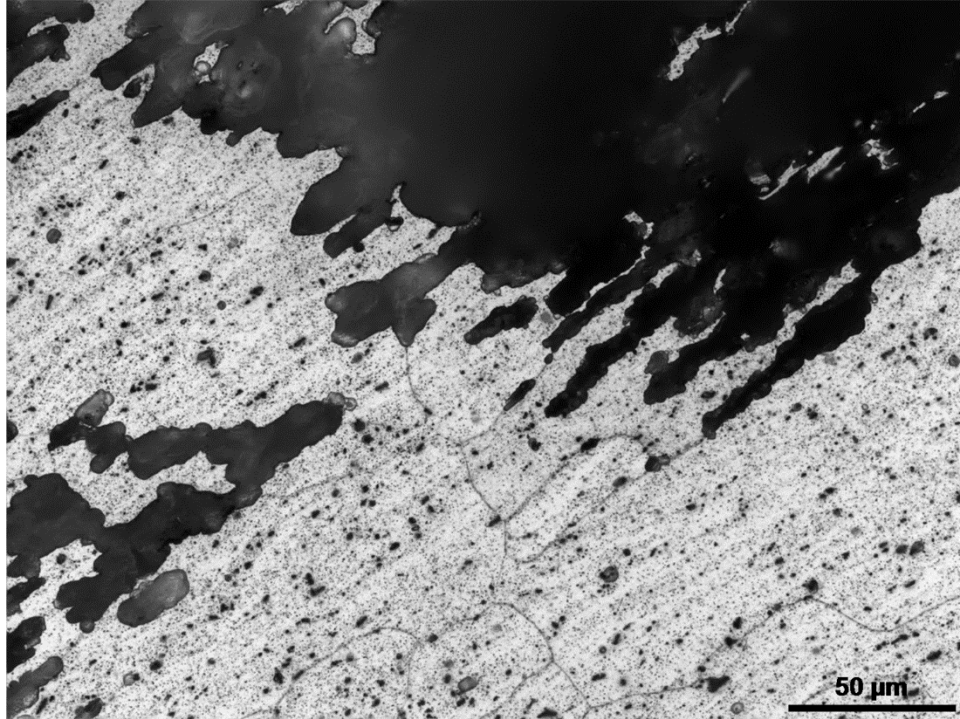


Figure A-89: Close-up on IGC and pitting (from Figure A-88).

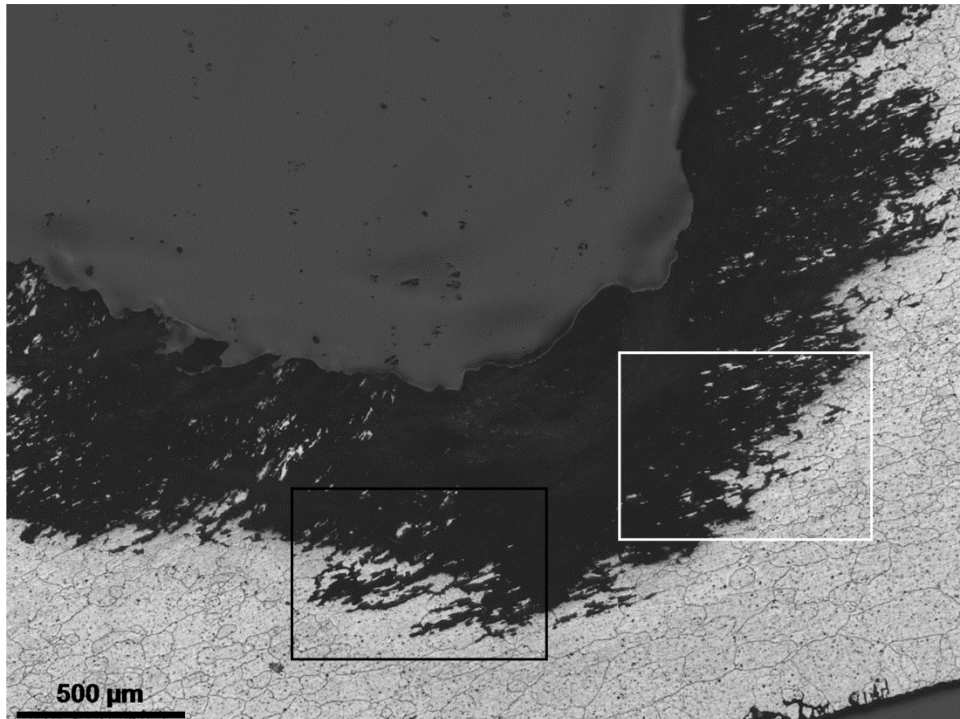


Figure A-90: Large pit on the outer diameter of the tie cross-section (from Figure A-84). The black and white boxes contain Figures A-91 and A-92, respectively.



Figure A-91: IGC and pitting near the bottom of the large pit (from Figure A-90).

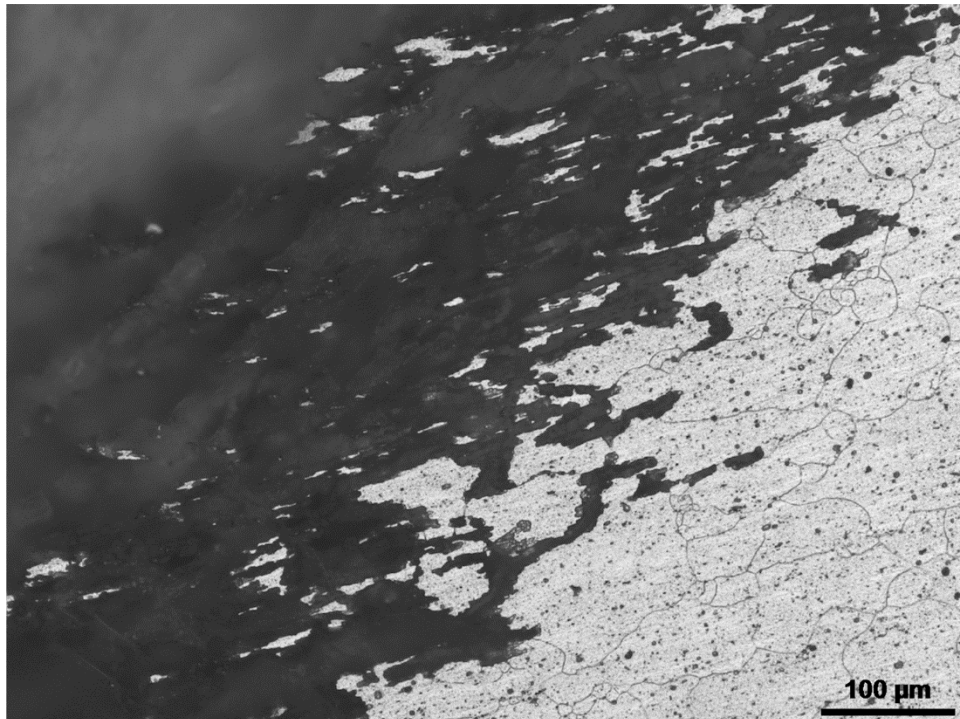


Figure A-92: IGC and pitting near the bottom of the large pit (from Figure A-90).

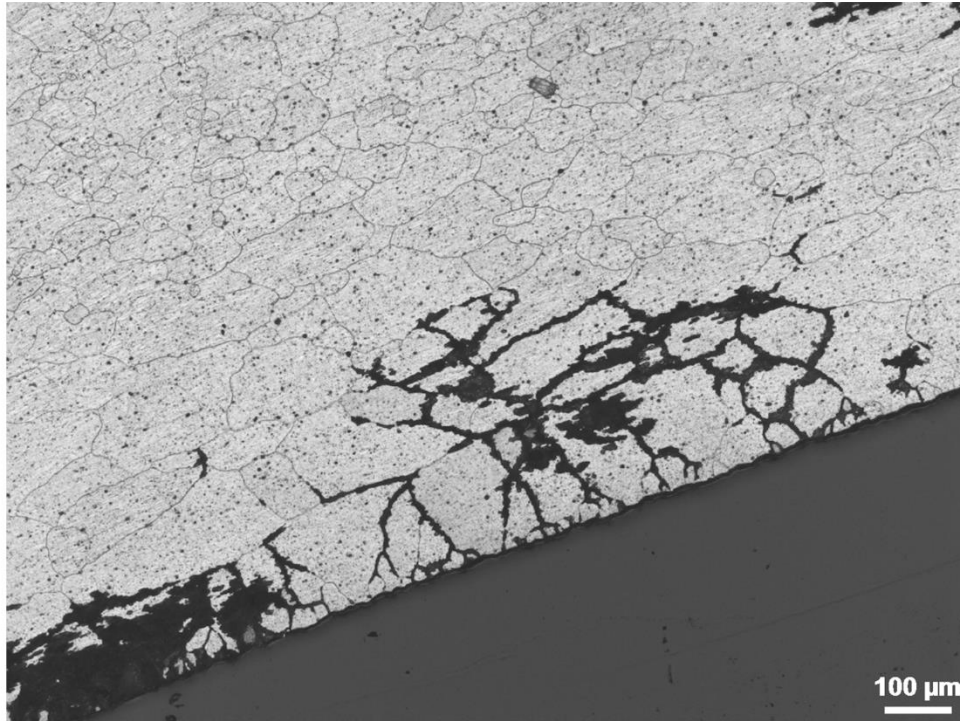


Figure A-93: IGC and pitting on the inner diameter of the tie cross-section (from Figure A-84).

#### *A-2.4.1.4 Tubular Tie – Hole Axial Cross-section*

The second tie cross-section (in the axial direction; labelled “Hole Axial”) and its microstructure are shown below in Figures A-94 through A-102. Corrosion damage was found on all of the cross-section surfaces (Figures A-94, A-95, A-97, and A-99). Pitting and IGC were observed both at and below the surface of the pits (Figures A-96, A-98, A-100, A-101, and A-102) as well as on un-pitted surfaces (Figures A-95 and A-96). As with the “Hole Circumference” cross-section (Section 2.4.1.3), the most severe damage was found on the portion of the cross-section which was immediately adjacent to the through-wall hole (Figures A-97 and A-98). Finally, there also appeared to be some preferential corrosion in the extrusion or drawing direction of the tie (Figures A-97, A-98, A-100, A-101, and A-102). It is believed that the corrosion is preferentially attacking both grain boundaries and any build-up in dislocation density in the extrusion or drawing direction.

Similar to the “Hole Circumference” cross-section (Section 2.4.1.3), the microstructure was comprised primarily of large, coarse aluminum grains. Precipitates ( $Mg_2Si$ ) and inclusions were also identified throughout the cross-section, in a fairly uniform distribution. There also appeared to be directionality to the microstructure – especially the precipitates and inclusions – in parallel to the extrusion or drawing direction. This stratification is due to processing of the material by either extrusion or drawing. The microstructure in this cross-section also appeared consistent with extruded 6061 tube [16–19].

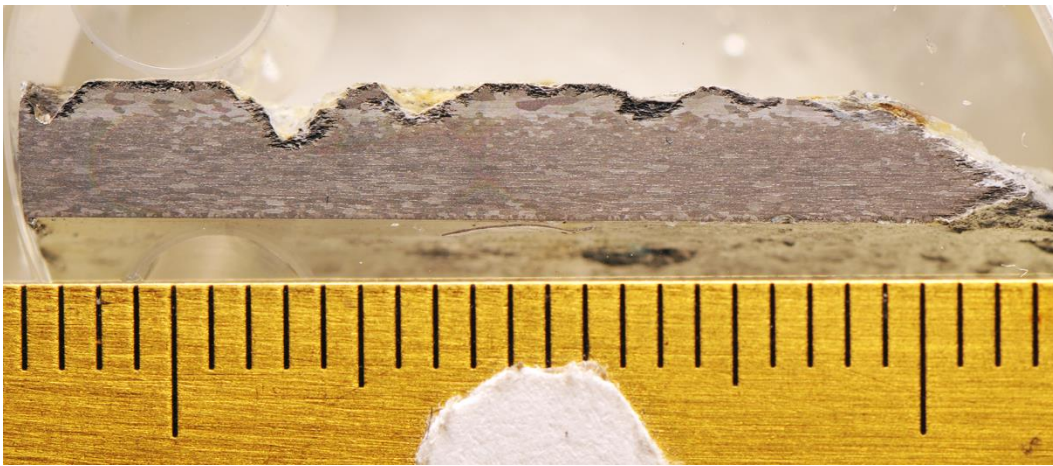


Figure A-94: Overall image of etched tubular tie cross-section (in the axial direction; labelled “Hole Axial”). Scale is in mm.

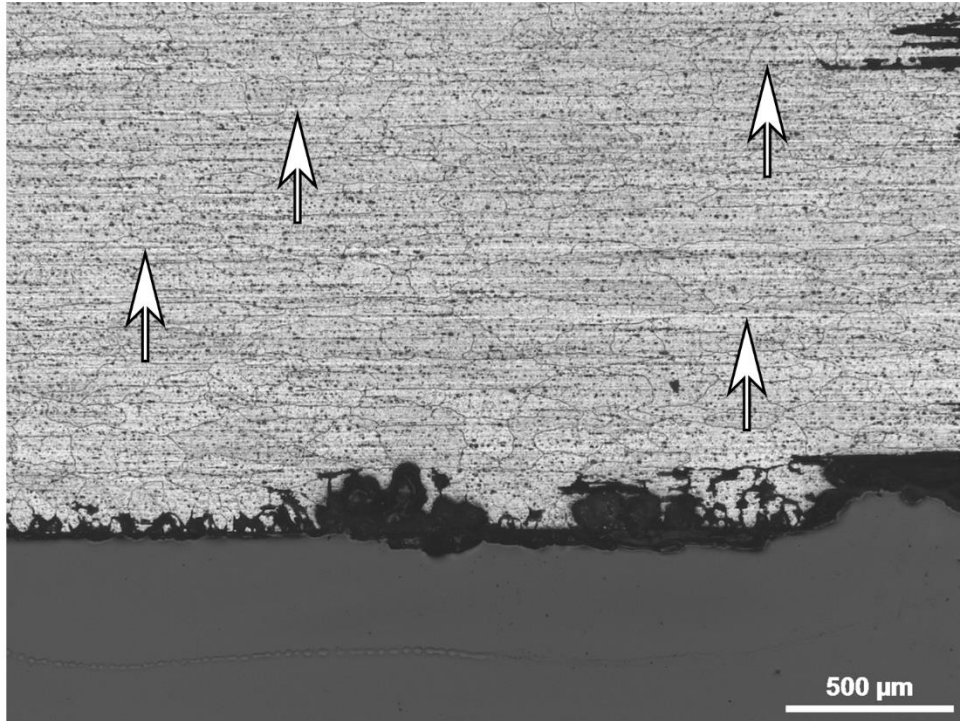


Figure A-95: Corrosion damage on the inner diameter of the tie cross-section (from Figure A-94). White arrows are perpendicular to the above-mentioned directionality of the microstructure.

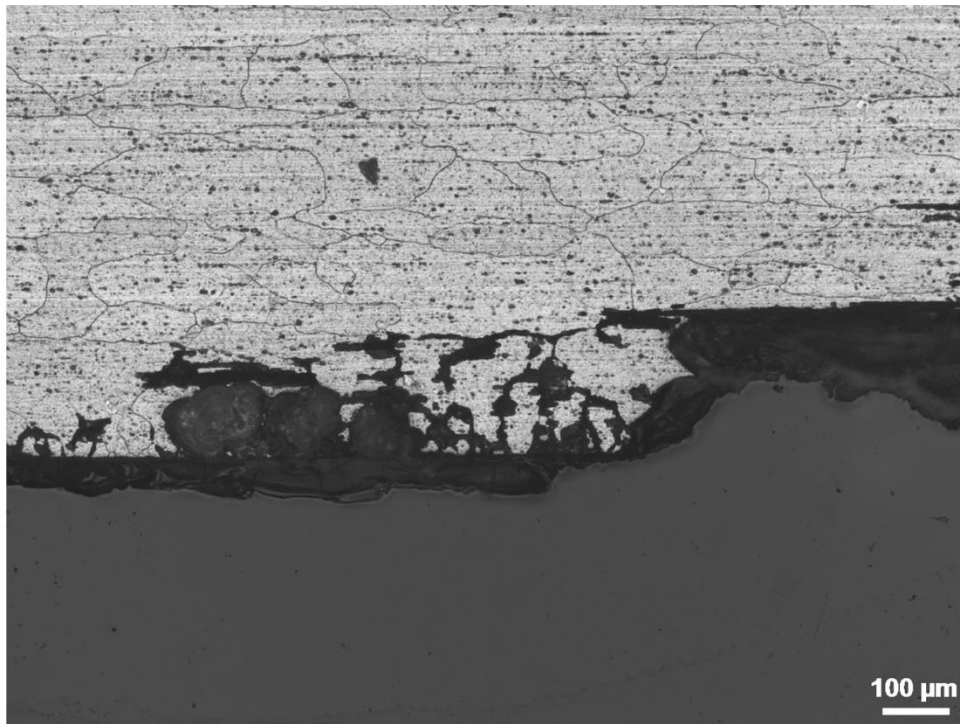


Figure A-96: Close-up on IGC and pitting (from Figure A-95).

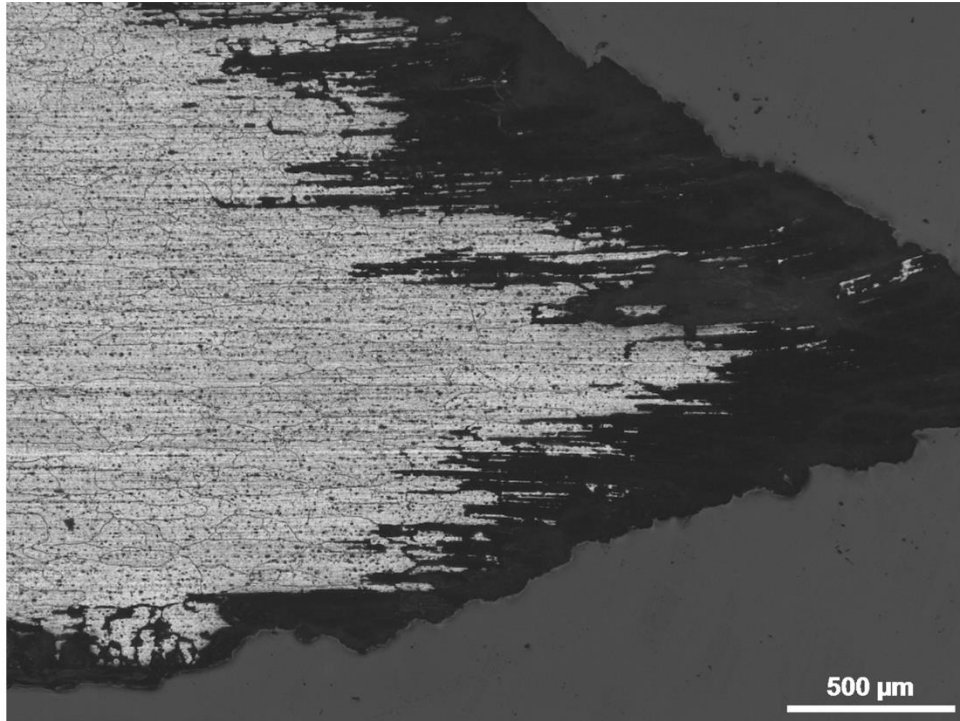


Figure A-97: Severe corrosion damage on portion of the tie immediately adjacent to the through-wall hole (from Figure A-94).

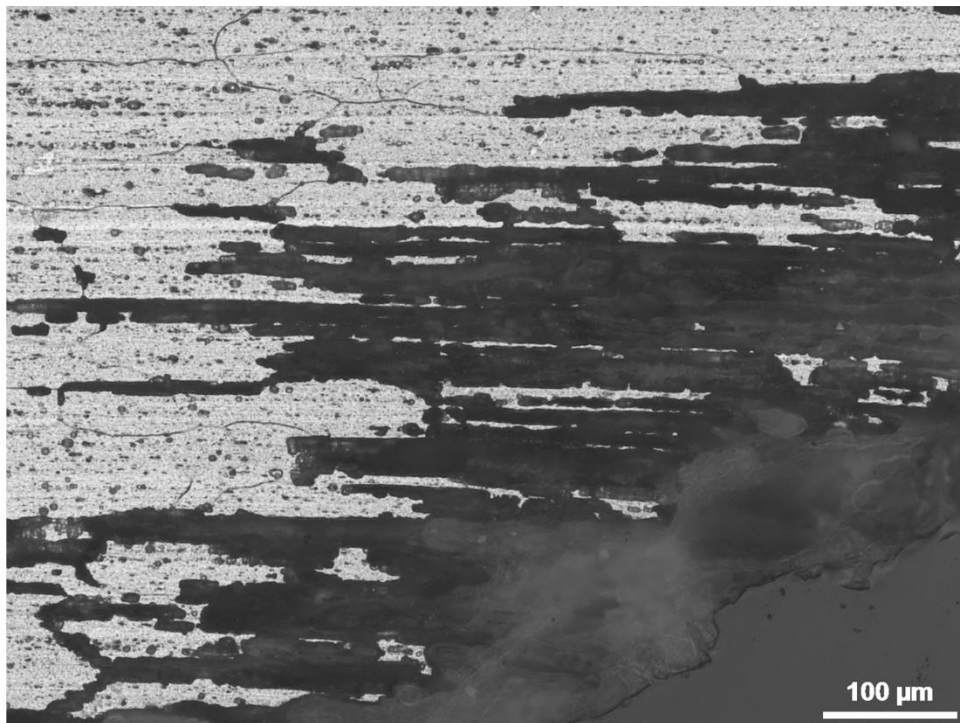


Figure A-98: Close-up on IGC, pitting, and preferential corrosion in the extrusion or drawing direction (from Figure A-97).

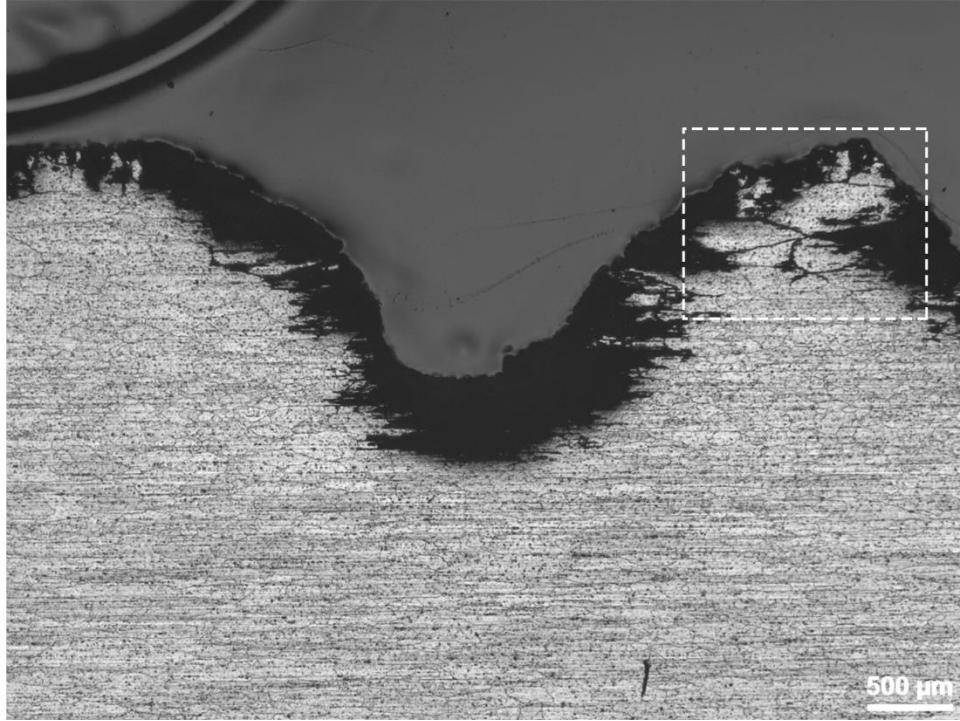


Figure A-99: Large pit on the outer diameter of the tie cross-section (from Figure A-94). The white dashed box contains Figure A-102.



Figure A-100: IGC, pitting, and preferential corrosion in the extrusion or drawing direction at the bottom of the large pit (from Figure A-99).

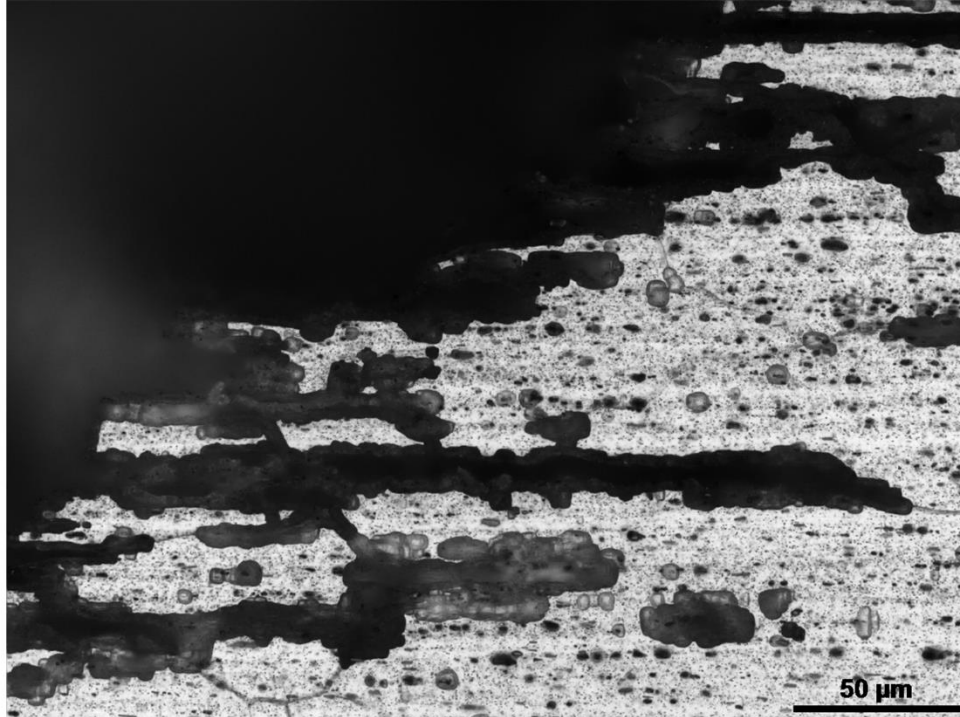


Figure A-101: Close-up on IGC, pitting, and preferential corrosion in the extrusion or drawing direction at the bottom of the large pit (from Figure A-100).

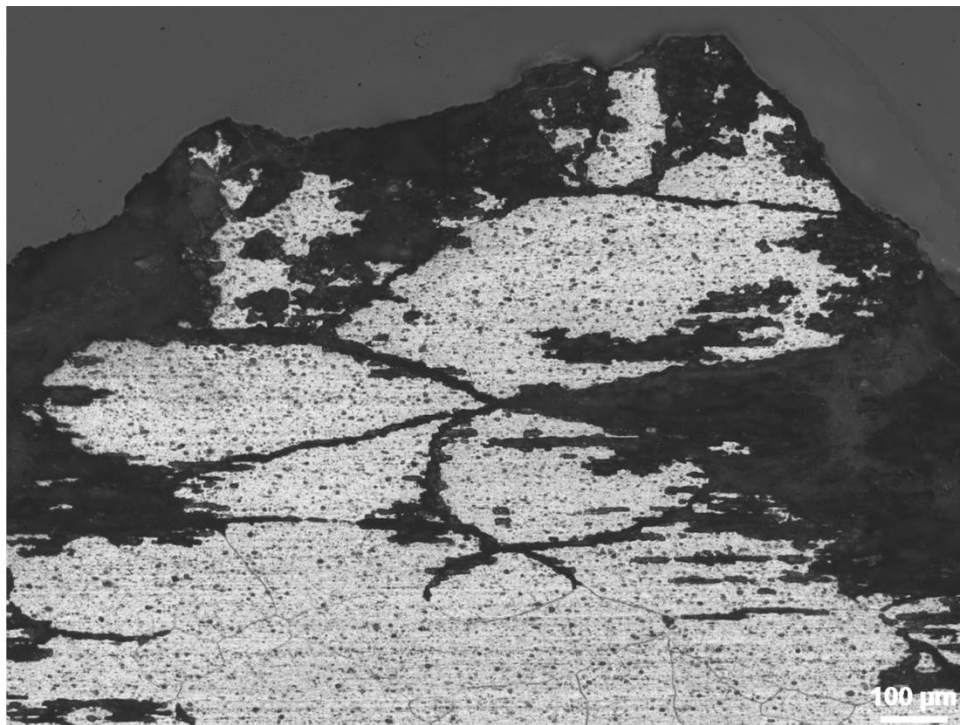


Figure A-102: IGC, pitting, and preferential corrosion in the extrusion or drawing direction on the outer diameter of the tie cross-section (from Figure A-99).

#### A-2.4.1.5 Tubular Tie – End Circumference Cross-section

The third tie cross-section (in the radial direction; labelled “End Circumference”) and its microstructure are shown below in Figures A-103 through A-106. Corrosion damage was found primarily on the outer diameter of the tie cross-section (Figures A-103 and A-104). IGC was also observed both at and below the surface of the pits (Figures A-105 and A-106). Overall, the corrosion damage was found to be less severe on this cross-section as compared to both cross-sections removed adjacent to the through-wall hole. It is believed that galvanic effects from the proximity of the stainless steel aeration piping are exacerbating the corrosion damage observed on both the “Hole Circumference” and “Hole Axial” cross-sections.

Similar to the other two cross-sections, the microstructure was comprised primarily of: large, coarse aluminum grains; and precipitates ( $Mg_2Si$ ) and inclusions that were fairly uniformly distributed. The microstructure in this cross-section also appeared consistent with extruded 6061 tube [16–19].

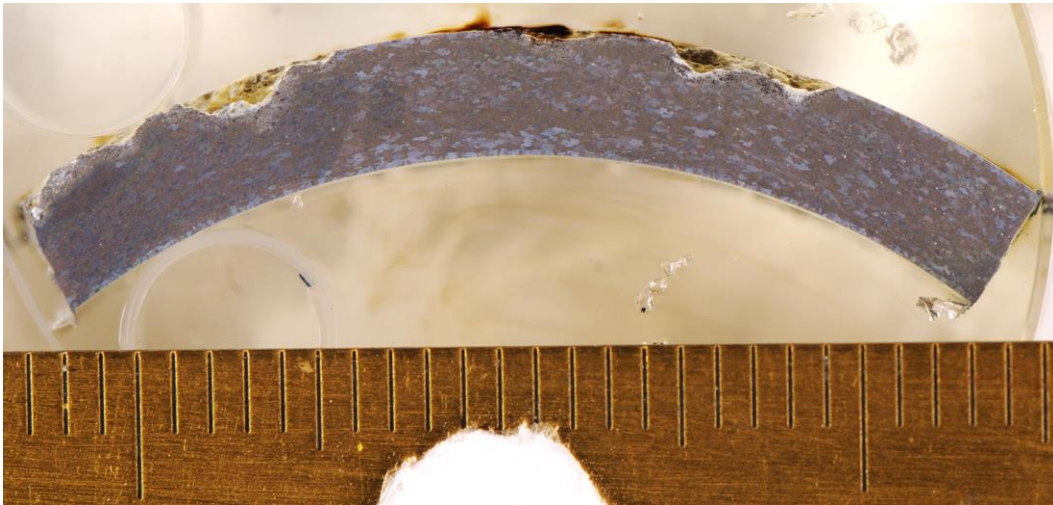


Figure A-103: Overall image of etched tubular tie cross-section (in the radial direction; labelled “End Circumference”). Scale is in mm.

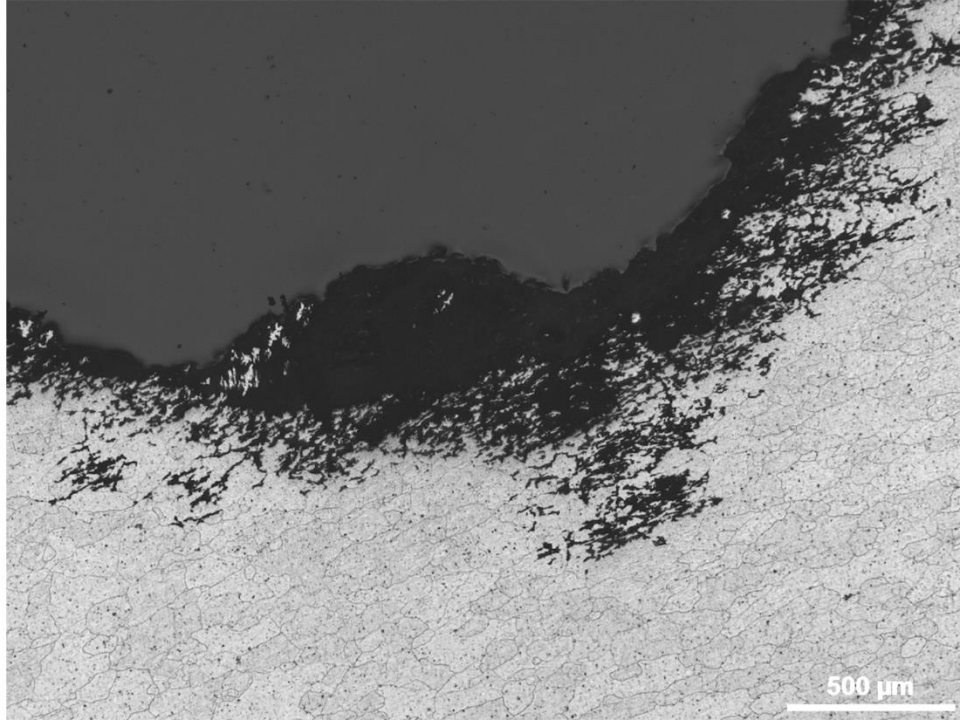


Figure A-104: Large pit on the outer diameter of the tie cross-section (from Figure A-103).

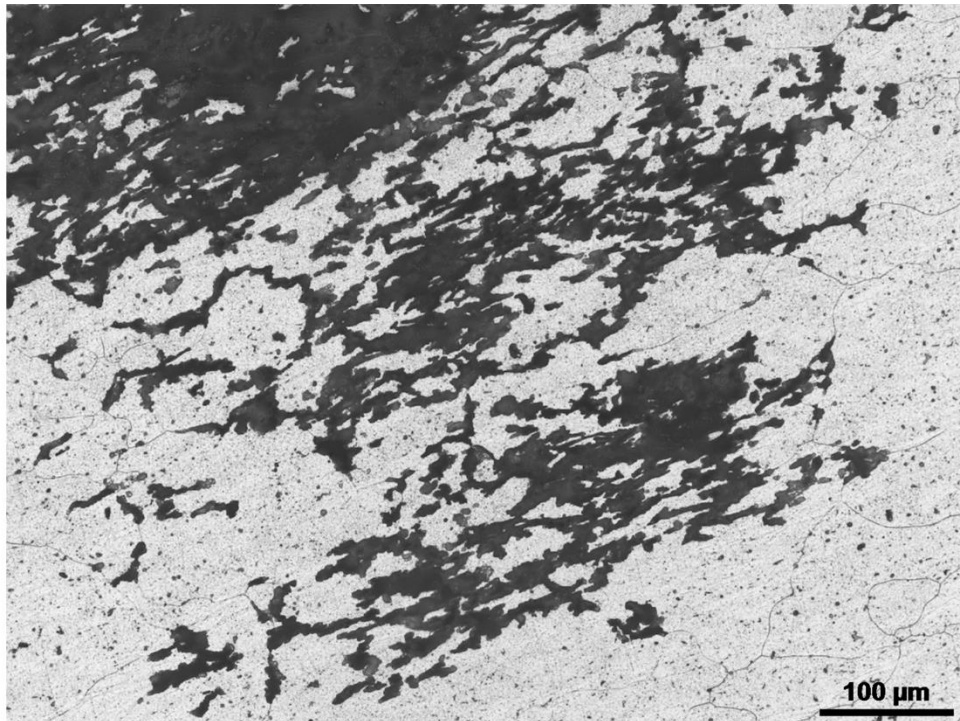


Figure A-105: IGC and pitting at the bottom of the large pit (from Figure A-104).

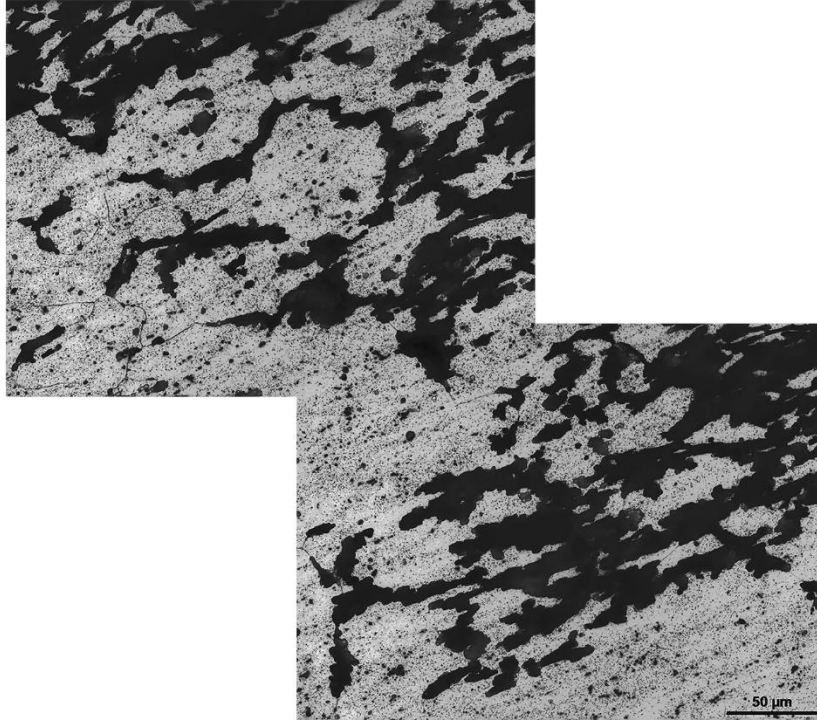


Figure A-106: Close-up on IGC and pitting (from Figure A-105).

#### *A-2.4.1.6 Aeration Line Bracket Cross-section*

The aeration line bracket cross-section and its microstructure are shown below in Figures A-107 through A-119. This cross-section (Figure A-107) is the same cross-section which was prepared for SEM examination. Pitting was found on all surfaces of the cross-section (Figures A-107, A-108, A-113, and A-115).

On the top and bottom of the cross-section, the pits appeared to be elliptical in shape, and exhibited signs of undercutting (Figures A-108 and A-113). Although pitting on the top and bottom of the cross-section appeared similar in shape, pitting on the top was deeper than on the bottom. At higher magnification, tunneling could be seen originating from and below pit surfaces (Figures A-109 through A-112, and A-114). Finally, crystallographic pits (in the shape of cubes) were found on the walls of the pit tunnels (Figures A-110, A-117, and A-119). Due to the etching process – as found with the floor cross-section – it becomes difficult to view the

crystallographic pitting. Therefore, both etched and un-etched images are provided when appropriate. Unless otherwise stated, all images are etched.

Pitting was also observed on the sides of the bracket; however, these pits appeared to be smaller in area, with either a round or irregular opening, and deeper (Figure A-115, A-116, and A-118). Both tunneling and crystallographic pits were also identified. Finally, there also appeared to be some preferential corrosion in the rolling direction of the bracket (Figures A-111, A-115, and A-118). It is believed that the corrosion is preferentially attacking both grain boundaries and any build-up in dislocation density in the rolling direction.

The microstructure was comprised primarily of flat, elongated aluminum grains. Precipitates (as  $Mg_2Al_3$  and to a lesser extent  $Mg_2Si$ ) and inclusions were also identified throughout the cross-section; both of which were fairly uniformly distributed. There also appeared to be directionality to the microstructure – in the grains, precipitates, and inclusions – in parallel to the rolling direction. This stratification is due to the sheet rolling process. Finally, the microstructure examined in the cross-section appeared consistent with rolled 5086 or 5083 sheet [16–21].

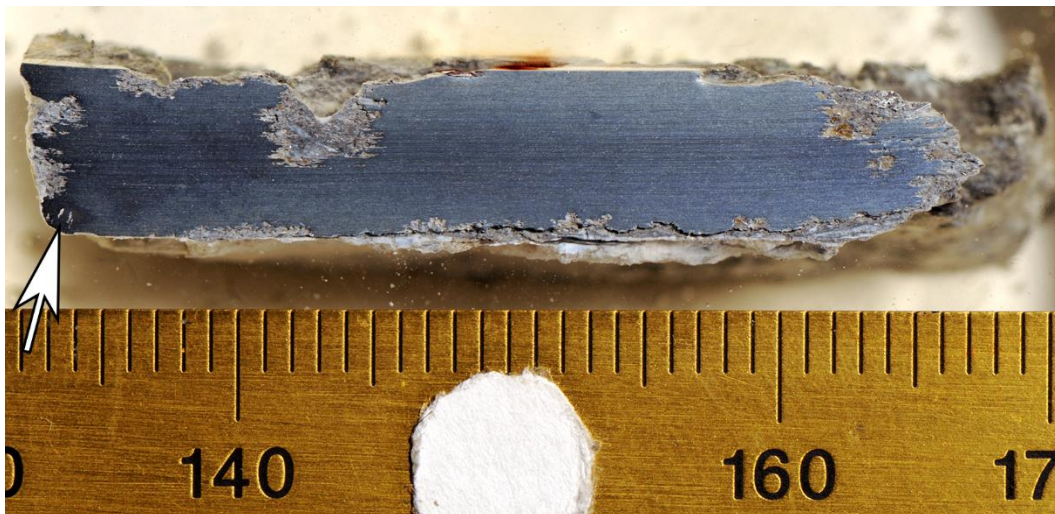


Figure A-107: Overall image of etched aeration line bracket cross-section. The mark on the bottom left corner (white arrow) is an artifact from the etching process. Scale is in mm.

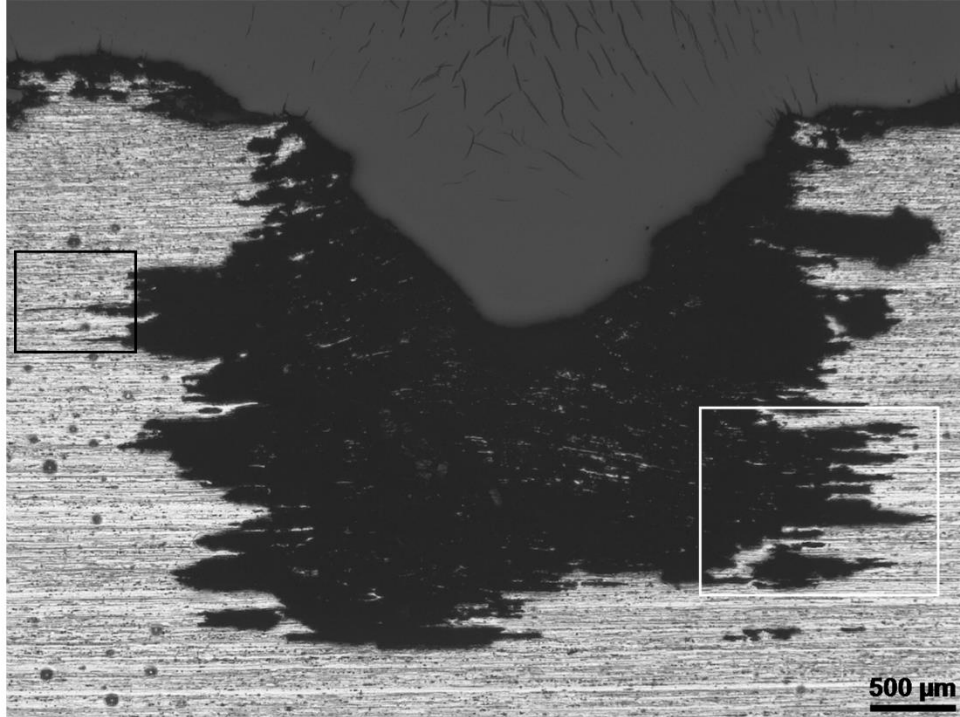


Figure A-108: Large pit on the top of the cross-section (from Figure A-107). The white box contains Figure A-109 while the black box contains Figure A-110.

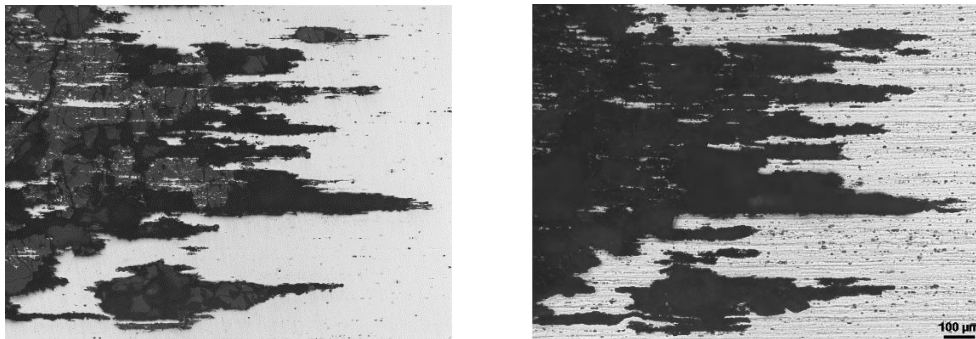


Figure A-109: Tunneling near the bottom right of the large pit (from Figure A-108). The left image is un-etched while the right image is etched.

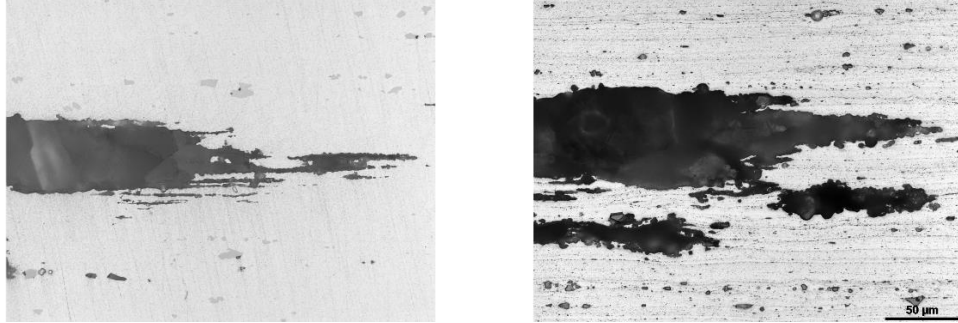


Figure A-110: Close-up on tunneling and crystallographic pitting (from Figure A-108 – near the top right corner). The left image is un-etched while the right image is etched.

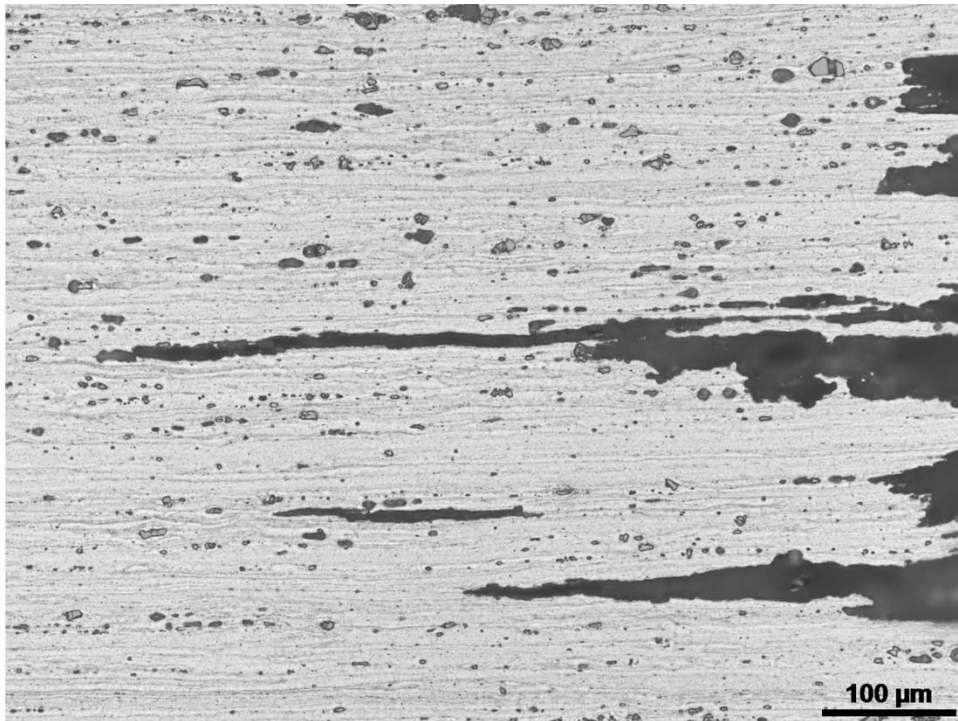


Figure A-111: Tunneling and preferential corrosion in the rolling direction on the left side of the large pit (from Figure A-108).

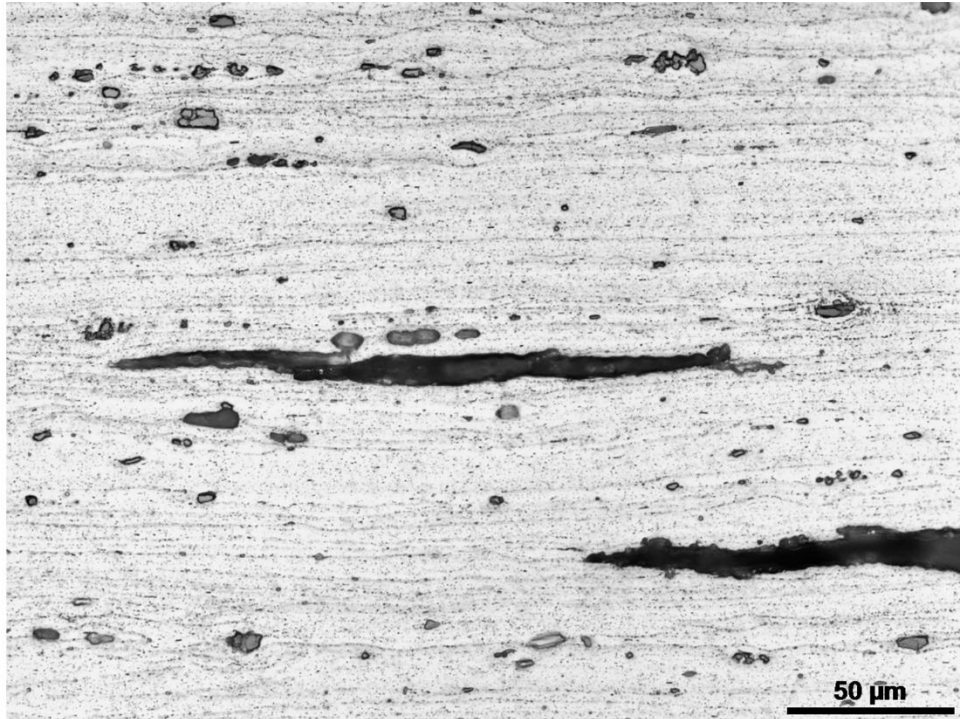


Figure A-112: Close-up on tunneling (from Figure A-111).

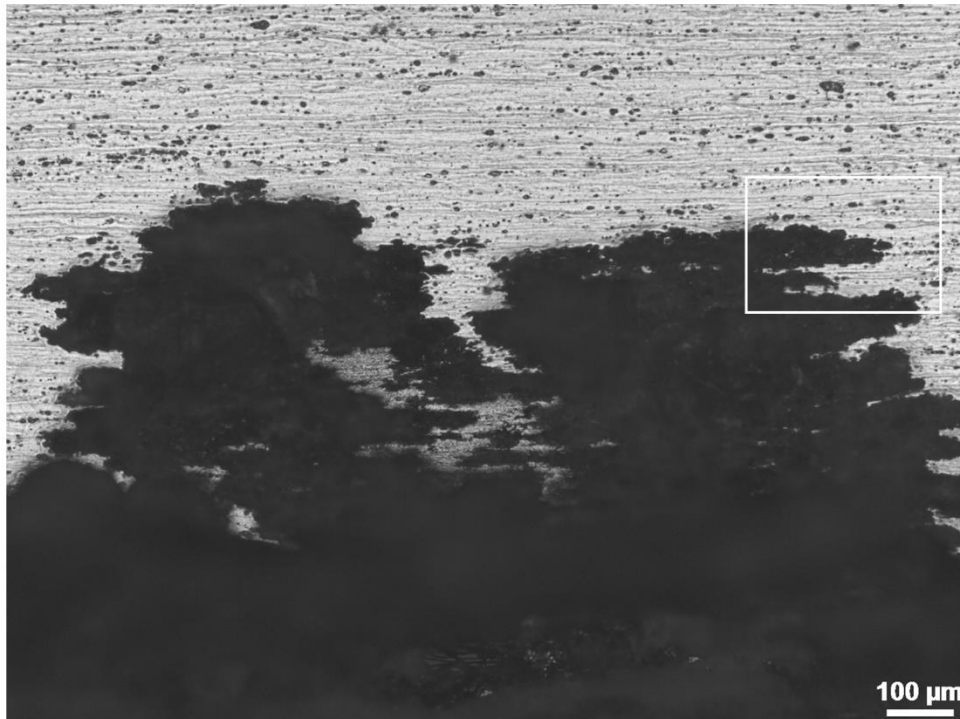


Figure A-113: Pits on the bottom right of the cross-section (from Figure A-107). White box contains Figure A-114.

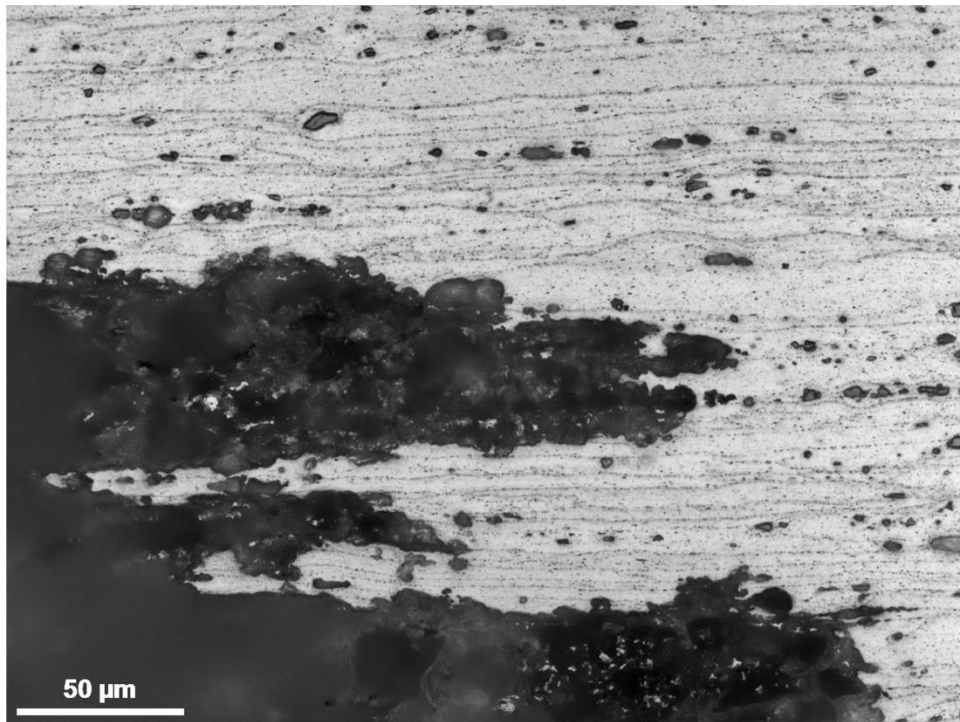


Figure A-114: Close-up on tunneling (from Figure A-113).

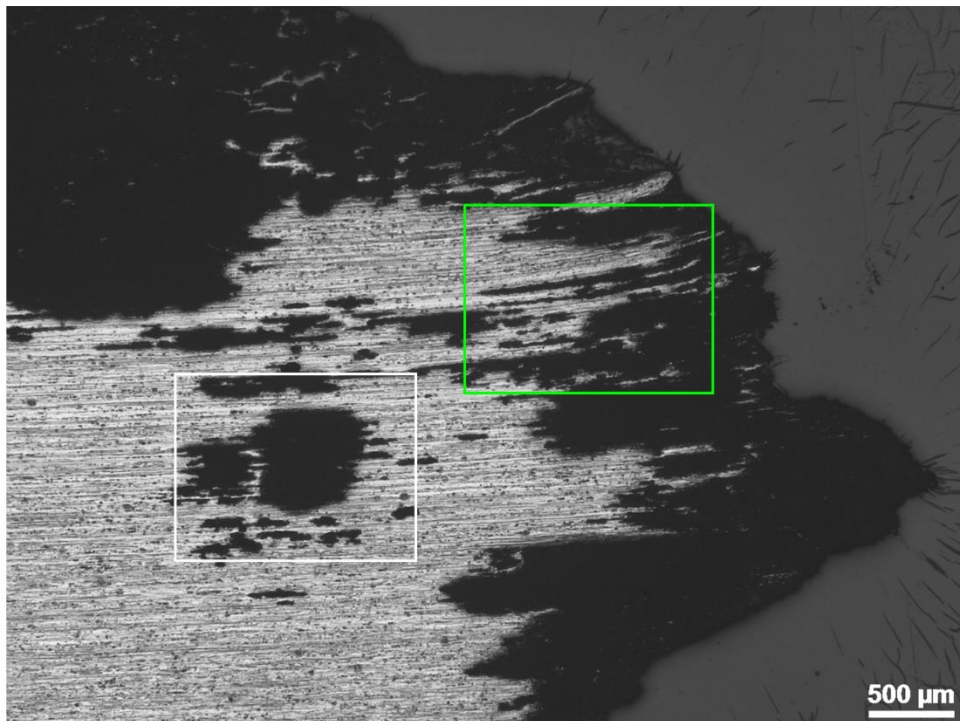


Figure A-115: Pitting, tunneling, and preferential corrosion in the rolling direction on the right side of the cross-section (from Figure A-107). The white and green boxes contain Figures A-116 and A-118, respectively.

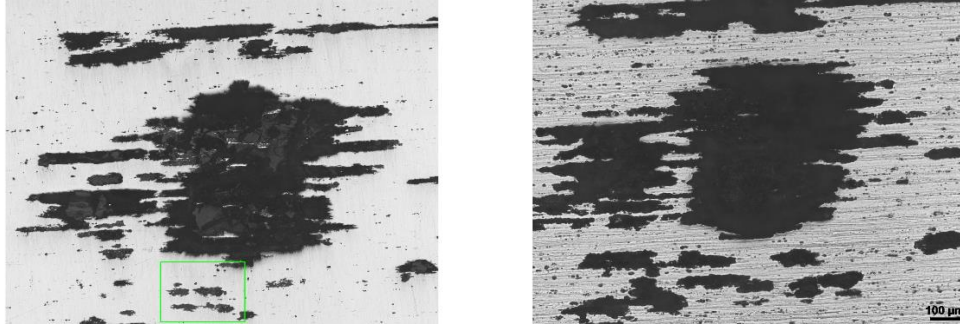


Figure A-116: Tunneling in the cross-section (from Figure A-115). The left image is un-etched while the right image is etched. The green box in the left image is Figure A-117.

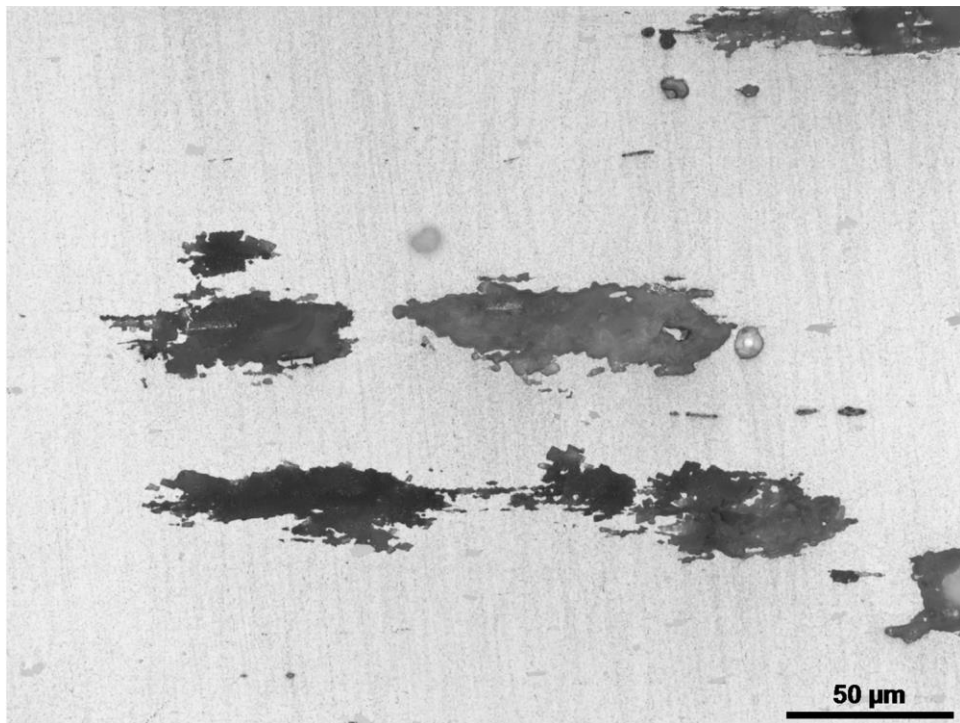


Figure A-117: Close-up on tunneling and crystallographic pitting (un-etched; from left image in Figure A-116).

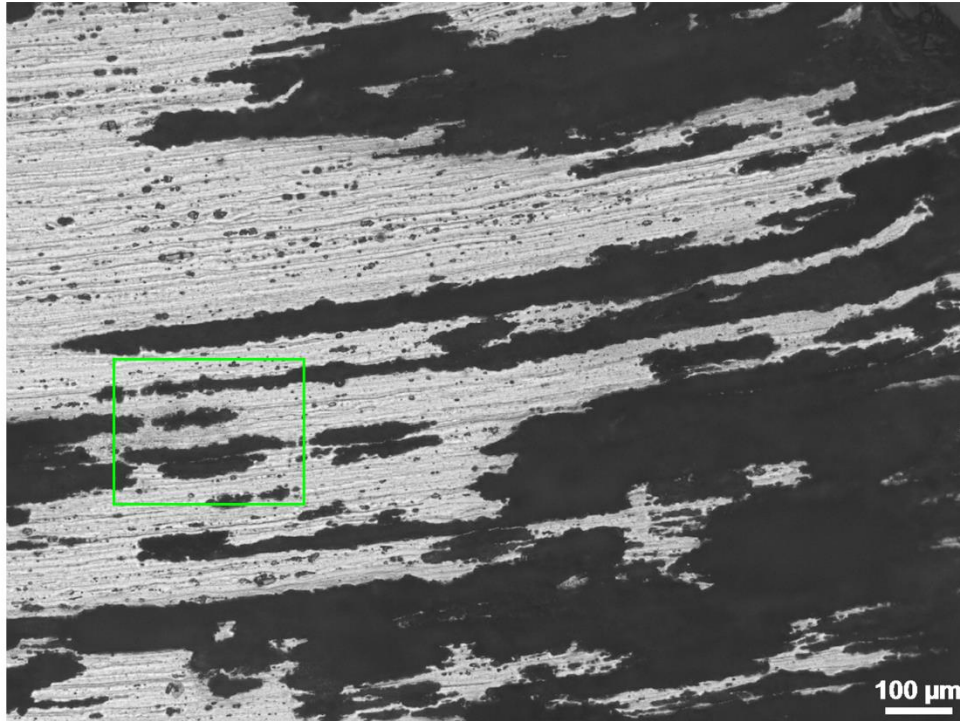


Figure A-118: Pitting, tunneling, and preferential corrosion in the rolling direction (from Figure A-115). The green box contains Figure A-119.

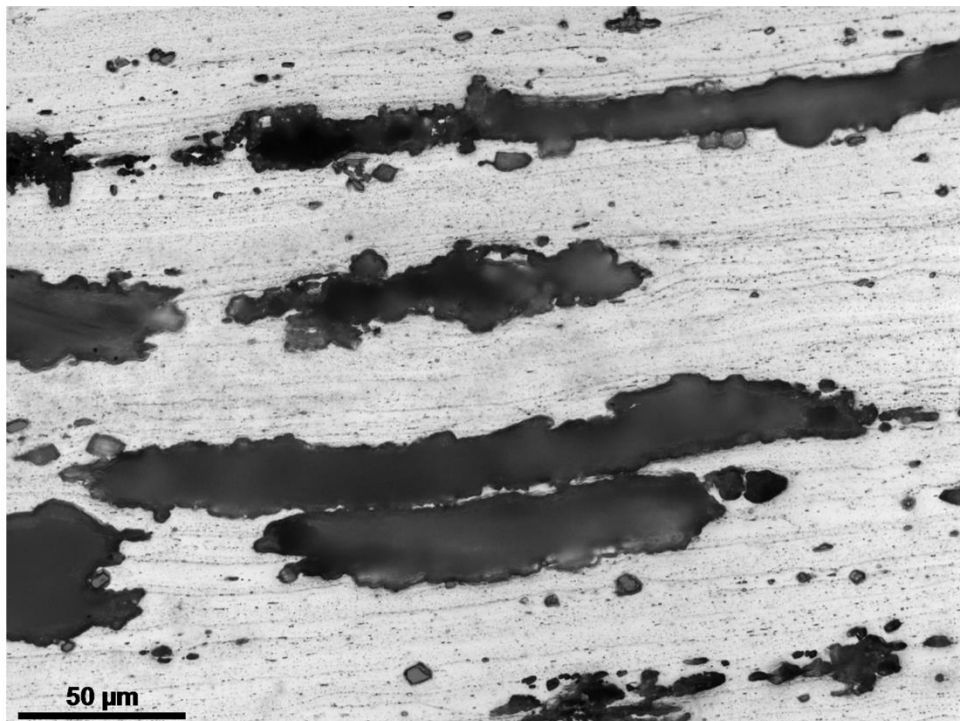


Figure A-119: Close-up on tunneling and crystallographic pitting (from Figure A-118).

A-2.4.2 *Hardness Testing (HT)*

Hardness testing was performed on all of the examined cross-sections from Sections 2.4.1.1 to 2.4.1.6. The testing was performed using a micro hardness tester with a 500 g load. Five Vickers hardness indents were taken across the thickness of the cross-sections. This testing found the hardness to be uniform throughout the sections as shown with the results presented in Table A-25. No indication of any unusually hard or soft zones were found. The wall and floor are seen to have lower hardness than the tie, which likely indicates a different alloy grade and/or temper (as noted in Table A-14). A differential in hardness values is expected; values between the grades and tempers of the 5000 and 6000 series alloys vary in literature [17]. The hardness of the bracket falls between the wall and floor and tie – the shape of the bracket suggests it was manufactured by plastically deforming a strip, hence it is expected that the hardness is higher than the base 5083/5086 grade for the wall and floor due to strain hardening, or that it was made of 5083/5086 in a different temper.

Table A-25: Hardness values of each component cross-section

Component	Alloy Grade*	Hardness [HV at 500 g Force]					
		1	2	3	4	5	Average ± CI
Wall	5086/5083	96	97	97	99	98	97 ± 1
Floor	5086/5083	90	88	90	89	83	88 ± 4
Tubular Tie (Hole Circ. †)	6061	120	126	120	129	128	124 ± 5
Tubular Tie (Hole Axial)	6061	126	120	120	126	127	124 ± 4
Tubular Tie (End Circ. †)	6061	119	119	124	120	125	121 ± 3
Bracket	5086/5083	113	119	115	115	117	116 ± 3

CI: 95% Confidence Interval; \*: As determined from analysis referenced in Table 14; †: Circumference

## **A-3.0 Discussion**

### **A-3.1 Corrosion Modes and Environmental Causes**

The results of the investigation revealed, and further confirmed that corrosion was the primary physical manifestation of severe damage to the aeration tank tubular tie and floor sections, as well as the aeration piping bracket. More specifically, the three modes of corrosion found on the tank floor and bracket were:

1. pitting,
2. crevice, and
3. galvanic corrosion.

These types of corrosion are identified based off their visual appearance and morphology. In addition to the three identified corrosion modes, IGC was also identified on the tubular tie. This additional corrosion type increases the total number of corrosion modes observed on the tubular tie from three to four. Note that the tank wall was not mentioned, for no damaged wall specimen was collected or metallographically examined. However, based on similarities observed in macrophotographs one could assume that pitting and crevice corrosion also existed on the walls (compare similarities in pit morphology in Figures A-8 and A-9 with A-16 and A-17). Descriptions of the four observed forms of corrosion are provide in Chapter 2 (specifically Section 2.6) of this thesis.

Overall, all corrosion was found to be underneath either artificial and/or naturally occurring crevice formers. Artificial crevices include: tooling or grinding marks, points of physical contact between components (such as between aeration piping and tubular ties, and between aeration piping and brackets), and in positions at welds (including weld toes, gaps between beads and start-stop locations). Meanwhile, naturally occurring crevices include insoluble deposits (such as solids or “sludge” found on the floor or tubercles found along the walls) or films of solids

which adhere to materials submerged in the process fluid (such as the process fluid coating the walls and tubular ties). This form of crevice corrosion is also known as under-deposit corrosion.

Multiple crevices locations were identified on the aeration tank components. The components and their respective pitting initiation sites are provided below in Table A-26.

Table A-26: Locations of crevices found on each of the aeration tank components

Component	Crevice Formers: Sources of Pitting Corrosion			
	Gaps between weld toes and beads	Grinding and tooling marks	Proximity and/or contact with aeration piping	Under “sludge”
Wall	✓	✓	✓	
Floor	✓		✓	✓
Bracket			✓	✓
Tie	✓		✓	✓

The appearance of the “crusty top-hat” deposits were similar to the tubercle shaped, white pustules which have been observed in corroding aluminum exposed to fresh water [3]. Initially, these tubercles are comprised primarily of gelatinous aluminum hydroxide [3]. The amorphous hydroxide will subsequently transform into various crystalline aluminum hydroxides (refer to Chapter 2, Section 2.6.1 for more information) [3,7]. The lack of crystalline aluminum hydroxide or oxide compounds in the XRD data of the “crusty top hat” deposits supports that these deposits contain amorphous aluminum hydroxides. Moreover, the EDX data indicates that these deposits are comprised primarily of aluminum and oxygen, which are majority elements (by atomic mass) in aluminum hydroxide.

The creamy white deposits collected from both the tubular tie and the aeration line bracket were similar in colour to the gelatinous or crystalline aluminum hydroxide. These deposits were also comprised primarily of aluminum and oxygen (via EDX). Furthermore, in the case of the deposits collected from the inner diameter of the tubular tie, gibbsite (crystalline aluminum hydroxide) was

identified. Finally, the lack of crystalline aluminum hydroxide or oxide compounds in the XRD data of the remaining creamy white deposits supports that these deposits contain amorphous aluminum hydroxides.

Regarding the “sludge” deposits, these were quite different in appearance than both the creamy white deposits collected from the components and the “crusty top hat” deposits removed from inside the aeration tank. This appearance may be caused by the presence of additional organic and inorganic materials or biological components. Similar to both the creamy white and “crusty top hat” deposits, the “sludge” deposits were also comprised primarily of aluminum and oxygen (via EDX and ICP-MS). Diaspore and corundum were identified (with XRD) in a few of the deposits. These crystalline compounds can be either aluminum corrosion products or naturally occurring minerals. Finally, as with the other types of deposits, the lack of crystalline aluminum hydroxide or oxide compounds in the XRD data of the remaining “sludge” deposits supports that these deposits contain amorphous aluminum hydroxides. It should be noted that it is possible that there was an insufficient volume percentage ( $< 0.1$  vol% [22]) of crystalline aluminum hydroxide present in the deposits, which subsequently led to their lack of detection during XRD.

Chlorine and sulphur were present in several locations. These elements either as ions (such as chloride) or as polyatomic anions (such as sulphate) are known to cause corrosion in aluminum and aluminum alloys [3,4]. Furthermore, the appearance of the cubic crystallographic pitting observed along the walls of the tunnels has been reported by Schmitt [23] in aluminum in acid-chloride and by Baumgärtner and Kaesche [24] in chloride solutions. As discussed previously, the origin of these elements include: chemical constituents which may be naturally present in the wastewater (such as urine, table salt, or dissolved inorganic compounds [14]), compounds which are produced via metabolic processes of the microorganisms that are treating the wastewater, or chemical additives (including

coagulants) which aid in the treatment of wastewater (such as aluminum sulphate (Alum) or polyaluminum chloride (PACl; Isopac) [14]).

Regarding the IGC found in the tubular tie, the cracks were identified both at and below the surface. From the collected evidence, the IGC appears to have initiated from any surface of the tie which was exposed to process fluid. Moreover, it is believed that the IGC was due to the composition of the wastewater process fluid – 6061 is susceptible to IGC in chloride solutions [25,26].

Additionally, elements such as copper, nickel, and lead were identified in deposits and in some cross-sections. These elements are known to be causes of corrosion in aluminum and aluminum alloys [3,4,7–10]. This corrosion occurs due to anodic dissolution of the aluminum, followed by the creation of a galvanic cell [3,4,7,9]. The origin of these elements is believed to be from the wastewater process fluid.

Besides the presence of the aforementioned elements (chlorine, sulphur, copper, nickel, and lead), the wastewater process fluid constituents – and their respective concentrations – can vary. Moreover, seasonal variations and possible additions of waste from other sources (such as other municipal or industrial wastewater) can lead to further variations in the process fluid composition. No attempt was made in determining the detailed composition of matter present in the aeration tank wastewater. Relevant aeration tank operating data for temperature (17.8 to 27.4 °C), dissolved oxygen (0.10 to 6.10 mg/L), pH (5.8 to 7.8), and chloride concentration ( $190 \pm 17$  mg/L) were, however, acquired and can be found in Appendix C. Some insight can be gained into the composition of the wastewater through the ICP-MS data of the collected deposits. Nearly all elements surveyed were identified in the tested deposits. Unfortunately, the ICP-MS data only provides the quantity of elements tested, and does not give any insight into how the elements were present (as chemical compounds with various structures) or interacting with each other.

At present, there is not enough evidence to state to what extent or even how stray current may be involved in the corrosion of the aeration tank. From a previous site inspection [2], a potential difference (non-zero), as well as current flow between the aeration tank and the plant were observed. Moreover, the measured current appeared to be flowing from the aeration tank to the plant (specifically the catwalk). This potential difference, and direction of current flow suggests that spontaneous corrosion was occurring. However, at this time, there is not enough evidence to either identify the exact cause(s) of the measurements previously reported, or why a measurable flow of current was occurring.

Besides the chemical aspects of the environment or stray current effects, the observed corrosion may have been induced from a biological component. There are several reasons for this assertion. First, and most obvious, the aeration tank is a *biological* reactor which treats wastewater with *microorganisms*. It is very possible that bacteria or fungi which corrode aluminum may be present in the aeration tank process fluid. Corrosion caused by microorganisms is known as microbiologically influenced corrosion (MIC). MIC is a type of crevice corrosion – specifically a form of under-deposit corrosion. Further information on MIC, as well as microorganisms (including bacteria and fungi) known to cause corrosion of aluminum is provided in Chapter 2, Section 2.6.2.

Second, the presence of “sludge” from the aeration tank process fluid may contain bacteria or fungi, which in a sessile state, form a biofilm. This biofilm can induce corrosion on the metal substrate – refer to Chapter 2, Section 2.6.2 for more information on biofilms and how they can lead to corrosion. Additionally, as corrosion occurs due to microbial action, the damage frequently leads to the formation of tubercles which cover the localized corrosion [7], and thus create a crevice.

Third (and final reason), the morphology of the pits observed on both the floor and aeration line bracket specimens are indicative of MIC. The appearance of

pits within pits, as well as undercutting and tunneling are common features observed in biologically induced pitting [27].

Nevertheless, even though there is probable cause to suspect involvement from microorganisms, in order to confirm whether microorganisms are indeed an environmental cause of the observed corrosion, further biological assessments and testing are required, and were beyond the scope of these initial investigations.

### A-3.2 Component Fabrication

From the collected ICP-MS and ICP-OES data, the wall, floor, and bracket chemistries were within the specified range of elemental composition for strain hardenable, 5086 and 5083 grade aluminum. The chemistry of the tubular tie, on the other hand, appeared to be within the stated range for age hardenable, 6061 grade aluminum. Additionally, from the metallographic examination, there were no indications that the collected aeration tank components were improperly fabricated. This statement is further substantiated by the results of the hardness testing, which found the hardness to be uniform throughout the tested cross-sections. Furthermore, no indication of any unusually hard or soft zones were identified.

Due to the presence of IGC on the tubular tie, as well as the tie being made from an age hardenable aluminum alloy that requires proper heat treating, additional examination was conducted. This examination was done by line scans which were performed on and across grains in three locations, throughout a cross-section of the tie. The grains examined appeared to be relatively uniform in composition throughout the length of the grain. Additionally, the hardness testing results across the tie cross-sections were relatively uniform, and free from unusually hard or soft zones. Therefore, the tubular tie appears to be free from grossly apparent fabrication or heat treatment errors. Again, it is believed that the IGC was due to the composition of the wastewater process fluid, since 6061 is susceptible to IGC in chloride solutions [26,25]. Microorganisms may also have

played a role in this mode of corrosion; however, additional biological assessments and *in situ* corrosion tests are required in order to prove or disprove any biological involvement.

Only brief guidelines were stated for what the aeration tank was to be constructed from or to. These guidelines include: “marine grade aluminum”, 5086 grade aluminum, and 5053 grade aluminum. It should be noted that 5053 grade aluminum is not a standard composition of 5000 series aluminum alloys [11]. More importantly, only material compositions were stated, and no information was presented in regards to the necessary tempers (thermomechanical process or heat treatment information), subsequent mechanical properties, or dimensional tolerances. Therefore, no argument can be made whether the material was of acceptable quality in accordance with specifications, for the specifications were themselves poorly specified. Since chemical composition data was indicated, an evaluation of the elemental composition, and if it was within tolerable ranges listed of the alloy designation, could be made (refer to the first paragraph of this section).

No direct mention of 6000 series aluminum alloys were present in the mechanical drawings of the vessels. In regards to the ambiguous “marine grade aluminum” specification, what alloys are covered under that blanket statement depends on who has written the aforementioned statement and what their views are on what is a “marine grade” aluminum alloy. Therefore, the tubular tie composition is acceptable in terms of the published composition of 6061 aluminum alloy; but it may not be acceptable as a “marine grade” aluminum alloy.

In regards to whether the mechanical properties of the components were acceptable in accordance with specifications, no mechanical properties were specified for the materials used to construct the aeration tanks. From the collected hardness data, there does not appear to be any heterogeneity in hardness across the thicknesses of the tested metallographic cross-sections. Moreover, no direct correlation could be made between the collected component hardness values to the

ultimate tensile strengths of the identified aluminum alloys. Furthermore, there are no specific hardness requirements listed for either the identified alloy chemistries, or the product standards to which the components may have been constructed. Additionally, because no material property specifications were provided, tensile testing was not performed.

Related to the proper heat treatment of the components, there was no evidence available to suggest that the materials were improperly heat treated. Since the aeration tank wall, floors, and bracket were constructed of strain hardenable grades of aluminum alloys (5086 or 5083), no heat treatment is specified. Additionally, the microstructures of the examined cross-sections from each of these three components appeared to be consistent with those reported in literature [16–21].

Meanwhile, the tubular tie was constructed of an age hardenable aluminum alloy (6061) which requires a heat treatment in order to achieve a certain microstructure, which subsequently provides the specified mechanical properties and desired performance. As previously mentioned, no heat treatment was specified by the construction documents. Moreover, the microstructures of the examined cross-sections from the tie appeared to be consistent with those reported in literature [16–19]. Finally, the hardness testing results across the tie cross-sections were relatively uniform, and free from unusually hard or soft zones. These hardness testing results further support that the tie was properly heat treated, at least throughout the tie geometry.

## A-4.0 Conclusions and Path Forward

### A-4.1 Conclusions

- The results of the investigation revealed, and further confirmed that corrosion had occurred on the aeration tank tubular tie and floor sections, as well as the aeration piping bracket. More specifically, four modes of corrosion were found, with three on the tank floor and bracket being pitting, crevice, and galvanic corrosion. In addition to those three corrosion modes, IGC was also identified on the tubular tie.
- Overall, all corrosion was found to be *underneath* either artificial and/or naturally occurring crevice formers (also known as under-deposit corrosion).
- The presence of elemental aluminum, oxygen, known crystalline aluminum hydroxides – as well as the general appearance and morphology – of the collected deposits (throughout the aeration tank), suggest that they contained aluminum corrosion products.
- Chlorine and sulphur were found present in deposits and examined cross-sections. These elements either as ions (such as chloride) or as polyatomic anions (such as sulphate; also classified as an oxyanion) are known to cause corrosion in aluminum and aluminum alloys [3,4]. Additionally, elements such as copper, nickel, and lead were identified in deposits and in some cross-sections. These elements are also known to be causes of corrosion in aluminum and aluminum alloys [3,4,7–10].
- Pitting damage appeared to be exacerbated by dissimilar metal interactions, through direct electrical connections. This includes contact between: 304/304L grade stainless steel aeration piping and brackets; aeration piping

and tubular ties; and, finally, bolting (nuts, bolts, and washers) and aeration piping brackets.

- At present, there is not enough evidence to state to what extent or even how stray current may be involved in the corrosion of the aeration tank. However, there is sufficient evidence to show that the aforementioned four modes of corrosion are *predominant* in the aeration tank, as well as presence of elements which are corrosive to aluminum.
- The observed corrosion may have been induced from a biological origin. Nevertheless, even though there is probable cause to suspect involvement from microorganisms, in order to confirm whether microorganisms are indeed an environmental cause of the observed corrosion, further biological assessments and testing are required.
- The wall, floor, and bracket chemistries were within the specified range of elemental composition for 5086 and 5083 grade aluminum. The chemistry of the tubular tie was within the stated range for 6061 grade aluminum. Additionally, from the metallographic examination and limited hardness testing, there were no indications that the collected aeration tank components were grossly improperly fabricated or heat treated. Further testing would be required to validate this assertion.
- Only brief guidelines were provided for materials of construction. More importantly, only material compositions were stated, and no information was presented in regards to the necessary tempers or heat treatment, subsequent mechanical properties, or dimensional tolerances.
- Regarding failure mechanisms, there does not appear to be a single failure mechanism, but more of a series of failure modes induced by several environmental causes. How, and to what extent, did the identified factors

exacerbate the observed modes of corrosion is not known, at least on a mechanistic level. Rather, it is believed that the aforementioned factors caused and accelerated the observed modes of corrosion. Furthermore, it is believed that there were poor considerations made for the design of the aeration tank, specifically regarding the dissimilar metal contact. However, it appears that the environment (i.e. process fluid) and its composition (both chemical and biological) may be the “main” causes of corrosion for the components in question.

#### A-4.2 Path Forward

- The observed corrosion may have been induced from a biological origin. Nevertheless, even though there is probable cause to suspect involvement from microorganisms, in order to confirm whether microorganisms are indeed an environmental cause of the observed corrosion, further biological assessments and testing are required.
- It is recommended that additional studies of material compatibility with wastewater (in the form of *in situ* corrosion testing) and biological assessments be performed. These tests will provide further evidence in determining whether aluminum alloys should or should not have been used in the construction of the aeration tanks.
- Corrosion testing of the various grades of aluminum alloys with process additives (specifically coagulants) should be performed in order to assess the additives’ corrosivity to the aluminum alloys present in the aeration tank.

## A-5.0 Sample Calculations

Below is a completed sample calculation for the average wall thickness and its respective confidence interval. The necessary equations used to perform the statistical analysis are provided in Chapter 3. In order to use a 95% confidence interval, it is assumed that the thickness measurement distribution is normal, the significance level ( $\alpha$ ) is 5%, and a 2-tailed interval is chosen. Also included is a table (Table A-27) of retrieved t-distribution ( $t$ ) values, which were used in all of the confidence interval calculations performed throughout Appendix A. The completed sample calculation for the average wall thickness and confidence interval is as follows:

$$\bar{x} = \frac{9.22 + 9.19 + 9.23}{3}$$

$$\bar{x} = 9.21 \text{ mm}$$

$$s_{Thickness} = \sqrt{\frac{(9.22 - 9.21)^2 + (9.19 - 9.21)^2 + (9.23 - 9.21)^2}{3 - 1}}$$

$$s_{Thickness} = 0.02 \text{ mm}$$

$$\bar{x} \pm t_{\alpha/2, n-1} \times \frac{s}{\sqrt{n}}$$

$$t_{0.025, 2} = 4.303$$

$$CI = 4.303 \times \frac{0.02}{\sqrt{3}}$$

$$CI = 0.06 \text{ mm}$$

$$\therefore 9.21 \pm 0.06 \text{ mm}$$

Table A-27: Select percentage points of the t-distribution [28].

<i>t</i> <sub>α/2, n-1</sub> Values	
<i>t</i> <sub>0.025, n-1</sub>	Value
<i>t</i> <sub>0.025, 2</sub>	4.303
<i>t</i> <sub>0.025, 3</sub>	3.182
<i>t</i> <sub>0.025, 4</sub>	2.776
<i>t</i> <sub>0.025, 6</sub>	2.447
<i>t</i> <sub>0.025, 12</sub>	2.179
<i>t</i> <sub>0.025, 15</sub>	2.131

## A-6.0 References

- [1] J.S. Pavelich, J.A. Nychka, Preliminary Findings Report: Visual Inspection and Corrosion Assessment of the EPCOR Borealis Waste Water Treatment Plant, Edmonton, AB, 2013.
- [2] J.S. Pavelich, J.A. Nychka, Additional Inspection Report: Additional Visual Inspection and Corrosion Assessment of the EPCOR Borealis Wastewater Treatment Plant, Edmonton, AB, 2014.
- [3] C. Vargel, Corrosion of Aluminium, Elsevier Ltd, Kidlington, UK, 2004.
- [4] J.R. Davis, ed., Corrosion of Aluminum and Aluminum Alloys, ASM International, Materials Park, OH, 1999. doi:10.1361/caaa1999.
- [5] ASTM B928, Standard Specification for High Magnesium Aluminum-Alloy Sheet and Plate for Marine Service and Similar Environments, West Conshohocken, PA, 2013. doi:10.1520/B0928\_B0928M-13.
- [6] ASTM G46, Standard Guide for Examination and Evaluation of Pitting Corrosion, West Conshohocken, PA, 2013. doi:10.1520/G0046-94R13.
- [7] R.W. Revie, ed., Uhlig's Corrosion Handbook, 3rd ed., John Wiley & Sons, Inc., Hoboken, NJ, 2011.
- [8] D.C. Bennett, R.A. Nixon, Corrosion and Materials Fundamentals for Engineers in Wastewater Treatment Plants & Collection Systems, 3rd ed., NACE International, Houston, TX, 2016.

- [9] J.R. Davis, ed., *Corrosion: Understanding the Basics*, ASM International, Materials Park, OH, 2000.
- [10] E.E. Stansbury, R.A. Buchanan, *Fundamentals of Electrochemical Corrosion*, ASM International, Materials Park, OH, 2000.
- [11] The Aluminum Association, *International Alloy Designations and Chemical Composition Limits for Wrought Aluminum and Wrought Aluminum Alloys*, Regist. Rec. Ser. Teal Sheets. (2015).  
[http://www.aluminum.org/sites/default/files/TEAL\\_1\\_OL\\_2015.pdf](http://www.aluminum.org/sites/default/files/TEAL_1_OL_2015.pdf)  
(accessed November 15, 2016).
- [12] P.R. Griffiths, J.A. de Haseth, *Fourier Transform Infrared Spectrometry*, 2nd ed., John Wiley & Sons, Inc., Hoboken, NJ, 2007.
- [13] J.I. Goldstein, C.E. Lyman, D.E. Newbury, E. Lifshin, P. Echlin, L. Sawyer, D.C. Joy, J.R. Michael, *Scanning Electron Microscopy and X-Ray Microanalysis*, 3rd ed., Springer, New York, NY, 2007.
- [14] L. Metcalf, H.P. Eddy, eds., *Wastwater Engineering Treatment and Resource Recovery*, 5th ed., McGraw-Hill Education, New York, NY, 2014.
- [15] ASTM E407, *Standard Practice for Microetching Metals and Alloys*, West Conshohocken, PA, 2007. doi:10.1520/E0407-07.
- [16] J.G. Kaufman, *Introduction to Aluminum Alloys and Tempers*, ASM International, Materials Park, OH, 2000.
- [17] J.E. Hatch, ed., *Aluminum Properties and Physical Metallurgy*, ASM International, Materials Park, OH, 1984.
- [18] L.F. Mondolfo, *Aluminum Alloys Structure & Properties*, Butterworth & Co. Ltd., London, UK, 1976.
- [19] *ASM Handbook Volume 9 Metallography and Microstructures*, ASM International, Materials Park, OH, 1985.
- [20] *ASM Handbook Volume 2 Properties and Selection: Nonferrous Alloys and Special-Purpose Materials*, ASM International, Materials Park, OH, 1990.
- [21] J.C. Free, P.T. Summers, B.Y. Lattimer, S.W. Case, *Mechanical Properties of 5000 Series Aluminum Alloys Following Fire Exposure*, in: *TMS2016 Annu. Meet. Suppl. Process.*, The Minerals, Metals, and Materials Society, 2016: pp. 657–664.

- [22] B.D. Cullity, *Elements of X-Ray Diffraction*, Addison-Wesley Publishing Company, Inc., Reading, MA, 1956.
- [23] C.R. Schmitt, Anomalous Microbiological Tuberculation and Aluminum Pitting Corrosion - Case Histories, in: *NACE-8, NACE*, 1985: pp. 69–75.
- [24] M. Baumgärtner, H. Kaesche, Aluminum pitting in chloride solutions: morphology and pit growth kinetics, *Corros. Sci.* 31 (1990) 231–236.
- [25] B.A. Shaw, M.M. McCosby, A.M. Abdullah, H.W. Pickering, The Localized Corrosion of Al 6XXX Alloys, *J. Miner. Met. Mater. Soc.* 53 (2001) 42–46. doi:10.1007/s11837-001-0087-7.
- [26] T. Minoda, H. Yoshida, Effect of Grain Boundary Characteristics on Intergranular Corrosion Resistance of 6061 Aluminum Alloy Extrusion, *Metall. Mater. Trans. A.* 33 (2002) 2891–2898. doi:10.1007/s11661-002-0274-3.
- [27] B.J. Little, J.S. Lee, *Microbiologically Influenced Corrosion*, John Wiley & Sons, Inc., Hoboken, NJ, 2007.
- [28] D.C. Montgomery, G.C. Runger, *Applied Statistics and Probability for Engineers*, 3rd ed., John Wiley & Sons, Inc., New York, NY, 2003.

# Appendix B – Volume to Surface Area Ratio of Aeration Tank

## B-1.0 Calculations

This appendix contains the data used to calculate the volume to surface area (V/SA) ratio of the corroded aeration tank. Note that the aeration tank surface area is the total surface area exposed to the process fluid, specifically of the aluminum walls, floor, and tubular ties only. The surface area does not include the 304 stainless steel aeration piping or diffusers. The surface area is calculated by adding up the surface area of the walls, floors, tubular ties, and subtracting the surface area of tubular ties in contact with the walls. Fluid volume is calculated by the dimensions of the tank minus the volume occupied by the tubular ties and the aeration piping. Finally, the pipe supports, brackets, and hardware (bolting, nuts, etc.) were considered negligible in the calculation of both the surface area and fluid volume; therefore, they weren't included. Also, any additional surface area due to welds was not included in the calculation of the total surface area. Relevant dimension data for required for both the surface area and volume can be found in reports written by the author [1,2].

$$SA_{Total\ Exposed} = SA_{Floor} + SA_{Walls} + SA_{Tubular\ Ties} - SA_{Tie\ Projected\ Area}$$

$$SA_{Floor} = (d_{Length} \times d_{Width}) \times n_{Number}$$

$$SA_{Floor} = (17069\ mm \times 3048\ mm) \times 1$$

$$SA_{Floor} \approx 5.20 \times 10^7\ mm^2$$

$$SA_{Walls} = (d_{Length} \times d_{Height}) \times n_{Number} + (d_{Width} \times d_{Height}) \times n_{Number}$$

$$SA_{Walls} = (17069\ mm \times 3048\ mm) \times 2 + (3048\ mm \times 3048\ mm) \times 2$$

$$SA_{Walls} = 1.04 \times 10^8 \text{ mm}^2 + 1.86 \times 10^7 \text{ mm}^2$$

$$SA_{Walls} \approx 1.23 \times 10^8 \text{ mm}^2$$

$$SA_{Tubular\ Ties} = (\pi \times d_{Outer\ Diameter} \times d_{Width}) \times n_{Number}$$

$$SA_{Tubular\ Ties} = \left( \pi \times 1.9 \text{ inch} \times 25.4 \frac{\text{mm}}{\text{inch}} \times 3048 \text{ mm} \right) \times 100$$

$$SA_{Tubular\ Ties} \approx 4.62 \times 10^7 \text{ mm}^2$$

$$SA_{Tie\ Projected\ Area} = \left( \pi \times \left( \frac{d_{Outer\ Diameter}}{2} \right)^2 \right) \times n_{Number}$$

$$SA_{Tie\ Projected\ Area} = \left( \pi \times \left( \frac{\left( 1.9 \text{ inch} \times 25.4 \frac{\text{mm}}{\text{inch}} \right)}{2} \right)^2 \right) \times 200$$

$$SA_{Tie\ Projected\ Area} \approx 3.66 \times 10^5 \text{ mm}^2$$

$$\therefore SA_{Total\ Exposed} = (5.20 \times 10^7 + 1.23 \times 10^8 + 4.62 \times 10^7 - 3.66 \times 10^5) \text{ mm}^2$$

$$SA_{Total\ Exposed} \approx 2.21 \times 10^8 \text{ mm}^2$$

$$V_{Solution} = V_{Aeration\ Tank} - V_{Tubular\ Ties} - V_{Aeration\ Piping}$$

$$V_{Aeration\ Tank} = d_{Length} \times d_{Width} \times d_{Height}$$

$$V_{Aeration\ Tank} = 17069 \text{ mm} \times 3048 \text{ mm} \times 3048 \text{ mm}$$

$$V_{Aeration\ Tank} \approx 1.59 \times 10^{11} \text{ mm}^3$$

$$V_{Tubular\ Ties} = \left( \pi \times \left( \frac{d_{Outer\ Diameter}}{2} \right)^2 \times d_{Width} \right) \times n_{Number}$$

$$V_{Tubular\ Ties} = \left( \pi \times \left( \frac{1.9\ inch \times 25.4 \frac{mm}{inch}}{2} \right)^2 \times 3048\ mm \right) \times 100$$

$$V_{Tubular\ Ties} \approx 5.58 \times 10^8\ mm^3$$

$$V_{Aeration\ Piping} = \left( \left( \pi \times \left( \frac{d_{Outer\ Diameter}}{2} \right)^2 \times d_{Length} \right) + V_{Pipe\ Cap} \right) \times n_{Number}$$

The following formula for the volume of the pipe cap can be found via reference [3].

$$V_{Pipe\ Cap} = \left( \frac{\pi}{3} \right) \times d_{Height}^2 \times \left( 3 \times \left( \frac{d_{Outer\ Diameter}}{2} \right) - d_{Height} \right)$$

$$V_{Pipe\ Cap} = \left( \frac{\pi}{3} \right) \times (30.2\ mm)^2 \times \left( 3 \times \left( \frac{2.375\ inch \times 25.4 \frac{mm}{inch}}{2} \right) - 30\ mm \right)$$

$$V_{Pipe\ Cap} \approx 57473\ mm^3$$

$$V_{Aeration\ Piping} = \left( \left( \pi \times \left( \frac{2.375\ inch \times 25.4 \frac{mm}{inch}}{2} \right)^2 \times 5651.7\ mm \right) + 57473\ mm^3 \right) \times 9$$

$$V_{Aeration\ Piping} \approx 1.46 \times 10^8\ mm^3$$

$$\therefore V_{Solution} = (1.59 \times 10^{11} + 5.58 \times 10^8 + 1.46 \times 10^8)\ mm^3$$

$$V_{Solution} \approx 1.58 \times 10^{11}\ mm^3$$

$$V_{Solution} = 1.58 \times 10^{11}\ mm^3 \times \frac{1\ cm^3}{(10\ mm)^3} \times \frac{1\ mL}{1\ cm^3}$$

$$V_{\text{Solution}} \approx 1.58 \times 10^8 \text{ mL}$$

$$\left(\frac{V}{SA}\right)_{\text{Aeration Tank}} = \frac{V_{\text{Solution}}}{SA_{\text{Total Exposed}}}$$

$$\left(\frac{V}{SA}\right)_{\text{Aeration Tank}} = \frac{1.58 \times 10^8 \text{ mL}}{2.21 \times 10^8 \text{ mm}^2}$$

$$\therefore \left(\frac{V}{SA}\right)_{\text{Aeration Tank}} \approx 0.72 \frac{\text{mL}}{\text{mm}^2}$$

## B-2.0 References

- [1] J.S. Pavelich, J.A. Nychka, Preliminary Findings Report: Visual Inspection and Corrosion Assessment of the EPCOR Borealis Waste Water Treatment Plant, Edmonton, AB, 2013.
- [2] J.S. Pavelich, J.A. Nychka, Additional Inspection Report: Additional Visual Inspection and Corrosion Assessment of the EPCOR Borealis Wastewater Treatment Plant, Edmonton, AB, 2014.
- [3] Had2Know, (n.d.). <http://www.had2know.com/academics/spherical-cap-volume-surface-area-calculator.html> (accessed December 1, 2016).

# Appendix C – Raw Process Data from Aeration Tank

This appendix contains the key monitoring data available for the corroded aeration tank from November 1, 2009 to August 31, 2011. One data point was collected per day for each of the parameters of interest, namely: influent flow rate ( $\phi_{\text{Influent}}$ ), pH, dissolved oxygen concentration (DO), temperature (T), Isopac drip rate ( $\phi_{\text{Isopac}}$ ), and Alum drip rate ( $\phi_{\text{Alum}}$ ). It should be noted that some data is missing from within the above-mentioned range of dates. The calculated statistical information (including 95% confidence intervals) for each of the metrics are provided below in Table C-1. Furthermore, all of the collected data for each of the metrics are shown in Figures C-1 through C-5.

Conductivity ( $\sigma$ ) and chloride concentration ( $[\text{Cl}^-]$ ) were measured from one of the other two, active aeration tanks. This data is also listed in Table C-1. Neither parameter could be measured in the corroded aeration tank, since the tank was removed from service and drained. Moreover, neither parameter was measured during the date range provided in the previous paragraph.

Table C-1: Aeration tank process data.

	Mean	Median	Mode	Min.	Max.	s <sup>1</sup>	Days ( <i>n</i> )	CI
$\phi_{\text{Influent}}$ [m <sup>3</sup> /day]	185	189	199	22	292	34	601	3
pH	7.1	7.1	7.2	5.8	7.8	0.3	599	0.0
DO [mg/L]	2.07	2.00	2.00	0.10	6.10	0.67	544	0.06
T [°C]	22.9	23.0	24.6	17.8	27.4	2.6	599	0.2
$\phi_{\text{Isopac}}$ [mL/min]	13.0	12.6	11.4	8.8	22.0	2.6	38	0.9
$\phi_{\text{Alum}}$ [mL/min]	22.4	22.8	17	1.4	32.0	5.6	178	0.8
[Cl <sup>-</sup> ] [mg/L]	190	NR	NR	173	207	NR	1	NR
$\sigma$ [μS/cm]	NR	NR	NR	1269	1294	NR	1	NR

1: Sample Standard Deviation; CI: 95% Confidence Interval; NR: Not Reported

Alum was recorded being added to the aeration tank on January 27, 2011. Prior to this date, Alum had only been recorded for three days (December 1<sup>st</sup> through 3<sup>rd</sup>). Alum continued to be dripped into the tank until July 20, 2011. On July 21, Isopac was instead added to the tank, and continued to be added until August 27, 2011. No dosage rate was reported for either Isopac or Alum after August 27.

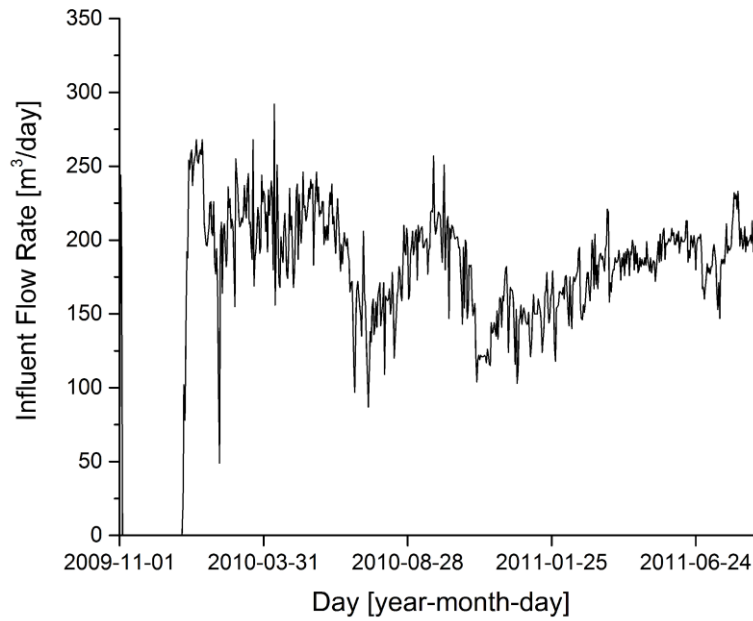


Figure C-1: Aeration tank influent flow rate.

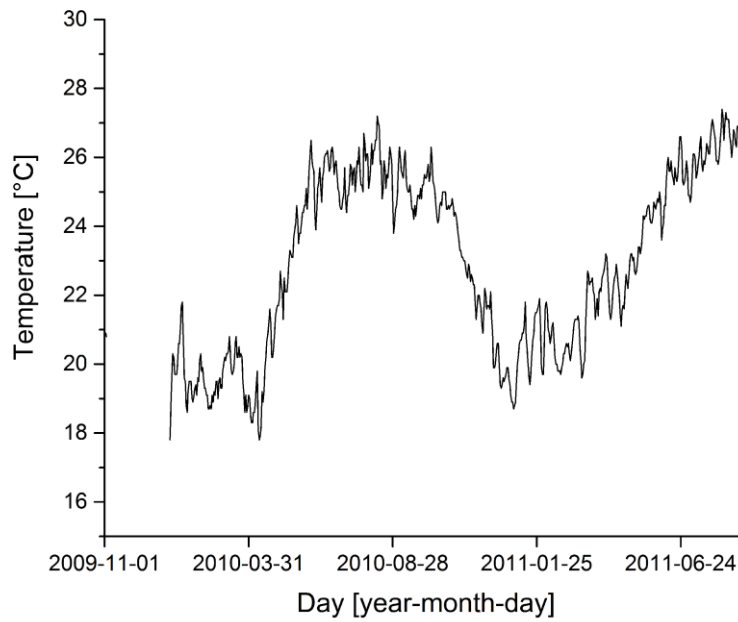


Figure C-2: Aeration tank temperature measurements.

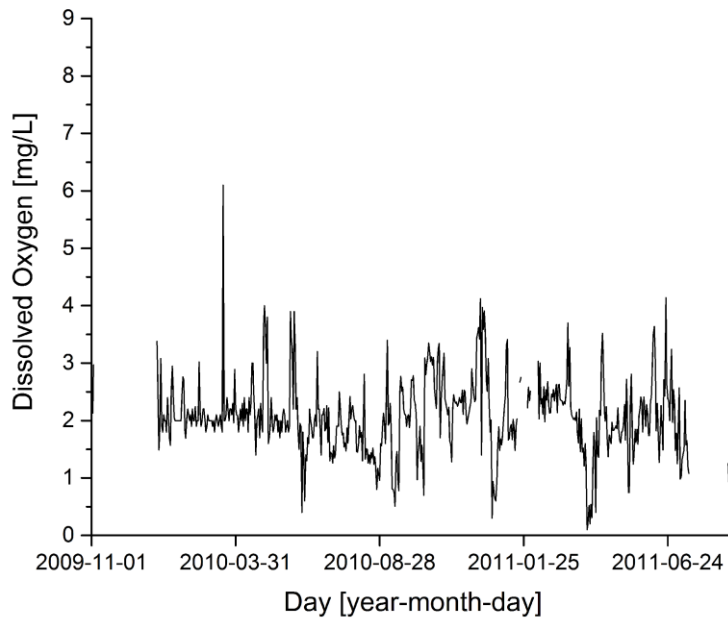


Figure C-3: Aeration tank dissolved oxygen measurements.

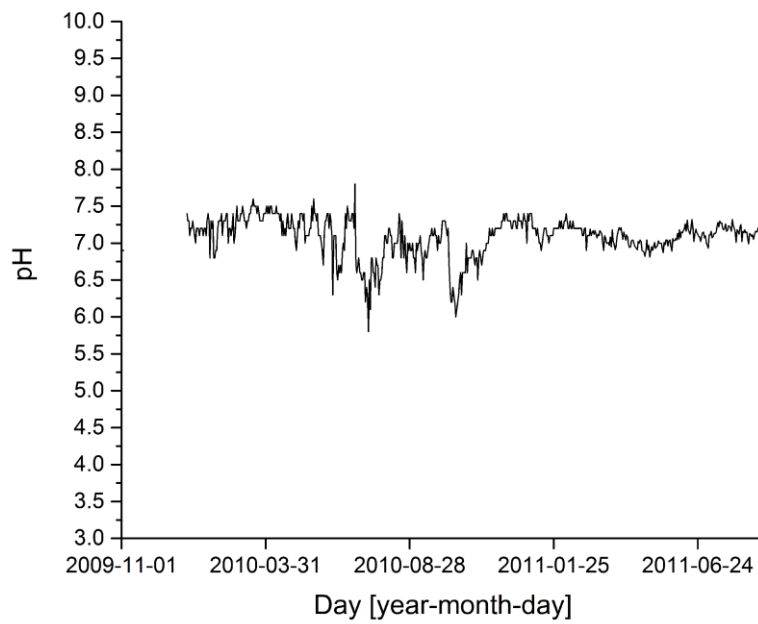


Figure C-4: Aeration tank pH measurements.

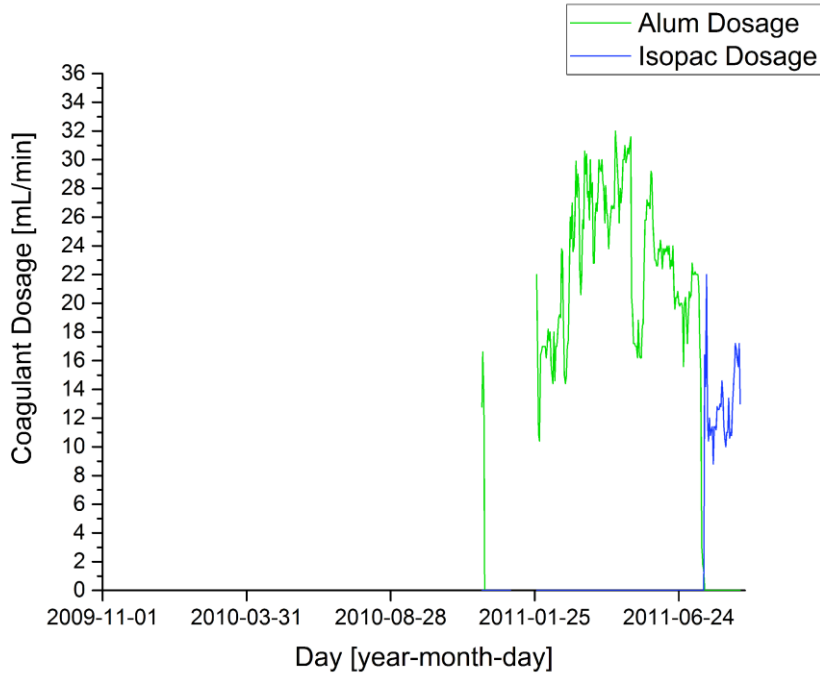


Figure C-5: Aeration tank Alum and Isopac drip rate.

Using the average Isopac and Alum dosage, as well as the average influent flow rate, the concentration of Isopac and Alum added to the aeration tank could be calculated. Provided below is a sample calculation for the volumetric concentration of Isopac.

$$c_{Isopac} = \frac{V_{Isopac}}{V_{Total}} \times 100 = \frac{V_{Isopac}}{V_{Isopac} + V_{Aeration\ Tank}} \times 100$$

$$c_{Isopac} = \frac{\phi_{Isopac} \times t}{(\phi_{Isopac} \times t) + (\phi_{Influent} \times t)} \times 100$$

$$c_{Isopac} = \left( \frac{\left( 13 \frac{mL}{min} \times 60 \frac{min}{hr} \times 24 \frac{hr}{day} \times 1 \text{ day} \right)}{\left( \left( 13 \frac{mL}{min} \times 60 \frac{min}{hr} \times 24 \frac{hr}{day} \times 1 \text{ day} \right) + \left( 185 \frac{m^3}{day} \times 10^6 \frac{mL}{m^3} \times 1 \text{ day} \right) \right)} \right) \times 100$$

$$\therefore c_{Isopac} = 0.010 \text{ volume } \%$$

# Appendix D – Corrosion Coupon Photographs

The following appendix contains the macro photography images of the thirty six corrosion coupons after the 28-day immersion testing. Table D-1 lists the coupon numbers for each electrolyte-alloy combination. Two sides of each coupon were photographed; hence, Figures D-1 through D-3 contain one side of the thirty six coupons, while Figures D-4 through D-6 contain the opposite side of each of the coupons.

Table D-1: Coupon numbers for the combination of materials and respective solutions used in this study.

	<b>Isopac</b>	<b>Alum</b>	<b>DIUF</b>
<b>5086</b>	1, 2, 3	4, 5, 6	7, 8, 9
<b>6061</b>	10, 11, 12	13, 14, 15	16, 17, 18
<b>5086 / 5083</b>	19, 20, 21	22, 23, 24	25, 26, 27
<b>304</b>	28, 29, 30	31, 32, 33	34, 35, 36

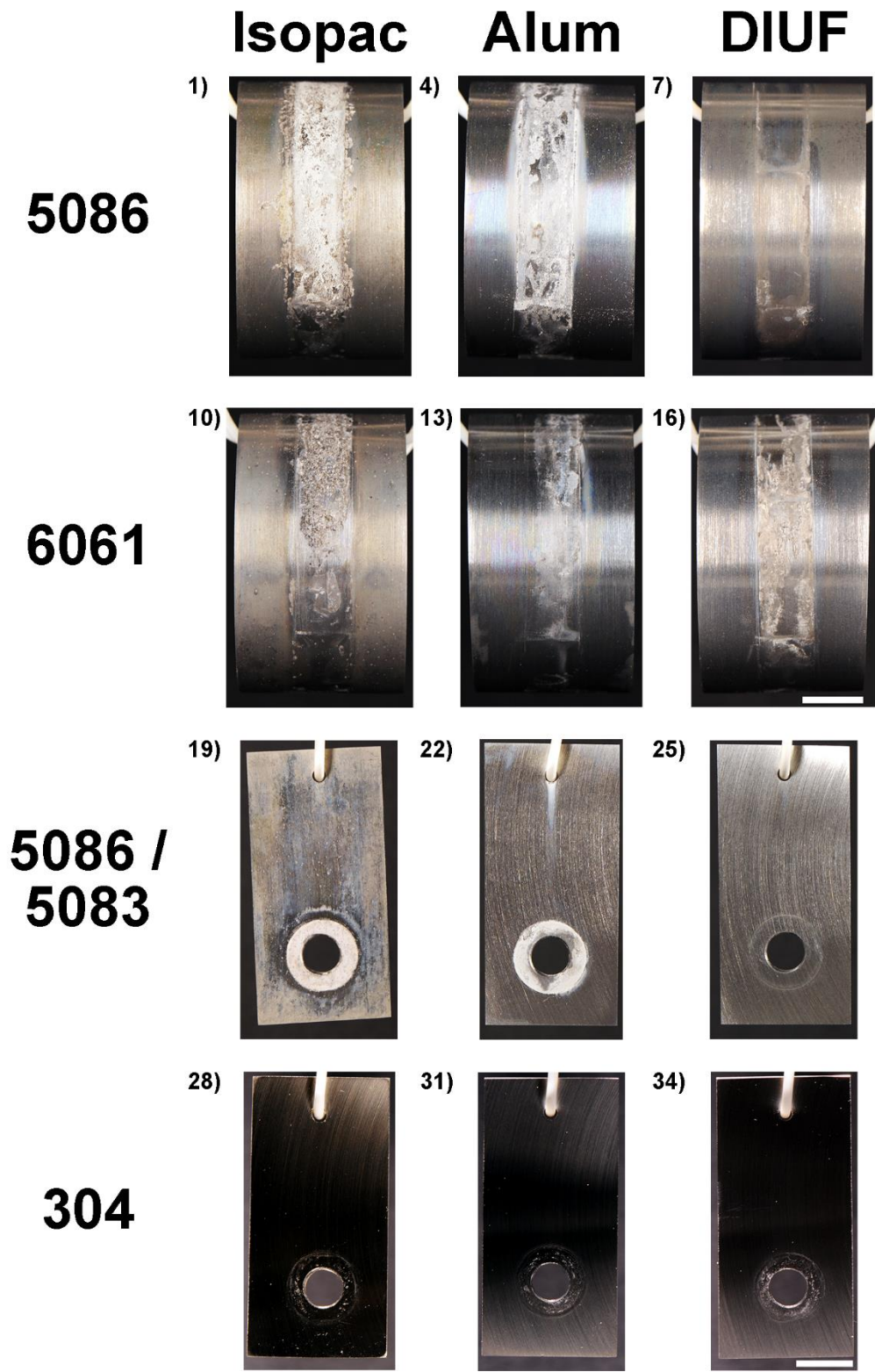


Figure D-1: Composite image of corrosion coupons of different alloys in various test solutions.

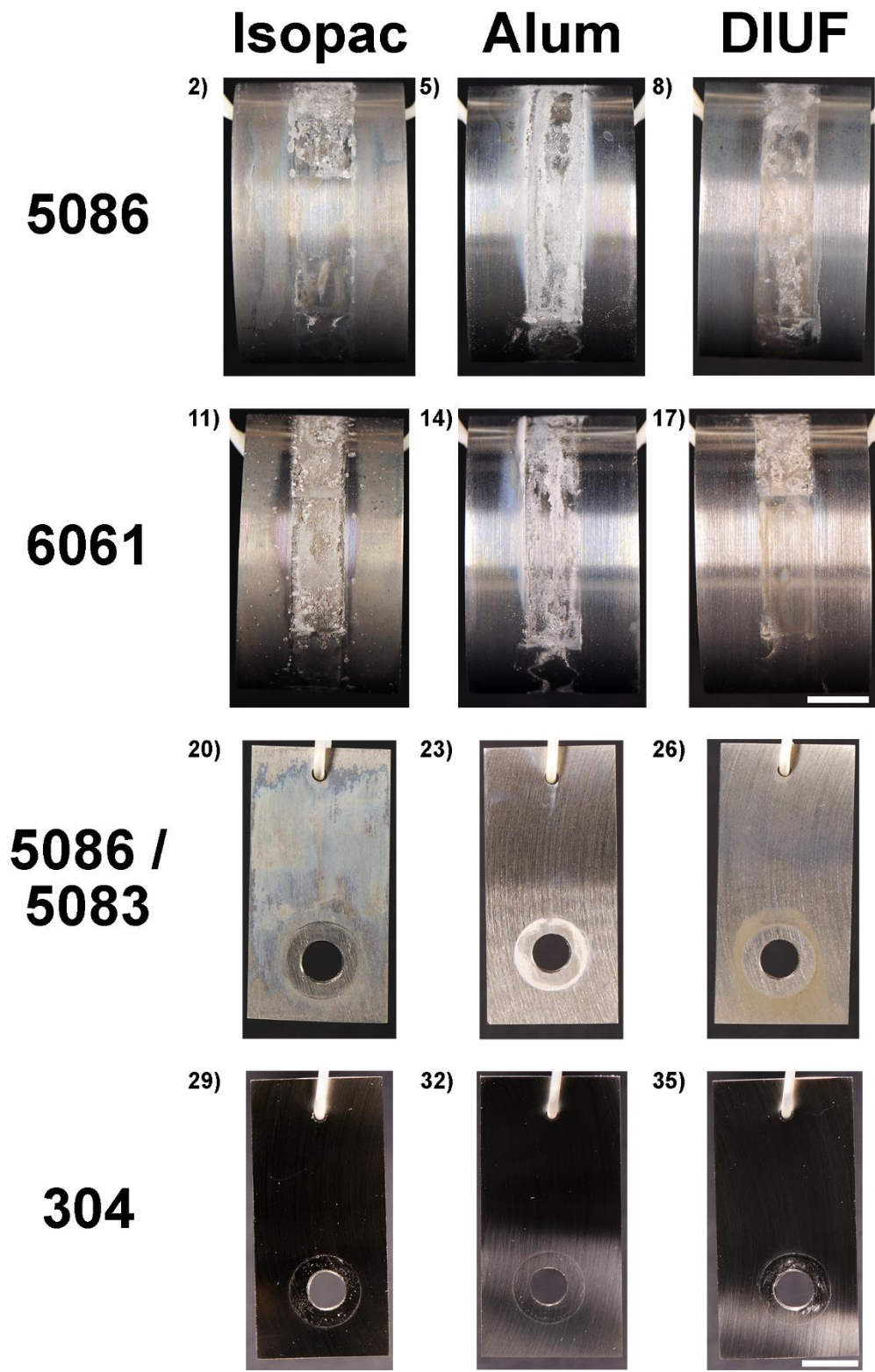


Figure D-2: Composite image of corrosion coupons of different alloys in various test solutions.

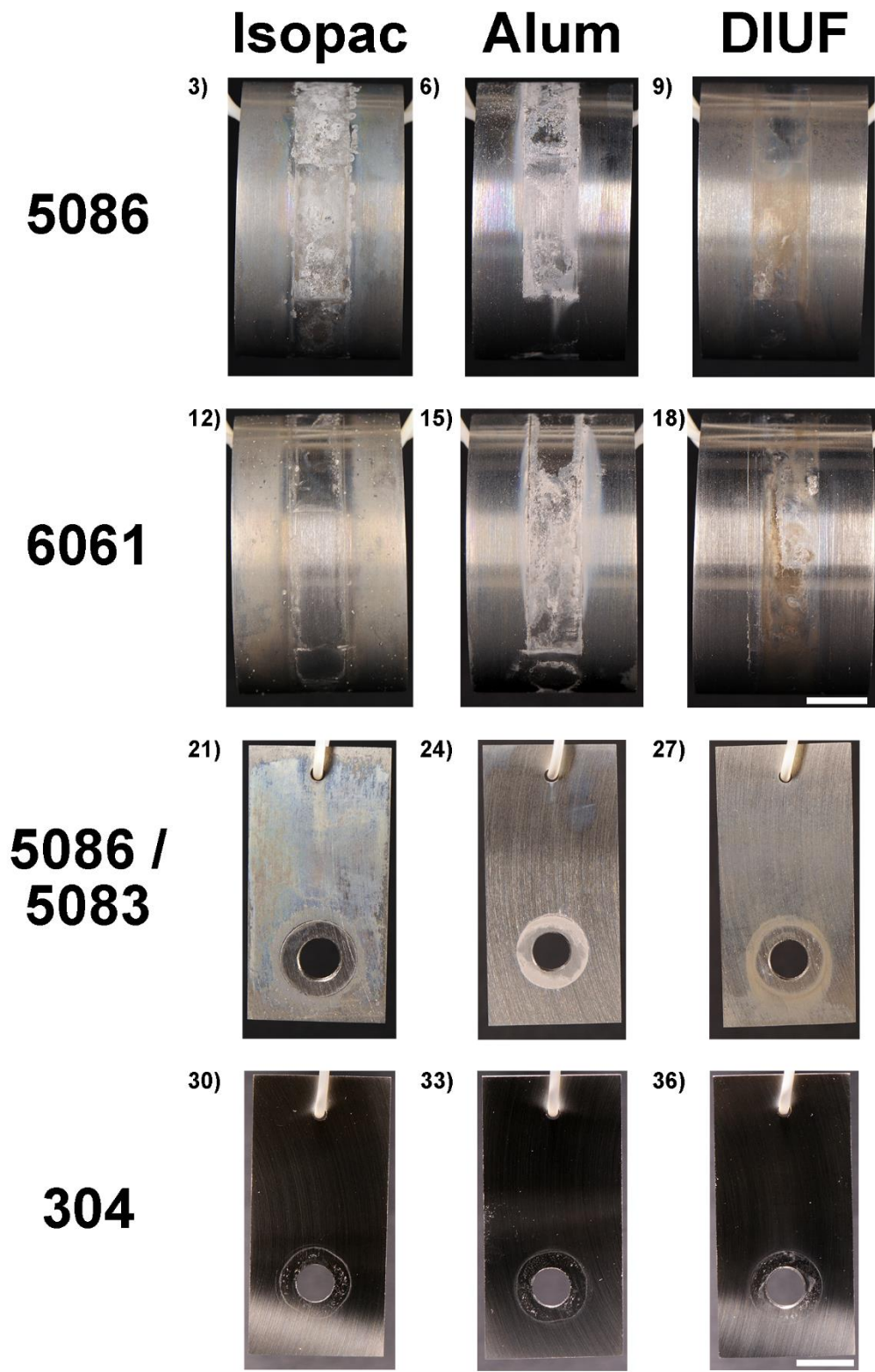


Figure D-3: Composite image of corrosion coupons of different alloys in various test solutions.

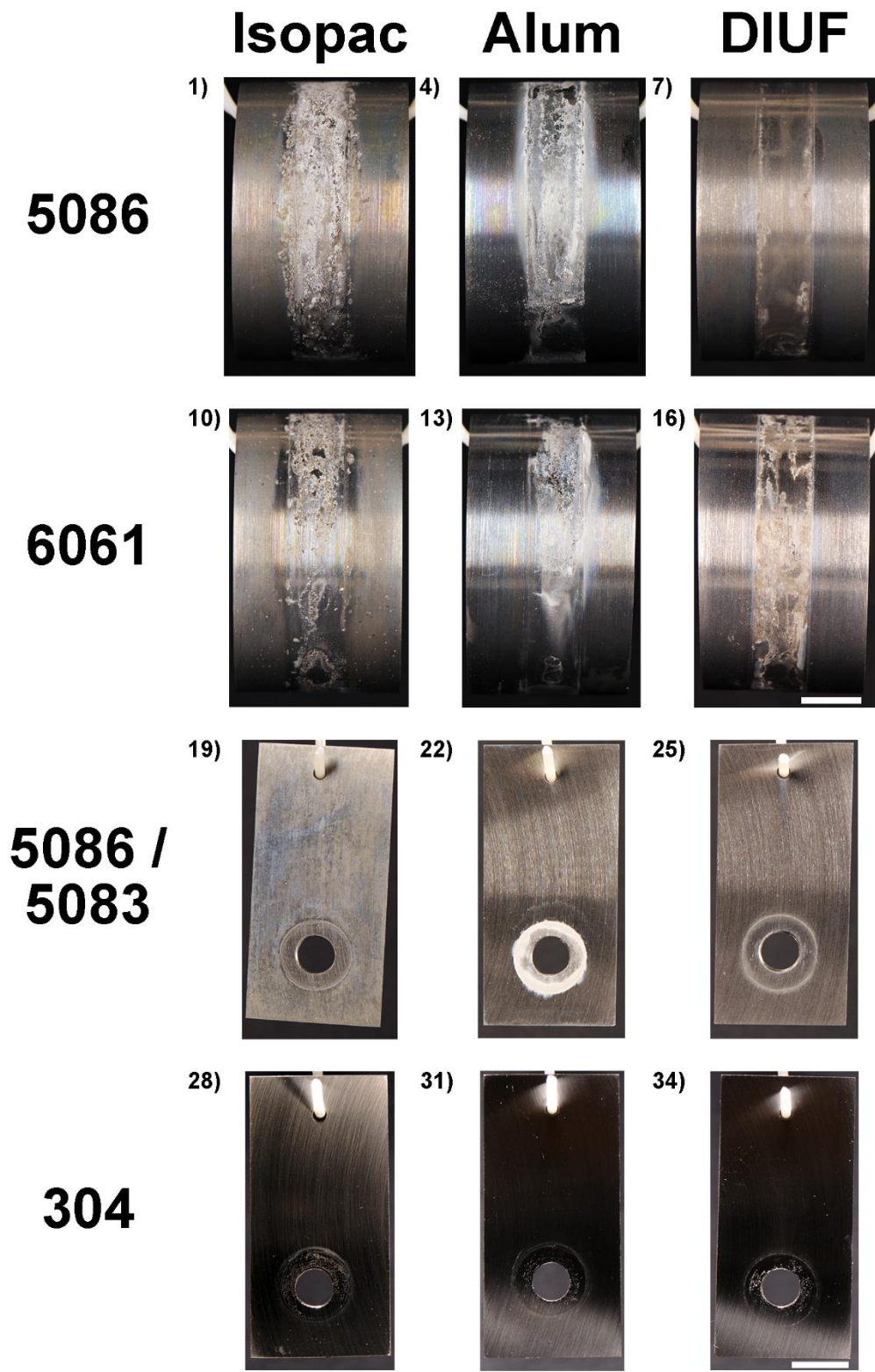


Figure D-4: Composite image of corrosion coupons of different alloys in various test solutions.

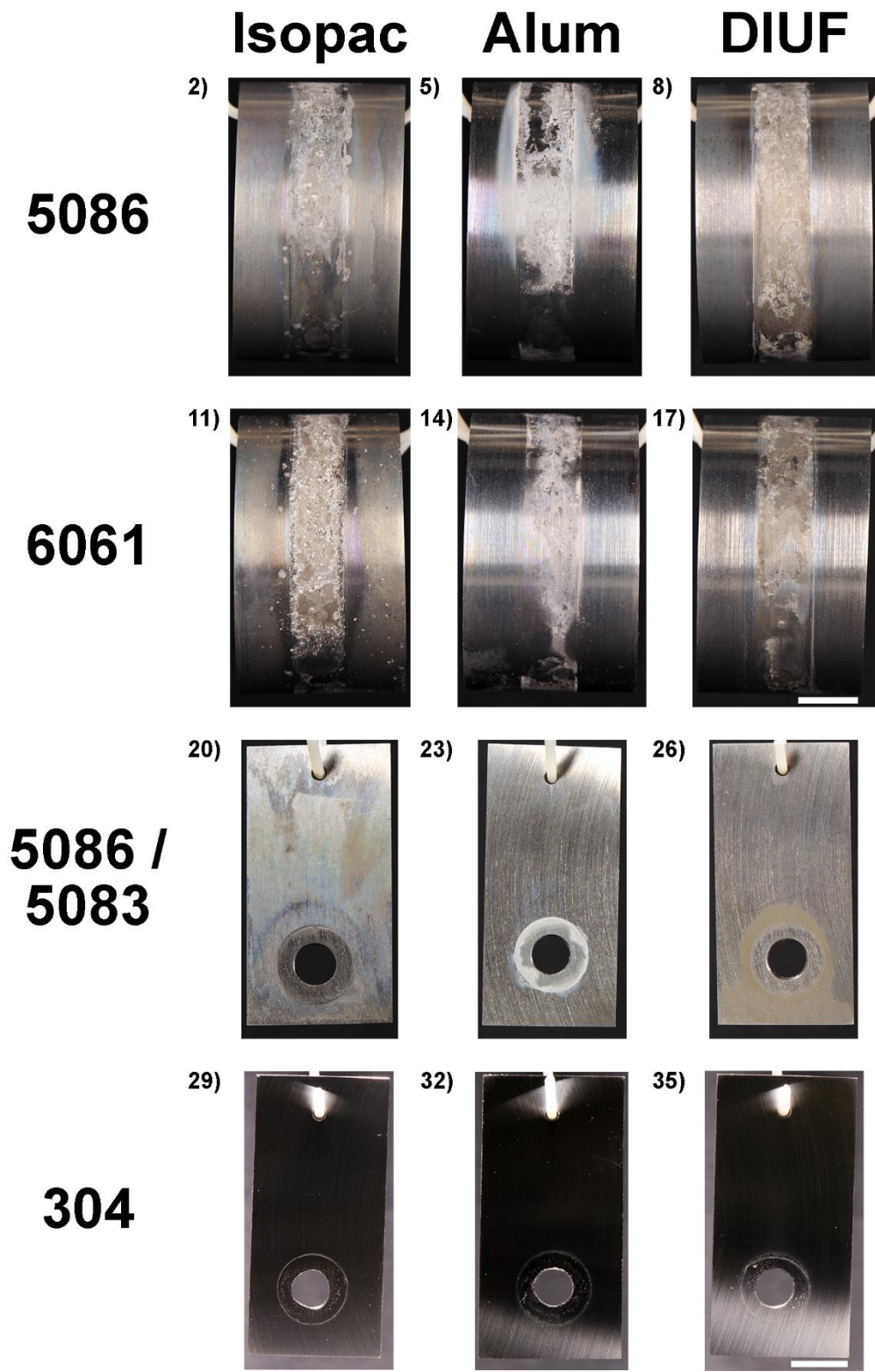


Figure D-5: Composite image of corrosion coupons of different alloys in various test solutions.

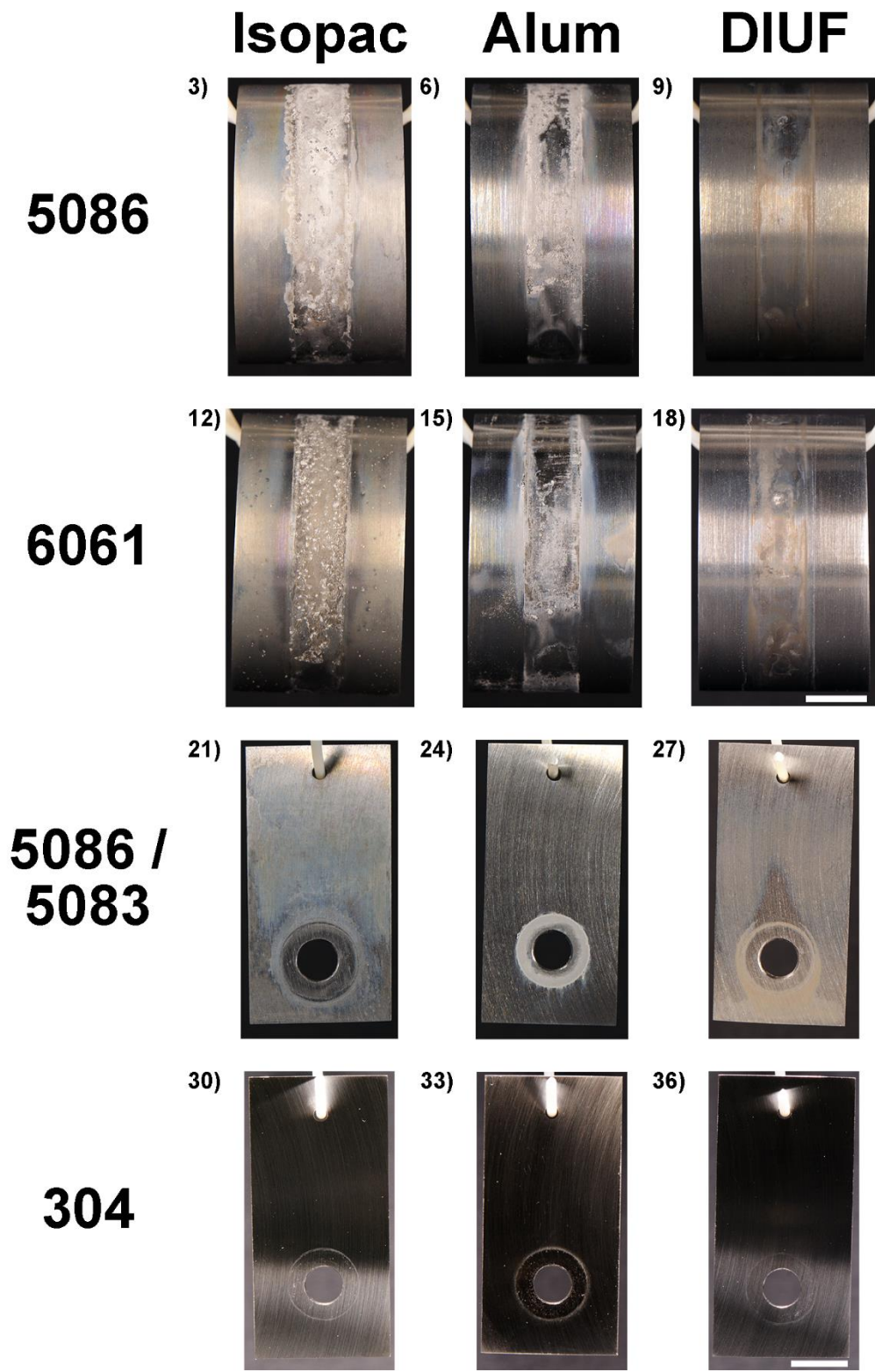


Figure D-6: Composite image of corrosion coupons of different alloys in various test solutions.

# Appendix E – Fourier Transform Infrared (FTIR) Peak Data

## E-1.0 Peak Data

Table E-1: FTIR peak data of aluminum oxides and hydroxides [1].

Phase / Composition	Element Bond Wavenumber (Peak Intensity) [cm <sup>-1</sup> ]			
	OH – Stretch	OH – Bind	Unassigned	Al-O Stretch
Gibbsite / $\gamma$ -Al(OH) <sub>3</sub>	3616.6 (M)	1015.2 (VS)	909.1 (W)	741.8 (S)
	3518.6 (S)	964.3 (M)	826.4 (M)	
	3428.2 (VS)		794.9 (S)	
	3378.4 (M)			
	3361.3 (S)			
Bayerite / $\alpha$ -Al(OH) <sub>3</sub>	3533.6 (M)	1016.2 (S)	862.1 (M)	776.4 (S)
	3518.6 (M)	975.6 (S)	813.0 (M)	
	3454.2 (M)		719.4 (M)	
	3401.3 (M)			
Boehmite / $\gamma$ -AlOOH	3262.6 (S)	1142.8 (M)		740.7 (S)
	3079.8 (S)	1069.5 (S)		
Diaspore / $\alpha$ -AlOOH	2924.0 (VS)	1069.5 (S)		720.0 (VS)
	2341.9 (M)	959.7 (S)		
	2114.2 (M)			
	1984.1 (M)			
Corundum / $\alpha$ -Al <sub>2</sub> O <sub>3</sub>			614.8 (M)	759.9 (VS)
			602.0 (S)	
			559.0 (M)	
			490.0 (W)	
			450.2 (S)	

VS = Very Strong Intensity; S = Strong; M = Medium; W = Weak

Table E-2: FTIR peak data of aluminum oxides and hydroxides [2].

<b>Compound / Composition</b>	<b>Wavenumber [cm<sup>-1</sup>]</b>
Aluminum Oxide / Al <sub>2</sub> O <sub>3</sub>	(600)
	950
	1560
	3500
Boehmite / AlOOH	710
	810
	1100
	1170
	3110
	3250
Bayerite / Al(OH) <sub>3</sub>	690
	810
	1040
	Three peaks near 3560

Table E-3: FTIR peak data of aluminum hydroxide bonds [3].

<b>Bond</b>	<b>Wavenumber Range [cm<sup>-1</sup>]</b>
AlO-H Stretch	3000 – 3700
HOH Bend	1300 – 1700
Al-OH Bend	800 – 1200
Al-O	< 800

Table E-4: Characteristic OH wavenumbers in stretching and bending regions [3].

<b>Phase / Composition</b>	<b>FTIR Peak Wavenumber [cm<sup>-1</sup>]</b>	
	<b>Stretch</b>	<b>Bend</b>
Diaspore / AlOOH	2950	963
Boehmite / AlOOH	3297	1080
	3090	1160
Bayerite / Al(OH) <sub>3</sub>	3655	820
	3618	867
	3550	916
	3470	978
	3431	1014
	3380	1047
Gibbsite / Al(OH) <sub>3</sub>	3623	803
	3530	836
	3474	917
	3396	975
	3380	1025

## E-2.0      References

- [1] K. Wefers and C. Misra, "Oxides and Hydroxides of Aluminum," 1987.
- [2] S. Gustafsson, "Corrosion properties of aluminium alloys and surface treated alloys in tap water," Uppsala University, 2011.
- [3] R. S. Alwitt, "The Aluminum-Water System," in *Oxides and Oxide Films*, Volume 4., J. W. Diggle and A. K. Vijh, Eds. New York, NY: Marcel Dekker, Inc., 1976, pp. 169–254.

# Appendix F – Corrosion Cell Monitoring Data

The following appendix contains the average temperature (T), dissolved oxygen concentration (DO), pH, and chloride concentration ( $[Cl^-]$ ) measurements collected during the 28-day immersion testing for the thirty six corrosion coupons. Table F-1 lists the coupon numbers for each alloy and solution combination. Figures F-1 through F-12 compare the DO, T, and pH measurements for the coupon alloy and electrolyte combinations (three coupons per combination; total of twelve combinations) to the same metrics as measured in the applicable control solution. Figure F-13 compares the previously-mentioned, three parameters between the Isopac, Alum, and DIUF control solutions. Finally, Figure F-14 contains the  $[Cl^-]$  measurements for the tested immersion cells and compares them to the  $[Cl^-]$  measured in the applicable control solution.

All four parameters are plotted as the average of three measurements taken of a single coupon (per combination) tested. The pH and  $[Cl^-]$  confidence intervals ( $n = 3$ ) were used as their respective error bars. Meanwhile, the accuracy of the DO probe ( $\pm 0.3$  °C for T;  $\pm 0.1$  mg/L for DO between 0 and equal to 8 mg/L, and  $\pm 0.2$  mg/L for DO greater than 8 mg/L) was used as the error bars for the T and DO values. (It should be noted that the error associated with the accuracy of both the T and DO measurements were greater than the calculated, respective confidence intervals; hence, the accuracy values were used instead.)

Also included in Figures F-1 through F-14 are shaded regions, which correspond to the operating range of the aeration tank parameters. Finally, DO and T measurements were not collected on day 14 of the DIUF control, and the  $[Cl^-]$  measurement was not collected on day 7 of the DIUF control.

Table F-1: Coupon numbers for the combination of materials and respective solutions used in this study.

	<b>Isopac</b>	<b>Alum</b>	<b>DIUF</b>
<b>5086</b>	1, 2, 3	4, 5, 6	7, 8, 9
<b>6061</b>	10, 11, 12	13, 14, 15	16, 17, 18
<b>5086 / 5083</b>	19, 20, 21	22, 23, 24	25, 26, 27
<b>304</b>	28, 29, 30	31, 32, 33	34, 35, 36

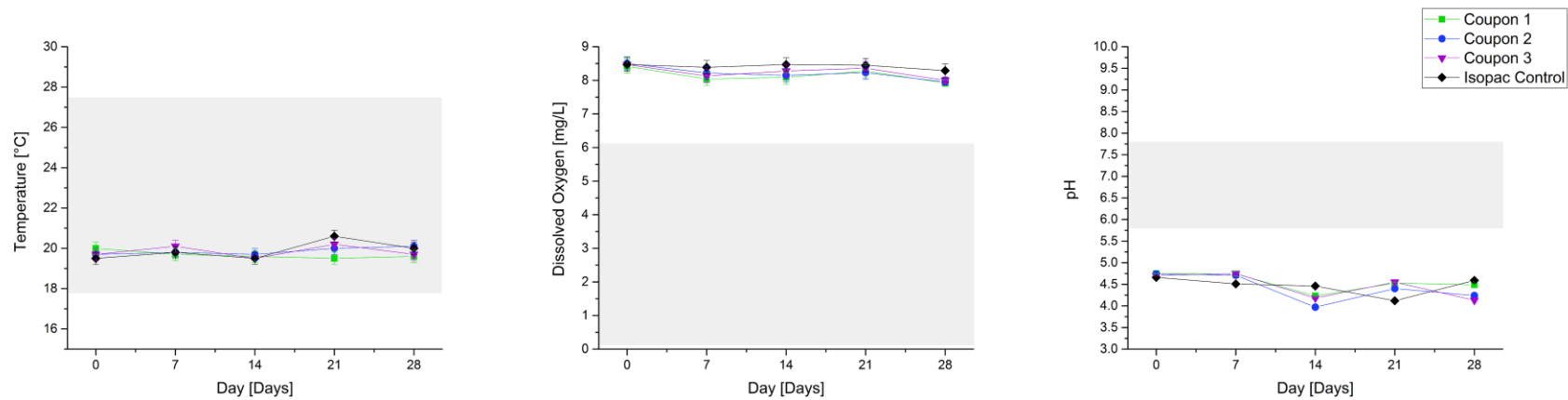


Figure F-1: Average T, DO, and pH measurements for coupons 1 through 3 compared to the Isopac solution. The shaded region in each graph is the operating range of the aeration tank.

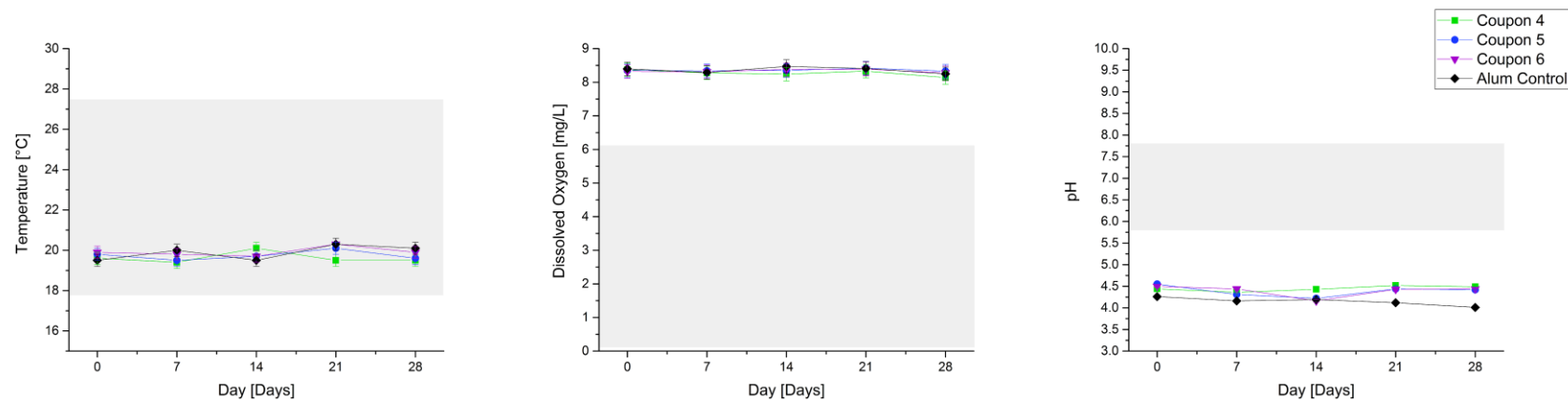


Figure F-2: Average T, DO, and pH measurements for coupons 4 through 6 compared to the Alum solution. The shaded region in each graph is the operating range of the aeration tank.

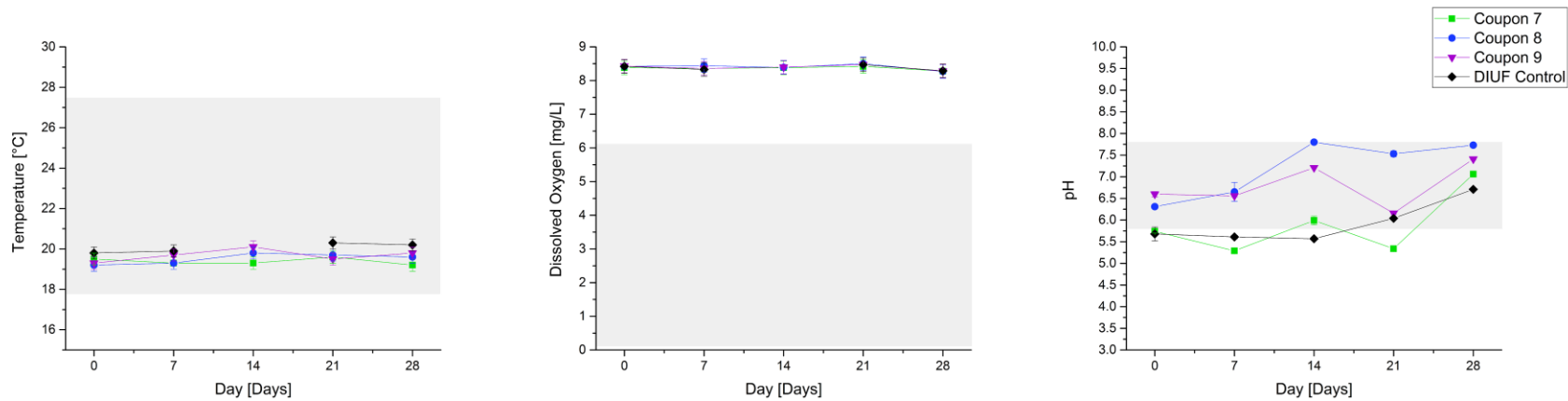


Figure F-3: Average T, DO, and pH measurements for coupons 7 through 9 compared to the DIUF solution. The shaded region in each graph is the operating range of the aeration tank.

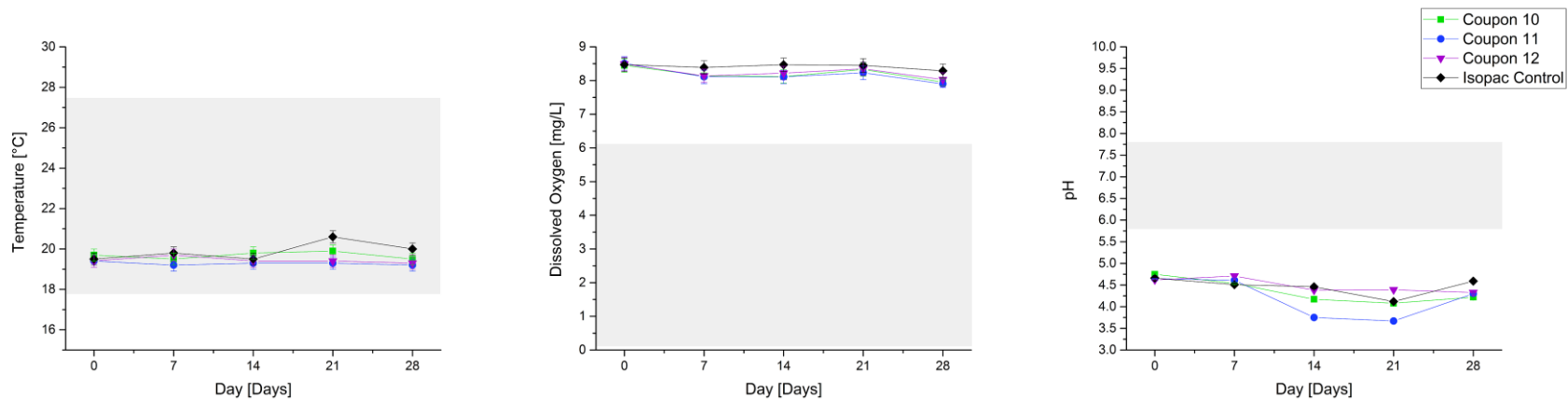


Figure F-4: Average T, DO, and pH measurements for coupons 10 through 12 compared to the Isopac solution. The shaded region in each graph is the operating range of the aeration tank.

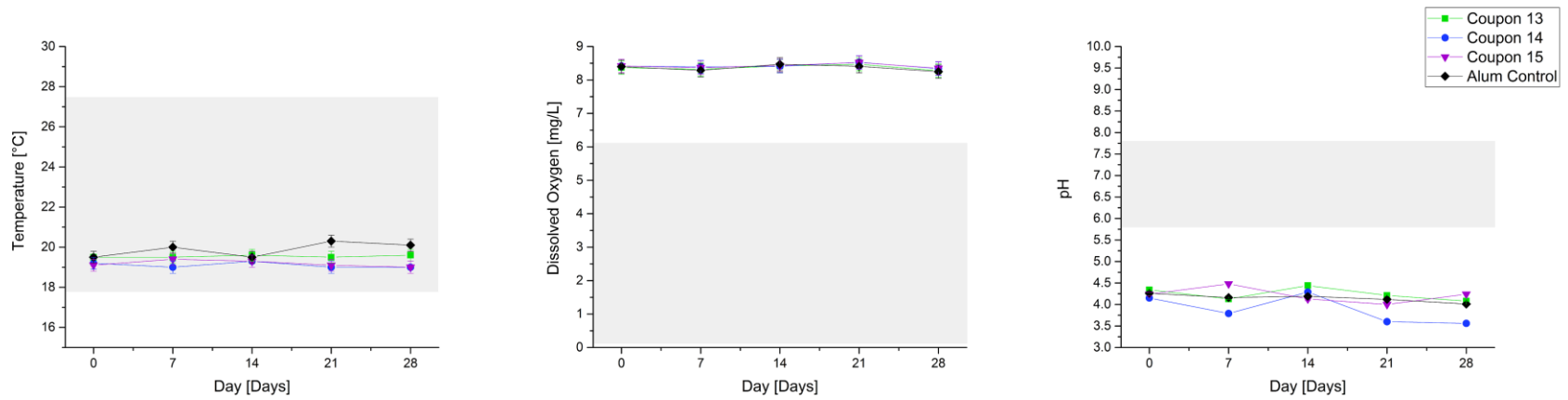


Figure F-5: Average T, DO, and pH measurements for coupons 13 through 15 compared to the Alum solution. The shaded region in each graph is the operating range of the aeration tank.

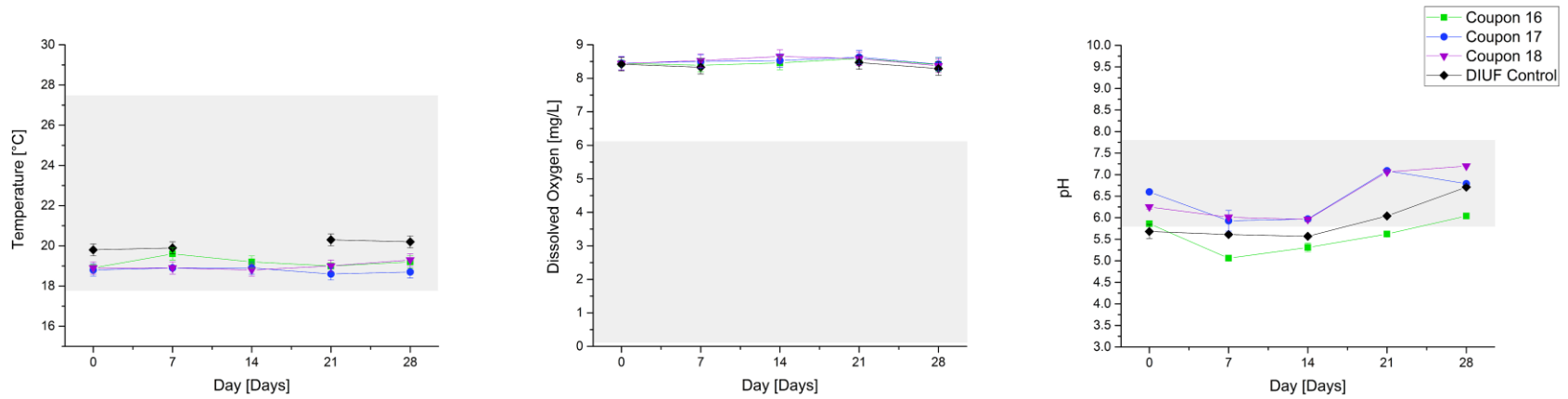


Figure F-6: Average T, DO, and pH measurements for coupons 16 through 18 compared to the DIUF solution. The shaded region in each graph is the operating range of the aeration tank.

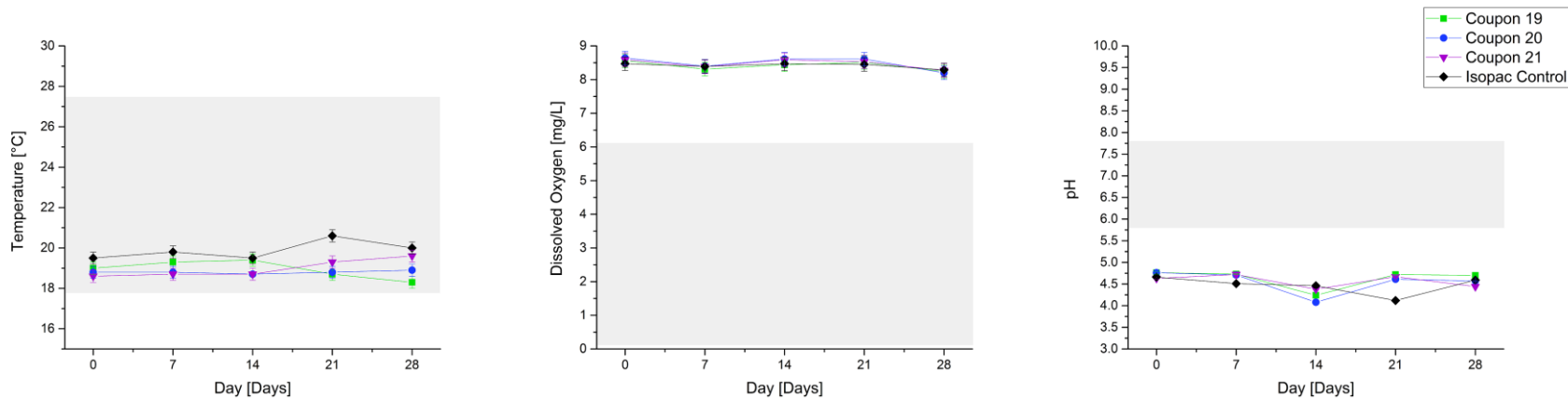


Figure F-7: Average T, DO, and pH measurements for coupons 19 through 21 compared to the Isopac solution. The shaded region in each graph is the operating range of the aeration tank.

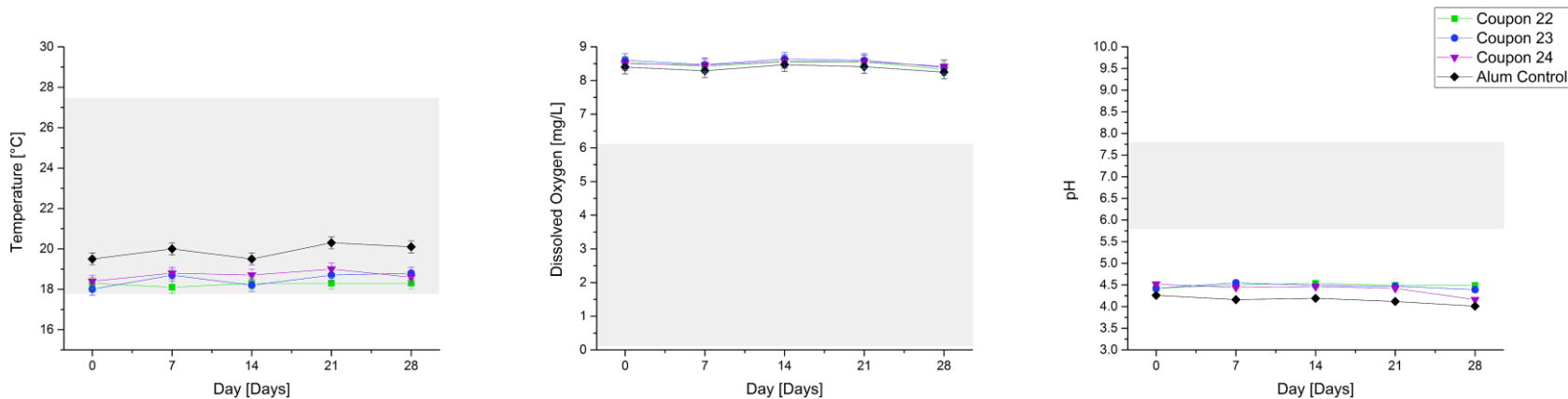


Figure F-8: Average T, DO, and pH measurements for coupons 22 through 24 compared to the Alum solution. The shaded region in each graph is the operating range of the aeration tank.

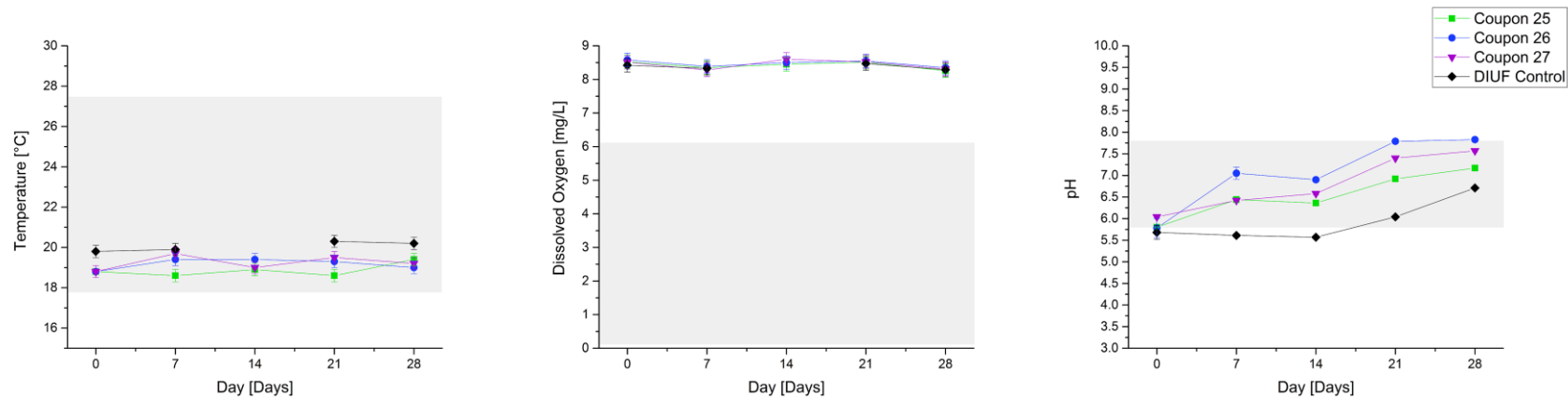


Figure F-9: Average T, DO, and pH measurements for coupons 25 through 27 compared to the DIUF solution. The shaded region in each graph is the operating range of the aeration tank.

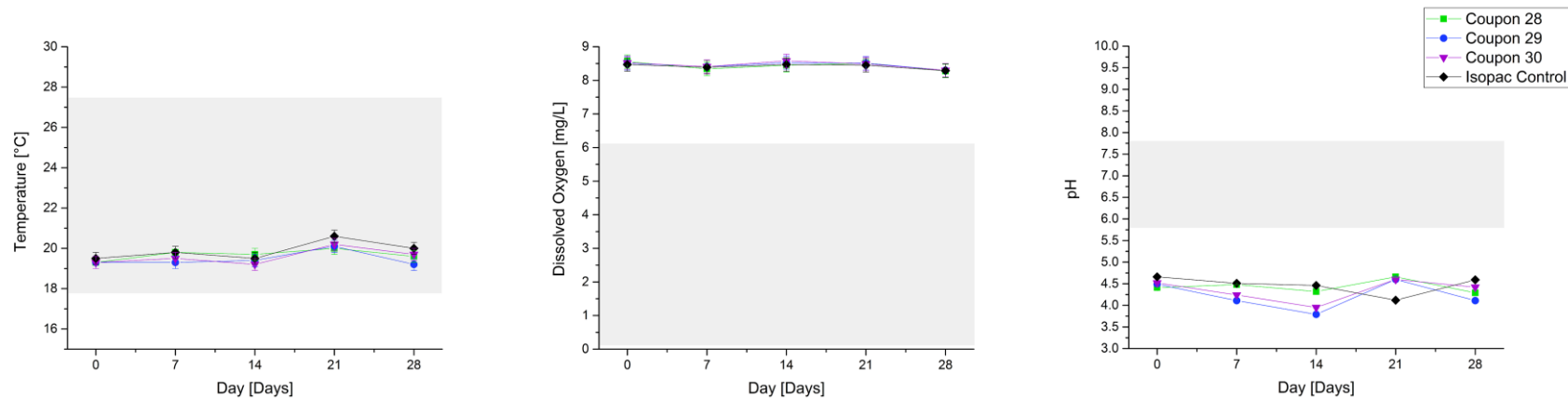


Figure F-10: Average T, DO, and pH measurements for coupons 28 through 30 compared to the Isopac solution. The shaded region in each graph is the operating range of the aeration tank.

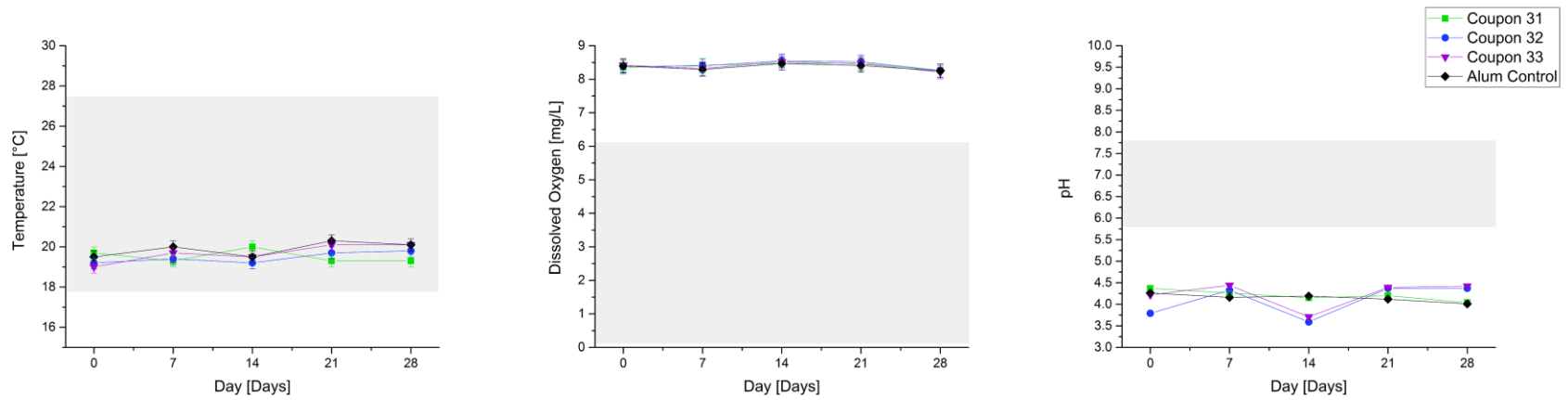


Figure F-11: Average T, DO, and pH measurements for coupons 31 through 33 compared to the Alum solution. The shaded region in each graph is the operating range of the aeration tank.

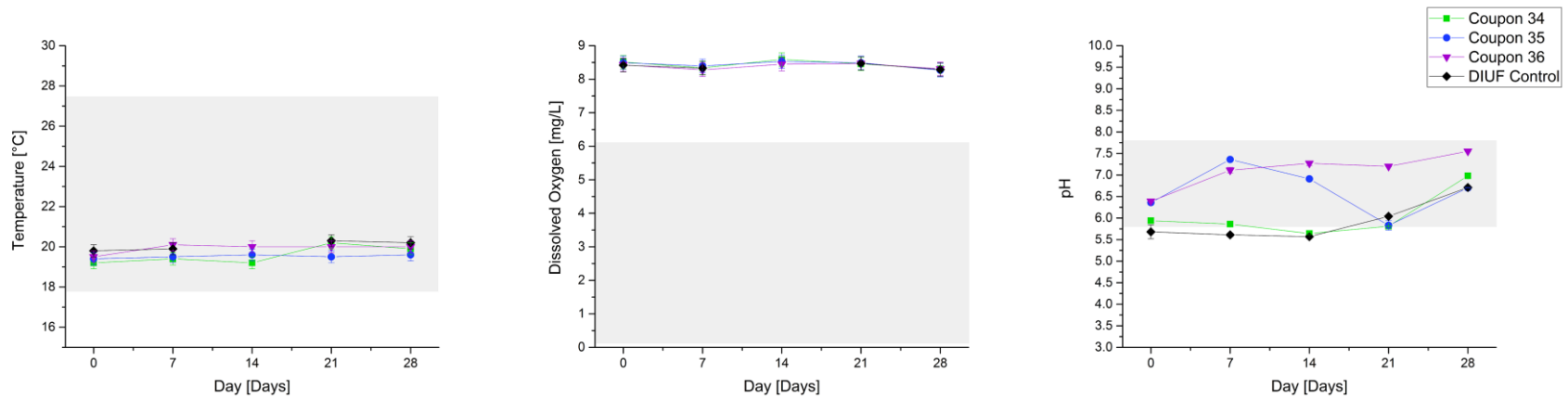


Figure F-12: Average T, DO, and pH measurements for coupons 34 through 36 compared to the DIUF solution. The shaded region in each graph is the operating range of the aeration tank.

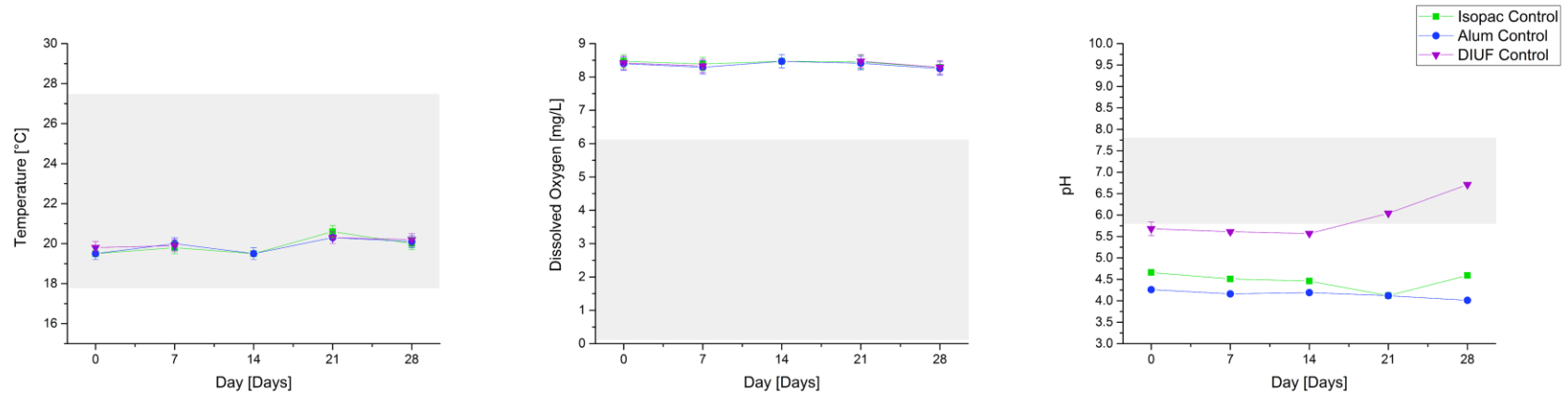


Figure F-13: Average T, DO, and pH measurements for the control solutions. The shaded region in each graph is the operating range of the aeration tank.

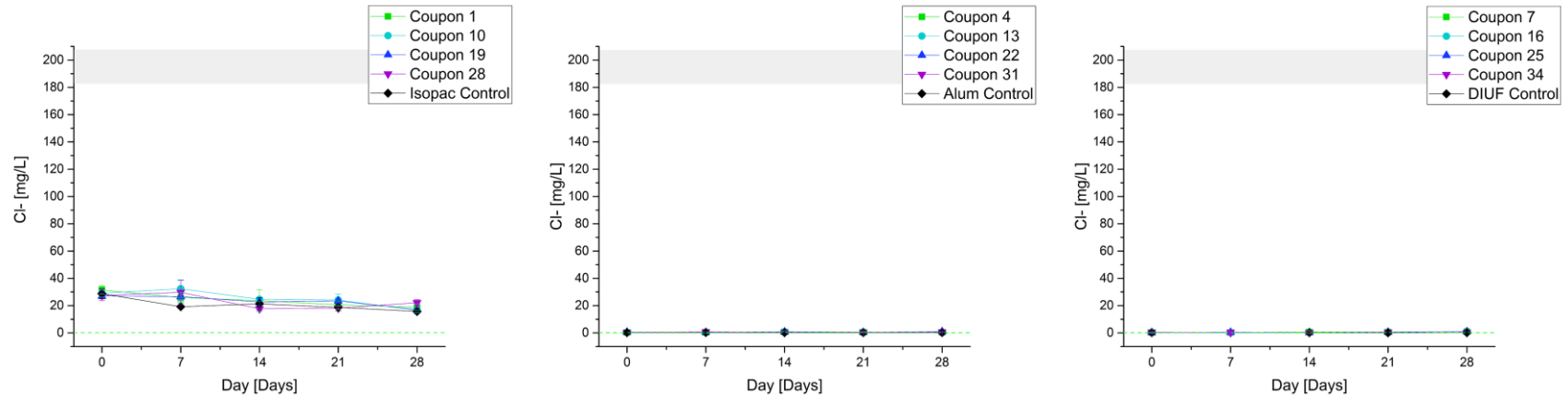


Figure F-14: Average  $Cl^-$  measurements for selected immersion cells compared to relevant control solution. The green dashed lines in the graphs containing the Alum (center) and DIUF (right) measurements is the detectability limit of the  $Cl^-$  probe (at 0.1 mg/L).